Intracellular Uptake of Quantum Dots by Microfluidic Stretching of Live Cells

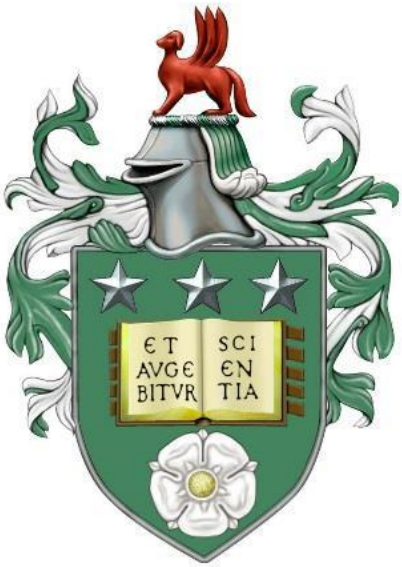

Abiral Tamang

University of Leeds

School of Physics and Astronomy

July 2021

Submitted in accordance with the requirements for the degree of
Doctor of Philosophy

Intellectual Property and attribution of work

The candidate confirms that the work submitted is his own and that appropriate credit has been given where reference has been made to the work of others. This copy has been supplied on the understanding that it is copyright material and that no quotation from the thesis may be published without proper acknowledgement. Others have aided significantly to the completion of this project and the candidate expresses his sincere gratitude for their contributing work. The contribution of others to this work has been explicitly indicated below:

Fern Armistead designed and fabricated the cross-slot microfluidic device. Andrew Harvie synthesised and characterised the Q2NS quinone molecule. Huijie Zhang performed the cyclic voltammetry experiments. Sunjie Ye synthesised the Au-PEG-FITC nanoparticles.

The work involving the FDM microscope discussed in Chapter 5 was performed in collaboration with the Serendipity Lab, University of Tokyo. Hideharu Mikami and Hiroshi Kanno performed the FDM experiments and collected the data. Julia Gala de Pablo and Stephen Evans wrote the MATLAB code for the image extraction and pixel distortion corrections. Sophie Meredith wrote the Python code for FDM image corrections and analysis. Kevin Critchley wrote the Python code to simulate the cell deformation and FDM imaging. In some parts of the thesis, figures have been reproduced from publications with permission from the copyright holder.

The publications co-authored by the candidate during the course of this studentship that did not contribute to the work reported in this thesis are:

1. Sunjie Ye, May C Wheeler, James R McLaughlan, Abiral Tamang, Christine P Diggle, Oscar Cespedes, Alex F Markham, P Louise Coletta, Stephen D Evans. Developing hollow-channel gold nanoflowers as trimodal intracellular nanoprobes. International Journal of Molecular Sciences, 19 (2018), 2327, 1-9.

   AT assisted with cell culture maintenance and confocal imaging

2. Takumi Komikawa, Masayoshi Tanaka, Abiral Tamang, Stephen D Evans, Kevin Critchley, Mina Okochi. Peptide-Functionalized Quantum Dots for Rapid Label-Free Sensing of 2, 4, 6-Trinitrotoluene. Bioconjugate chemistry, 31 (2020), 1400-1407.

AT assisted in the quantum dot synthesis and characterisation.

3. Thanawat Suwatthanarak, Masayoshi Tanaka, Taisuke Minamide, Andrew J Harvie, Abiral Tamang, Kevin Critchley, Stephen D Evans, Mina Okochi. Screening and characterisation of CdTe/CdS quantum dot-binding peptides for material surface functionalisation. RSC Advances, 10 (2020), 8218-8223.

AT assisted in the quantum dot synthesis and characterisation.

For Mum, Da, Julie Di and Little AJ

And

The disciples of the Fenton

Acknowledgements

I would like to thank my supervisor, Dr Kevin Critchley, for the continuous support and encouragement throughout the course of my PhD. I would also like to thank Prof. Stephen Evans for his insightful supervision and for pushing me to do better. My sincere gratitude to the National Overseas Scholarship Scheme, Ministry of Tribal Affairs, Government of India, for sponsoring me for my studies here in Leeds. I thank the Indian Embassy in Birmingham for supporting my stay here in the UK. I would like to thank our collaborators at the University of Tokyo: Prof. Keisuke Goda, Dr Hideharu Mikami and Hiroshi Kanno for letting us use their FDM microscope and for assisting me in the data analysis. I would like to express my gratitude to our collaborating group in the Tokyo Institute of Technology, led by Prof. Mina Okochi and Dr Masayoshi Tanaka for hosting me and for giving me the opportunity to work in their laboratory. I thank Mirei Hayashi, Takumi Komikawa and Thanawat Suwatthanarak for all the interesting side projects, pints and karaoke.

I thank Dr Ben Johnson for all the arrangements and support, especially through many difficult times and for taking care of my every little request. I thank Dr Zabaeda Aslam and Dr Nicole Hondow for helping me with the TEM experiments. Many thanks to Martin Fuller for helping me with the TEM sample preparations. I thank Dr Thomas Hughes and Dr Arindam Pramanik from St. James's Hospital, Leeds for providing us with the different cell lines.

I am very grateful to Fern Armistead for helping me in most of my cell deformation experiments, providing me with the microfluidic devices and for sharing the joy of the most delicious ramen in Tokyo. I thank Andrew Harvie for passing me the quantum dots knowledge, for being a legend and for sharing Ben Stokes' experience at cricket. Thanks to Julia Gala de Pablo for helping me with the coding for FDM and fluorescence data analysis, for the numerous suggestions and for the flexible beta. Sophie Meredith has been immense for writing the code for my FDM analysis and I thank her for being my running buddy and for the delicious Christmas morning eggs benedict. I thank Lucien Roach for helping me with the gold nanoparticle work, for being the greatest housemate and I wish someday he would be 19 feet tall. Many thanks to Christa Brown for helping me with the rheology and DLS measurements and for all the late-night El Faro's and Saltaire beers. I thank Holly Linford for pushing me to work harder when I was struggling, for all the valuable suggestions and for shaving my head. To Christa and Holly,

I will always cherish every third of the dukes' donuts. I thank Sunjie Ye for providing me with the gold nanoparticles, TEM analysis and for delicious hotpots. Many thanks to George Newham for providing me with the silica nanoparticles, for his insightful suggestions and for finishing the bottle of 'Sake' with me. I would like to thank Tahani Algobami for helping me in many of our side projects and for the constant source of enthusiasm. I thank Joel Whipp for helping me with the ICP-MS experiments and for annoying everyone else in the office. I thank Damien Batchelor for training me on rapid prototyping, craft beers and for the amazing tennis and badminton rallies. Many thanks to Huijie Zhang for performing the cyclic voltammetry experiments and for carrying the crashpad to Wales and back. I thank Ashley Hancock for training and helping me on the spectrometers and for losing me at the Fruity. Thanks to Emily Darwin for being the best friend, for Lucy, for the ridiculous climbing sessions and for the burgers at Five Guys. Special thanks to Anne Stikane for sharing the lovely house and for all the binge-watching. Many thanks to Aileen Delaney for organising fun activities and for raising the spirits. I will always cherish the long walks with Samuel Moorcroft; black mirror with Jack Henry, poker with Matthew Hughes, Matthew Bourne, Harrison Laurent and Jordan Tinkler; cricket with Liam Hunter and Jamie Goodchild; basketball in Greece with Grace Porter; Fenton chat with Meghan Innes; and climbing with Delanyo Kpeglo and Shajeth Srigengan. I thank all of MNPeople for the best time I had in Leeds.

Back home, I express my sincere gratitude to Dr Dipankar Mandal for always encouraging me and for all the valuable advice. To my friends Richard, Shradha and Bhawana for always being there for me. To my brother Aditya, whom I will always look up to. To Julie Di for inspiring me to do my best. And to my mum, you are my hero.

Abstract

The redox state of cells is fundamental in regulating many essential cellular functions. In cancer cells, redox behaviour is critical in understanding the progression of the disease and developing potential therapies. Redox sensing in live cells with nanoparticles (NPs) is an attractive prospect, particularly with quantum dots (QDs), due to their inherent stable photoluminescence and versatility in surface functionalisation. Typically, NPs are delivered into live cells through endocytic pathways and remain trapped in vesicles, limiting their ability to probe the cellular environment. Hence, high-throughput non-endocytic delivery of NPs into live cells is highly desirable for intracellular redox sensing.

In this study, non-endocytic uptake of QDs using hydrodynamic cell deformation via a cross-slot microfluidic device has been demonstrated. This shear-induced hydrodynamic stretching of the cells leads to transient membrane disruption, that allows endosome-free delivery of QDs into the cytoplasm. The method is vector-free, inexpensive, high-throughput and reproducible. Confocal fluorescence microscopy showed that increased hydrodynamic deformation leads to an increase in QD delivery. Scanning transmission electron microscopy confirmed that QDs were freely dispersed in the cytoplasm, free from endosomes. Quinone ligand-modified QDs showed reversible quenching depending on its oxidation-reduction state, which was suitable for redox sensing in live cells. The redox-sensitive QDs were introduced into the cells through cell deformation using the cross-slot microfluidic device in breast cancer and non-malignant cells. These redox-sensitive QDs in breast cancer cells having estrogen receptors (MCF7 and T47D) showed higher photoluminescence compared to the cancer cells without these receptors (MDA-MB-231) and the non-malignant cells (MCF10A). Hence, the QD-based redox-probes were capable of sensing the reducing environment in live cells. From the ultrafast fluorescence frequency multiplexer division microscopy, it was observed that there is an outflow of intracellular materials on cell deformation, suggesting that the transport of materials is bi-directional across the membrane pores.

With the potential biological applications, the photoluminescent quantum yield of CdSe quantum rods was enhanced significantly by epitaxial ZnS shell growth and chloride ion treatments. An effort was made to transfer the CdSe/ZnS core/shell quantum rods into the aqueous phase by amphiphilic polymer treatment.

Table of Contents

List of Abbreviations and symbols

$\boldsymbol{A}$	Corrected cell area
AAPH	2,2'-Azobis(2-amidinopropane) dihydrochloride
ADC	Adenocarcinoma
$\boldsymbol{A_c}$	Cross-sectional area of the microfluidic channel
$\boldsymbol{A_s}$	Surface area of the cell
AC	Alternating current
AOD	Acousto-optic deflector
AOFS	Acousto-optic frequency shifter
AM	Acetoxymethyl
ATP	Adenosine triphosphate
AuNP	Gold nanoparticle
$\boldsymbol{A^m}$	Measured cell area
$\boldsymbol{A_p}$	Cell cross-sectional area
BF	Bright field
CCD	Charge coupled device
$\boldsymbol{C_D}$	Drag coefficient
CV	Cyclic voltammogram
D	Diffusion coefficient of QDs
DC	Direct current
$\boldsymbol{D_H}$	Hydraulic diameter
DI	Deformation Index
DLS	Dynamic light scattering
DMEM	Dulbecco's modified eagles medium
DMSO	Dimethyl sulfoxide
DMEM/F-12	Dulbecco's modified eagle medium/nutrient mixture F-12
DNA	Deoxyribonucleic acid
DPBS	Dulbecco's Phosphate Buffer Saline
$\boldsymbol{d}$	Minimum resolvable distance by optical microscope
$\boldsymbol{E}$	Elastic modulus of linear spring
$\boldsymbol{E^o}$	Reduction potential

EDX	Energy dispersive x-ray
EGF	Epidermal Growth Factor
$\boldsymbol{E_{pc}}$	Cathodic peak
$\boldsymbol{E_{pa}}$	Anodic peak
ER	Estrogen receptor
ESCRT	Endosomal sorting complex required for transport
$\boldsymbol{E_n}$	Particle energy
$\boldsymbol{E_g}$	Band gap energy of the bulk material
FAD	Flavin adenine dinucleotide
$\boldsymbol{F_c}$	Compressive force
$\boldsymbol{F_S}$	Shear force
$\boldsymbol{F_T}$	Total force
FBS	Foetal Bovine Serum
FDM	Frequency-division multiplexing
FEG	Field emission gun
FEGTEM	Field emission gun transmission electron microscopy
FITC	Fluorescein isothiocyanate
FL	Fluorescence
FOV	Field of View
FRET	Förster resonance energy transfer
FWHM	Full-width-half-maxima
G	Total QD uptake
GSH/GSSG	Glutathione reduced/oxidised
H	Cell height
h	Plank's constant
$\boldsymbol{h'}$	Height of microfluidic channel
HAADF	High Angle Annular Dark Field
HBS	Half beam splitter
HEK	Human epidermal keratinocytes
HER2	Human epithelial receptor 2
HRTEM	High resolution transmission electron microscopy

i	Imaginary number
ICP-MS	Inductively coupled plasma mass spectrometry
IDC	Invasive ductal carcinoma
IPA	Isopropanol
J	QD diffusion rate
LD_{50}	Lethal dose, 50%
LUMO	Lowest unoccupied molecular orbital
MC	Methyl Cellulose
$\mathbf{m_c}$	Mass of charge carrier
mRNA	messenger ribonucleic acid
MTT	3-(4,5-dimethylthiazol-2-yl)-2,5-diphenyltetrazolium bromide
NAD^+/NADH	Nicotinamide adenine dinucleotide oxidised/reduced
$NADP^+$/NADPH	Nicotinamide adenine dinucleotide phosphate oxidised/reduced
NIR	Near Infrared
NP	Nanoparticle
OD	Optical density
ORR	Optical redox ratio
P_m	Membrane permeability
$\boldsymbol{p}$	Fluid pressure
P_r	Perimeter of the microfluidic channel cross-section
PB	Phosphate buffer
PDMS	Polydimethyl Siloxane
PEG	Polyethylene Glycol
PMAL	Poly(maleic anhydride-alt-1-tetradecene), 3-(dimethylamino)-1-propylamine derivative
PL	Photoluminescent
PLQY	Photoluminescent quantum yield
PR	Progesterone receptor
$\boldsymbol{P_o}$	Membrane permeability at deformation
Q	Flow rate
QAM	Quadrature amplitude modulation
QD	Quantum dot

QnNS	Ubiquinone
QR	Quantum rod
Q2NS	Ubiquinone-modified ligand
R	Radius of the QD
RA-QD	Redox active-quantum dot
RNA	Ribonucleic acid
ROS	Reactive oxygen species
RPMI 1640	Roswell Park Memorial Institute (RPMI) 1640 (cell culture medium)
Re	Reynolds number
$\boldsymbol{R_c}$	Channel Reynolds number
$\boldsymbol{R_p}$	Particle Reynolds number
r	Distance from the centre of the QD
r_p	Radius of the particle
$\boldsymbol{r_d}$	Donor-acceptor distance
SAED	Selected area electron diffraction
SD	Standard deviation
SDC	Spatial dual-comb
SE	Standard error
SERS	Surface enhanced Raman spectroscopy
SHE	Standard hydrogen electrode
SNR	Signal-to-noise
STEM	Scanning transmission electron microscope
TCSPC	Time-correlated single photon counting
TDPA	Tetradecylphosphonic acid
TEM	Transmission electron microscopy
TGA	Thioglycolic acid
TOPO	Trioctylphosphine oxide
TOP	Trioctylphosphine
Trx	Thioredoxin
U	Velocity of the fluid
UV	Ultra-violet
V	Potential energy of the electron

Vis	Visible
v_{max}^{s}	Amplitude scan velocity
W	Cell width
$\mathbf{w}$	Width of microfluidic channel
$Zn(DDTC)_2$	Zinc diethyldithiocarbamate
$\boldsymbol{\Psi}$	Particle wave function
$\Delta \boldsymbol{E}$	Emission energy of the QD
$\boldsymbol{\mu_m}$	Reduced mass
$\boldsymbol{m_e^*}$	Effective mass of the excited electron
$\boldsymbol{m_h^*}$	Effective mass of the excited hole
μ	Viscosity
$\dot{\boldsymbol{\gamma}}$	Strain rate
$\boldsymbol{\sigma(t)}$	Applied stress
$\boldsymbol{\sigma_0}$	Maximum stress
$\boldsymbol{\varepsilon(t)}$	Strain
$\boldsymbol{\eta}$	Viscosity of dashpot
λ	Wavelength
n	Refractive index
θ′	Half convergence angle of the focus of lens
θ	Initial phase shift in the velocity waveform
$\boldsymbol{\rho}$	Fluid density

List of Figures

microfluidic device (bright field (BF), fluorescent (FL) and merged channels). The corrected normalised total fluorescence intensity scatter trace plots from the cells for b) 5 and c) 10 µl/min flow rates. d) Comparative normalised total fluorescence intensity from a typical event before and after the scan velocity related distortion correction. Each point represents the position of the cell during its motion in the FOV. The colour of the point represents the normalised total PL-intensity from the cells with respect to the scale bar on the bottom right of the figure. The arrows indicate the direction of flow.

Figure 5-4. Correction on the FDM microscope images due to the lifetime effect of the fluorophore. a) Schematic of the FOV with cell in the extensional flow region of the cross-slot microfluidic device as a function of modulation frequency along the y-direction. b) The amplitude of function $R(y)$, which is the correction functions curve for the FDM images as a function of the modulation frequency for calcein (τ = 2.9 ns).

Figure 5-5. The normalised total fluorescence intensity scatter trace plots for the FDM images of MCF7 cells stained with calcein with the scan velocity profile correction and the lifetime effect of the fluorophore correction from the cells deformed through the cross-slot microfluidic device for a) 5 and b) 10 µl/min flow rates. c) Comparative normalised total fluorescence intensity from a typical event before and after the lifetime effect correction for calcein (τ = 2.9 ns). Each point represents the position of the cell during its motion in the FOV. The colour of the point represents the normalised total PL-intensity from the cells with respect to the scale bar on the right of the figure. The arrows indicate the direction of flow.

Figure 5-6. Normalized total fluorescence intensity from a typical single-cell event as observed through the FDM at the extensional flow region of the cross-slot microfluidic device with stained with calcein at a) 5 ul/min and b) 10 ul/min flow rates. The solid red lines represent exponential decay fits (R^2 > 0.96).

Figure 5-7. Schematic of the FDM image distortion due to cell motion with respect to the scan directions when the cells move a) perpendicular and down, b) perpendicular and up, (c) parallel and left, and d) parallel and right to the scan direction (the dashed lines showing the actual cell size).

Figure 5-8. The comparative normalised total fluorescence intensity scatter trace plots for the FDM images of MCF7 cells stained with calcein, before and after the cell motion distortion corrections. The scan velocity profile correction and the lifetime effect of the fluorophore corrections were performed for all plots prior to the analysis. a) The uncorrected and b) corrected scatter plots for distortion due to cell motion for Q = 5 and 10 µl/min, respectively. Each point represents the position of the cell during its motion in the FOV. The colour of the point represents the normalised total PL-intensity from the cells with respect to the scale bar on the right of the figure. The arrows indicate the direction of flow.

Figure 5-9. Typical events of cell deformation captured using FDM, with and without the cell motion distortion correction for MCF7 cells stained with 1 µM calcein, deformed through the cross-slot microfluidic device. Plots for Q = 5 µl/min with the frame number showing a) the change in the cell area, b) the normalised fluorescence intensity and for Q = 10 µl/min with c) change in cell area and d) the normalised fluorescence intensity, with and without the correction to distortion due to cell motion.

Figure 5-10. Normalised mean total fluorescence intensity of Calcein luminescence from MCF7 cells from the FDM images as a function of distance travelled in the extensional flow region of the cross-slot microfluidic device for a) 5 µl/min and b) 10 µl/min flow rates, with and without the correction for the distortion due to cell motion. Data expressed as mean ± SD (N >350 events). These plots are derived from the scatter trace plots shown in Figure 5-8.

Figure 5-11. Comparative normalised mean total fluorescence intensity from MCF7 cells stained with calcein as a function of distance travelled in the extensional flow region of the cross-slot microfluidic device from the FDM images for a) 5 µl/min and b) 10 µl/min flow rates. Data expressed as mean ± SD (N >350 events)

Figure 5-12. Results of the simulation of the cell distortion due to the motion of the cells with respect to the scanning beam velocity for a circle of radius 14 µm. a) the radii in x- and y-direction and b) the position of the circle for a maximum cell speed ~ 2% of the scan velocity which is equivalent to the Q = 5 µl/min data. c) the radii and d) the position of the circle in the FOV for maximum cell speed ~4% of the scan velocity, equivalent to Q = 10 µl/min data.

Figure 5-13. Results of the simulation of the cell distortion due to the motion of the cells with respect to the scanning beam velocity for a circle of radius 14 µm. a) Typical images of the simulated circle showing distortion, moving at a cell speed of 7 % of the scan velocity. The cells move downwards for images i-iv and across towards the right for images v-viii. The cell radii in x- and y-directions for cell speed equal to b) 7, c) 10 and d) 20 % of the scanning beam speed. e) the percentage distortion in the area of the cell as measured by the simulation of cell distortion with respect to the flow rate. The fitting curve(red line) is an exponential growth with R^2> 0.99.

Figure 5-14. Typical FDM images of the MCF7 stained with calcein cells without distortion corrections (Bright field, FL channel and merged) post deformation at a) region 1 and b) region 2. The arrows represent the direction of flow.

Figure 5-15. Typical FDM images of the MCF7 stained with calcein cells with the distortion corrections (Bright field, FL channel and merged) post deformation at a) region 1 and b) region 2. The arrows represent the direction of flow.

Figure 5-16. FDM analysis of MCF7 cells stained with calcein, post deformation at regions 1 and 2 (Q = 100 µl/min). Comparative a) DI, b) mean total fluorescence emission intensity from the cells for the two regions (Data expressed as mean ± SE). The 2-sample t-test showed the p-values for the pair were <0.001. The scatter plots show the total fluorescence intensity from the cells as a function of cell area for regions c) 1 and d) 2.

Figure 5-17. Optical characterisation of Au-FITC NPs. a) The absorbance spectra, b) the emission spectra and c) hydrodynamic size measured using DLS of the Au-FITC NPs for different batches having different sizes.

Figure 5-18. TEM images of the Au-FITC NPs of different sizes used for the uptake study in MCF7 cells using microfluidic deformation experiments for a) batch 'A', b) batch 'B' and c) batch 'C'. d) Size distribution histogram of the Au-FITC NPs from the TEM images with log-normal fitting curves.

Figure 6-3. Typical UV-Vis and PL emission spectra of CdSe QRs synthetised with six rapid injections of the Se-precursors every 5 min.

Figure 6-4. TEM images of CdSe QRs for six Se-precursor injections at intervals of a) 3 min and b) 5 min with i) dark field images, histograms of the ii) length, iii) width and iv) aspect ratio of the rods (N >500 each). c) Elemental mapping of the QRs with i) bright field and the corresponding ii) Se, iii) Cd and iv) merged maps.

the inset shows the CdSe core and CdSe/ZnS (3h shell growth) QRs under UV illumination. In d) the solid lines represent the actual traces and the dotted lines represents the bi-exponential decay fits (R^2 >0.99 for all cases). e) Lifetime decay constants and f) decay amplitudes of the bi-exponential fits with the number of Se-precursor injections. Data expressed as mean ± S.D.

Figure 6-7. TEM images of a)CdSe core QRs and b) CdSe/ZnS core/shell QRs with histograms of length, width and aspect ratio (N >300 each). The histograms are presented with normal distribution.

Figure 6-8. Schematic showing the passivation of the surface traps on the CdSe QRs with the TDPA-$CdCl_2$ treatment.

Figure 6-9. Cl^- ion treatment of the CdSe QRs. a) PL emission spectra (inset: QRs under UV-light), b) UV-Vis absorbance spectra and c) PLQY of the untreated, 96 and 192 Cl^- ions/nm^2 of QR surface. d) PLQY of the Cl^- treated CdSe rods 24 h post-treatment with and without cleaning. e) Normalised PL intensity decay traces of the Cl^- treated QRs. The solid lines represent the actual traces and the dotted lines are the bi-exponential fits (R^2 > 0.99 each). e) Lifetime decay constants and f) decay amplitudes of the bi-exponential fits with the number of Se-precursor injections. Data expressed as mean ± SD.

Figure 6-10. TEM images of CdSe QRs treated with 192 Cl^- ions/nm^2 of QR surface.

Figure 6-10. Schematic showing the encapsulation of the CdSe/ZnS core/shell QRs with the amphiphilic PMAL to convert from hydrophobic to hydrophilic particles.

Figure 6-11. Conversion of hydrophobic CdSe/ZnS QRs in chloroform into and hydrophilic rods. a) The fluorescence emission spectra (b) total integrated emission and (c) PLQY of the hydrophilic QRs with different PMAL:QR ratios. The control QRs with PMAL:QR = 0 represents the hydrophobic QRs in chloroform for comparison. The insets of b) and c) show the transition of the QRs from the hydrophobic state in chloroform to aqueous phase in white and UV-light, respectively.

List of Tables

1. Introduction and background

1.1. Overview

The aim of this study was to investigate the importance of cytosolic redox-sensing in live cells. The redox environment is crucial in determining the fate of the cells and many cellular functions. Most cancer cells have a more reducing cytoplasmic environment than healthy cells. Understanding the redox behaviour of different cancer cells is essential in deciphering the development and progression of the disease, and thus advancing therapies. Biosensing in live cells using nanoparticles (NPs) an extremely active area of research, with quantum dots (QDs) being particularly attractive due to their characteristic stable photoluminescence and adaptability of surface functionalisation. Here, the aim was to sense the reducing cytoplasm of different live breast cancer cells with QDs engineered for redox-sensing.

High-throughput delivery of NPs to live cells is highly desirable for intracellular imaging and sensing. However, the NPs delivered through endocytic pathways remain trapped within endosomes which severely limit their ability to probe the cytoplasm. Several methods of particle delivery have been reported in the literature with varying degrees of success. Non-endocytic delivery of QDs by cell membrane disruption of cells using microfluidic devices has proven to be reproducible, vector-free, high throughput and inexpensive. This project used hydrodynamic cell deformation in a microfluidic device to generate transient membrane pores, allowing non-endocytic delivery of QDs. A cross-slot microfluidic device was used, where shear forces were found to induce optimum QD uptake.

Redox sensitive QDs were fabricated by conjugating quinone electron accepting ligands to the QDs. The quinone in its oxidised form was capable of quenching the QD emission by capturing the excited electron from the conduction band. However, when the quinone was reduced, the quenching mechanism was suppressed and the QD photoluminescence was restored. This reversible switching of the QD emission, depending on the redox state of the quinone ligand is suitable for sensing the redox environment in cells. The redox-sensitive QDs were introduced into the cells using the cross-slot microfluidic device for non-endocytic delivery in breast cancer and non-malignant cells. Comparisons were made using the redox-sensitive QDs between the

breast cancer cells having estrogen receptors (MCF7 and T47D), the cancer cells without the estrogen receptors (MDA-MB-231) and non-malignant cells (MCF10A).

It is also essential to understand the nature of particle uptake and the fate of the cell on hydrodynamic deformation. An effort was made to understand the nature of the flow of fluids through the membrane pores using high-speed confocal microscopy. This would give insight into the fundamental understanding of cells under mechanical stress and membrane poration.

To study the effect of particle geometry on cellular uptake, attempts to enhance the photoluminescence of CdSe quantum rods were made. Quantum rods (QRs) have interesting optical properties but suffer from low photoluminescence efficiency. This is because QRs have a large surface-to-volume ratio which leave many surface traps for the excited electrons that prevent radiative recombination. Two different methods, epitaxial ZnS shell growth and halide passivation using chloride ions were adopted to passivate the surface traps and improve the photoluminescence efficiency of CdSe QRs. QRs could be transferred into aqueous phase using amphiphilic polymers which are suitable for biological applications.

1.2. Quantum dots

QDs are semiconductor nanoparticles that typically have a diameter of 10 nm or less. Due to their small size, being comparable to the Bohr exciton radius, their electronic properties differ greatly from the bulk material [1]. For a bulk semiconductor material, a forbidden bandgap exists between the valence and the conduction bands. An electron from the valence band can be excited thermally to the conduction band at finite temperatures, making them capable of electrical conduction. However, as the size of the material decreases below the Bohr exciton radius, the electronic band structure becomes more discrete (figure 1-1a). As a result, the QD electronic structure resembles an individual atom and are sometimes referred to as artificial atoms [2]. QDs bridge the gap between bulk material and molecules. This phenomenon is called quantum confinement and can be understood by applying Schrödinger's time-independent equation to the QD charge carriers,

$$E\Psi(r,\theta,\phi) = -\frac{\hbar^2}{2m_c}\nabla^2\Psi(r,\theta,\phi) + U\Psi(r,\theta,\phi) \qquad (1.1)$$

where $\hbar$ is $h/2\pi$ with h being the Plank's constant, m_c is the mass of the charge carrier, $U(r,\theta,\phi)$ is the potential energy, and $\Psi(r,\theta,\phi)$ is the particle wave function. If the electron and the holes are always inside the QD, then we can assume that the potential outside the QD is infinite. Hence, the system is similar to a particle in a box, with the surface of the QD defining the walls of the box [3]. As such, the solution for Schrödinger's equation, modified for a sphere, and using spherical coordinates is given as:

$$\Psi_n(r) = \frac{1}{r\sqrt{2\pi R}} \sin\left(\frac{n\pi r}{R}\right) \tag{1.2}$$

$$\text{with} \quad E_n = \frac{\hbar^2 n^2}{2m_c R^2} \quad ;n = 1,2,3,\ldots \tag{1.3}$$

Here, r is the distance from the centre of the QD, R is the radius of the QD and E_n is the carrier energy. Equation 1.3 demonstrates the particle in a box behaviour of the QD. It also shows that with the decrease in QD size, the absorption energy increases, as a result, the bandgap increases with the decrease of the size of the nanocrystals which is called the quantum size effect (Figure 1-1a). For example, the bandgap can be tuned between 2.5 and 4.0 eV depending on the size of the CdS QDs [4,5]. An electron excitation creates two charges, the electron in the conduction band and the hole in the valence band, which are collectively termed as "exciton". The exciton collectively propagates with a reduced mass μ_m given as:

$$\frac{1}{\mu_m} = \frac{1}{m_e^*} + \frac{1}{m_h^*} \tag{1.4}$$

Here, m_e^* and m_h^* represent the effective mass of the excited electron and hole, respectively. The relation between the emission energy of the QD with the size of the particle-based on effective mass approximation is given by the Brus equation as follows:

$$\Delta E(r_p) = E_g(r_p) + \frac{h^2}{8{r_p}^2}\frac{1}{\mu_m} \tag{1.5}$$

where $\Delta E(r)$ is the emission energy of the QD, $E_g(r)$ is the bandgap energy of the bulk material, which is characteristic of the material, and r_p is the radius of the particle [6]. The second term on the right-hand side of the equation is manifested due to the quantum confinement. The equation explains that the energy of the emitted light, and consequently its wavelength, depends on the QD size. As such, the size-controlled tuneable band gap of QDs

contributes to its wide applications in optoelectronics, optical and biomedical imaging, biosensing and as probing/delivery agents.

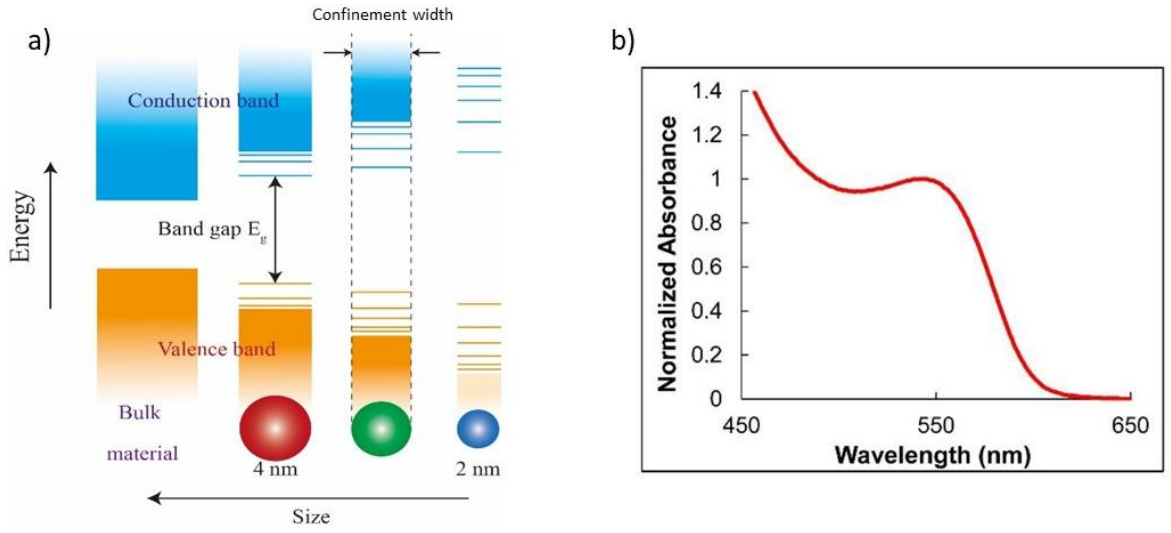

Figure 1-1. a) Size dependent band structure of QDs in comparison to bulk material and b) a typical absorption spectrum of QDs (Image taken from [7]*).*

1.2.1. Photon absorption and emission by QDs

Typical absorption spectrum of a QD sample is given in Figure 1-1b. If the photon has enough energy to excite the electron to the discrete energy levels past the bandgap, the QD is in the excited state. If the photon energy is below the minimum energy required for excitation, there will be no absorption. This corresponds to the higher wavelength region in Figure 1-1b. As the energy of the exciting photon increases (decreasing wavelength), the first order excitation peak (1s) becomes visible which is termed as the first excitation peak. However, we must understand that QDs in a given sample are polydisperse and would have different energies corresponding to the first excitation peak. Hence, the width of the peak would depend on the degree of particle polydispersity. Beyond the first excitation peak, the energy levels become more tightly packed as seen in the schematic of figure 1-1a. As a result, for excitation with photons of higher energies (lower wavelengths), the individual absorption peaks become difficult to resolve.

After the absorption of the photon, a so-called "hot" electron-hole pair is generated [8]. The exciton then cools through a combination of phonon emissions and Auger processes, such that

the electrons and the holes make their way to the conduction band minimum and valence band maximum, typically with a lifetime of the order of a few picoseconds [9–11]. Finally, the electron and the hole recombine by giving out energy in the form of fluorescence.

1.2.2. Surface traps and passivation

For the small size of the particles, the surface properties become very influential. Since the surface-to-volume ratio of QDs is significantly high, a large number of atoms are on the surface giving rise to unsaturated dangling bonds. These bonds have electronically active states which act as "surface traps" for both electrons and holes (Figure 1-2), causing recombination of the electron-hole pairs through non-radiative processes [12]. As such, the photoluminescent quantum yield (PLQY) of the QDs is significantly dropped.

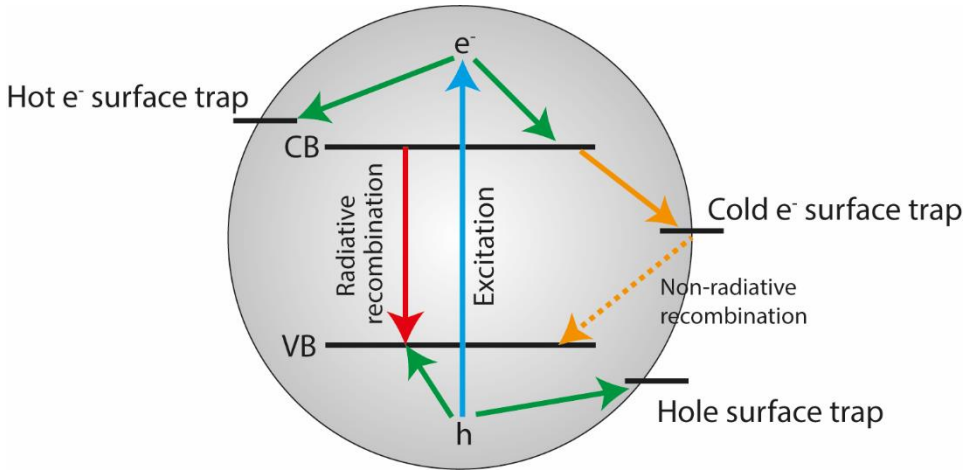

Figure 1-2. Schematic for the possible charge recombination and trapping in QDs. VB and CB represent the valence and the conduction bands, respectively.

1.2.2.1. Ligand passivation

Typically, QD surfaces are passivated with organic ligands which suppress some of the surface trap states by forming a bond where the 'dangling bond' would have existed. The surface ligands also colloidally stabilize the particles, decrease the toxicity, enhance solubility and functionality with the use of desired molecules [13–16]. Ligand selection is crucial and has a considerable effect on the quality of the QD performances. The presence of the passivating

ligand helps in the nucleation process during the QD synthesis by regulating the availability of reagents, the morphology and the size distribution of the particles, growth rate and reaction pathways [17]. Depending on the application, a wide range of ligands can be used to passivate the QDs. For example, the ligands can be charged, neutral or zwitterionic. In addition, They can be solubilizing ligands such as polyethylene glycol (PEG), lipids and polymers [13]. Functional ligands for sensing, delivery and targeting have been used which can range from small molecules, proteins and polymers, to peptides and exotic complexes [18,19]. The role of ligands in colloidal QDs will be discussed in section 1.2.2.2.

1.2.2.2. Colloidal QDs in aqueous phase

Colloidal stability of QDs would require them to be freely dispersed in the suspension medium. The surface ligands play an important role in providing this stability to the QDs, in addition to their role in surface trap passivation and functionalisation. Typically, QD synthesis requires high temperature, as such, organic solvents are more favourable. This requires ligands to be hydrophobic. However, for the purpose of biological applications, QDs need to be in the aqueous phase and hence have hydrophilic ligands. The conversion from hydrophobic to hydrophilic QDs can be approached in several ways. The most common way is through ligand exchange, which involves removal of hydrophobic ligands, simultaneous replacement with hydrophilic ligand and transfer into the aqueous phase [20–22]. However, the process is usually sensitive to many factors such as temperature, pH, ionic strength, and reagent concentrations, making it extremely challenging. In addition, the ligand exchange procedure can cause the QD properties to degrade due to incomplete ligand replacement. This can produce increased number of surface trap states to emerge causing the PLQY to decrease [23]. Another approach is to encapsulate the QDs with amphiphilic polymers which can conceal the hydrophobic ligands [24–26]. Although this method is significantly easier compared to the ligand exchange, the addition of large polymers increases the overall hydrodynamic size of the QDs and decrease the control over the surface chemistry. Coating the hydrophobic QDs with lipids is another way of achieving the hydrophilicity of QDs. The amphiphilic nature of lipids allows the encapsulation of QDs in micelles [27,28]. Alternatively, synthesis of QDs in the aqueous phase have been developed recently which can bypass the complication of ligand modification [29–31]. This is

achieved by using small molecules with amine or carboxyl functional groups which ensure colloidal stability in the aqueous phase.

Thiol derivatives are efficient ligands in passivating surface electron traps that show a high binding constant with Cd-based QDs. As such, they are widely used in QD functionalisation [32–34]. However, it was also observed that excess thiol quenched the emission, decreasing the PLQY [35]. This arises due to the presence of three lone pairs on the S-atom of the thiolate. One lone pair can donate electrons to the Cd^{2+} orbitals while the other two remaining lone pairs act as hole traps in the valence band [36]. For CdTe QDs stabilised with thioglycolic acid (TGA) (which is the QD used for experiments in this thesis) a lower proportion of TGA yields a higher concentration of Cd-thiol complexes, giving better surface passivation [23,37]. Hence optimisation of TGA/ Cd^{2+} ratio can give high PLQY QDs colloidally stable in the aqueous environment [38].

1.2.2.3. Shell passivation

The steric hindrance between the ligand molecules does not allow all trap states on the surface to be passivated. To overcome this insufficient passivation of surface traps, the QD "core" is passivated by shell growth with a material having a different bandgap, creating a potential barrier around the core [39–40]. Depending on the relative band structure of the shell material in comparison to the core, the core/shell QDs can be classified into three categories as illustrated in Figure 1-3.

When the shell material grown on the QDs core has a higher bandgap (e.g. CdSe/ZnS, InP/ZnS and $CuInS_2$/ZnS core/shells), the exciton is confined within the core [40–42]. This is similar to QDs with just cores, however, the passivation of the surface trap improves the PLQY and photochemical stability and is the Type-I core/shell QDs (Figure 1-3a) [43].

For the Type-II QDs, one of the conduction or valence band edges of the shell lies in the bandgap of the core, as such, there is a separation of the electron and the holes into different regions (Figure 1-3b). In other words, the staggering band alignment ensures one of the charges will be confined to the shell while the other is in the core [41]. This spatial separation allows efficient extraction of charges, as the recombination lifetime of the exciton is much

larger compared to just the cores. Hence, they are suitable for many photovoltaic and photoconduction applications such as photoelectrochemical cells and QD-sensitised solar cells [43–44]. Some examples of Type-II core/shell QDs are GaSb/GaAs, CdTe/CdSe, CdSe/ZnTe.

The quasi-Type-II core/shell QDs (e.g. CdTe/CdS and CdSe/CdS) have a small offset in either the valence or the conduction band alignment (Figure 1-3c), resulting in the confinement of one of the charges in the core, whereas the other is delocalised in the whole QD [45]. In addition to the desired band alignment with the core, the shell material also needs to have a lattice that is closely matched with the core. Large lattice mismatch causes the formation of traps leading to non-radiative recombination of the exciton. Also, increased shell thickness leads to increased surface inactivity of the QDs that causes a drop in the quantum yield [46].

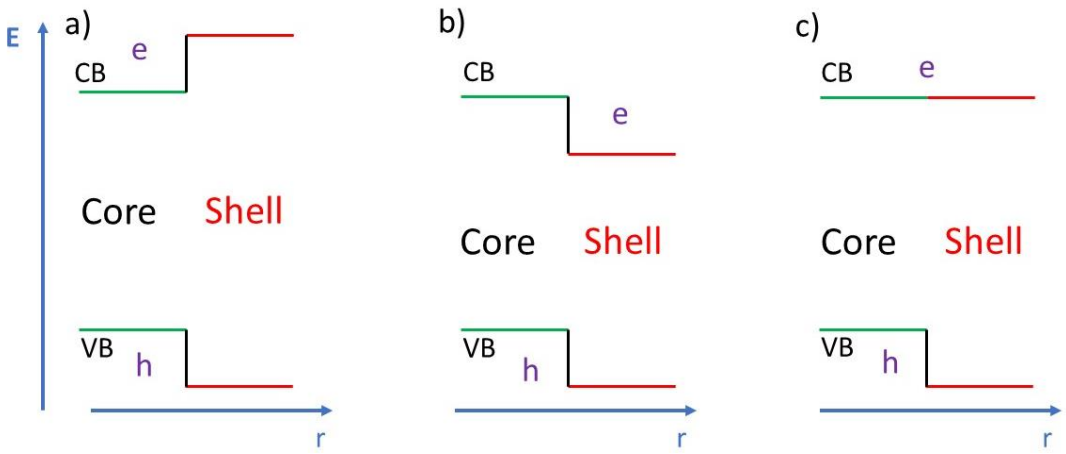

Figure 1-3. Schematic for the band alignment in core/shell QDs with a) Type-I b) Type-II and c) quasi-Type-II behaviour. VB and CB represent valence and conduction bands, respectively. The position of electrons (e) and holes (h) in the band structures of the QDs have been shown.

1.3. QDs in cellular biology

To understand the complexity of cellular behaviour, it is crucial that we decode the functioning of intracellular mechanisms and pathways. This knowledge is key to unlocking our understanding of life and the treatment of diseases. One way of extracting information about cellular behaviour is through the application of functional NPs. Cellular behaviour is regulated through biomolecules such as proteins, nucleic acids (DNA and RNA), lipids, smaller molecules

and ions. Information about the functions and performance of these cellular components can be tapped by the interaction with NPs. Through many years of development, NPs can now be engineered to extract information from specific intracellular locations and pathways. However, the delivery of these NPs to specified locations has been a challenge in live cells due to endosomal capture. Among the NPs, the inherent properties of QDs such as tunable fluorescence emissions, high quantum yield, broad excitation spectrum, low toxicity, superior photostability and low photo-bleaching makes them highly suitable for biosensing and imaging applications [19,47,48]. The advantages of QDs over conventional organic dyes are that they can be excited over a large wavelength range, the emission spectra are symmetric and narrow, and they are resistant to photobleaching [49]. In addition, the QDs appear brighter than the organic dyes as their molar extinction coefficient is 10-50 times larger [50]. Hence, the QDs' absorption rate of the excitation photon flux will be much higher than the organic dyes.

The use of QDs enable detection over longer durations of biological processes in live cells [51]. Single QDs have been successfully tracked over an extended period of time in cells of up to a few days [52]. Intracellular labelling of cellular structures, receptors and specific molecules have been achieved using QDs with targeting ligands [53–57]. This has aided in obtaining information regarding cellular architecture, protein localization and biomolecular interactions. Intracellular labelling has also been achieved with streptavidin-QD conjugates with biotinylated targets [19,58]. QDs can monitor vital cell parameters such as the redox potential, giving insight into the basic physiological functions of the cells [59–61]. This is achieved through selective quenching of QDs depending on the redox state of the cells which will be discussed in detail in section 1.8.

1.3.1. Cellular toxicity of QDs

QDs in biosensing, targeting and imaging has emerged as a successful application in recent studies. However, most of them are made of materials which are toxic and detrimental to the health of the living cells and tissues [62-64]. There are various factors that contribute to the degree of toxicity of QDs such as their size, charge distribution, physiochemical properties, capping ligands, oxidative and mechanical stability [65–67]. For *in vitro* studies, toxicity also depends on the type of cells, exposure time, concentration and the nature of the QD uptake

[68–69]. For cadmium based QDs, cellular toxicity is mainly caused by the release of Cd^{2+} ions from the QD surface leading to oxidative stress [70–72]. They also induce apoptosis, interfere with calcium signalling, damage and inhibit repair of DNA [73]. Shell passivation of Cd-based QDs, typically with ZnS, has been known to reduce the toxic effects in addition to improving the optical behaviour [74]. The QD toxicity also depends strongly on the nature of the surface ligands and their charge.

1.3.2. Cell membrane and uptake

The cell membrane protects the subcellular organelles from the external environment, provides structural support and regulates the exchange of materials [75]. It exerts control over the traffic of molecules, ions and water, which are necessary for cell survival. The cell membrane is generally composed of amphiphilic phospholipids, each with a hydrophilic head and hydrophobic tail as shown in Figure 1-4. These are arranged into a bilayer in which the hydrophobic tails form the inside of the membrane, with the head groups facing outwards. The membrane is also decorated with other lipids such as cholesterol, glycolipids and a variety of membrane proteins which regulate the entry and exit of materials from cells [76]. In general, the phospholipid bilayer is selectively permeable with small nonpolar molecules (e.g., O_2, CO_2, and ethanol) able to passively diffuse through the membrane. On the other hand, water-soluble polar molecules (e.g., glucose, amino acids, ions) need assistance to cross the membrane as they are repelled by the hydrophobic tails of the bilayer. Transmembrane channels are pores on the lipid bilayer formed by protein complexes that selectively regulate the transport of ions (e.g., K^+, Ca^+, Na^+, Cl^-), water, alcohols and gases [77–79]. Membrane receptors are specialised transmembrane proteins that regulate the traffic and signalling of antibodies, neurotransmitters, hormones, cytokines and nutrients into the cells [80]. These receptors have three distinct regions: the extracellular domain recognises the ligands and the signals from the environment; the transmembrane domain forms the pore through the membrane to allow the diffusion of signalling ions, and the intracellular domain produces the intracellular response by interacting with the organelles [81]. Membrane transporter proteins mediate the movement of ions, nutrients, drugs and other molecules in and out of the cells through either passive or active mechanisms [82]. Passive transport occurs through structural

transitions of the transmembrane protein where the direction of the flow is determined by the electrochemical potential. In active transport, the solute is transported across the membrane against the concentration gradient. This is achieved by utilising energy from adenosine triphosphate (ATP) or through ion movement [83]. Many recent drug discovery programmes target these membrane receptors and transporters due to their specific uptake and signalling capabilities [84–86]. Transporter facilitated the delivery of nanoparticles (NPs) have been achieved by targeting the selective membrane receptor proteins [87].

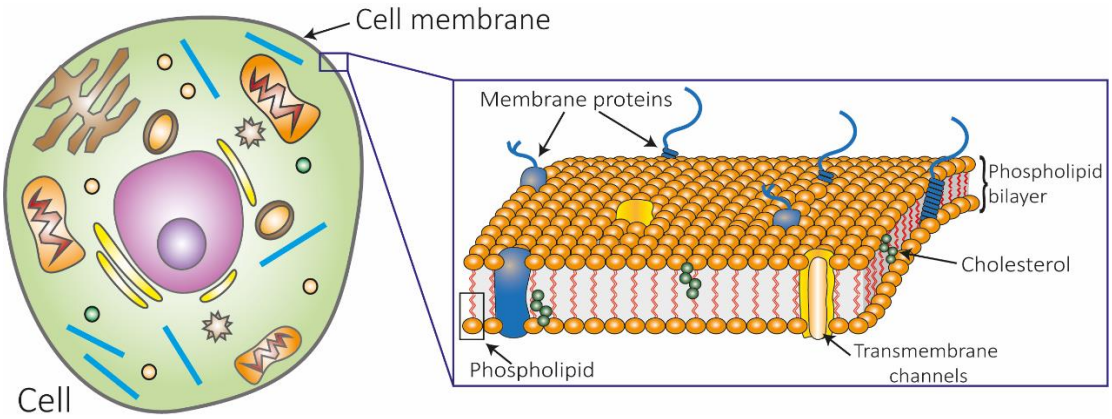

Figure 1-4. Illustration of a cell with the enlargement of the cell membrane showing the phospholipid bilayer.

1.3.2.1. Endocytosis

The entry of macromolecules, fluids and large particles is regulated through more complex mechanisms in eukaryotic cells which are collectively termed endocytosis. It is the process by which the cell membrane surrounds a material to internalise it, subsequently budding to form an intracellular vesicle [88]. The particles are engulfed along with their suspension fluid by membrane invagination and inward budding, followed by pinching off to form endosome vesicles [75]. The membrane deformation is due to the patchy distribution of polymerised actin at the site. In addition, bacteria and viruses exploit endocytosis as the primary route of entry into cells [89]. Based on the mechanism of uptake, endocytosis can be subdivided into five categories: namely, phagocytosis, clathrin-mediated endocytosis, caveolae-mediated endocytosis, clathrin/caveolae-independent endocytosis, and macropinocytosis.

Phagocytosis is the ingestion of large particles (≥ 0.5 µm) by a few specialised cells and involves recognition and binding by cell membrane receptors [90]. The major function of phagocytosis is the uptake of pathogens, cell debris, and dead cells. Specialised cells called phagocytes, such as macrophages, dendritic cells, neutrophils and monocytes are capable of particle recognition through membrane receptors [91]. Once the particle has been recognised by the membrane receptors, the cell membrane will distort to engulf it (Figure 1-5). For the uptake of NPs through phagocytosis, opsonins (antibodies, complementary proteins, laminin or fibronectin) are adsorbed to the particle surface, which is recognised by the phagocytes. This uptake depends on the surface properties, size and shape of the NPs or QDs [75,92,93].

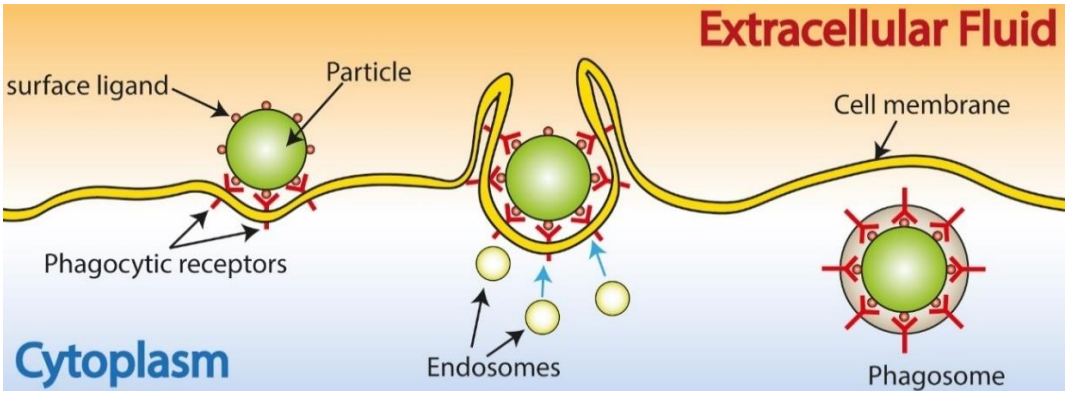

Figure 1-5. Schematic for the mechanism of phagocytosis.

Clathrin-mediated endocytosis is the internalisation of nutrients and particles by cells through the extensive remodelling of the plasma membrane by the coordinated action of several proteins to form clathrin-coated endocytic vesicles [88,94]. These proteins assemble at the endocytic site and initiate the formation of the clathrin-coated pit by membrane invagination. Cargo binding is performed by the adaptor proteins which serve as recognition sites on the cell membrane followed by the formation of the clathrin pit around the invagination, as shown in Figure 1-6 [95,96]. The formation of a clathrin-coated endosome is completed by the scission of the invagination at the neck by the action of the enzyme dynamin. These endosomes are 100-150 nm and also engulf the extracellular fluid along with the cargo. For the uptake of NPs through the clathrin-mediated endocytic route, it has been observed that positively charged particles show higher uptake and cellular interaction [75]. Delivery through clathrin-mediated endocytosis of QD conjugates with peptides and glycoproteins which bind to membrane receptors has also been demonstrated in past studies [97,98].

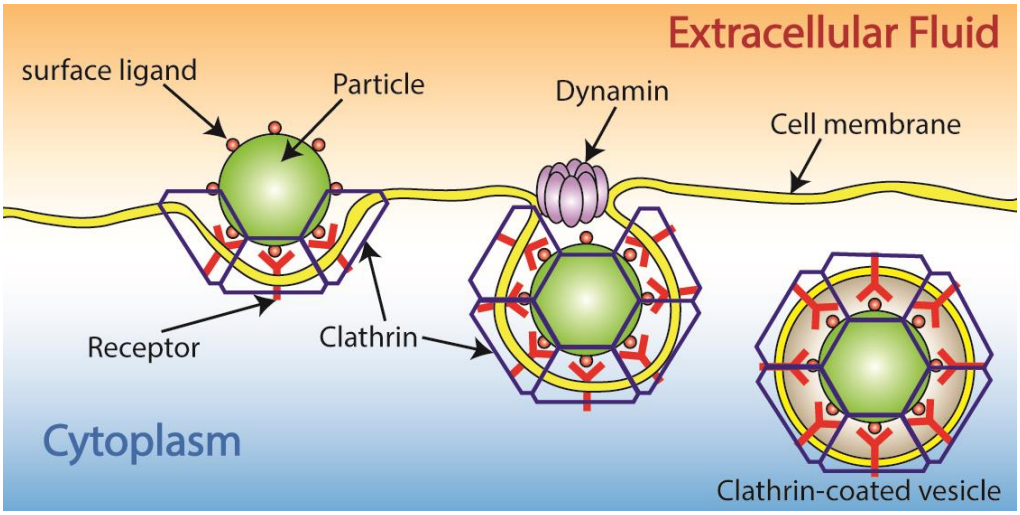

Figure 1-6. Schematic for the mechanism of clathrin-mediated endocytosis.

Caveolae-mediated endocytosis is responsible for many cellular functions such as signalling, lipid regulation and vesicular transport [91]. 50-80 nm-sized flask-shaped invaginations of the cell membrane called caveolae are formed by lining the cell membrane with the dimeric protein caveolin (Figure 1-7). Caveolin, along with other proteins is responsible for the formation and the stability of these invaginations. Similar to the case of clathrin-mediated endocytosis, dynamin is responsible for the pinching off of the vesicle from the membrane [99]. Caveolae are promising for targeted drug delivery due to tissue-specific molecules which overcome the endothelial-cell barrier to reach underlying tissue[100]. NPs have been demonstrated to enter cells selectively through the caveolae-mediated endocytosis [101].

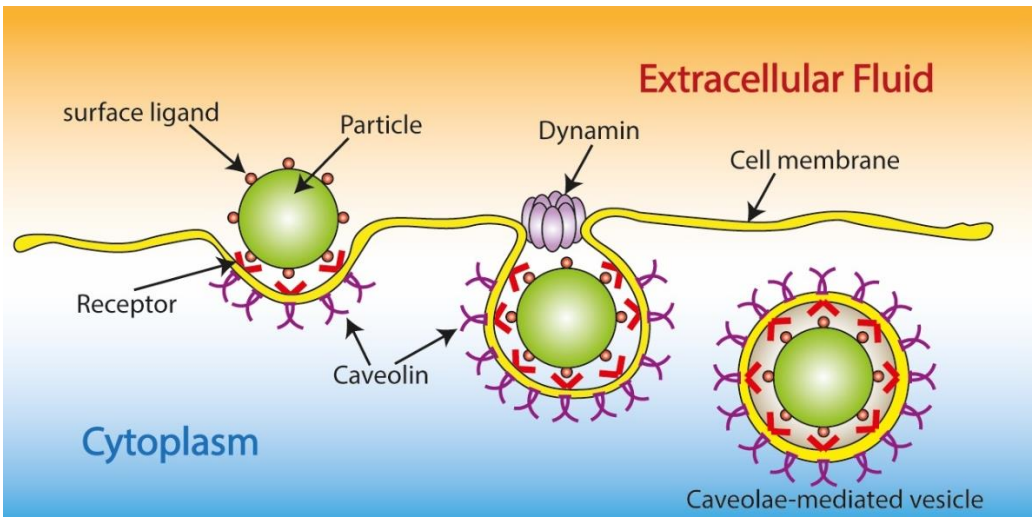

Figure 1-7. Schematic for the mechanism of caveolae-mediated endocytosis.

Clathrin/caveolae-independent endocytosis through selective internalisation of glycolipids, proteins, cholesterol, lipid-raft associated receptors have been reported, which plays an important role in signal transductions and transcytosis [102]. NPs with foliate modifications have been internalised into the cell through this method [75].

Macropinocytosis is a non-selective method for the uptake of nutrients and particles by engulfing a large volume of external fluid by membrane extensions [91]. The membrane extensions are driven by actin regulation forming large vesicles (0.2-5 µm) where particles uptake takes place regardless of the specific receptors (Figure 1-8) [103]. As such, this is the mechanism by which non-receptor targeted NPs and QDs are likely to be taken into the cell [104–106].

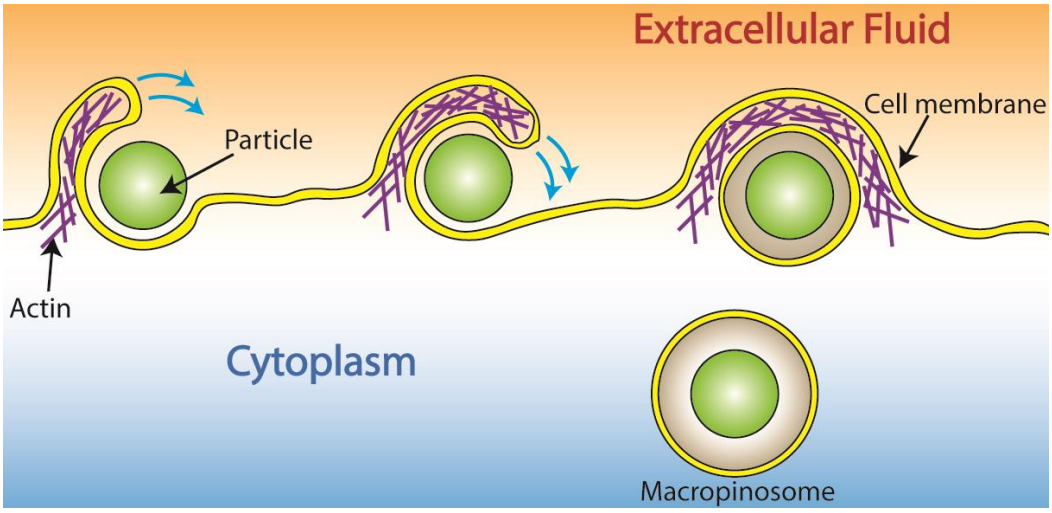

Figure 1-8. Schematic for the mechanism of macropinocytosis.

1.3.2.2. Factors affecting NP uptake

The uptake of NPs depends on several particle properties, including surface chemistry, size, shape and mechanical properties. As mentioned in the previous section, many of the receptor-mediated endocytic methods for the uptake of NPs depend upon their interaction with cell membrane receptors. Hence, the surface chemistry of the NPs is crucial for the particle uptake through endocytic pathways. Since the cell membrane is slightly negatively charged, the uptake of positively charged particles is faster than the neutral or negatively charged particles, as it is facilitated by electrostatic attraction [107]. The uptake of positively charged NPs occurs via membrane disruption through charge driven surface defects [108,109]. This surface disruption can cause increased cytotoxicity of these anionic NPs. On the other hand, neutral and negatively charged NPs favour entry into the cells via endocytic pathways [107]. Hydrophobicity of the particles has a significant influence on the cell membrane interaction and NP internalisation. Hydrophobic NPs can penetrate the lipid bilayer as they are stable in the hydrophobic core of the membrane, whereas the hydrophilic particles prefer interaction with the membrane surface which can induce endocytosis [75]. A wide variety of ligands have been used to functionalise the NP surface which include polymers, proteins, peptides, acids and nucleic acids, which have a significant impact on the endocytic pathways and the particle interaction within the cell [107]. These ligands and functional groups on the NPs surface can dictate the fate of the particle inside the cell with the intention of targeting specific intracellular sites for sensing and labelling.

The internalisation of NPs depends on the ability of the membrane to deform and wrap around the particle, which is strongly influenced by the particle size. For very small particles (≤ 5 nm), such as QDs, the membrane is not energetically capable of forming endosomes due to excessive curvature [107]. However, smaller particles can be internalised in clusters. The uptake of particle clusters causes aggregation, which is not favourable for sensing and labelling. From theoretical studies, the optimum particle size for maximum endocytic uptake rate has been predicted to be ~25 nm radius [110,111]. For very large particles, the formation of endosomes will be hindered by the membrane tension for wrapping the NPs.

The shape of the NPs is another factor that affects the efficiency of the particle uptake by cells. Various shaped NPs have been used in cell studies including the 1-dimensional nanotubes and wires, 2-dimensional nanosheets and graphene-based nanomaterials, and 3-dimensional

particles such as spheres, cylinders, rods, cubes and ellipsoids [112]. It has been reported that the uptake of spherical NPs is more efficient than other particles [91]. The uptake efficiency decreases with the increasing aspect ratio of the NPs [113,114]. However, some studies have shown that carbon nanotubes can enter the cells efficiently through physical penetration without endocytosis [115–117]. Hence, the absolute volume and the surface chemistry of the NPs are considered to be more influencing factors for the uptake than the particle shape [114,118]. Studies, both experimental and theoretical, have shown that the uptake of NPs can be influenced by other particle parameters, such as the orientation of the NPs at the membrane approach, nature of the particle core, ligand coordination, stiffness and other mechanical properties [91,107,119–124].

1.3.2.3. Fate of the NPs inside the cells

For the delivery of NPs through endocytosis, the particles remain confined in the vesicles and are trafficked within the cells via complex mechanisms [125]. The NPs intracellular trafficking depends on the type of cells and the properties of the particles such as surface charge, size and shape. The internalised NPs first encounter the early endosomes which are membrane-bound intracellular vesicles. Through differentiation and maturation processes, the early endosome transforms into a late endosome which integrates with the lysosome. The lysosomes contain several enzymes which are capable of degrading the NPs [126]. As such, the particles will not be able to function within the cell and will eventually be discarded. In addition, the pH variation from endosomes (~6.5) to lysosomes (~4.5-5.0) can alter the surface properties of the NPs. It has also been reported that the accumulation of NPs and QDs in lysosomes leads to increased cell damage due to the toxicological effect of the particles [91]. To overcome lysosomal degradation, strategies of endosomal escape must be incorporated into the NP and delivery design [127]. Hence, the delivery of intact NPs into the cytoplasm is a major challenge for pharmacological applications in live cells.

1.3.3. Non-endocytic uptake of NPs

As we have seen from the previous section, the particles remain confined in endosomes and are ultimately degraded by lysosomal action, unless they are designed for endosomal escape [127]. This feature of the NPs will add to the complexity of the particle design and could require compromises to be made that affect the end goal. Hence, it is vital that the NPs are delivered into the cells free of endosomes. There are various methods of non-endocytic delivery of NPs into live cells reported with varying degrees of success. These methods can broadly be surface functionalisation of the particle with ligands and moieties which can readily penetrate the cell membrane, or disruption of the membrane to facilitate particle diffusion. Here, we emphasise membrane disruption techniques with a focus on intracellular delivery of QDs.

1.3.3.1. Membrane disruption for non-endocytic delivery

There has been an increasing trend in the cytosolic delivery of NPs through cell membrane disruption techniques [128]. The techniques focus on generating transient membrane pores or defects which facilitate the uptake of particles directly into the cytoplasm. These methods have proven to be attractive for non-endocytic delivery of NPs as they do not rely on the membrane receptors for internalisation. Hence, the uptake is independent of the surface functionalisation of the particles. This significantly reduces the complications in particle design which is critical for endosomal escape in receptor-mediated deliveries. Direct cytosolic delivery also ensures effective targeted delivery of the NPs within the cell. These methods are independent of the cell type and the nature of cargo [129]. Membrane disruption-based delivery can be broadly divided into two categories: direct penetration and membrane permeabilisation. Some of the major techniques which fall under these categories have been discussed in the following sections.

1.3.3.1.1. Direct penetration

Delivery of NPs via direct penetration of the cell membrane includes techniques such as microinjection and nanowires/nanoneedles as shown in Figure 1-9. Microinjections are sharp microcapillary pipettes, capable of rupturing the cell membrane and penetrating the cytoplasm. The cargo is directly introduced into the cytoplasm (Figure 1-9a) through the microcapillary, monitored using an optical microscope. This method is highly efficient in determining the fate of NPs in the cells as there is precise control over the delivery site and quantity [130]. Microinjections have been widely used for the intracellular delivery of proteins, peptides, nucleic acids, liposomes and NPs, including QDs [128]. Direct injection of QDs via microinjection has been widely reported showing homogeneous distribution within the cytosol and efficient intracellular targeting [131]. In spite of the major advantages, the technique requires specialised skill, precise control and it is only possible to treat one cell at a time, making it low-throughput. Hence, it is not suitable for NP delivery for a large cell population.

Nanowires or nanoneedles are elongated thin nanostructures with a cross-section of a few hundred nanometres or less. They are fabricated into arrays of vertically aligned structures. The cells adhere onto this substrate and the nanoneedles penetrate the cell membrane (Figure 1-9b) [132,133]. These nanoneedles are in the order of micrometres in length and are hollow, which can facilitate the delivery of NPs directly into the cytosol. Park *et. al.* have demonstrated the direct delivery of QDs to the cytosol using arrays of vertically aligned carbon nanosyringes [134]. In principle, this method of delivery can be scaled up for high-throughput by increasing the substrate area accommodating many cells. The number of particles injected can be efficiently controlled by the flow of the cargo suspension. Also, the highly localised interface of the nanoneedles and the cells ensure strong physical effects of treatments (eg, electric, magnetic or mechanical) locally, making the delivery more efficient [135]. However, a recent study has shown that delivery via nanoneedles is partially mediated through endocytic pathways selectively upregulated at the cell-nanoneedle interface, which causes endosomal localisation of the cargo [136].

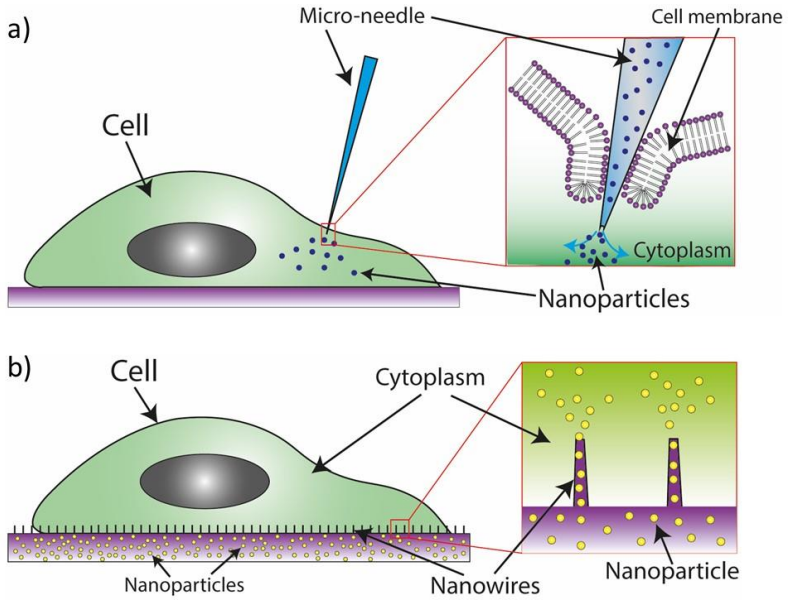

Figure 1-9. Delivery of nanoparticles by direct penetration of the cell membrane. Intracellular delivery via a) microinjection and b) penetrating nanowires.

1.3.3.1.2. Permeabilisation

Uptake through membrane disruption by permeabilisation involves strategies that generate transient membrane pores which allow the diffusion of the particles present in the extracellular medium. Permeabilisation of the cell membrane can be achieved by various means such as electrical, thermal, chemical or mechanical stress [128]. The particle of interest is dispersed in the cell suspension or the extracellular medium, which is followed by the membrane disruption process. Transient membrane pores are generated and the particles diffuse into the cytoplasm according to their concentration gradient. The cells actively begin to repair the membrane and restore its health which ends the particle diffusion. It is important that the membrane disruption process be optimised and limited so that the cells are capable of full recovery and membrane repair without permanent damage. The membrane repair by the cells post-disruption will be discussed in section 1.6.2.

Electroporation is a popular method for membrane permeabilisation which involves the treatment of cells with electric pulses (Figure 1-10a). The electric pulses (0.2-1.5 V), typically in the order of microseconds to a second, induce transmembrane electrical potential with the accumulation of the charges at the cell membrane [137]. It was reported by Tsong that when the transmembrane electric potential reaches a certain critical value of ~1 V, the breakdown

of the cell membrane occurs leading to the formation of pores [138]. Conventionally, bulk treatment of cells is carried out in suspension along with the cargo material in a cuvette, in a solution of the conducting buffer, placed between the two electrodes [139]. With the application of the voltage, hydrophilic membrane pores are generated and the particles diffuse into the cytosol. Studies have shown that the permeabilised area of the membrane can be controlled by pulse strength and the pore size by the pulse duration [140]. Electroporation has been extensively used to deliver various QDs into the cytoplasm [141,142]. However, the major issue for QD delivery by electroporation is that strong electric pulses cause the particles to aggregate [131]. Additionally, electroporation can induce cell swelling, cytoskeleton disruption and denaturation of membrane proteins [143]. Integration of electroporation with microfluidics can give precise control over membrane permeabilisation which cannot be achieved by electroporation on its own. Microfluidic electroporation, due to the smaller scale, does not require high voltages for high pulse power and can facilitate real-time monitoring of single cells for delivery efficiency [144]. It has been demonstrated that the exact amount of cargo can be driven into the cytoplasm by electric pulses through a nanochannel for a cell precisely positioned in a microchannel [145].

Membrane permeabilisation by thermal treatment of cells occurs due to the dissociation of the lipid bilayer when the kinetic energy of the constituent molecules becomes greater than the hydrophobic forces that hold the membrane together. The strategy involves putting cells through a heating-cooling cycle, generating membrane pores that allow the diffusion of particles into the cytosol, followed by cell recovery. Membrane integrity with supraphysiological heating of the cells (37 to 70 ^{o}C) was assessed by the leakage of calcein from the cells by Bishof *et al.* [146]. They found that the membrane disruption was a function of both time and temperature of heat treatment. However, bulk heating of the cell suspension for membrane disruption can have detrimental effects on cellular functions, mostly due to protein denaturation and increased diffusion of lipids, as such, it has rarely been employed for uptake studies [128]. A more efficient method for heat-induced membrane disruption is by using localised laser irradiation of the cell membrane. The membrane disruption site can be localised for cargo delivery with the assistance of surface-adsorbed nanoparticles (Figure 1-10b), which acts as the nucleating site for heat treatment [147,148].

Similar to localised thermal treatment, optoporation is the disruption of the cell membrane with a high-intensity pulsed laser [129]. Membrane permeabilisation occurs through a number of mechanisms when exposed to the focused light beams, which can be a combination of mechanical stress, chemical effects such as reactive oxygen species (ROS) generation, cavitation bubbles, heating and shear stress. Favourable optoporation for cargo delivery has been achieved by femtosecond-pulsed source [149,150]. Delivery of QDs into developing *Xenopus laevis* embryos by NIR laser optoporation with low tissue damage has been reported Umanzor-Alvarez *et al.* [151]. The disadvantage of optoporation based delivery is the requirement of specialised expertise to handle high-intensity laser, high cost and low-throughput treatment.

Sonoporation is the method of membrane permeabilisation via acoustic pressure using ultrasound (20 kHz to GHz). The high-intensity ultrasound focused on the membrane causes disruption by microbubble cavitation (Figure 1-10c). As the bubble vibrates in the vicinity of the cell, its shrinking and expanding causes pushing and pulling of the membrane leading to shearing stress, poration and NP delivery [152]. This method of delivery is becoming popular as it is non-invasive, cost-effective, safe and widely available in preclinical research [153]. Evaluation of successful delivery to the target tissue by sonoporation is often carried out using QDs [154]. The major limitation of sonoporation is the lack of control over nature and the randomness of cavitation. Lui *et al.* reviewed that the uptake efficiency is <50% for ultrasound exposed cells *in vitro* with low cell viability [155]. This low viability for *in vitro* systems could be caused by uncontrolled cavitation-related effects such as generation of ROS or high localised temperature.

Chemical membrane disruption can be achieved in a variety of manners for the internalisation of NPs. The majority of them can be categorised under permeabilisation by organic solvents, surfactants, artificial detergents, oxidising agents and natural proteins [128]. Short-chain alcohols can produce membrane disruption by increasing the fluidity of the membrane for cargo delivery [156]. Surfactants such as detergents produce membrane pores by inserting themselves in the lipid bilayer and causing structural distortion. The stages of membrane disruption by detergent are shown in Figure 1-10d. Detergents are amphiphilic molecules and because of their cone-shape, having a large head compared to the membrane lipids, the structure of the outer leaflet of the bilayer assumes an intrinsic curvature with the inserted

detergent [157]. This generates a curvature strain on the outer monolayer, leading to a disorder of the hydrophobic chain, making the membrane flexible. Finally, membrane pores are produced by bilayer dissolution by sequestering lipid-detergent micelles. Pore-forming protein monomers assemble forming oligomers and insert onto the membrane to form pore complexes, which have been used for intracellular delivery of various molecules and NPs [128]. However, these approaches for membrane disruption and delivery using detergents and pore-forming proteins are limited due to lack of control and delayed pore formation kinetics.

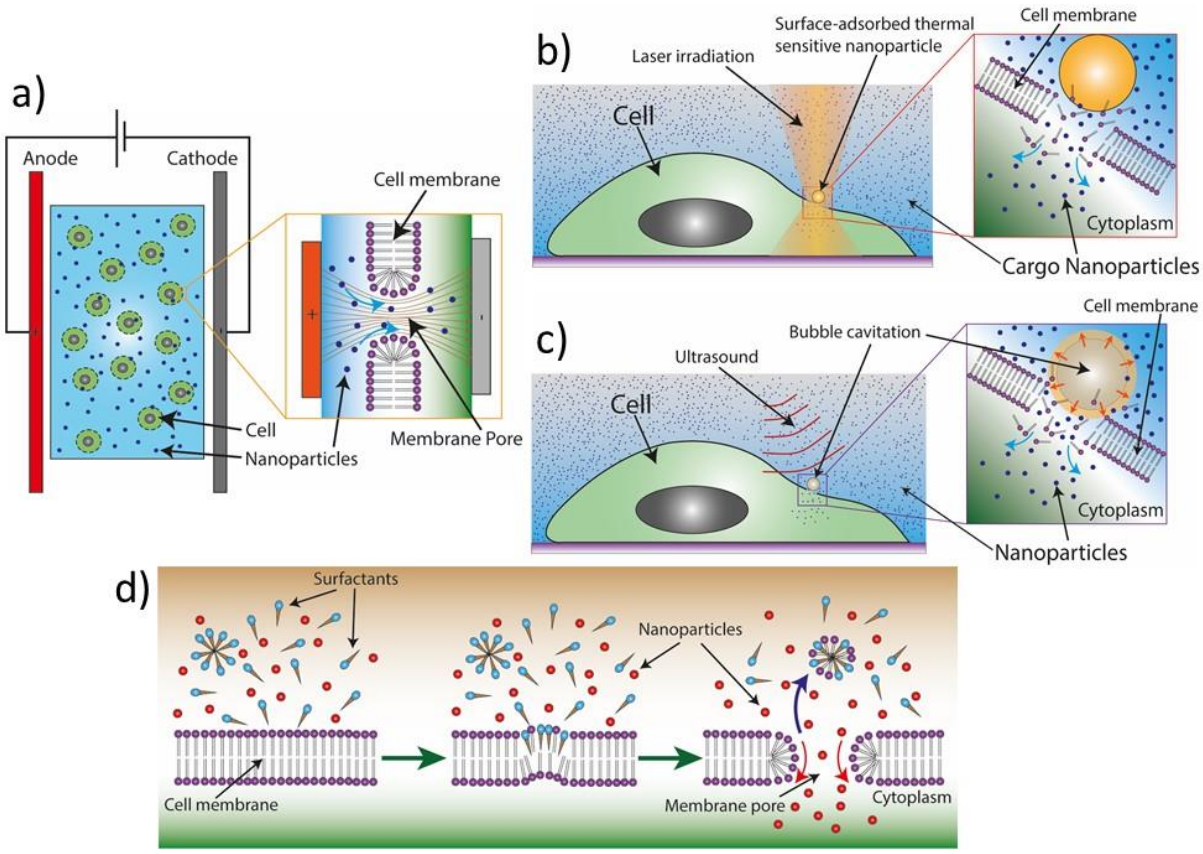

Figure 1-10. Intracellular nanoparticle delivery by membrane permeabilisation. a) Membrane disruption by electroporation for cells in suspension with the NPs. b) Delivery of cargo-nanoparticles by membrane disruption assisted by surface-adsorbed nanoparticle irradiated with laser. c) Bubble cavitation by ultrasound for membrane disruption and nanoparticle delivery. d) Steps involved in bilayer dissolution and poration for nanoparticle delivery by the action of surfactants.

Mechanical membrane disruption is gaining popularity for vector-free intracellular delivery as it is simple and cost-effective. Permeabilisation of the membrane is mechanically achieved by contact of the membrane with a foreign object, pressure gradient induced hydrostatic/osmotic

changes or shearing forces of the suspension fluid. Bulk treatment of adhered cells by shaking glass beads and scraping with rubber spatula have been reported for the mechanical disruption-mediated delivery of a variety of materials including QDs, however, these methods lack precise control and show excessive cell damage [128]. Microfluidics has revolutionised the way mechanical disruption of the cell membrane can be achieved for non-endocytic delivery of NPs with high efficiency and is discussed in detail in the following section.

1.3.4. Microfluidics cell deformation and intracellular delivery of NPs

Microfluidics has been a revolutionising technology in the *in vitro* studies of cells for toxicity, diagnosis, treatment, drug and particle delivery [158,159]. Compared to bulk methods, there is efficient control over particle delivery with respect to the mechanical forces acting on the cells, time of treatment, integrated processing, sorting, reproducibility and homogeneity. These factors are easily controlled by the geometry of the microfluidic device, particle and cell concentrations and the flow rate through the device. This method is cost-effective, high-throughput, easy to execute and able to work with small volumes. In addition, the channels of the device, which are in the order of a few to hundreds of microns, can mimic the flow condition in capillaries and small terminal lung airways. Microfluidic devices usually have a controlled flow of small volumes of fluids in microchannels and micro-chambers. The geometry of the devices can be engineered according to requirements in both two- and three-dimensions [160]. Microfluidic devices are usually fabricated with glass or by moulding of a semi-flexible polymer, polydimethylsiloxane (PDMS) and thermoplastics [161]. PDMS microfluidic devices stand out in current research due to their ease of fabrication, integration and reproducibility [162]. Cell permeabilisation and particle delivery via microfluidics are categorised by either contact-mediated or fluid shear-mediated deformations.

1.3.4.1. Contact-mediated deformation

The group lead by Langer and Jensen pioneered the contact-mediated deformation for non-endocytic uptake by demonstrating the delivery of QDs by squeezing cells rapidly through narrow constrictions [163]. Cells were deformed at 10,000 cells/s showing 35% delivery

efficiency while maintaining 80-90% viability (Figure 1-11). In their follow-up work, Sharei *et al.* 2013 demonstrated intracellular delivery by squeezing cells through a series of constrictions that were 30-80% smaller than the cell diameter [164]. Transient membrane pores were generated in a controlled manner by the compressive and the shearing forces acting on the cells by constriction squeezing. Non-endocytic delivery at 20,000 cells/s of 3 and 70-kDa dextran was demonstrated which increased with flow rate, constriction length, smaller constriction width and the number of constrictions. The method was also used to demonstrate the role of Ca^{+} in the membrane recovery kinetics post-deformation [165]. The drawbacks, however, are that the small features can be susceptible to blockages, the size dependency of the constrictions on cell type, the narrow range of flow rate for optimised delivery and viability.

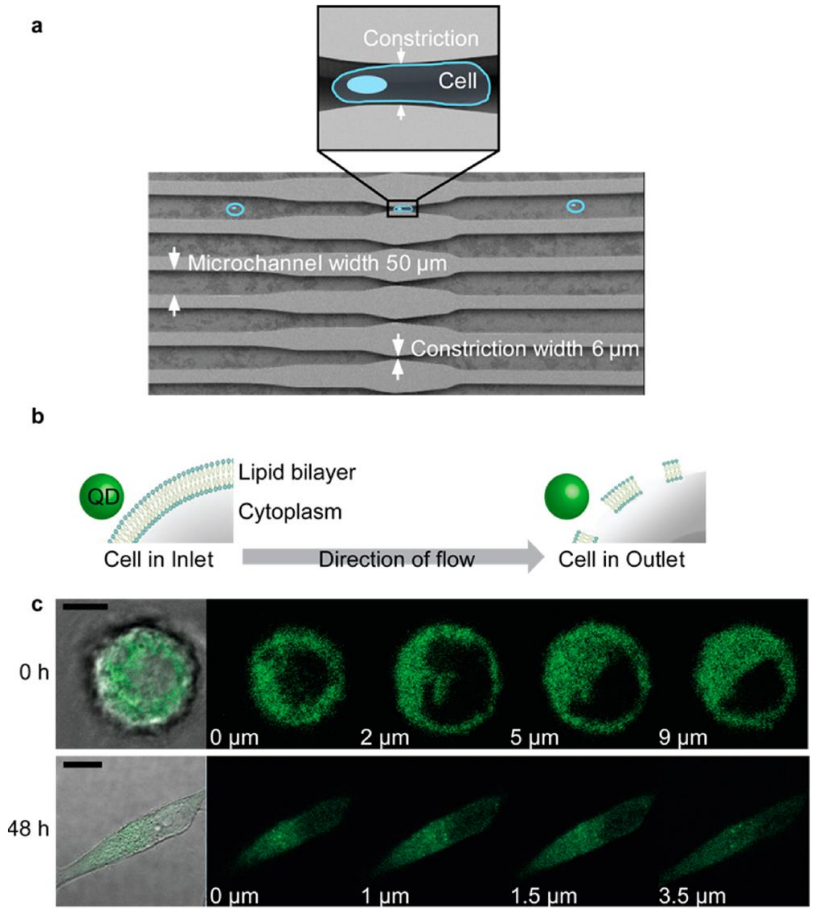

Figure 1-11. Microfluidic constrictions for cell squeezing for non-endocytic delivery of QDs. a) Schematics of the constriction and the cell deformation b) Schematic of the QD uptake hypothesis via cell membrane poration c) Confocal images of the cells deformed with QDs at various z-heights. Reprinted with permission from Lee et al. [163]. *Copyright (2012), American Chemical Society.*

To further enhance the delivery efficiency, Joo *et al.* very recently combined droplet microfluidics with contact-mediated deformation as shown in Figure 1-12, for internalisation of 2000 kDa dextran, mRNA and plasmid DNA [166]. In this approach, the cell and the cargo are initially encapsulated in water-in-oil droplets and squeezed through a series of narrow constrictions. The droplet squeezing with the encapsulated cells generate membrane pores and the cargo is delivered efficiently (up to 98%) by the recirculating fluid within the droplet. This reduces the total cargo consumption and near-zero clogging was reported by droplet use. This droplet-based intracellular delivery has the potential to be incorporated with other membrane disruption strategies for enhanced uptake efficiency.

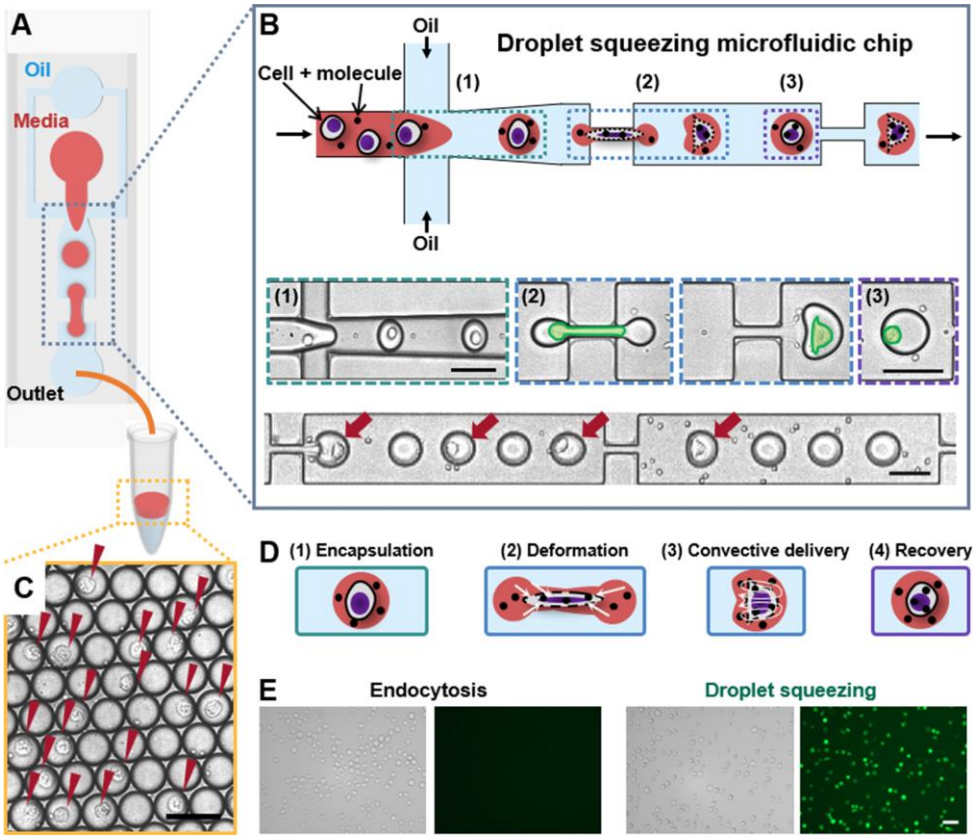

Figure 1-12. Intracellular delivery via droplet squeezing mechanoporation. A) Schematic of the microfluidic device for droplet squeezing. B) Illustration and high-speed microscope images of (1) Cell encapsulation, (2) droplet squeezing through constriction and (3) uptake and cell restoration. C) Encapsulated cells in monodispersed droplets. D) Schematics showing the stages of intracellular delivery through droplet squeezing. E) Comparative images (bright field and fluorescence) of K562 cells with 3-5 kDa FITC-dextran delivered via endocytosis and droplet squeezing. Reprinted with permission from Joo et al. [166]. *Copyright (2021), American Chemical Society.*

1.3.4.2. Shear-mediated deformation

Shear-induced permeabilisation for intracellular delivery can be achieved in several ways. The rapid motion of fluid close to the cell membrane induces torsion in the lipid head arrangement of the bilayer, leading to instability and eventually membrane rupture [167]. This microfluidic method of membrane disruption is less invasive compared to contact-mediated deformations [128]. A consistent zone of fluid shear was generated in narrow confinements with a simple microfluidic device consisting of an array of parallel cones [168]. The size of these channels was larger than the cell diameter, as such, the deformation was produced purely due to shearing forces (Figure 1-13a).

Recently, Chung's group has shown shear-induced delivery through different microfluidic geometries [169–172]. For one of the designs, cells were subjected to shearing and compressive forces by colliding them onto a sharp pin at a T-junction as shown in Figure 1-13b [169]. Membrane disruption by the collision allowed material independent intracellular delivery at high-throughput while maintaining high cell viability. Notably, the delivery efficiency increased with the Reynolds number (ratio of inertial and viscous forces, discussed in detail in section 1.4.2), suggesting that the membrane disruption is higher with the inertial force dominating over the viscous force. The high Reynolds numbers (Re) were achieved by using high flow rates in the devices. Additionally, the device is also susceptible to partial clogging due to small features on the device.

Kizer *et al.* demonstrated single-step hydrodynamic membrane disruption and intracellular delivery of macromolecules by fluid shearing, using a cross-slot microfluidic device named 'Hydroporator' [170]. As the two opposing fluid flows collide at the centre of the cross-slot junction, called the extensional-flow region, the suspension fluid and the cells slow down and come to a stop at the centre of the junction. This is called the stagnation point and the cells deform purely by hydrodynamic forces of the moving fluid around them. This generates the transient membrane pores which allow the cargo in suspension to diffuse into the cells (Figure 1-13c). They achieved almost 90% delivery efficiency for 3-5 kDa FITC-dextran in K562 cells. The uptake experiments were performed at a relatively high Reynolds number (Re ≈133-189), implying noticeable inertial dominated flow. Uptake at shear-dominated flow at low Re (high viscosity) has not been explored. Additionally, although it has been mentioned that there is an expulsion of intracellular material during deformation, evidence of the phenomenon has not

been provided [170]. The cross-slot microfluidic device will be discussed in further detail in section 1.5.

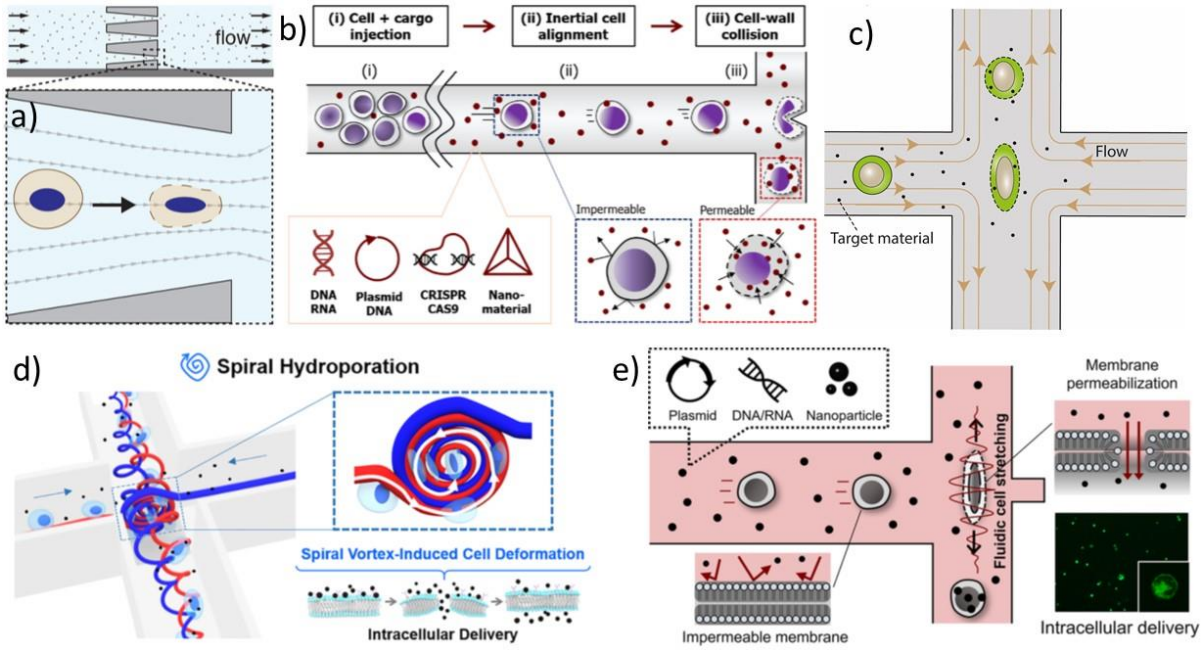

Figure 1-13. Methods for membrane disruption through shear-mediated microfluidics. a) Cell deformation with flow through wide constriction. Reprinted with permission from Stewart et al. [128]. *Copyright (2018) American Chemical Society. b) Schematic for the intracellular delivery via the T-junction with the sharp pin microfluidic device. Reprinted with permission from Deng et al.* [169]. *Copyright (2018) American Chemical Society. c) Intracellular uptake by cross-slot microfluidic deformation. d) Schematic of the cell deformation and intracellular delivery via spiral hydroporation. Reprinted with permission from Kang et al.* [171]. *Copyright (2018) American Chemical Society (Further permission related to the material excerpted should be directed to the ACS). e) Schematic of the intracellular delivery and fluorescence images of K562 cells with 3-5 kDa FITC-dextran via T-junction with cavity microfluidic device. Reprinted with permission from Hur et al.* [172]. *Copyright (2020) American Chemical Society.*

Vortex-induced hydrodynamic cell deformation was shown to effectively deliver large particles, such as 200 nm gold and 150 nm mesoporous silica NPs while maintaining high cell viability (up to 94%) with the same cross-slot geometry [171]. The cell suspension with the NPs was injected into both of the two opposing inlet channels at different flow rates ($Re \approx$ 0-366). It was observed that due to the asymmetric flow, a strong spiral vortex was generated near the stagnation point, making the cells spin before exiting from one of the outlets (Figure 1-13d). The cells were further made to collide with the T-junction wall, causing further membrane disruption. Using this dual-action method of cell deformation, they claim to achieve up to 96.5% efficiency in uptake at a high throughput of up to 1×10^6 cells/min. It is yet to be explored

how this spiral hydroporator will perform in NP delivery for high viscosity fluids (i.e., at low Re). Recent, modification to the T-junction microfluidic device with the inclusion of a cavity (Figure 1-13e) substantially increases the cell stretching by the elongational recirculating flow [172]. The membrane disruption produced in this technique was reported to deliver NPs, including QDs into hard-to-transfect primary cells.

1.4. Microfluidics background

Microfluidics is the technology of manipulating small volumes of fluids in channels that have at least one dimension < 1 mm. The miniaturisation of fluid flow enables precise spatiotemporal control of mixing, treatment, manipulation and analysis. As many common laboratory processes from cell culture to chemical reactions can be carried out on specially designed microfluidic chips, this technology is commonly referred to as "lab-on-a-chip". The low volume and the downscaled system enable high-throughput treatments and automation of processing and analysis with relative ease. Numerous studies have been conducted in understanding the fluid inertia in the microchannels and their potential applications collectively referred to as 'Inertial microfluidics' [173]. Inertial microfluidics involves investigating fluid-structure and fluid-particle interactions and behaviours.

1.4.1. Navier-Stokes equation

For an incompressible Newtonian fluid flowing through the microchannels, its motion is governed by the Navier-Stokes equation:

$$\rho\left(\frac{\partial v}{\partial t} + v.\nabla v\right) = -\nabla p + \mu\nabla^2 v + f \qquad (1.6)$$

Here, ρ is the density of the fluid, v is the fluid velocity, p is the fluid pressure, μ is the fluid viscosity and f is a term due to the external force acting on the fluid elements such as gravitation or electromagnetic forces. The equation describes the conservation of the linear momentum of the fluid [174]. The term on the left-hand side of the equation represents the inertial forces due to the fluid acceleration. The first term on the right-hand side represents the external pressure applied on the fluid which determines the direction of flow and the

second term represents the viscous forces. The equation of continuity representing the conservation of mass is described as:

$$\frac{\partial \rho}{\partial t} + \nabla.(\rho v) = 0 \quad (1.7)$$

For an incompressible fluid, the density remains constant, as such equation 1.7 simplifies to:

$$\nabla.v = 0 \quad (1.8)$$

Hence, the Navier-Stokes equation and the fluid flow can be simplified with certain assumptions. Also, typically, the effect of gravity is neglected for fluid flow in microchannels in comparison to the inertial, viscous and pressure effects.

1.4.2. Reynolds Number

The behaviour of the fluid motion is also characterised by the Reynolds number which is the ratio of the inertial to the viscous forces, described for a flow in pipe or tube as:

$$Re = \frac{inertial\ forces}{viscous\ forces} = \frac{\rho v D_H}{\mu} \quad (1.9)$$

D_H is the hydraulic diameter of the pipe or tube and is dependent on the cross-sectional geometry of the microchannel. Typically, the channels in the microfluidic devices are rectangular, thus D_H can be represented as:

$$D_H = \frac{4A_c}{P_r} = \frac{2wh'}{w+h'} \quad (1.10)$$

Where A_c is the area of cross-section, P_r is the perimeter, w is the width and h' is the height of the channel. For viscous force dominated flow, i.e., at low Re, the fluid flows in smooth, continuous streamlines which is known as laminar flow as shown in Figure 1-14a [175]. For the flow of water (ρ ~ 1000 Kg/m^3, μ ~ 0.001 Pa.s) at a velocity of v = 0.01 m/s through a rectangle cross-section of a microchannel with w = h' = 100 µm, Re is approximately 1. Since most microfluidic channels in devices are usually 10s of micrometres, Re is typically <1. For low velocity and high viscosity, Re <<1 can be achieved in microchannels and is referred to as Stokes flow or creeping flow. Here, the Navier-Stokes equation can be simplified by neglecting the inertial term:

$$\mu\nabla^2 v - \nabla p = 0 \qquad (1.11)$$

when no external forces acting on the fluid. Equation 1.11 is linear and time-independent and it is possible to predict fluid motion and the position of the particles in laminar flow with relative ease. As Re increases, the inertial forces become prominent and the flow deviates from laminar behaviour. For the intermediate flow regime ($1 < Re < 100$), the flow remains laminar but is influenced by the geometrical effects of the channel [174]. In this weak-inertial regime, curved channel structures can generate transverse components of velocity, leading to secondary flows which can be effectively manipulated for particle focusing and separation [176]. As Re further increases, inertial forces dominate and the flow transitions from laminar to more chaotic. The transition to turbulent flow (Figure 1-14b) occurs at a critical Re which depends on the geometry of the channel. This transition is typically reported to occur between $2300 < Re < 4000$ [177].

In a microfluidic system, particles suspended in fluid experience additional drag and lift forces [178]. For such cases, the flow of particles through a channel can be described by two variations of the Reynolds number:

$$R_c = \frac{\rho\, v_{max}\, D_H}{\mu} \qquad (1.12)$$

$$R_p = R_c \frac{a^2}{D_H^2} = \frac{\rho\, v_{max}\, a^2}{\mu\, D_H} \qquad (1.13)$$

R_c is the channel Reynolds number (equation 1.12) which describes the unperturbed flow in the channel. R_p is the particle Reynolds number (equation 1.13) which shows dependence on both channel and particle parameters. Both Reynolds numbers depend on the maximum flow velocity, v_{max}, whereas only R_p shows additional dependence on the particle diameter, a. From the mean channel velocity-based definition of Reynolds number, R_c can be related to Re as:

$$R_c = \frac{2}{3} Re \qquad (1.14)$$

For R_p <<1, the particle flow in the microchannel is dominated by viscous forces. This makes the particle travel with the local fluid velocity due to viscous drag. In this regime, particle distribution is conserved and there is no migration across streamlines. With the increase of R_p

>1, particle migration across streamlines occurs as the effect of the channel walls become more prominent.

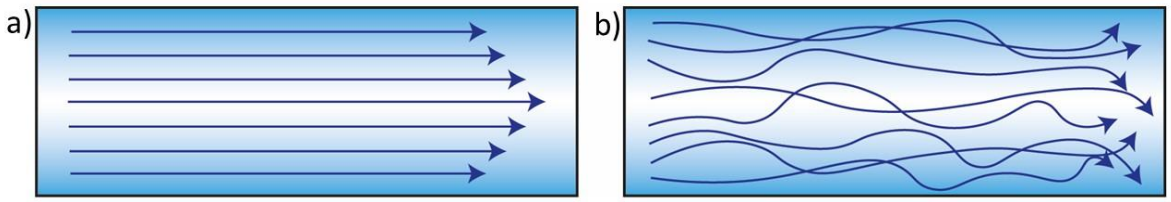

Figure 1-14. Schematics of a) laminar and b) turbulent flow of fluid.

1.5. Cross-slot microfluidics

In the cross-slot microfluidic device, the cells are hydrodynamically stretched by an extensional flow at the stagnation point (Figure 1-15). The cells arrive at the cross-slot junction at a constant speed and are rapidly deaccelerated to zero velocity at the stagnation point. The cells deform by a combination of compressive and shear forces as shown in Figure 1-15a. The cell leaves the extensional flow junction through one of the orthogonal outlets and recovers its original shape as it travels. Gossett *et al.* introduced the technique of Deformability Cytometry for mechanical phenotyping of cells using the cross-slot microfluidic device [179]. They estimated the compressive forces (F_c) acting on the cell at the centre of the extensional flow due to the fluid inertia as:

$$F_c = 0.5\,\rho\,U^2\,C_D\,A_p \qquad (1.15)$$

Where, ρ is the fluid density, U is the velocity of the fluid, C_D is the drag coefficient on the cell and A_p is the cell cross-sectional area. C_D depends on the Re and for Stokes flow conditions, it is given as $C_D = 24/Re$. However, when inertial forces cannot be neglected, C_D was estimated by Brown and Lawyer [180], by correlating with experimental data of terminal velocity of falling spheres over a large range of Re as:

$$C_D = \frac{24}{Re}\left(1 + 0.150\,Re^{0.681}\right) + \frac{0.407}{1 + {}^{8710}/_{Re}} \qquad (1.16)$$

This equation correlated the experimental data satisfactorily and is recommended for Re< 2×10^5. The shear force (F_S) acting on the cells due to the fluid viscosity was determined using:

$$F_S = \dot{\gamma}\mu\,(4\pi r^2) = 2\,\pi\,U\,\mu\,r \qquad (1.17)$$

Here, μ is the viscosity of the fluid, $\dot{\gamma}$ is the strain rate and r is the radius of the cell [181]. The shear stress is highest near the channel walls, as such, the shear force experienced by the cells would depend on the cell size [182]. The total force acting on the cell for hydrodynamic stretching at the stagnation point is a combination of inertial and shear forces:

$$F_T = F_C + F_S \tag{1.18}$$

The ratio of these forces can be tailored to achieve either an inertial or shear-dominated regime through manipulation of flow rate and fluid viscosity [181,183]. Cell deformation events are captured by a high-speed camera at high throughput. Deformation cytometry for the cross-slot device is the study of the characteristics of the cells based on their deformation index (DI) which is given as:

$$DI = \frac{H}{W} \tag{1.19}$$

where, H and W are the height and the width of the deformed cells at the stagnation point (Figure 1-15b).

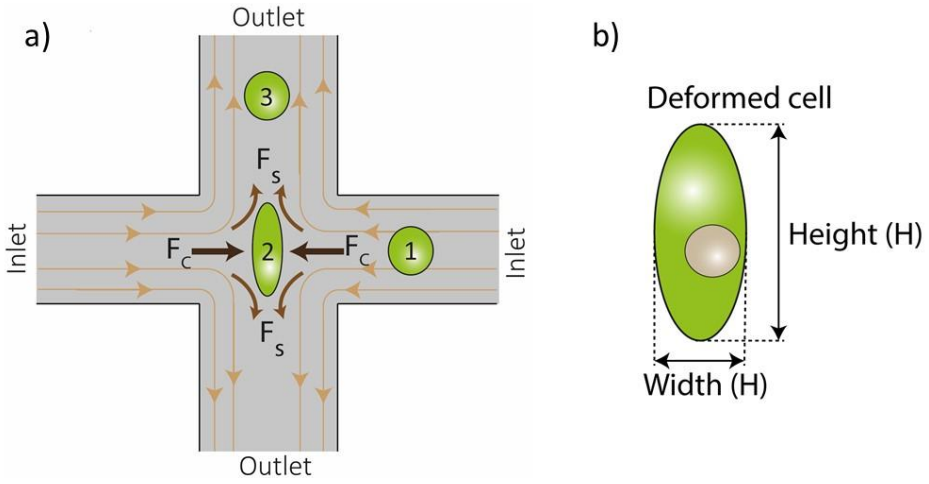

Figure 1-15. Schematics showing the deformation of cell in the cross-slot microfluidic device. a) Stages of cell deformation with 1 showing the approach of the cell from the inlet to the stagnation point. Stage 2 is the hydrodynamic cell deformation process at the stagnation point by the action of compressive (F_C) and shear (F_S) forces. The cell recovers its shape in stage 3 post-deformation in the outlet channel. b) Parameter of the deformed cell measured from the high-speed videos for analysis.

1.5.1. Inertial and shear regimes

As mentioned earlier, cell deformation in the inertial or shear-regime can be obtained by tailoring the suspension fluid velocity and viscosity. Armistead *et al.* demonstrated the dependence of Re on flow rate using equations 1.9 and 1.10 for the cross-slot device, for two different viscosities of the suspension fluid (Figure 1-16a) [181]. The calculations were made for a channel width of 35 µm and channel height of 25 µm, which are the dimensions of the device used for this thesis. The lower viscosity suspension fluid (LVSF) had a viscosity of 1 cP (centipoise), which resembles water. This showed a linear increase in Re with increasing flow rate. By contrast, the higher viscosity suspension fluid (HVSF) has a viscosity of ~33 cP and Re showed a significantly lower increase with flow rate. The dotted line represents Re = 40 which has been employed as the boundary between the shear and the inertial regimes. For the HVSF, the Re remains within the shear regime and was used for all experiments in this thesis. The viscosity of 33 cP for the cell suspension fluid was obtained by adding 0.5% methylcellulose (MC) (w/v) to phosphate buffer saline (PBS), details of which are provided in section 2.5.4. F_C and F_S as a function of flow rate and Re were also plotted in the same article using equations 1.15 and 1.17, respectively for the different viscosities. Figure 1-16b shows the dependence of the forces with flow rate at the stagnation point for fluid of viscosity μ =1 cP. F_C surpasses F_s at ~40 µl/min and dominates with increasing flow rate, well into the inertial regime with Re>40. For the HVSF (~33 cP), Figure 1-16c shows the dominance of F_S, with Re<11 up to the flow rate of 200 µl/min. This depicts the shear-regime of flow. All experiments in this thesis were performed at flow rate < 200 µl/min and at ~33 cP viscosity, well within the shear regime.

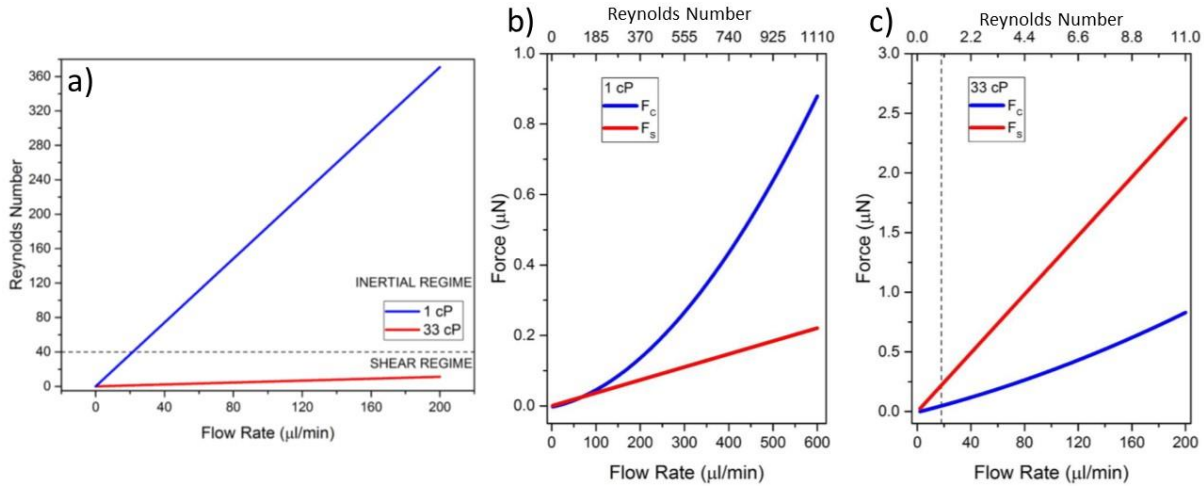

Figure 1-16. Characterisation of fluid flow in inertial and shear regimes. a) Reynolds number with flow rate of the fluid through the cross-slot device at viscosities of μ = 1 and 33 cP plotted from equation 1.9. The dotted line represents Re = 40 which demarcates the boundary between shear and inertial-regimes. Plots of compressive (F_C) and shear (F_S) forces with flow rate of the fluid through the cross-slot device determined from equations 1.15 and 1.17 for viscosities of the fluid at b) μ = 1 cP and c) 33 cP. The dotted line in figure c) represents Re =1. Figures reprinted from Armistead et al. 2019 [181].

1.6. Biomechanics of cell deformation

Cell deformability is a complex process resulting from interaction and repair responses coordinated through several organelles. This can include the roles of the cell membrane, nucleus and cytoskeletal constituents of microtubules, actin and intermediate filaments. Deformability cytometry has been used effectively in phenotyping cancer cells, as they show reduced stiffness compared to their healthy counterparts [179,181,184]. Alterations to the subcellular components during disease progression result in changes to deformability. Hence, cell deformability is a physical biomarker for diseases, which can affect the subcellular responses. The biomechanics for deformation can be understood through the viscoelastic cell response.

1.6.1. Viscoelasticity of cells

Viscoelasticity is the property of materials showing both viscous and elastic behaviour under deformation. An ideal solid shows purely elastic properties, such that when the deforming force is removed, the body regains its original configuration without energy dissipation. On the other hand, an ideal viscous Newtonian liquid will deform at a constant rate until the stress is removed with the dissipation of the deforming energy and will not regain the original configuration. Viscoelastic materials fall between an ideal solid and an ideal liquid. Such materials show hysteresis in the stress-strain curve, in which the area of the loop is equivalent to the energy dissipated during the deforming cycle. They also exhibit stress relaxation, which is the reduction of stress with time under constant strain. Viscoelastic materials also show creep behaviour, which is the continuous deformation under persistent mechanical stress. Cells are known to exhibit viscoelastic properties under applied mechanical stress, responding differently depending on the applied stress, strain and strain rate [185]. Different techniques have been employed to understand the viscoelastic response of cells, with varying values of elastic moduli depending on the technique and the model used.

The Kelvin-Voigt model has been widely for whole-cell deformations as it fits the viscoelastic behaviour well. This model was used to explain the viscoelastic properties of the cells deformed in the cross-slot microfluidic device [181,183]. In this approach, the viscoelastic behaviour of the materials was modelled using a circuit arrangement of a linear spring and a dashpot in parallel. A dashpot is a mechanical damping device that resists motion due to viscous forces and the spring represents the elasticity. The applied stress, $\sigma(t)$ to this system, is given by:

$$\sigma(t) = E\varepsilon(t) + \eta\frac{d\varepsilon(t)}{dt} \qquad (1.20)$$

Where $\varepsilon(t)$ is the strain, E and η is the elastic modulus and the viscosity associated with the linear spring and the dashpot, respectively. In the cross-slot device, as the cell enters the extensional flow junction, the stress increases from zero to maximum (σ_0), occurring at the stagnation point. Using this model, the velocity profile was simulated in the shear-dominated regime (μ =33 cP) at a flow rate of 5 µl/min, for ρ =1005 kg/m^3 using the finite element software COMSOL Multiphysics [181]. The 3D simulation mimicked the cross-slot geometry used for the experiments (channel width = 35 µm, channel height =25 µm) for incompressible

fluid with a single-phase laminar model and outlet pressure of 0. The results showed sinusoidal fitting to the velocity profile as shown in Figure 1-17a and b, where the initial linear velocity at the inlet drops to 0 at the stagnation point. The velocity increases at the same rate as the fluid makes its way towards the outlet. From equation 1.17, in the shear-dominated regime, the deforming force is proportional to the velocity, as such, the stress ($\sigma(t)$) also varies as a sine function. Hence:

$$\sigma(t) = \sigma_0 \, (1 + \sin(\omega t)) \tag{1.21}$$

where $\omega = 2\pi/T$, for a period T. Using equation 1.21 to solve equation 1.20:

$$\varepsilon(t) = \frac{\sigma_0}{(\eta^2\omega^2 + E^2)E}\Big[(\eta^2\omega^2 - E\eta\omega + E^2)e^{-Et/\eta} - E\eta\omega\cos(\omega t) + \eta^2\omega^2 + E^2\sin(\omega t) + E^2\Big] \tag{1.22}$$

Using this sine-oscillating Kelvin-Voigt model, the strain trace was fitted for the HL60 cells (Flow rate = 5 µl/min, viscosity of suspension fluid, μ = 33 cP, R^2 = 0.98) with time, and the elastic modulus was calculated as E =(0.30 ± 0.03) kPa (Figure 1-17c).

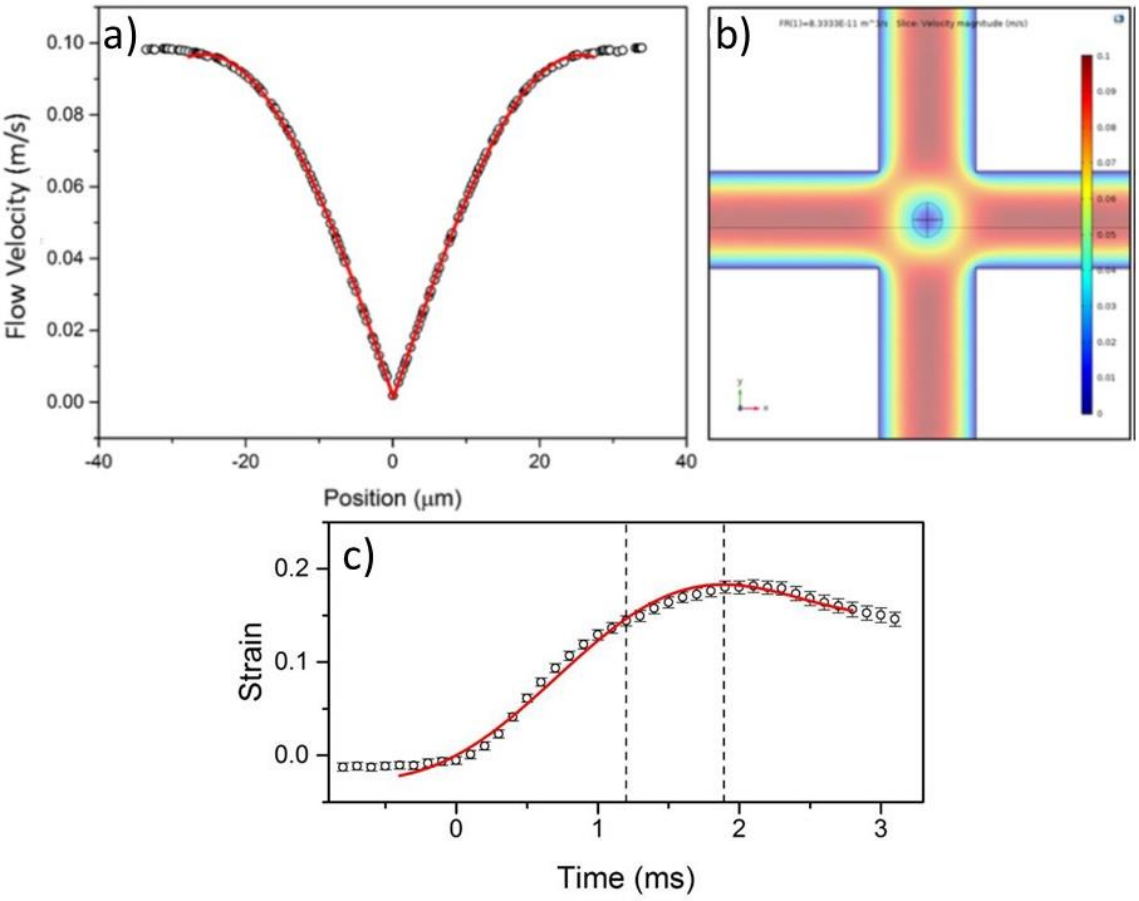

Figure 1-17. a) The velocity profile for the cross-slot microfluidic device at the flow rate of 5 µl/min using COMSOL, where position 0 is the stagnation point. b) COMSOL generated velocity magnitude across the extensional flow region of the cross-slot microfluidic device. c) Strain profile of N=50 HL60 cells at fluid viscosity μ =33 cP and flow rate of 5 µl/min. The red line represents the sine-oscillating Kelvin-Voigt model fit. Figures reprinted from Armistead et al. 2019 [181].

1.6.2. Cellular response to deformation and membrane disruption

Mechanical forces induce cellular response and can influence proliferation, morphological changes and migration. Upon deformation, most cells initially show elastic behaviour for a short time (seconds to a few minutes), but mostly viscous behaviour over a longer time period [186]. A rheological study shows that for epithelial cells, the cytoplasm is mostly viscous, whereas the surface appears elastic due to actin association with the membrane [187]. The biochemical response to mechanical stimuli is termed mechanotransduction and the predominant mediators are reported as ions channels, cytoskeletal proteins and signalling molecules [188]. Here, we will focus on the cellular response to membrane disruption.

The major responses of the cell to membrane disruption are immediate repair of the pores and return to homeostasis [128]. Multiple membrane repair processes can take place simultaneously which depend on the size of the pores, cell type and environmental conditions. Artificial lipid bilayer membranes have shown self-sealing capabilities without assistance from repair proteins, where the driving force is the lipid disorder at the curved edges, minimising the edge tension [189]. Membrane tension at the pores is also known to be reduced by cellular mechanisms, such as inward or outward budding followed by scission of the damaged section and patching of the pores by addition of intracellular membrane via vesicle fusion [190]. Larger pores (> 200 nm) tend to be repaired through rapid exocytosis, plugging and patching of the membrane, whereas smaller pores are repaired through endocytosis or shedding through disposable vesicles. Extracellular calcium ions are known to be vital for active cell membrane repair through various mechanisms. In fact, the absence of extracellular Ca^{2+} causes inhibition of cell membrane repair processes such as contraction, exocytosis, internalisation, patching or plugging [191]. Ca^{2+} is reported to be essential for the recruitment of wound repairing ESCRTs proteins (Endosomal Sorting Complex Required for Transport) and calcium-binding proteins (Annexins and calpains) at the damage site [192,193]. A study on cell deformation for intracellular delivery via constriction squeezing of cells showed that the presence of extracellular Ca^{2+} allows membrane repair within 15-30 s [194].

Cell swelling has been observed post-membrane disruption for different permeabilisation techniques due to the intake of water through osmosis [195–197]. The uptake of water into the cells is influenced by the presence of ions such as Na^+ and Cl^-, hence the composition of cell suspension buffer can determine the fate of cell swelling post permeabilisation. The cells can regain their natural volume after swelling, however, it can also lead to stress signalling actions and even cell death.

After the completion of the membrane repair, homeostasis begins to restore the intracellular conditions. These include recuperation of the ATP and K^+ levels, recovery from oxidative stress and restoration of cytoskeletal integrity [128]. If the cells are unable to restore their health even after the membrane repair, irreversible changes to cellular homeostasis can lead to cell death. Mechanical disruption can lead to permanent deformation of the cells which is referred to as cell plasticity. For the cross-slot microfluidic device, it was seen that beyond a certain high flow rate (>600 µl/min) in the inertial regime, HL60 cells begin to rupture and the viability drops

significantly [181]. This is caused by irreparable membrane damage and the permanent disruption of the cytoskeleton. However, if the deforming forces are below the region of permanent damage, the cells have the ability to recover post deformation. Adhered MCF10A cells have been reported by Ho *et al.* to show no plasticity after cyclic microfluidic deformations via cyclic compression [198]. Hence under optimised conditions, effective membrane disruption and intracellular delivery can be obtained without cell stress or permanent damage by remaining within the limits allowed for cell recovery.

1.7. Progression of Cancer

Normal healthy cells are under control from cellular signals as to when they can divide, differentiate or die. On the other hand, cancer cells have developed autonomy such that they can proliferate in an uncontrolled continuous manner enabled by gene mutations. These mutations can occur during mitosis when there are errors in DNA replication. However, these errors are relatively low and the cells are equipped with DNA repair mechanisms. Moreover, apoptosis is usually triggered when the damage to the DNA is irreversible. With the influence of genetics and environmental factors (carcinogens), multiple mutations can occur and accumulate with time. Cancerous growth (the primary tumour) occurs when the DNA mutations disrupt the normal cell proliferation and the induced apoptosis behaviours. Further mutations are necessary for the mass of cancer cells to thrive by promoting blood vessel growth. If they are unable to promote the growth of blood vessels, it leads to the starving of the cells (necrosis). Under optimal conditions, cells from primary tumours can break away and enter the bloodstream and lymphatic systems. This causes metastasis which is the secondary cancer growth in other parts of the body. As the cancer cells progress between stages, they can adapt to their new environment and eventually colonise.

1.7.1. Warburg effect

One of the most salient characteristics of cancer cells is that the manner in which they metabolise glucose is distinct from normal cells. Normal cells produce energy mostly through the oxidation of pyruvate in the mitochondria. By contrast, cancer cells metabolise glucose

through aerobic glycolysis in the cytoplasm to produce energy which is termed the Warburg effect (Figure 1-18a). A large amount of energy in the form of adenosine triphosphate (ATP) is required by the cancer cells to proliferate rapidly. Glycolysis is the conversion of glucose into pyruvate with the generation of 2 ATP from 2 adenosine diphosphate (ADP) which can be simplified as shown in Figure 1-18b. The process is far less efficient, generating only 2 ATP molecules compared to the oxidative phosphorylation in the mitochondria producing 36 ATP molecules for healthy cells. However, the rate of glucose metabolism is higher through aerobic glycolysis. Hence, large glucose uptake by the cancer cells is necessary for tumour progression [199]. With the maturation of the cancer cells, the dependency on glucose uptake and glycolytic activity is significantly increased. In addition, there is a remarkable loss in mitochondrial activity which has been suggested to be key for cancer cell survival by inhibition of apoptosis [200,201].

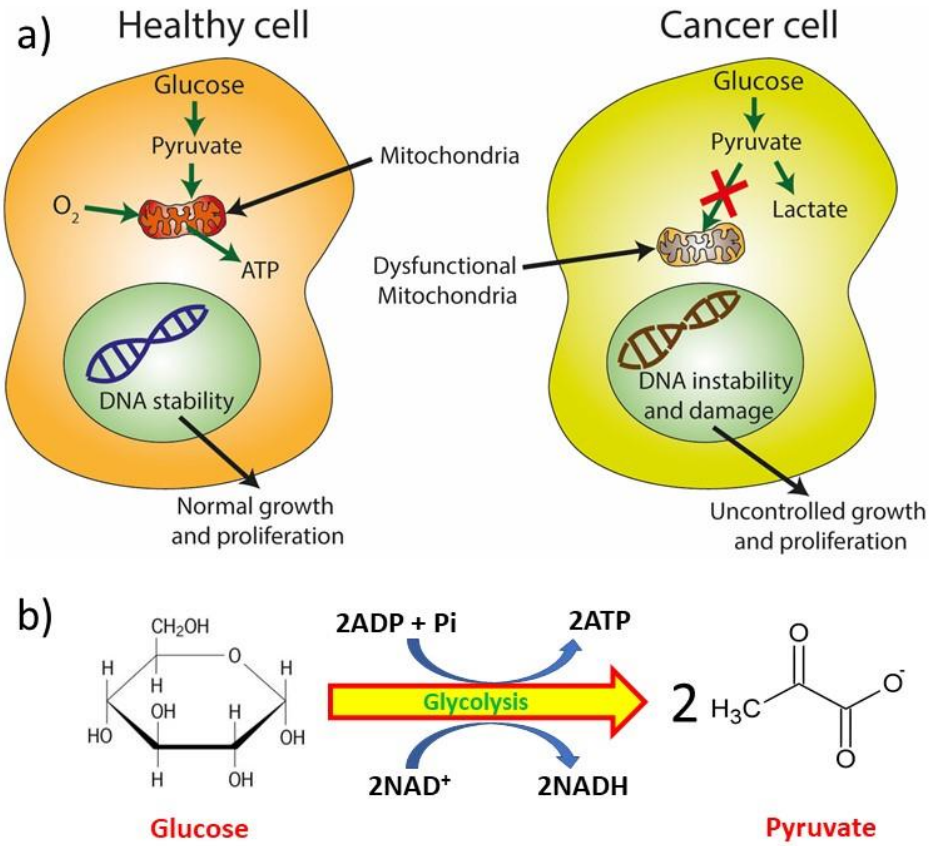

Figure 1-18. a) Schematics of healthy and cancer cells showing the difference in the glucose metabolism. b) The simplified glycolysis process showing the conversion of glucose into two pyruvate molecules with the generation of 2 ATP and 2 NADH.

1.7.2. Redox couples

Reactive oxygen species (ROS) such as H_2O_2 and superoxide anion ($^{\bullet}O_2^-$) are constantly generated in the cells through various processes. Elevation of the oxidised state can be detrimental to cellular health and needs to be regulated via redox reactions. Redox reactions are constantly taking place in the cells and are essential for metabolism, growth and proliferation. For these processes, the cells derive energy from oxidation reactions which involve the transfer of an electron from organic molecules to oxygen, resulting in the overall reducing environment of cells [202]. Redox couples are responsible for the flow of these electrons and hence for the redox environment in the cells. Most oxidation-reduction processes in cells involve the conversion of these molecules from one form to the other. Some of the universal redox couples are oxidised/reduced glutathione (GSSG/2GSH); nicotinamide adenine dinucleotide (oxidised, NAD^+; reduced, NADH) and nicotinamide adenine dinucleotide phosphate (oxidised, $NADP^+$; reduced, NADPH). The ratio of these interconvertible species determines the redox state of the cells.

Glutathione is the major thiol-disulphide redox buffer having the highest concentration of the redox-active compound in the cells, with GSH at 1-11 mM in the cytosol [202]. The interconversion of the GSSH/2GSH couple is given as:

$$GSSH + 2H^+ + 2e^- \rightarrow 2GSH \qquad (1.23)$$

Hence, their high concentration at low redox potential (-240 mV) has a major contribution to the reduced cellular redox state [203]. Studies have shown that glutathione redox potential could be as low as -320 mV which suggest that the GSH:GSSH molar ratio could be as high as 50,000:1 [204]. The abundance of GSH provides the cell with reducing capabilities from ROS, heavy metals and foreign compounds. Many types of cancer cells, such as breast, lung and ovarian cancers show elevated levels of GSH [205].

The NAD^+/NADH redox couple has essential roles in metabolic pathways such as glycolysis (Figure 1-17b) and oxidative phosphorylation. During glycolysis, NAD^+ reduces to NADH, which can be reoxidised to NAD^+ in the cytoplasm, for example, during the conversion of pyruvate to lactate. This redox couple also play important role in the regulation of ageing, embryonic development and in diseased conditions such as cancer and diabetes. As mentioned above,

during the Warburg effect in cancer cells, the partial breakdown of glucose for rapid ATP generation leads to NADH accumulates in the cytoplasm. The switch from oxidative phosphorylation to aerobic glycolysis in cancer cells increases the net cytosolic NADH [206]. It is also reported that NADH regulates the release of intracellular Ca^{2+} [207]. Hence, NADH levels can be significant in the repair of membrane disruptions and these potential mechanisms could be investigated in the future.

Like many of the other redox couples, $NADP^+$/NADPH is involved in many cellular processes such as metabolism, biosynthesis of fatty acids, gene expression, calcium homeostasis, ageing and cell death. NADPH is a cofactor in reductive reactions and acts as an electron source while protecting cells from redox stress and toxic metabolites. The $NADP^+$/NADPH ratio is approximately 1:100 in cells and tissues making it an excellent source of electrons.

The thioredoxin redox-couple, TrxSS/Trx$(SH)_2$ is another thiol-based redox couple responsible for reducing cysteine moieties in DNA-binding sites. Thioredoxins are proteins that can form intramolecular disulphide bonds and assist in the refolding of disulphide containing proteins [202]. The redox couples are also interdependent on each other, as such, the GSSH/2GSH ratio heavily depends on the $NADP^+$/NADPH ratio [208]. The cellular redox potential (-335 to -350 mV) is lower than NADPH/$NADP^+$ potential (-315 mV), such that for the reduction of GSSH, the NADPH/$NADP^+$ ratio needs to be high [203]. NADPH acts as a reducing source for both GSH and thioredoxin. The flavin adenine dinucleotide redox couple FAD/$FADH_2$ ratio is associated with energy metabolism through oxidative phosphorylation. FAD is a stronger oxidising agent than NAD^+, hence its presence has a significant impact on the redox environment of the cytoplasm. The presence and the influence of some of these redox couples will be discussed with respect to breast cancer cell lines in the next section.

1.7.3. Redox state in breast cancer cells

Cancer cell lines provide an ongoing source of self-replicating malignant cells which have been widely studied to investigate many aspects of cancer. The studies made on breast carcinoma is based on the *in vivo* and *in vitro* studies of a large number of breast cancer cell lines. However, the number of cell lines employed for most of the breast cancer studies is very small with MCF7, T47D and MDA-MB-231 making up more than two-thirds of the cell lines used. The

breast cancer cell lines have been classified on the basis of gene expression of three important receptors: estrogen receptor (ER), progesterone receptor (PR) and human epithelial receptor 2 (HER2) [209]. Although MCF10A are normal (benign) epithelial breast cells obtained from a patient with fibrocystic disease, they have been immortalised and widely used to compare with the breast cancer cell lines. The properties of the cell lines used for investigation in this thesis with respect to the above-mentioned gene expressions are shown in Table 1.1 [209–211].

Cell line	ER	PR	HER2	Type	Original tissue
MCF7	+	+	−	IDC	M
T47D	+	+	−	IDC	M
MDA-MB-231	−	−	−	AC	M
MCF10A	−	−	−	F	N

Table 1-1. Properties of the breast cell lines investigated in the thesis. ER: estrogen receptor, PR: progesterone receptor, HER2: human epithelial receptor 2, IDC: invasive ductal carcinoma, ADC: adenocarcinoma, F: fibrocystic disease, M: metastasis and N: Normal. '+' and '−' indicate the presence and absence of the hormone-receptors.

Estrogen can bind to the cell surface for an ER+ breast cancer cell via estrogen receptors which account for ~80% of all cancers [212]. Similarly, 60% of breast cancer cells are PR+ that can bind to the progesterone hormone. These hormone-receptor-positive cells tend to grow slower than the hormone receptor-negative cells and are responsive to hormonal therapy. HER2 is a receptor tyrosine-protein kinase which under normal conditions promote breast development. However, it accounts for 25-30% of breast cancers when overexpressed. MDA-MB-231 is a triple-negative breast cancer cell line, lacking both ER and PR receptors, as well as HER2 amplification. As such, they are aggressive, invasive, grow quickly and with limited treatment options. All three cancer cell lines are metastasised with MCF7 and T47D being invasive ductal carcinoma (IDC) and MDA-MB-231 cells, adenocarcinoma.

ER has been reported to show an increase in glucose transport and glycolysis [206]. ER also regulates isocitrate dehydrogenase activity which results in the reduction of NAD^+ to NADH. As such, the ER+ breast cancer cell lines would have higher NADH levels in the cytosolic environment compared to the ER- and the non-malignant cells. Using a two-photon fluorescence lifetime and polarising imaging of intrinsic NADH, Yu and Heikal demonstrated

that the average concentration of NADH in breast cancer cells (Hs578T) is 168 ± 49 μM, which is ~1.8 fold higher than that in normal breast cells (Hs578Bst) at 99 ± 37 μM [213].

The comparative autofluorescence of NAD(P)H and FAD have been used to evaluate the redox state of cells [214]. NADH is oxidised to NAD^+ and FAD is reduced to $FADH_2$ during oxidative phosphorylation. Additionally, since NAD^+ reduces to NADH during glycolysis, the ratio of NADH and FAD is considered as the measurement of the balance between glycolysis (cancer cells) and oxidative phosphorylation (normal cells). Due to their similar fluorescence emission, NADH and NADPH are collectively termed as NAD(P)H, however, it is difficult to differentiate their individual contributions spectroscopically. NAD(P)H can be excited by UV light (~325-380 nm) and emit blue fluorescence (~425-490 nm), whereas FAD excites in the blue light region (~430-460 nm) emitting green fluorescence (~530-570 nm) [215]. Their redox counterparts (NAD^+ and $FADH_2$) do not show autofluorescence. Optical redox ratio (ORR) is defined in several ways but is essentially the ratio of the fluorescence of NADH and FAD. Ostrander *et al.* described ORR as NADH/FAD fluorescence emission ratio as measured using confocal microscopy for ER+, ER- and normal cells [206]. They observed a significant increase in the ORR of the cancer cells lines compared to the normal cells. For the normal MCF10A cells, the FAD emission was higher than the NADH intensity (ORR <1). ER- cells showed an increase in ORR compared to the non-malignant cells, indicating the increase in the NADH by higher dependency on glycolysis with malignancy. ER+ cell lines showed a drastic increase in NADH/FAD intensity ratio compared to the ER- cells with MCF7 and T47D cells having ORR > 4 and 3, respectively. This indicates the increase in the reducing redox environment of the cells with malignancy and further with the presence of ER expression.

1.8. QD redox sensors

QD biosensors work on the principle that the interaction of the target analyte and the moiety alters or produces a detectable change in the photoluminescent intensity or the lifetime of the QD. Typically, the QD and the moiety are linked via bioconjugation techniques (e.g., Streptavidin and biotin affinity) or by an alkyl chain. There must be an interaction between the QD exciton and the sensing moiety, depending on the presence of the target analyte. QD redox sensors are based on the principle of reversible luminescence quenching by the interaction of

moiety with the target analyte, either by charge transfer or Förster resonance energy transfer (FRET). In a FRET-based redox sensor, the excited donor (QD) loses the energy associated with the excitation in a non-emissive process to an acceptor. The energy transfer occurs through dipole-dipole interaction from the QD donor to the acceptor [216]. Since the FRET efficiency is donor-acceptor distance-dependent (FRET rate ~r_d^{-6}; r_d: donor-acceptor distance), the pair should be in close proximity. Additionally, there must be an overlap of the emission spectrum of the donor and the absorption spectrum of the acceptor so that the energy transferred can excite the acceptor.

On the other hand, the charge-transfer-based redox sensors involve the depopulation of the excited states by the transfer of electrons or holes. The r_d in this case does not need to be extremely small for charge transfer compared to the FRET-based sensor. Additionally, there is no constraint to match the emission and the excitation of the donor-acceptor pairs. Hence, QDs of different emission wavelengths can be used for the same acceptor. A variety of redox-active compounds, such as metal complexes, dyes, organic molecules and ions have been used for photoinduced electron-transfer-based QD redox sensing [59]. Sensing can be achieved by charge transfer from excited QD to acceptor by changing the redox state of the acceptor, measuring the change in transfer efficiency or by measuring the association or disassociation of the acceptor from the QD surface [8]. Sensing involving a change of the acceptor redox state is achieved by either blocking or allowing the transfer of charge to the acceptor and will be the approach taken for this thesis.

Dopamine has been widely used as the electron acceptor for redox sensing with the QD donors as its reduction potential is biologically relevant. Clarke *et al.* showed the CdSe/ZnS QD-dopamine conjugates increase in fluorescence under oxidising conditions for staining of the dopamine-receptor expressing cells [217]. Here, dopamine acts as an electron donor and is responsible for quenching by hole trapping in its reduced state. The Mattoussi group demonstrated CdSe/ZnS QD-dopamine conjugate pH-dependent *in-vitro* electron-transfer from QD to oxidised dopamine [59]. In this case, the dopamine in the reduced configuration did not facilitate the transfer of electrons from QD resulting in the increase in photoluminescence (PL). They also showed that the pH-dependent quenching of the QD-dopamine conjugates is attributed to the charge transfer interactions between QD and the two configurations of dopamine, namely the oxidised quinone and the reduced catechol [218].

With the increase of pH from acidic to basic, the QD PL decreased as the catechol becomes a better electron donor and quinone becomes a better electron acceptor.

QD-ubiquinone derivative conjugates were shown by the Long group to exhibit redox-sensitive fluorescence [61,219]. Ubiquinone or coenzyme Q_{10} can exist in oxidised, semi-reduced and reduced states (Oxidised, QnNS; Reduced, HQnNS), enabling it to act as a single or double electron carrier. In the oxidised state, the ubiquinone derivatives capture the excited electrons in the conduction band of the QD, resulting in quenching. This chemical reduction resulted in the high PL recovery of HQnNS-QD compared to the unmodified QDs, which occurs due to the passivation of the surface traps by ubiquinone. Additionally, it was shown that a shorter alkyl linker resulted in improved quenching efficiency as the decreased spacer distance allows faster electron transfer. The recovery of QD photoluminescence by reducing the QD-bound quinone with NADH in the presence of NADH dehydrogenase was used to measure the concentration dependence of NADH oxidation [61]. They also demonstrated PL recovery through the reduction of QnNS-QD by enzyme complex I in the human neuroblastoma SH-SY5Y cell line [219]. The fluorescence modulation of this redox sensor by enzyme complex I, which is an NADH dehydrogenase specific to ubiquinone, allowed visualisation of the spatial distribution of this enzyme within the cells.

1.8.1. CdTe/CdS QD-Q2NS redox sensor

For an effective QD-based redox sensor, the quenching process via charge transfer to the acceptor must be significantly faster than the radiative exciton recombination. To achieve this, the timescale of charge transfer could be made significantly shorter, or the radiative recombination could be made longer, or both. Harvie *et al.* report a CdTe/CdS core/shell QD conjugated with an electron-accepting quinone ligand redox sensor [45]. These are quasi-type-II core/shell QDs and as described in 1.2.2.3. This design can be exploited for its charge separating properties with electrons remaining confined to the CdS shell, while the holes remain in the CdTe core. This charge separation significantly increases the radiative recombination lifetime over core QDs. The QDs were conjugated with redox-sensitive quinone molecules Q2NS (Figure 1-19), previously reported by the Long group to exhibit switchable quenching. When the Q2NS are in the oxidised state, the excited electrons are rapidly

transferred to the oxidised quinone, outcompeting other processes such as cooling to the band-edge, radiative and non-radiative recombination. The charge-transfer luminescence quenching is mediated via a 'hot' surface electron trap state. Using the atomistic semiempirical pseudopotential method, it was predicted that the transfer time of the electrons to the oxidised Q2NS ranges between 2-8 ps and 40-70 ns, for the shortest and the longest distance between the excited electron and the quinone respectively. This prediction was in agreement with the transient absorption and PL lifetime experimental data. Hence, an increase in the number of Q2NS per QD improves the speed of electron transfer. With the Q2NS ligand reduced, the rapid electron capture mechanism by the quinone is removed and the PL emission of the QD is restored through normal recombination. Hence, this QD-Q2NS can be suitable for sensing the redox environment in cells and was employed for investigation in this thesis. It is hypothesised that the reducing environment of the cytoplasm would reverse the quenching of QD luminescence, with the degree of recovery depending on the reducing capability of the cells. This would allow a distinction to be drawn between healthy cells, with a lower reducing potential and hence lower QD luminescence, and cancerous cells with higher reducing potential and increased recovery of luminescence. Maximum PL recovery is achieved if all Q2NS is reduced, as such, for the proof-of-concept MCF7 cells were chosen as they have a high reducing redox environment. The reducing capability of the cells would depend on the cell type, as seen in sections 1.7.2 and 1.7.3., and also on the treatment of cells such as chemically induced oxidative stress.

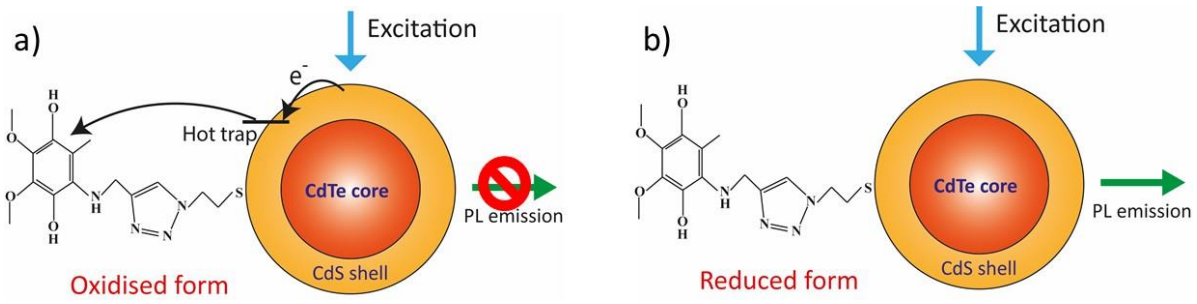

Figure 1-19. CdTe/CdS core/shell quantum dots with the quinone Q2NS ligands in the (a) oxidised state showing the capture of electron via hot trap state by the quinone quenching the QD emission and (b) reduced states where the electron trapping mechanism is absent where the QD emission is restored.

1.9. Quantum rods

Colloidal Quantum rods (QRs) are interesting materials from both fundamental and application aspects. They represent the transition between 0-dimension (QDs) to 1-dimension (nanowires) nanomaterials. They have distinctive optical characteristics such as linearly polarised absorption and emission, which could lead to many orientation-sensitive biological and electro-optical applications [220]. QRs give linearly polarised emission along the length of the crystallites with the degree of polarisation dependent on the aspect ratio of the rods [221]. They show a wider absorption cross-section, and enhanced charge separation compared to their QD counterparts [222]. The quantum confinement in the 0-dimensional QDs is in all three dimensions, however, for the 1-dimensional QRs, the confinement is along the radial direction and shows bulk-like behaviour along its length [223]. Hence, QRs can simultaneously show properties such as size-dependent band-gap and emission of quantum confinement, to large absorption cross-section and long-distance charge separation of the bulk crystals. The relative ease of assembly of QRs into superlattices and superstructures makes them a promising candidate for lasing devices. Furthermore, the lasing threshold for QRs is lower compared to QDs. The gain performance in QDs is compromised by the size-dependent, strong and rapid Auger relaxation processes. In QRs, the lasing threshold is significantly reduced due to the slower, non-radiative Auger recombination, increase in both the absorption cross-section Stokes shift that weakens the reabsorption interferences [224]. QRs can form liquid-crystalline phases and their ability to align in macroscale has useful optoelectrical properties with applications in photovoltaic and hybrid solar cells [225]. The difference in the properties of QRs compared to QDs can be advantageous in bioimaging. The larger absorption cross-section, narrow emission spectra and faster radiative decay are some of the improvements in using QR bio probes [226]. The large availability of surface area per particle can facilitate the accommodation of multiple moieties for more versatile cellular sensing.

The enhancement of the PLQY of the CdSe QRs typically requires multi-step processes with difficult to handle reagents, discussed in the following sections. Here, two simple and safe methods to increase the photoluminescence efficiency of the QRs have been presented. Attempts to make hydrophilic transitions of the QRs have been presented for potential biological applications.

1.9.1. Quantum rod synthesis

The Alivisatos group demonstrated that the shape of the CdSe particles can be controlled by the combination of the changes to the crystal growth kinetics and organic surfactants [221,227]. Spherical QDs will be formed if the overall growth rate is slow, whereas, if the growth is fast in sequential steps, it leads to the formation of QRs. The growth of the QRs is carried out in two steps: nucleation of the CdSe spheres followed by anisotropic growth. The wurtzite structure of the CdSe nanocrystals favours anisotropic growth in the ⟨002⟩ direction post-nucleation at extremely high monomer concentrations. Hence, the elongation of the particle occurs leading to the formation of QRs. Shieh *et al.* demonstrated control growth of colloidal CdE (E =Se, Te or S) QRs and QR heterostructures via sequential injections of chalcogen precursor [228]. This is a simple approach in which stepwise injection of the chalcogen precursor promotes epitaxial deposition in the ⟨002⟩ direction, which is the most reactive facet of the wurtzite CdE nanocrystals. After the initial nucleation, the addition of more chalcogen precursors at low supersaturation lowers the chance of further nucleation and favours rod growth. The length of the QRs is determined by the number of injections and will continue to increase until the Cd-TDPA complex precursor is depleted. To demonstrate the generalisation of the method, they synthesised QR heterostructure of CdS/CdTe/CdS and CdTe/CdSe/CdTe by interchanging between the injected chalcogen precursors.

1.9.2. Quantum rods and quantum yield

The main drawback of QRs is their low PLQY of ~1% for bare CdSe rods. This low efficiency of photoluminescence conversion in QRs is attributed due to the large surface-to-volume ratio of the rods. A large surface area enables the presence of a large number of surface defects that are very efficient in trapping the excited charge carriers, leading to nonradiative exciton recombination [229]. The enhancement of the quantum yield of QRs is typically achieved by the core/shell configurations, similar to the case of QDs. However, the morphology adopted is typically dot-in-rod core/shell QRs. Carbone *et al.* reported such CdSe/CdS QRs with 70-75% PLQY for short rods (aspect ratio<10) [230]. The CdS precursor is rapidly injected into the reaction flask containing preformed CdSe spherical seeds. Rather than forming separate seeds,

the CdS preferentially grows on the CdSe seeds since the activation energy for the homogeneous nucleation is higher than heterogeneous growth. The PLQY decreases with an increasing aspect ratio (>10) due to the rise in the number of surface traps in the CdS region. Another morphology reported for core/shell QRs is the rod-in-rod particles with PLQY of 79% for CdSe/CdS [231].

Epitaxial shell growth on QR cores with a material of larger bandgap (CdS, ZnS or both), similar to the QDs as discussed earlier, has also been reported to enhance the PLQY [221,232]. The thickness of the shell also plays a significant role in the QRs' photoluminescence efficiency [233]. A thin shell is able to passivate the surface traps effectively and the PLQY is enhanced. However, as the shell thickness increases, new defects in the mid-gap begin to form due to the strain relaxation at the core-shell interface. As these defects increase with shell thickness, the PLQY decreases. To reduce the mid-gap defect, strain-controlled shell morphology was recently adopted with the surface from flat, to islands and even helical shells [234].

For the CdSe/ZnS core/shell QRs, the most commonly used zinc precursor is diethylzinc [235]. However, diethylzinc is extremely difficult to handle as it ignites upon contact with the atmosphere and reacts violently with water. Hence, the use of this precursor is limited to the inert atmosphere within the glove box. Other zinc precursors have been used for shell growth of QRs with varying degrees of experimental impediments and efficiencies [236]. A promising candidate is zinc diethyldithiocarbamate ($Zn(DDTC)_2$) which could enable CdSe/ZnS core/shell QD synthesis via a single-molecule precursor in a safe and simple manner. Although it has been used in QD shell growths, its potential as a shell material for CdSe QRs has not been extensively explored. Recently, $Zn(DDTC)_2$ was used to synthesise CdSe/CdS/ZnS QR-in-matrix with 85% PLQY in which the ZnS outer layer promotes the assembly via crosslinking [237].

The Binks group has achieved ~97.2 % PLQY for CdTe QDs by the treatment with chloride ions [238,239]. The chloride ions are successful in passivating almost all of the surface traps and eliminating unwanted non-radiative recombination processes. Additionally, the chloride ion treated QDs were significantly more stable when exposed to air compared to the untreated QDs. For this thesis, two methods of enhancing the PLQY of the CdSe QRs have been adopted: ZnS epitaxial shell growth using the $Zn(DDTC)_2$ precursor for the shell material and chloride ion treatment of the QRs. The methods have been compared for PLQY enhancement, stability and ease of transformation into hydrophilic rods.

1.9.3. Hydrophilic QRs

For the purpose of biological applications, it is essential that the QRs are hydrophilic. Organometallic synthesis of QRs results in hydrophobic capping ligands which makes them insoluble in water. Hence, to passivate the hydrophobicity of the QRs several methods have been reported such as the use of silica matrix encapsulation, hydrophilic PEG grafted lipids, mercapto acids as coupling reagents, ligand exchange and amphiphilic polymers [240,241]. However, most of these methods cause adverse effects on the photoluminescence properties of the QRs, through interactions between solvents, ligands and the environment. Recently, using a dihydrolipoic acid zwitterionic ligand-based cap-exchange, CdSe/CdS QRs were efficiently made dispersible in water [242]. However, the QRs were almost completely quenched during the process. Fortunately, the photoluminescence of the QRs was recovered via exposure to near UV to blue radiation.

For the purpose of this thesis, encapsulation of the hydrophobic QRs was performed using an amphiphilic polymer, poly(maleic anhydride-alt-1-tetradecene), 3-(dimethylamino)-1-propylamine derivative (PMAL). Although this encapsulation increases the hydrodynamic size of the particles, it was chosen due to its simplicity. The amphiphilic polymers organise themselves around the particle with their long hydrophobic chains coupling with the hydrophobic ligands of the QRs [24]. This leaves the hydrophilic end of the amphipols exposed to the solvent. The advantage of this method over the ligand exchange procedures is that it can prevent the QR surface from damage that could hamper the photoluminescence efficiency.

1.10. Scope of project and chapter overview

The scope of this thesis was to establish non-endocytic delivery of QDs to the cytoplasm of live cells for redox sensing via membrane disruption using hydrodynamic shearing forces in a cross-slot microfluidic device. Although, non-endocytic delivery of NPs has been reported through cell squeezing using microfluidic constrictions [128], detection of the redox state in live cell cytoplasm has not yet been reported. Redox sensing in live cell cytoplasm can provide an understanding of how the malignancy in cells develop with the changing redox environment.

This can help understand the proliferation, metabolism and metastasis of cancer cells. Additionally, it can be useful in phenotyping cells on the basis of their cytoplasmic redox state.

Fluid motion about the transient membrane pores can give vital information regarding the diffusion and flow of particles and cellular contents. The leakage of intracellular materials in addition to the uptake of particles by cell deformation would be crucial in determining the diffusive nature of fluid flow across the membrane pores, the longevity, size and the number of the pores and their repair dynamics.

Additionally, methods to improve the photoluminescent efficiency of QRs were explored with the potential to be applied for biosensing in the future. Enhanced photoluminescent efficiency of QRs can have broader applications solar cells, lasing devices and in polarisation microscopy.

The structure of the thesis is as follows:

Chapter 2 describes the experimental techniques used for the thesis. Additional details such as theory and reasoning for some of the methods have been given where it was felt to be essential.

Chapter 3 gives the details of the CdTe/CdS QD synthesis and characterisations. The MCF7 cells were hydrodynamically deformed through the cross-slot microfluidic device in the shear dominated regime for the uptake of QDs over a range of flow rates. The viability of the cells was measured with deformation and QD uptake. Confocal microscopy was used to measure the fluorescence intensity from the cells. TEM images were taken to establish the non-endocytic nature of QD delivery.

Chapter 4 focuses on the redox sensing in live cells via the microfluidic delivery of quinone conjugated redox-active QDs (RA-QDs). The cellular response of the RA-QDs was established using MCF7 cells and was later used to compare with the response from other breast cancer cell lines (T47D and MDA-MB-231) and non-malignant breast cells (MCF10A). The viability of the different cells was investigated for different concentrations of QDs and RA-QDs, and the deformations indices were compared. The cellular response via the RA-QDs probes upon chemical alteration of the redox environment (chemically induced reactive oxygen species) was also examined.

Chapter 5 is an effort to understand membrane poration and fluid motion through the transient membrane pores generated by the hydrodynamic deformation of cells in the cross-slot microfluidic device. The outflow of intracellular fluids by membrane disruption through hydrodynamic deformation was investigated using high-speed frequency-division multiplexing microscopy. Uptake of differently sized Au-PEG-FITC NPs on cell deformation was also investigated to give an indication of the size of the membrane pores.

Chapter 6 gives studies that aim to enhance the photoluminescence efficiency of CdSe QRs. Two approaches, epitaxial ZnS shell growth and chloride ion treatments were investigated and compared. An effort was made to transform the CdSe/ZnS core/shell QRs into hydrophilic particles by using an amphiphilic polymer.

Chapter 7 concludes the main findings of the thesis. Chapter 8 provides an outlook into the potential future works based on the findings of this thesis. Emphasis is given to establishing a model for membrane poration through cell deformation and uptake of nanoparticles.

2. Experimental Methods

2.1. Synthesis of CdTe/CdS QDs stabilised with thioglycolic acid

The CdTe/CdS core/shell QDs stabilised with thioglycolic acid (TGA) (Figure 2-1) were synthesized using the method previously described [37,72]. 0.985 g of $Cd(ClO_4)_2.6H_2O$ (Merck) was dissolved in 100 ml of water. 400 µl TGA (Merck) was added under stirring which turned the solution turbid. The pH of the solution was adjusted to 11.2 by dropwise addition of 1M NaOH solution which results in a transparent solution. The solution was placed in a three-neck flask and was bubbled with N_2 for 3 h. 20 ml of 0.5 M H_2SO_4 was also bubbled with N_2 for 3 h and was carefully injected onto 0.2 g of Al_2Te_3 lumps (Absco Limited) to produce H_2Te gas which was passed through the cadmium precursor solution under nitrogen flow (Figure 2-2a). The change in the colour of the solution to red indicated the formation of CdTe nanocrystal seeds. They were grown into larger QDs under reflux at 100 ^oC under N_2 atmosphere (Figure 2-2b). The duration of the reflux determined the size of the QDs and consequently its emission wavelength. The smallest QDs <2 nm, with emission in the green region of the spectra were obtained after reflux of 10-15 min, whereas larger QDs emitting in the red region required a longer reflux time of up to two days. The CdS shells on the CdTe nanocrystals were grown by the addition of thiourea in the reaction mixture followed by further reflux of 45 min and up to 7 h. Thiourea releases sulphur at raised temperature for the CdS. The QD solution was cooled and stored at 4 ^oC until further use.

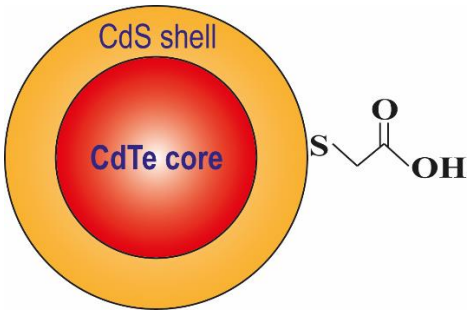

Figure 2-1. CdTe/CdS core/shell QDs stabilised with thioglycolic acid.

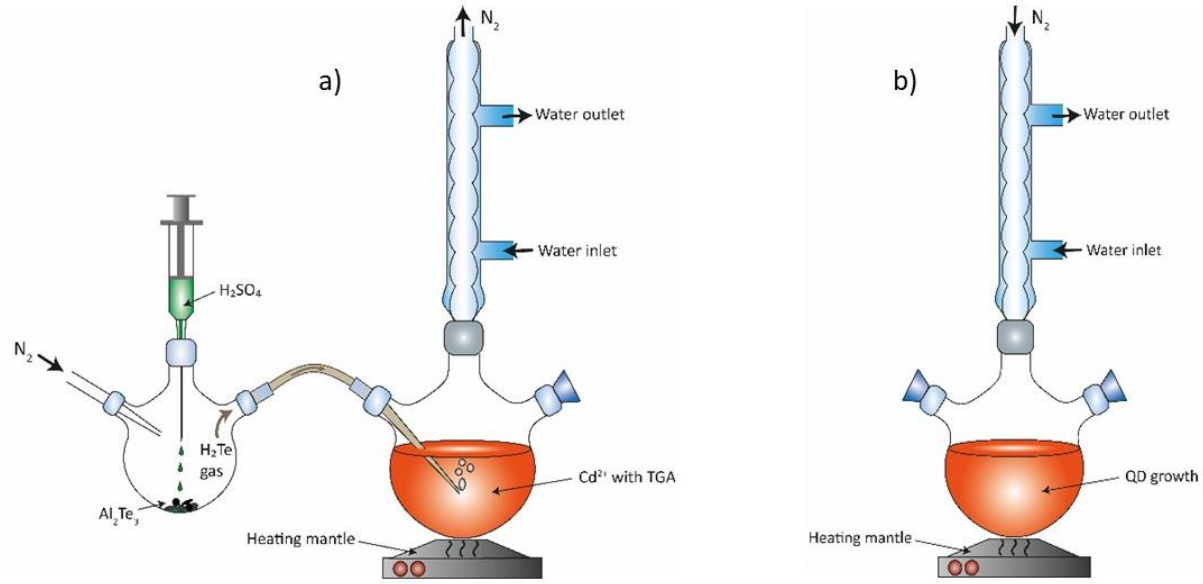

Figure 2-2. Schematic of the experimental apparatus arrangements for the synthesis of CdTe/CdS QDs with a) the setup for the injection of the H_2Te gas into the Cd precursor and b) for the growth of QDs under reflux.

2.1.1. Cleaning of the QD dispersions

The colloidal solution of the as-prepared CdTe/CdS core/shell QDs passivated with TGA stored at 4 ^{o}C in the dark is very stable. This is due to the presence of excess TGA in the solution preventing the ligand loss from the surface and surface oxidation. Hence, the QDs remain relatively free from degradation. The as-prepared QD solution contains other reaction products and precursors which need to be removed for analysis and experiments. The QDs were cleaned twice with excess isopropanol (IPA) at IPA:QD solution of 2:1 (v/v), added to the crude QD solution which precipitates the particles, but the by-products remain dissolved. The mixture was centrifuged at 4000 g for 10 min. The QD pellet was dispersed in Milli-Q water in the desired concentration (1-5 µM).

2.2. Ligand exchange with electron acceptor Quinone ligand

The electron-accepting quinone compound (Q2NS) was synthesised according to the method described by Harvie *et al.* [45]. The molecule consists of a quinone group which is the electron acceptor conjugated to a disulphide linker via click chemistry (Figure 2-3). The disulphide bond

allows the sulphur to form a thiolate bond with the cadmium of the QD surface. A clean solution of QDs in Milli-Q water (1-5 µM) was sonicated under vacuum to remove any dissolved gas and stored in an oxygen-free glove box. Q2NS in dimethyl sulfoxide (DMSO) (Thermo Fisher Scientific) was added to the QD solution (Q2NS:QD = 20:1 molar ratio) and left overnight under N_2 atmosphere in the dark. The resultant solution was cleaned twice with excess IPA (IPA:QD = 5:1 v/v) and was resuspended in Milli-Q water. This is the quinone-based redox-active QDs (RA-QDs). The effective binding of the Q2NS ligand to the QD surface was confirmed by the PL quenching of the QD emission using fluorescence spectroscopy. The quenching was considered to be effective for cellular uptake experiments when >99%.

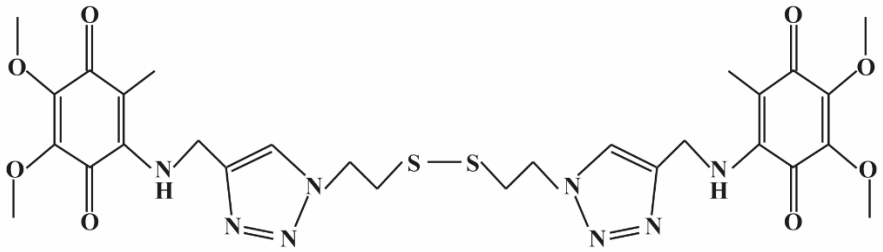

Figure 2-3.The schematic of the Q2NS compound with electron-accepting quinone group conjugated.

2.3. QD characterisation

2.3.1. UV-Vis NIR spectroscopy

As described in the section 1.2, the electronic transition occurs from the valence band to the conduction band when the photons are absorbed by the QDs. These transitions lead to the formation of absorption bands. The ultra-violet/visible/near-infrared (UV-Vis-NIR) absorption spectroscopy gives the measure of the absorption of light as a function of wavelength. QDs show many electronic transitions in this range of the electromagnetic spectrum, hence absorption spectroscopy is important in investigating their optical properties. The absorbance of the sample was measured against a “blank” reference which is the solvent or the dispersal medium of the sample. The absorption spectra were recorded by using a beam splitter to divide the incident light into two which was passed through the sample and the blank in identical cuvettes. The absorption spectrum of the sample was generated by subtracting the absorbance of the blank. UV-Vis-NIR spectroscopy of the diluted nanocrystal solutions was

recorded with Cary 5000, Agilent Technologies and Lambda 35, Perkin Elmer. The concentration of the QD solution was determined from the absorbance and the position of the first exciton absorption maxima as described by Yu *et al.* which will be described in detail in section 3.1 [5]. The absorbance of the colloidal QD dispersion is proportional to its concentration and Yu *et al.* calculated the molar extinction coefficient (ε) and determined the concentration using the Beer-Lambert law:

$$A = \varepsilon\, c\, L \qquad (2.1)$$

where, A is the absorbance, c is the molar concentration and L is the path length of the light through the sample.

2.3.2. Fluorescence Spectroscopy

The steady-state photoluminescence (PL), or fluorescence, spectroscopy has two main modes of operation: emission spectrum and excitation spectrum. The former is more common when the excitation wavelength is fixed and the emission intensity as a function of wavelength is acquired. On the other hand, excitation spectra can be collected by sequentially exciting through a wavelength range, but this time fixing the emission wavelength and collecting the fluorescence intensity. In practice, the sample was placed in a cuvette (quartz or plastic) and was illuminated constantly with a collimated beam of light. The wavelength of the excitation beam was controlled by a monochromator (Figure 2-4 left-hand side). The emitted light from the sample passed through another monochromator, typically fixed at 90^{o} to the excitation source which minimised the excitation light reaching the detector. The light which had passed through the 'emission' monochromator was incident on a detector where the intensity was measured. A reference signal was measured from the excitation directly to account for the fluctuations of excitation intensity and the wavelength-dependent intensity of the light source. The emission spectra of the QD solutions were recorded by FLS 980, Edinburgh Instruments and LS 55, Perkin Elmer (Figure 2-4). As the QDs have a broad excitation range, the diluted samples were excited at fixed wavelengths (within 360-400 nm) significantly lower than the first absorption maximum.

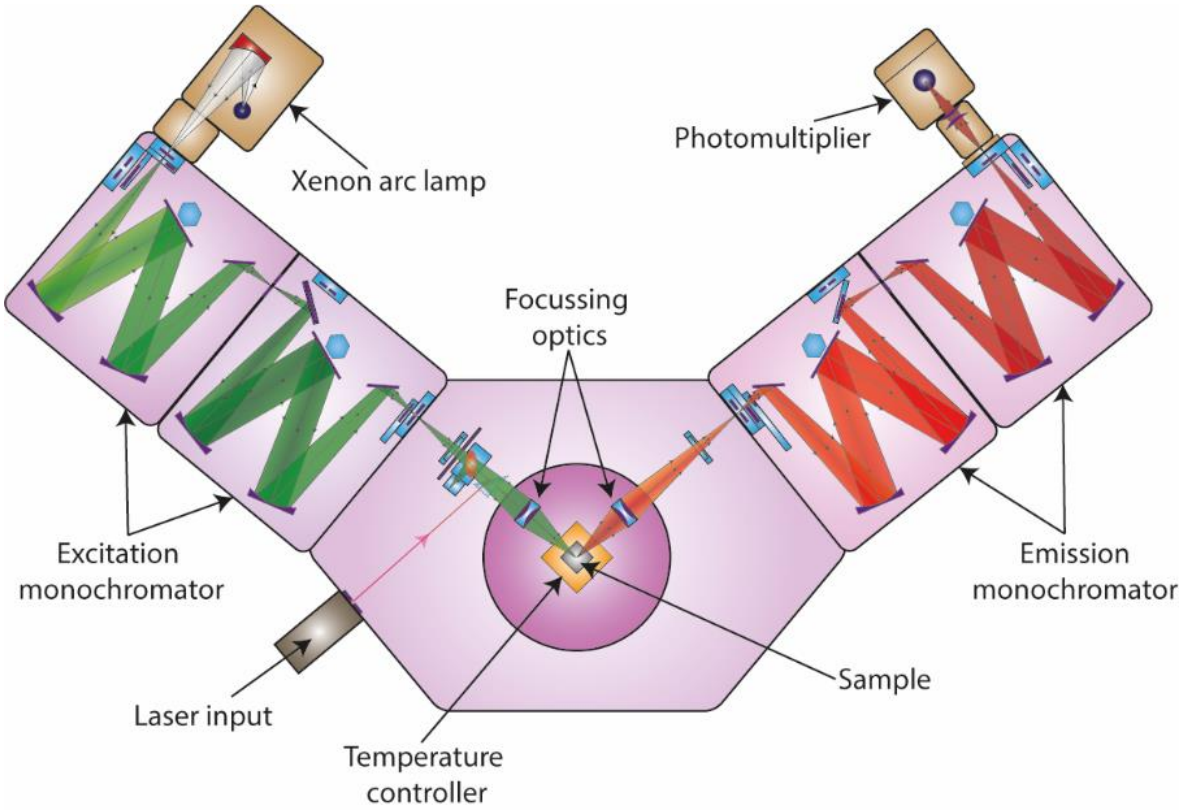

Figure 2-4. Schematic of the fluorescence spectrometer (Figure adapted from the FLS 480, Edinburgh Instruments manual). Excitation was performed with a halogen light source with the beam passed through two monochromators. The emission beam passed through two monochromators to reach the photomultiplier detectors.

2.3.3. PLQY determination

Photoluminescence Quantum Yield (PLQY) for a fluorescent sample is the percentage of the ratio of the number of photons emitted to the number of photons absorbed. To accurately measure the PLQY, it is essential to be able to record all the emitted and the absorbed photons by the sample. This was achieved by using an integrated sphere, whose inner surface is covered in highly reflecting white coating. PLQY of the QDs was measured by FLS 980, Edinburgh Instruments using integrated sphere (SM4, Edinburgh Instruments Ltd.). The excitation beam entered the integrating sphere through a small port and was incident on the sample using a reflecting mirror (Figure 2-5). The light emitted from the sample and the light that was not absorbed reflects several times arbitrarily on the white reflecting surface of the sphere. Ultimately, all the light was incident on the baffle, used for separating entry and exit ports, and emerged out of the sphere through another small port and finally to the detector. The reduction in the excitation peak intensity of the nanocrystal samples was measured against

that of that blank solvent. This reduction in the excitation peak intensity corresponds to the absorbance by the nanocrystals. The emission peak was measured and its integrated ratio with the difference of excitation intensity was represented as PLQY in percentage.

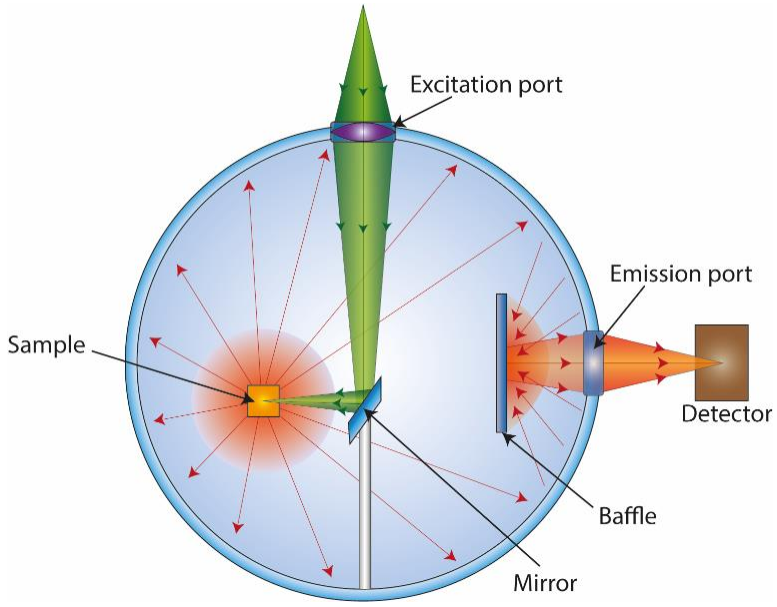

Figure 2-5. Schematic of the integrating sphere. The excitation beam was incident on the sample with a reflecting mirror. The light emitted from the sample and the non-absorbed incident light reflected arbitrarily in the sphere which finally emerged from the emission port to the detector. (Figure adapted from the FLS 980 series reference guide, Edinburgh Instruments manual).

2.3.4. PL lifetime

The PL lifetime is the characteristic time that the electron remains in the excited state before recombining with the valence band hole. The lifetime of QDs is typically ~10s of ns but can be as large as hundreds of ns for some particle type. The sample, in the cuvette, was excited with a short pulse laser (typical pulse width ~90 ps @ 10 MHz) and the time between excitation and detection of emission was measured at a fixed wavelength for a large number of pulses via a photomultiplier. This is the principle of time-related single-photon counting (TCSPC). The measurement was stopped when a large number of events had been detected (5000-10,000 peak counts) which can be set to the duration of the measurements, maximum count for a given time or was user-defined. The emission intensity was plotted as a function of time post-excitation, where the intensity from the ensemble decays exponentially. However, since there

can be many decay processes, each with a different rate, they generally form the fit to the data shown in equation 2.2.

$$I_{Fl} = y_0 + \sum_i A_i \, e^{-t/\tau_i} \qquad (2.2)$$

Here y_0 is a constant, τ_i are fluorescence lifetimes, and A_i are the corresponding amplitudes. By fitting equation 2.2 to the lifetime data, it is possible to identify time constants associated with certain recombination processes. The best practice is to fit the data to a minimum number of exponential decay terms, i.e., start with a monoexponential, biexponential, then triexponential functionals until a satisfactory fit is made. It is rare that greater than a triexponential fit is applied as it has seven parameters that are fitted and thus the certainty and confidence in each parameter are increased. The PL lifetime of the diluted QD samples was measured using FLS 980, Edinburgh Instruments using an EPL-475 diode pulsed laser (Edinburgh Instruments).

2.3.5. Electron microscopy of QDs

Optical microscopies have a limited resolution and are unable to image NPs. This is because the diffraction limited resolution of an optical microscope is estimated by the Abbe limit as:

$$d = \frac{\lambda}{2\, n\, sin\theta'} \qquad (2.3)$$

Where, d is the minimum resolvable distance, λ is the wavelength of the light, n is the refractive index of the medium, and θ' is the half convergence angle of the focus of the lens. The term $n\, sin\theta'$ is called the numerical aperture of the lens and ~0.9 for typical practical lenses. Even for the smallest visible wavelength of ~380 nm, the resolution achieved is >200 nm. Hence, optical microscopes are unable to visualise NPs. Higher resolution for NPs imaging can be achieved by using electron beams. From the wave-particle duality, the de Broglie wavelength of an electron with momentum p can be defined as:

$$\lambda = \frac{h}{p} \qquad (2.4)$$

where, h is the Planks constant. Hence, the resolution of imaging with electron beams would depend on their momentum. Bright field Transmission Electron Microscopy (TEM) along with

scanning electron microscopy, is one of the two major modes of imaging using the electron beam. The electron source is the cathode, typically a field emission gun (FEG) kept at a high potential with the anode of 50-200 kV or more. Electrons were accelerated at this high potential and were focused by a pair of condenser lenses to a tight beam (Figure 2-6a). The TEM was kept at low pressure (10^{-4} – 10^{-5} Pa) using vacuum pumps to avoid collision of the electron beam with air molecules. The beam passed through an aperture and was incident on the sample. The electrons will either absorb, scatter or pass straight through the sample (Figure 2-6b). The samples are imaged mostly through scattering at high resolution as they appear darker against the transmitted beam. The transmitted beam was focused on a charge-coupled-device (CCD) detector and the bright field image was constructed. The resolution of the image will depend on the wavelength of the electron beam.

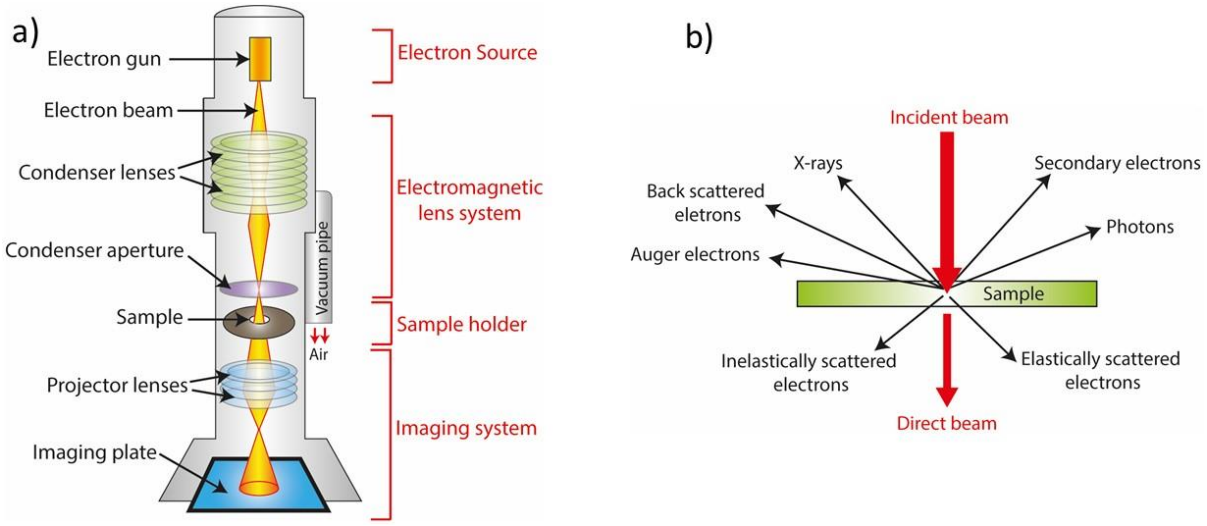

Figure 2-6. Simplified schematics of a) TEM and b) the electron-matter interactions occurring from the incident electron beam on the sample.

The electron beam can eject the inner orbital electrons from the atoms in the sample creating a hole. Higher orbital electrons fill the hole in the inner orbits by releasing X-rays which are characteristics of the sample element. Energy Dispersive X-ray (EDX) spectroscopy is the study of the emitted X-ray spectra from the sample to identify and quantify the elemental composition.

The electrons scattered at high angles can be collected to generate dark-field images of the sample in the scanning transmission electron microscopy (STEM) mode. The electron beam was focused into a fine spot to scan the sample in a raster pattern. The high angle scattered electrons were collected by the high-angle annular dark-field (HAADF) detector which forms a ring around the electron beam. STEM mode is advantageous for imaging biological samples with materials like QDs, due to higher contrast in the dark field.

For the TEM analysis of the QDs and NPs, dilute solutions of the samples (~1 µM) were drop cast on the copper grid with holey carbon film (Agar Scientific) and allowed to dry in air. TEM imaging was performed using FEI Tecnai TF20 and FEI Titan Themis Cubed 300. EDX spectroscopy of the nanocrystals was recorded with AZtec EDX system, Oxford Instruments.

2.4. Microfluidic device fabrication

2.4.1. Master wafer fabrication

The microfluidic cross-slot devices were made in two steps: the manufacture of the negative master wafer followed by the device casting using polydimethylsiloxane (PDMS) polymerization. The negative master wafer was made from SU8 2025 with 25 µm thickness on a silicon substrate as shown in Figure 2-6. SU8 is an epoxy-based photoresist material that gets cross-linked when exposed to UV radiation while the unexposed parts can be dissolved and washed. The silicon substrate was cleaned with Decon90 (surface active cleaning agent), piranha solution (3:1 v/v mixture of sulphuric acid and 30 % hydrogen peroxide) and Milli-Q water, followed by drying at 180-200 ^{o}C. The SU8 was spin-coated on the substrate for 10 min at 500 rpm and baked at 55 ^{o}C for 30 min. The wafer was gradually cooled to 20 ^{o}C. The microfluidic designs were etched on the wafer by direct-write laser lithography using a 2 µm UV-laser of wavelength 375 nm with 300-400 mJ/cm^2 intensity (MicroWriter ML^{TM}, Durham Magneto Optics). The wafer was baked again to 55 ^{o}C for 30 min and cooled, allowing the SU8 to cross-link. The wafer was developed with ethyl lactate ($C_5H_{10}O_3$) solvent (EC solvent) for ~2 min and washed with IPA (~1 min) to remove the non-crosslinked photoresist, i.e., the areas that were not exposed to the UV light. This was followed by hard baking at 180 ^{o}C for 15 min to remove any cracks in the SU8.

The device height was measured using the Stylus Profiler (Bruker Dektak). It uses a mechanical probe to perform a line scan on the wafer surface to acquire the surface topology, giving the height of the device channels. The design of the device used for the experiments in this thesis is described in section 2.4.3.

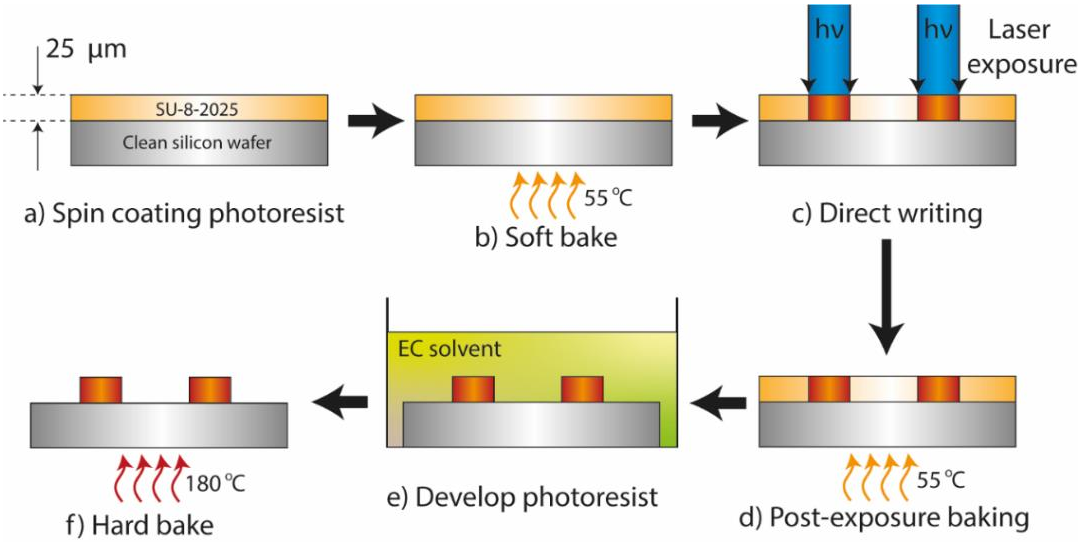

Figure 2-6. Schematic of the steps involved in the fabrication of the silicon master wafer of the microfluidic devices.

2.4.2. PDMS device fabrication

The cross-slot PDMS microfluidic devices were made from the negative master wafer in steps shown in Figure 2-7. The polymer and the cross-linking oligomer were mixed at a 1:10 ratio (v/v) and centrifuged at 4000 rpm for 1 min. The curing agent contains a platinum-based catalyst that supplements the formation of 3-dimensional Si-CH_2-CH_2-Si cross-linkages. This mixture was poured on the master wafer, which was placed in a desiccator, under vacuum, for 30 min to remove air bubbles. The PDMS was cured by baking at 75 °C for 1 h. The PDMS mould was carefully removed from the master wafer and holes were punched for the inlets and outlets of the microfluidic devices. The PDMS and the glass were placed in the plasma-cleaning chamber (Zepto, Diener electronics) and plasma-treated for 1 min of O_2 at 0.8-1 mbar. The PDMS was bonded to a glass slide to complete the device by oxygen plasma treatment. This technique is called plasma bonding where both the PDMS and the glass slide are exposed to oxygen plasma which makes the surfaces extremely clean facilitating the bonding process.

Plasma treatment of PDMS exposes the silanol groups (Si-OH) at the surface which forms strong covalent bonds when in contact with glass (Si-O-Si). The linking process produces water molecules which are removed by baking at 70 ^{o}C for >1 h.

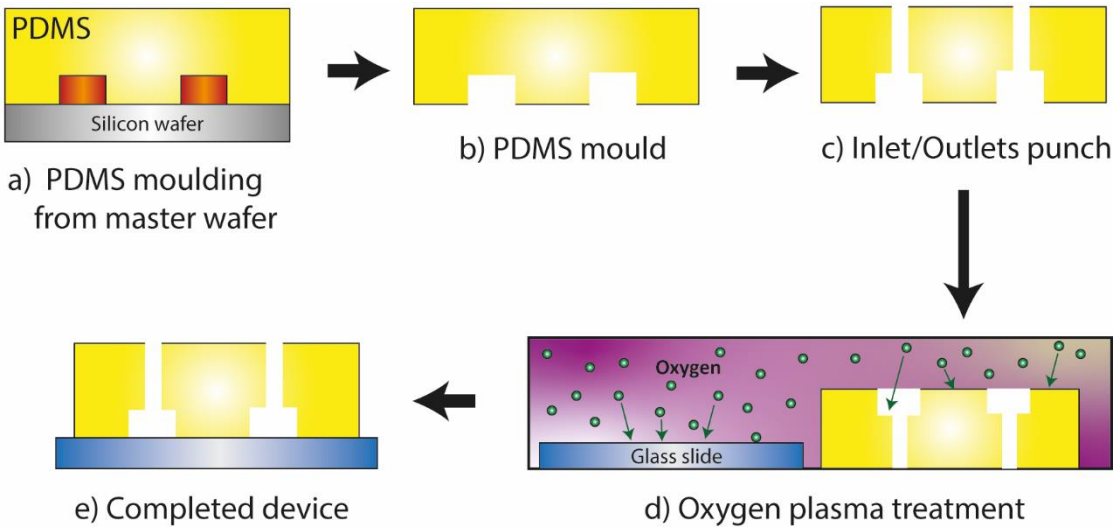

Figure 2-7. Schematics showing the steps involved in the fabrication of the PDMS microfluidic devices. The steps shown are a) the PDMS moulding from the master silicon wafer, b) removal of the PDMS mould from the master wafer, c) hole punching of the inlets and outlets of the device, d) the oxygen plasma treatment of the PDMS mould and the glass substrate and e) the completed device after the binding of the PDMS mould and the glass substrate.

2.4.3. The cross-slot device

The cross-slot microfluidic device as shown in Figure 2-8, has a single inlet followed by a filter made up of an array of rhombus-shaped pillars with 50 µm separation between them [181]. This arrangement was capable of trapping any object bigger than 50 µm, such as debris or cell clumps and prevent blocking of the device. The inlet split into two channels and was redirected to intersect at a junction of two inlets channels flowing towards each other and two orthogonal outlets channels. This is called the extensional-flow junction (Figure 2-8c) where the cell deformation occurred due to the motion of the suspension fluid. The channels width and height at the extensional-flow junction were 35 and 25 µm, respectively. The samples flow through the outlets after passing the extensional-flow junction which expanded in width and was collected from the outlets with the help of plastic tubing.

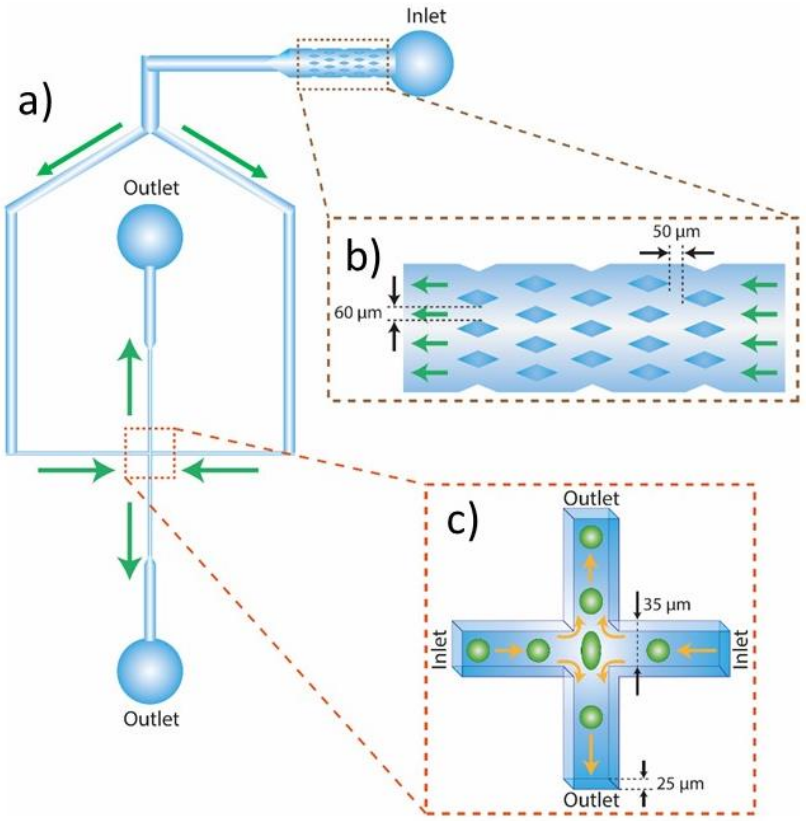

Figure 2-8. a) The cross-slot microfluidic device with the arrows showing the direction of flow. b) on-chip filter placed after the inlet for trapping large objects preventing the blocking of the device c) extensional-flow junction where the cells deform.

2.5. Live cell experiments

2.5.1. Cell culture

All cell culturing was performed in a Class II A1 Biosafety cabinet. The cells were seeded in 75 or 25 cm^2 flasks and grown in a moisture-controlled incubator at 37 ^oC with 5% CO_2. The cells were sub-cultured when they reached 70-80% confluency.

2.5.1.1. MCF7 cells

MCF7 are adherent breast cancer cells and were obtained from the European Collection of Authenticated Cell Cultures (ECACC catalogue no. 86012803) as frozen stock. The MCF7 (Michigan Cancer foundation-7) was isolated from a 69-year-old patient in 1970. They were cultured in Dulbecco's Modified Eagles Medium (DMEM) (Sigma) supplemented with 10%

Foetal Bovine Serum (FBS) (Sigma), 2 mM glutamine (Thermo Fisher) and penicillin 100 units/ml streptomycin 100 µg/ml (Sigma). Penicillin-streptomycin was added to prevent both gram-positive and gram-negative bacterial infections. MCF7 cells were sub-cultured every 3-4 days. The media was removed and the cells were washed with Phosphate Buffer Saline (PBS). Trypsin (TrypLE, Thermo Fisher Scientific) was added to the flask and incubated for 2 min at 37 ^{o}C with 5% CO_2. Trypsin, which is a proteolytic enzyme, causes cell dissociation from the flask by breaking down the proteins responsible for adhesion. The flask was gently tapped to detach the cells from adhesion to the surface. A small amount of growth media was added to deactivate the trypsin and the cells were pipetted several times to avoid the formation of cell aggregates. The cells were seeded 1-in-4 by volume in new flasks and volume was made up with DMEM culture medium.

2.5.1.2. T47D and MDA-MB-231 cells

T47D and MDA-MB-231 are adherent breast cancer cells and were provided from St. James' University Hospital, Leeds. T47D was isolated from a 54-year-old patient from a pleural effusion with an infiltrating ductal carcinoma (ECACC catalogue no. 85102201). MDA-MB-231 was isolated from a 51-year-old patient (ECACC catalogue no. 92020424). They were cultured in RPMI-1640 medium (Sigma) supplemented with 10% FBS, 2 mM glutamine and penicillin 100 units/ml streptomycin 100 µg/ml. They were sub-cultured every 2-3 days in the similar manner described in section 2.5.1.1. with RPMI-1640 culture medium.

2.5.1.3. MCF10A cells

MCF10A are non-malignant human breast epithelial cells that were provided from St. James' University Hospital. The MCF10A (Michigan Cancer Foundation – 10A) cells were isolated from a 36-year-old female. These cells display some features of normal breast epithelium. The media composition for this cell line was adopted from Satheesha *et al.* and represented in table 2.1 [244]. The stock Epidermal Growth Factor (EGF) (Peprotech) was suspended at 100 µg/ml in Milli-Q water and the aliquots were stored at -20 ^{o}C. Hydrocortisone (H-0888, Sigma) was suspended at 1 mg/ml in 200 proof ethanol (99.5 % anhydrous, Sigma) and stored at -20 ^{o}C.

Cholera Toxin (C-8052, Sigma) was suspended in Milli-Q water at 1mg/ml, allowed to reconstitute for 10 min and stored at 4 ^{o}C. Insulin (I-1882, Sigma) was dissolved in Milli-Q water containing 1% glacial acetic acid at 10 mg/ml. The solution was shaken, allowed to reconstitute for 15 min and stored at -20 ^{o}C. For every type of medium, the additive components were premixed and passed through sterile 0.2 µm filters before adding to DMEM/F-12 medium. The cells were sub-cultured every 2-3 days, similar to the description in section 2.5.1.1 with the growth medium described in table 2-1.

Component	Growth medium	Resuspension medium	Assay medium
DMEM/F-12	500 ml	40 ml	50 ml
Horse Serum (Invitrogen)	25 ml (5%)	10 ml (20%)	1 ml (2%)
EGF	100 µl (20 ng/ml)	--	--
Hydrocortisone	250 µl (0.5 mg/ml)	--	25 µl (0.5 mg/ml)
Cholera toxin	50 µl (100 ng/ml)	--	5 µl (100 ng/ml)
Insulin	500 µl (10 µg/ml)	--	50 µl (10 µg/ml)
Penicillin-Streptomycin 100x solution (Invitrogen)	5 ml	0.5 ml	0.5 ml

Table 2-1. Media compositions for MCF10A cells.

2.5.2. Freezing and storage of cells

To store the cell for future use, the cells were first trypsinised when 70-80% confluent. The cell viability was measured using Trypan blue dye (Thermo Fisher Scientific), which is unable to pass through the membrane of live cells. The dead cells can absorb the dye due to their compromised cell membrane. The haemocytometer is a counting chamber having engraved grids on the surface, which allows the number of cells to be counted in a known volume. The viability was calculated in percentage of the ratio of the live cells to the total cells counted. Cell freezing was performed only if the viability was > 95%. They were suspended in respective growth media with 5% DMSO. The cells were transferred to cryotubes (~1 ml) at a concentration of ~1×10^{6} cells/ml, measured using a haemocytometer. The cells were gradually frozen in an IPA bath container, kept overnight in the -80 ^{o}C freezer. Finally, the cells were transferred and stored in a liquid nitrogen container until further use. For reviving the cells back from the frozen state, they were thawed to room temperature and dispersed in T25

culture flasks with 5 ml media. The cells were allowed to adhere in incubation at 37 ^{o}C with 5 % CO_2 atmosphere for 3 h. After the cells had been attached, the DMSO containing media was replaced with fresh culture media.

2.5.3. Toxicity studies of cells with QDs

Cadmium-based QDs are known to be carcinogenic and toxic to cells [245]. It was therefore necessary to investigate the toxicity of these QDs to the cell lines (MCF7, T47D, MDA-MB-231 and MCF10A) used for experiments in this thesis. The viability assays were performed for both QDs and RA-QDs. Cells were seeded in 96 well plates (clear bottom Costar 96-well) at 5000 cells/well with 200 µl of the respective culture media. The cells were treated with either QD or RA-QDs at different concentrations (0 to 10 µM) and incubated at 37 ^{o}C with 5% CO_2 for 18 h (N = 5 wells each). The media with excess QDs were removed and the wells were washed twice with PBS and finally replaced with 100 µl fresh culture media.

The cell viability was measured according to the MTT (3-(4,5-dimethylthiazol-2-yl)-2,5-diphenyltetrazolium bromide) assay using the Vybrant MTT Cell Proliferation Assay kit (Thermo Fisher Scientific). The presence of NADPH-dependent cellular oxidoreductase enzymes in the cytoplasm reflects on the number of viable cells present. These enzymes are capable of reducing the MTT to its insoluble formazan. Each well with 5000 cells, pre-exposed to quantum dots as mentioned above, were treated with 12 mM MTT solution prepared in sterile PBS. The plate was incubated at 37 ^{o}C with a 5% CO_2 for 4h during which, MTT was converted to formazan. The formazan was also dissolved in 50 µl DMSO and incubated for 10 min at 37 ^{o}C with 5% CO_2 atmosphere. The absorbance was measured at 540 nm using a plate reader (SpectraMax M5, Molecular Devices). The viability of the treated cells was measured against the control cells without any treatment, which was considered to have 100 % viability.

2.5.4. Cell deformation analysis and QD uptake

For the deformation experiments, the cells were detached from the culture flask by trypsinisation as described earlier in section 2.5.1.1. The cells were pelleted by centrifuging at

100 g for 5 min. Cells at a concentration of 0.5-1 × 10^6 cell/ml were resuspended in the running buffer consisting of Dulbecco's Phosphate Buffer Saline (DPBS, Sigma) with 0.5% (w/v) methylcellulose (MC, Sigma) and passed through a cell strainer (40 µm pore size, Fisher Scientific Ltd.) to ensure monodispersity of the cells in the buffer. MC increases the viscosity of the PBS considerably (from ~1 cP to ~33 cP). The cells were loaded into a syringe and passed through the cross-slot device by a syringe pump (PHD ULTRA™ Syringe pump, Harvard Apparatus) at different flow rates (Q =25 to 175 µl/min). The syringe was connected to the microfluidic device using a fine boring polythene tubing (Smiths Medical™). The deformation of the cells was visualised and imaged/video recorded with a high-speed camera mounted on the inverted microscope (Nikon Eclipse Ti).

For the QD uptake experiments, the QDs were cleaned with IPA and resuspended in water. They were sterilized by passing through a 0.2 µm Acrodisc 25 mm syringe filter. The cells were prepared for squeezing in DPBS with 0.5% MC in a similar manner as described earlier. 100 nM QDs were added to the cells suspension before passing through the cell strainer. The cells were deformed through the cross-slot device at different flow rates and incubated with the QDs for 15 min at room temperature, with a total QD exposure time of 30 min. Cells were pelleted by centrifugation (100 g for 5 min) and washed twice with DPBS by centrifugation at 100 g for 5 min, to remove any excess QDs. Finally, the cells were suspended in their respective culture media or DPBS for further analysis. For the viability studies, the cells were treated in the same manner with different concentrations of QDs (0 to 5 µM), followed by the MTT assay described in section 2.7.

2.6. Confocal microscopy of cells

Confocal microscopy has the advantage over the traditional epifluorescence microscopy for fluorescence imaging with improved resolution, by blocking out light from the out-of-focus planes using a pinhole. Epifluorescence microscopes detect light from the entire depths of the sample, as such, even the out of focus regions are imaged. The pinhole of the confocal microscope, block the out-of-focus PL emissions, which results in improved resolution for a small depth of field and reduced background fluorescence (Figure 2-9). This also allows high-resolution 3-dimensional imaging by stacking the 2-dimensional images from the different

planes of the sample. DMi8 (Leica) confocal microscope (with the z-focus resolution of ~0.05 µm) was used for imaging the cells with QDs and the preparation of the cell sample for imaging is described in the next section.

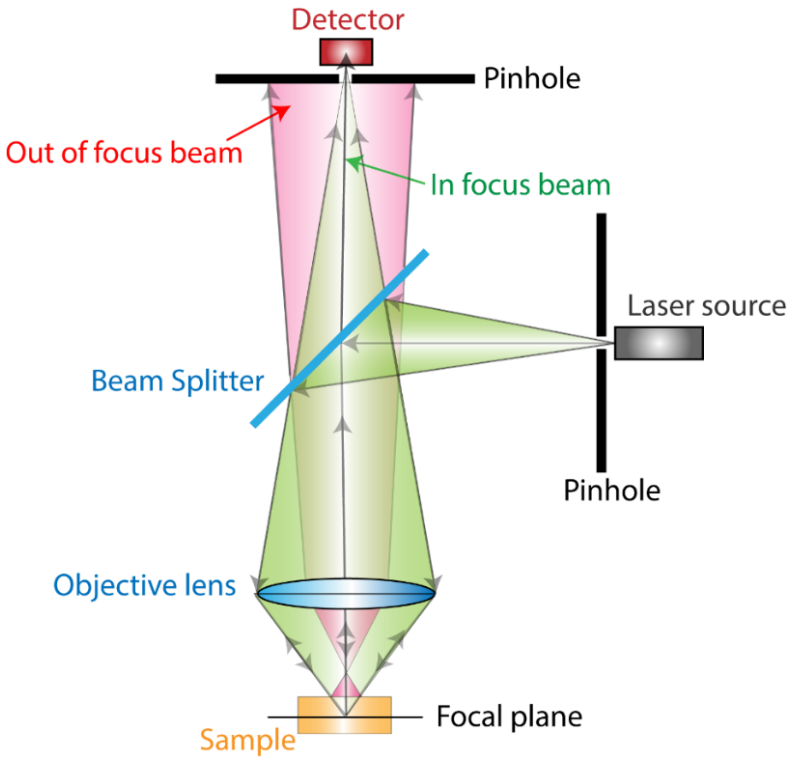

Figure 2-9. Simplified schematic representation of the operation of the confocal microscope. Light from the focal plane (green) passes through the pinhole to the detector whereas light from the other planes (pink) are blocked off.

2.6.1. Confocal analysis of QD uptake

The cells were deformed with QDs and washed, as described in section 2.5.4. were suspended in 200 µl culture media in 8 well cover-glass incubation chambers (Lab-Tek II, VWR International). The chamber was mounted on the confocal microscope (DMi8 Leica) for simultaneous fluorescence and bright field imaging of the cells. The samples were irradiated with 488nm/552nm lasers depending on the emission wavelength of the QDs and were imaged using 10× objective lenses. The intensity of the fluorescence from each cell was measured using customised MATLAB script, which detected the cells as circles using the function "imfindcircles" from the bright field image which were overlayed to the corresponding

fluorescent images. The total fluorescence emission intensity was measured from each of the cell traces. For each sample, >2000 cells were considered and the total fluorescence intensity was averaged.

2.7. Toxicity studies of cells deformed with QDs

The cell viability is typically measured by incubation in Trypan blue dye as mentioned in section 2.5.2. However, Trypan blue cell viability measurement depends on the staining of the dead cells with the compromised cell membrane, which allow the diffusion of the dye. However, the cells deformed through the cross-slot device have a compromised cell membrane, and the longevity of these pores is not yet established. As such, we choose the MTT assay to measure the cell viability of the deformed cells with QD uptake.

The cells were deformed at different flow rates (25-175 µl/min) with either 100 nM QDs or RA-QDs. The cells were washed twice in DPBS and resuspended in their respective culture medium. They were seeded in 96 well-plate (clear bottom Costar 96-well) at 5000 cells/well (N=5 wells). The plate was incubated at 37 ^{o}C with 5% CO_2 for 18 hours and the MTT assay was performed as described above in section 2.5.3. For the viability study of the cells deformed with QDs using the cross-slot microfluidic device, the total QD exposure time was limited to 30 min.

2.8. Electron microscopy of cell sections

Cells were deformed and collected as described before in section 2.5.4. with 100 nM QDs at a flow rate of 100 µl/min. After washing twice with DPBS to remove excess QDs, the cells were fixed with a freshly prepared 2.5% glutaraldehyde solution in 0.1 M phosphate buffer (PB) overnight. The cells were washed twice for 30 min with PB and fixed in 0.1% osmium tetraoxide for 1h. The cells were pelleted and washed twice with PB to remove the excess osmium tetraoxide. The cells were now dehydrated by treating in ascending concentrations of alcohol (20%, 40%, 60%, 80% and twice with 100% ethanol) for 30 min each.

The cells were then embedded in resin for making the microtome sections. Firstly, the cells were treated with 2 changes of propylene oxide for 20 min each, followed by incubation in

50%-50% araldite-propylene oxide solution overnight. The cells were subsequently incubated in 75%-25% araldite-propylene oxide for 3 h and fresh neat araldite for 3-8 h. The cells were transferred into fresh araldite which was allowed to polymerize at 60 ^{o}C overnight. The resin-embedded cells were made into thin slices (90-100 nm) using an ultramicrotome (Reichert Jung Ultracut E). The cell sections were placed onto TEM copper grids with carbon film for electron microscopy analysis. Both TEM and STEM techniques were used to image the cell sections using FEI Tecnai TF20.

2.9. Quantification of QD uptake in cells by ICP-MS

It is essential to physically quantify the number of QDs in the cells in order to determine the effectiveness of membrane disruption via hydrodynamic deformation in the cross-slot microfluidic device. Inductively coupled plasma mass spectrometry (ICP-MS) is a technique used for the detection of trace elements in biological samples [246]. The liquid sample is desolvated, vaporised, atomised and finally ionised by the inductively coupled plasma. These ions on reaching the mass analyser are subject to the time-varying electric field. Only a particular mass-to-charge (m/z) ratio of the ions result in a stable flight trajectory at specific combinations of alternating current (AC) and direct current (DC) potentials. A mass filter quadrupole separates ions based on their m/z ratios and the electron multiplier detector counts the incident ions for quantification.

For the ICP-MS sample preparation, a large number of MCF7 cells (~27-43 million cells each) were deformed through the cross-slot microfluidic device with 100 nM CdTe/CdS QDs at different flow rates of 0, 50, 100 and 150 ul/min. A negative control sample was also prepared with MCF7 cells with no QD treatment. The cells were washed and dispersed in DPBS in the same manner as described in section 2.5.4. The cells were pelleted by centrifugation at 4000 g for 10 min and digested in 1 ml aqua regia (3:1 v/v mixture of hydrochloric acid and nitric acid). The acid digestion of the cells was assisted by heating the sample at 90 ^{o}C for 2 h. Samples were diluted with Milli-Q to a final volume of 10 ml. Any undissolved components were removed by centrifugation at 4000 g for 30 min.

The cadmium in the cells was quantified using the ICP-MS (Perkin Emler Elan DRCe) with Perkin Elmer s10 auto-sampler. The MS measurements were taken at m/z 111 at an estimate of 20 ppt of Cd. The quantification was performed against a calibration curve made using Cadmium Standard for ICP/MS, Caritas PPT Grade, SPEX CertiPrep™ (Fisher Scientific) with 100 ppt, 1 ppb, 10 ppb and 100 ppb of Cd.

2.10. Cyclic voltammetry of RA-QDs

When the electron in the QD gets excited to the conduction band, radiative recombination will not occur if the electron gets extracted by an electron-accepting ligand. As a general rule, the lowest unoccupied molecular orbital (LUMO) of the electron-accepting ligand should lie below the QD conduction band [247]. Hence to investigate the effective quenching of the QDs using the Q2NS molecules, it is essential to estimate where the LUMO of the quinones lies with respect to the CdTe/CdSe QD band alignments.

Cyclic voltammetry (CV) is an electrochemical technique used to measure the oxidation and reduction processes of a species [248]. It can measure the reduction potential which is the potential energy an electron must have to reduce the species. The redox species in solution is immobilised on the working electrode surface and CV measurement of the redox potential is performed conventionally with respect to the standard hydrogen electrode (SHE). A reference electrode is maintained at a constant potential and the potential difference of the working electrode along with a counter electrode is measured against it. The counter electrode is a conductive metal emersed in the same solution as the working electrode. Current is measured for the working electrode for several forward and backward potential scans. From the CV plot, the anodic and the cathode peaks are identified, and the reduction potential (E^o) is given as:

$$E^o = \frac{E_{pc} + E_{pa}}{2} \qquad (2.5)$$

Where, E_{pc} and E_{pa} are the cathodic and anodic peaks, respectively. The CV for the RA-QDs was performed on a working electrode having a 100 nm gold layer on glass, which was incubated with a solution of 1 mM 6-mercaptohexanol and 0.2 mM 6-amino-1-hexanethiol in ethanol to impart a net positive charge to the electrode surface. They form a self-assembled monolayer which was gently rinsed with water. 1 µM solution of RA-QDs (Q2NS:QD = 20:1

molar ratio) in HEPES buffer (pH 7.2, 50 mM) was incubated with the electrode for 1h to immobilise the RA-QDs on the electrode (Figure 2-10). The CV was performed to obtain the reduction potential against a mercury/mercurous sulphate reference electrode at a scan rate of 50 mV/s. CV was also performed for QDs without the quinones with the same conditions, as a negative control.

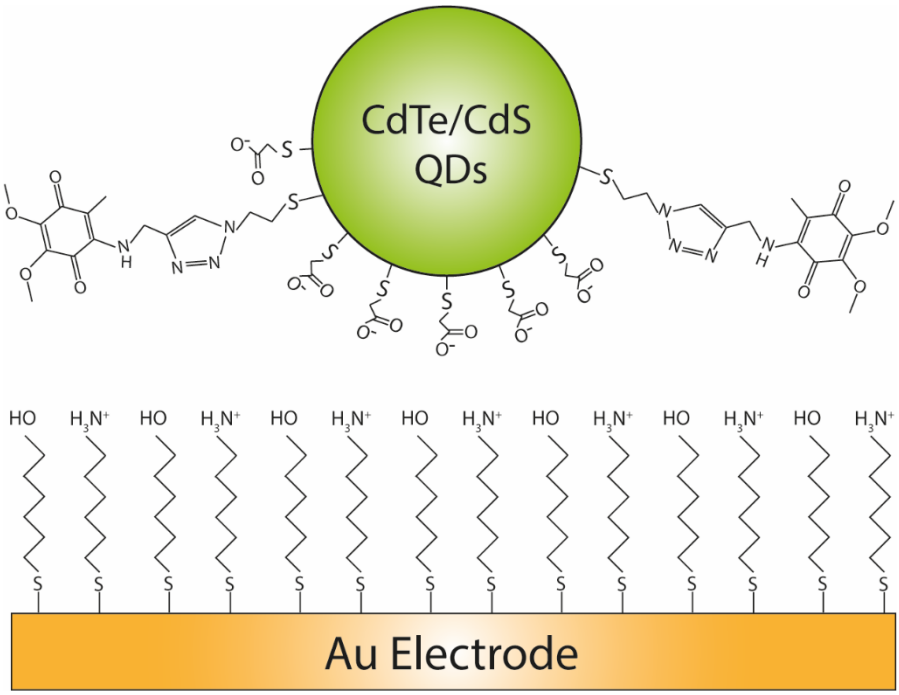

Figure 2-10. Immobilisation of RA-QDs the gold electrode. RA-QDs have a mixed population of TGA and Q2NS ligands and are electrostatically immobilised on the electrode which has a monolayer of self-assembled 6-mercaptohexanol and 6-amino-1-hexanethiol mixture.

2.11. NAD$^+$/NADH and NADH measurement in cells from standard kit

To compare the reducing environment of the different breast cell lines, it is essential to know the ratio and the quantity of one of the major redox couples in cells: the NADH/NAD$^+$. The NAD/NADH Quantification Kit (Sigma Aldrich) was used to determine the NADH/NAD$^+$ ratio and the NADH levels in the different breast cell lines. To make the standard curve of NADH, 10 µl of 1mM NADH standard was diluted with 990 µl NADH/NAD extraction buffer to prepare a 10 µM standard solution. 0, 2, 4, 6, 8 and 10 µl of the standard was added to wells in a 96-well

plate (Thermo Scientific) to produce 0-100 pmole/well standard in duplicates. NADH/NAD extraction buffer was added to each well to bring the volume to 50 µl.

The cells were brought to 70-80% confluency and were detached by trypsinisation (TrypLE, Gibco). The viability of the cells was checked with Trypan blue (Thermo Fisher Scientific) and the cell concentration was measured using a haemocytometer. Only cells with a viability > 95% were considered for the experiment. They were washed with cold DPBS and pelleted at 2000 rpm for 5 min. NAD^+/NADH extraction was performed with the extraction buffer (400 µl per $2X10^5$ cells) followed by 2 cycles of freeze/thawing on dry ice of 20 min each and vortexed. This was followed by vortexing the cells for 10 s and centrifuging at 13,000× g for 10 min to remove any insoluble materials. The cells could contain enzymes that can rapidly consume NADH, as such, the samples need to be deproteinised. This was achieved by filtering the samples through a 10 KDa cut-off spin filter (Amicon® Ultra-4 Centrifugal Filters, Merck). For the NADH and NAD_{total} detection, 50 µl of the sample extract was added in N =5 wells each. For the NADH detection, 200 µl aliquots of the sample extracts were heated at 60 ^oC for 30 min in a water bath and quickly cooled on ice, decomposing the NAD in the process. Any precipitates were removed by centrifugation at 2000 rpm for 5 min. 50 µl of the sample extract was added N =5 wells each.

Master reaction mix was prepared with 2 µl NAD Cycling Enzyme Mix and 98 µl NAD cycling buffer for each well. The concoction was added and mixed thoroughly by pipetting. All NAD in the NAD_{total} reaction will be converted to NADH by the NAD Cycling Enzyme Mix. The samples were incubated for 5 min at room temperature and 10 µl of the NADH developer was added to each well. The cells were incubated at room temperature for 4 h. The well plates were incubated for 4 h at the end of which 10 µl of the Stop Solution was added to each well and the absorbance was measured at 450 nm in the plate reader (SpectraMax M5, Molecular Devices).

The background value obtained from the blanks (0 pmole NADH) was subtracted from all readings. The NADH and NAD_{total} were determined from the standard curve and a new standard curve was set up each time the assay was run. The NADH and concentrations were expressed as pmole/10^6 cells. The ratio of NAD^+/NADH was determined as follows:

$$NAD^+/_{NADH} = \frac{NAD_{total} - NADH}{NADH} \quad (2.6)$$

2.12. AAPH treatment of cells deformed with QDs

To monitor the change in the photoluminescence of the RA-QDs in cells with alteration of the redox state of the cells, 2,2'-Azobis(2-amidinopropane) dihydrochloride (AAPH) was used to generate chemically-induced ROS in the cells. The Cells deformed with redox-active QDs were imaged under the confocal microscope according to the methods described in sections 2.5.4 and 2.6.1. The cells in suspension were continuously imaged for 30 min to check the stability of the PL emission. AAPH solution in Milli-Q water was added to the cell suspension to alter the redox state of the cells gently from the side of the imaging chambers as to not disturb the cells at a final concentration of 30 mM. The cells were further imaged for 30-45 min. As controls, cells incubated with redox-active QDs were also treated and imaged in the same manner without deformation. In addition, images of the cells were taken in the same manner for cells deformed or incubated with QDs having no quinones for comparison.

2.13. Imaging of adhered cells

Adhered cells in the culture flasks were washed with DPBS and treated with their respective FBS-free culture media containing 1µM Hoechst 33342 (nuclear stain, Thermofisher) and 1 µM mitotracker green (for mitochondria staining, Invitrogen) for 30 min. The cells were washed again twice with DPBS followed by deformation with QDs and RA-QDs as according to the methods described in sections 2.5.4 and 2.6.1. After the cleaning of the cells post deformation with DPBS, they adhered to an 8-well incubation chamber (Lab-Tek II, VWR International) pre-treated with 1 µM poly-L-lysine for 24 h. The cells were incubated at 37 ^oC with 5 % CO_2 atmosphere overnight to allow the adhesion in their respective culture media.

For the cells treated with RA-QDs, AAPH was added to the culture media at a final concentration of 30 mM to monitor the change in the PL-emission of the RA-QDs with the altered redox state of the cells.

2.14. FDM microscopy of MCF7 cells with calcein

It has been reported that there is a volume exchange incurred by the cells when deformed through microfluidic constrictions during the intracellular delivery of large macromolecules [249,250]. The cells lose their intracellular fluids by structure-induced compression which was demonstrated by the drop in the cell volume during squeezing. The volume was regained when the cells take in the suspension fluid post-deformation. This 'convective' volume exchange drives intracellular delivery. Although, volume loss is indicative of the outflow, the release of intracellular fluid has not been demonstrated so far during membrane disruption. Additionally, it would be interesting to see how the loss of cellular fluid occurs for the shear-induced deformation of cells. For this purpose, the high-speed frequency-division multiplexing (FDM) confocal microscope was used to detect the loss of intracellular fluids through the fluorescence measurements of cytoplasmic stain, calcein from the cells, during and after deformation via the cross-slot microfluidic device.

For traditional approaches of fluorescent microscopy, increasing the scan scanning speed would mean shorter pixel dwell time, which results in the reduction of the signal-to-noise ratio. For The FDM microscope developed by the Goda group (Figure 2-11a), this problem was overcome by integrating a spatially distributed, broadband, spatial dual-comb (SDC) and quadrature amplitude modulation (QAM) [251]. The SDC beam illuminated the sample that allowed the acquisition of broadband high-resolution spectra with high signal-to-noise at high speeds.

Briefly, the SDC beam was generated by splitting a continuous laser beam into two by a half-beam splitter (HBS) as shown in Figure 2-11b. One of the beams (comb 1) was frequency-shifted by an acousto-optic deflector (AOD) and diffracted. These diffracted beams have multiple beam components, propagating in different directions and having different optical frequency shifts. The second beam (comb 2), with the help of an acousto-optic frequency shifter (AOFS) was frequency-shifted which was again passed through another AOD for a second frequency-shifting and finally diffracted. Combs 1 and 2 were recombined at a second HBS to produce a discrete beam array, with beams having different beat frequencies, that is the spatially distributed dual frequency comb. The spatially distributed frequency comb is displayed in Figure 2-11c, showing the driving signals of the AODs and AOFS. In this frequency-

domain, the AODs have a modulation bandwidth of Δf and a tone spacing of δf, such that $\Delta f = (n-1)\,\delta f$, where n is the number of tones. The frequency shift was set to be > $(n+1)\,\delta f$, so that combs 1 and 2 did not overlap. The two frequency combs overlapped in the spatial-domain at the second HBS. They formed a linearly aligned array of focal spots after passing the objective lens. Pairs were formed at each focal spot by the closest comb lines, the second closest comb lines, and so on. In this way, the comb beam had n comb lines with a modulation bandwidth of $2\Delta f$, which was double the bandwidth of the AODs.

QAM was employed in the FDM-based system to obtain the spectral efficiency of the standard point-scanning confocal microscopy. It is a technique to double the effective bandwidth by combining two amplitude-modulated signals. In QAM, two beams were prepared with a phase difference of $\pi/2$ using the two AODs, with one set to linearly polarise at 45° and the other right circularly polarise (Figure 2-11d). They were combined at the HBS, where the vertical (in-phase) and the horizontal (quadrature) components of the QAM-SDC beam were extracted by the polarisation beam splitter. The target sample was illuminated by the QAM-SDC beam and the in-phase and the quadrature components were simultaneously measured by a photodetector and digitised.

The QAM-SDC beam generation is shown in Figure 2-11e. A non-polarising HBS was used to combine the two combs spatially, with both in-phase and quadrature beams generated. The FDM microscope shows a maximum frame rate of 16,000 frames/s for confocal fluorescence imaging and is only limited by the fluorescence lifetime of the fluorophores. Hence, the FDM has wide applications with high-speed confocal imaging for high throughput flow cytometry. Recently, the Goda group has made improvements on the FDM by integrating with time-division multiplexing that allows single-pixel microscopy at an even higher frame rate of 32,000 frames/s [252].

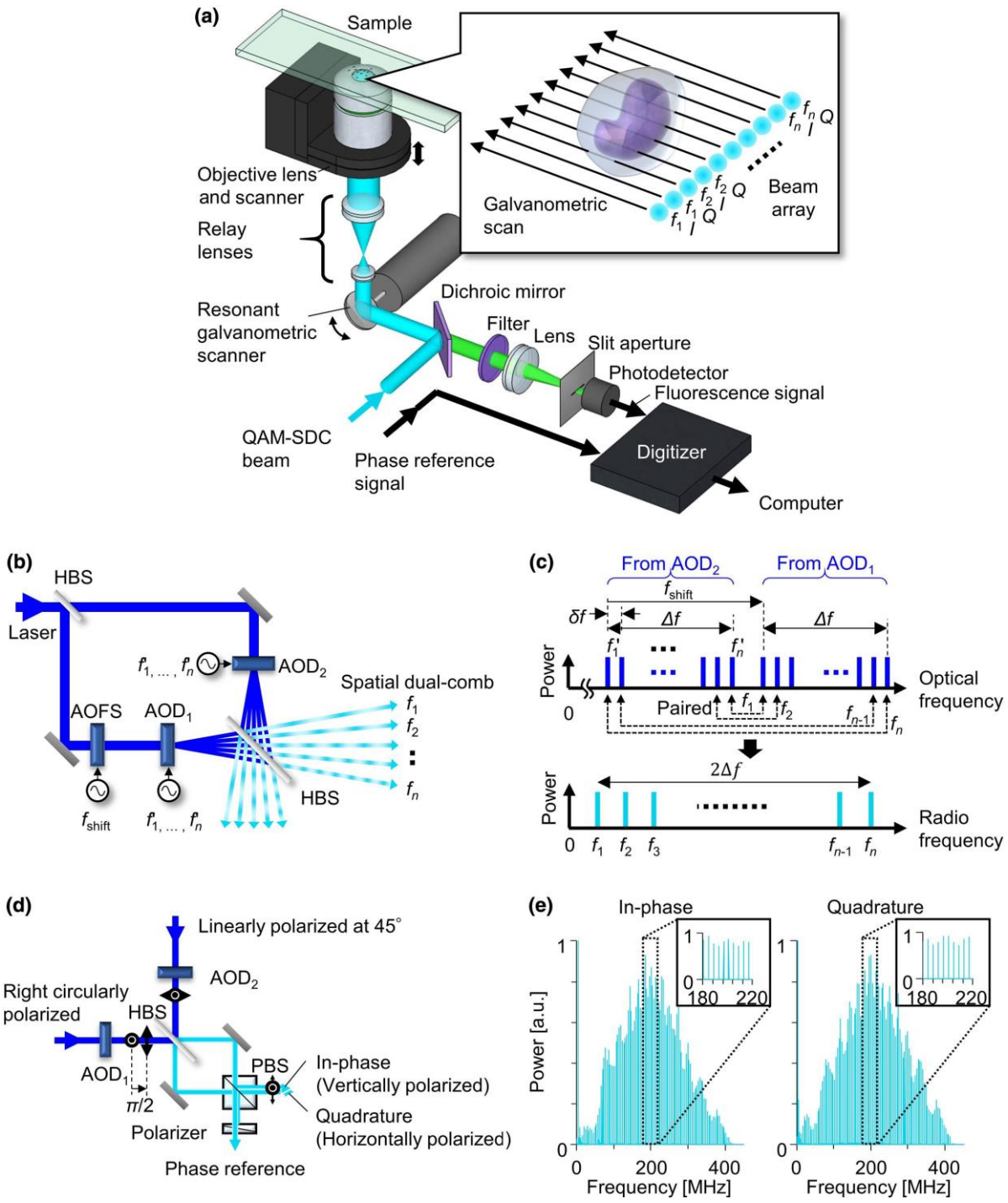

Figure 2-11. The FDM confocal fluorescence microscope. (a) Simplified schematic of the microscope. (b) The spatial dual-comb (SDC) beam generator. (c) The two frequency combs having the optical frequency domain and the radio frequency domain of the SDC beam. (d) The QAM-SDC beam generator. (e) The in-phase and the quadrature components of the QAM-SDC beam which illuminates the sample, where the inset shows the equally spaced frequency comb lines. Reprinted with permission from [251] © The Optical Society.

2.14.1. Cell preparation and deformation at stagnation point

MCF7 cells were incubated with 1 µM calcein-AM (AM: Acetoxymethyl) (Cambridge Bioscience) in DPBS for 30 min at 37 ^{o}C with 5% CO_2. The non-fluorescent calcein-AM is a membrane-permeable dye which converted into fluorescent calcein by esterases in the cells through cleaving of the AM group. The cells were washed with DPBS and detached using a trypsin dissociation reagent. The cells were suspended in the running buffer (PBS with 0.5% (m/v) methylcellulose) and passed through a 30 µm cell strainer. The cells were deformed through the cross-slot device at flow rates of 5 and 10 µl/min. The ultrafast confocal FDM microscope was used to visualise the fluorescence intensity from the cells passing through the stagnation point (Figure 2-12).

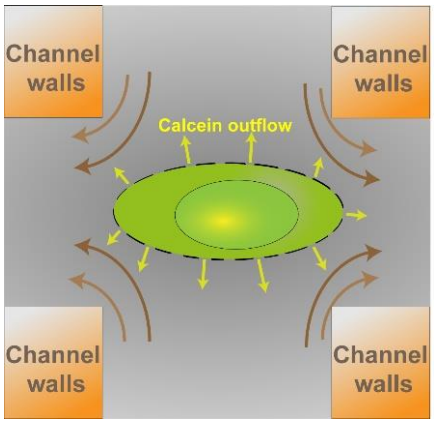

Figure 2-12. Schematic showing the outflow of calcein from the cells through the membrane pores on deformation by the cross-slot microfluidic device.

Customised MATLAB script was used to extract the binary files, which when converted to .tiff files, were cut into individual frames. These individual frames were put together as a video (.avi files) so that the deformation of the cell at the stagnation point could be visualised. This was performed for the fluorescence channels as well as the bright field. A merged video by overlapping the bright field and the fluorescence channels were also generated. The images have distortions and altered fluorescence due to the inherent properties of the FDM. The pixel distortion occurs in these images due to the velocity scan profiles of the beam comb. This distortion causes the pixel at the end of each frame to be extended and squeezed at the centre

along the x-direction and was corrected using the same MATLAB code. A customised Python code was used to analyse the fluorescence from the cells in each frame by combined tracking of the cells in the bright field and the fluorescent channels fitted with an ellipsoid. In addition to the velocity scan correction, correction due to the fluorescence lifetime effect of the fluorophore and the distortion due to motion of the cells were also made using the same Python code. The details of all the corrections steps are described in chapter 5. The total fluorescence intensity from the cells was measured for each step of the corrections to observe and trace the effect of these improvements.

2.14.2. Imaging cells post deformation

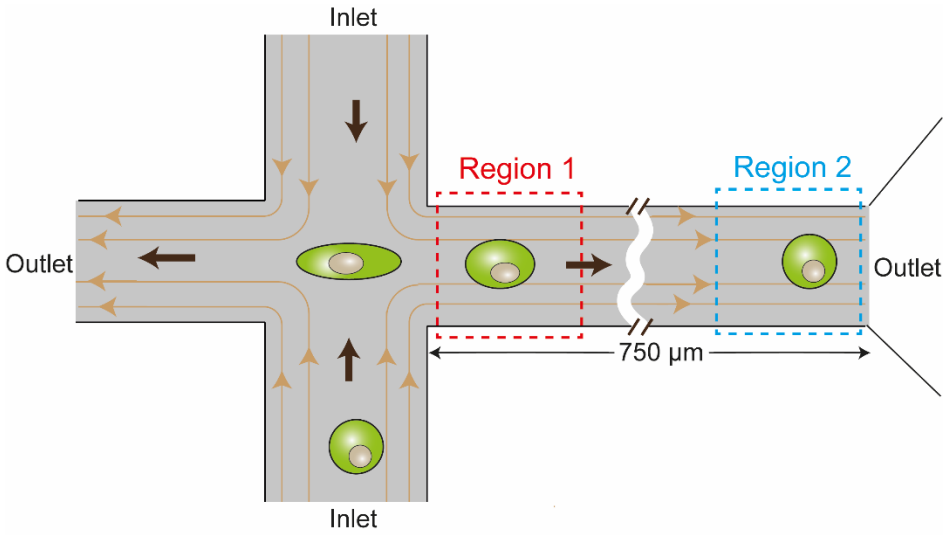

Figure 2-13. Schematic showing the two regions of interest for fluorescence quantification of cells with 1µM calcein post deformation at 100 µl/min flow rate using the FDM microscope.

MCF7 cells with 1µM calcein-AM prepared as above were deformed through the cross-slot device at a flow rate of 100 µl/min flow rate and imaged at two regions of interest (Figure 2-13) post-deformation which were 750 µm apart in the microfluidic channel (end-to-end). The images were corrected for the distortion due to the scanning velocity profile and the effect due to the lifetime of the fluorophore. The total fluorescence intensity from the cells was measured for a population of cells at each position and was compared to observe the leakage of calcein from the membrane pores between the two regions.

2.15. Au-PEG-FITC NPs for cellular uptake

To investigate the effect of particle size on the cellular uptake by hydrodynamic deformation in the cross-slot microfluidic device, Au NPs of different sizes were synthesised. A fluorescent tag, FITC-PEG-SH (FITC: Fluorescein isothiocyanate, PEG: Polyethylene glycol) were conjugated with these particles (max absorbance 495 nm, Emission: 515-520 nm., Mol wt. 3400 Da, NANOCS). The smallest Au NPs (Batch A) were prepared by rapid injection of $NaBH_4$, a reducing agent into the mixture of $HAuCl_4.3H_2O$ and Na-citrate in Milli-Q under vigorous stirring [253–255]. Two batches (Batches B and C) of the larger Au NPs were synthesised using the well-known Turkevich method [256–258]. By varying the amount of sodium citrate added dropwise to the boiling Au-precursor ($HAuCl_4.3H_2O$), the size of the particles was controlled. The molar ratio of the Au-precursor to sodium citrate used for the synthesis of these Au NPs were 1:1.94 and 1:1 for batches B and C, respectively. The Au NPs were pelleted by centrifugation at 15,000 g, the supernatant removed and the particles were redispersed in Milli-Q. The absorbance spectra of the ×10 diluted colloidal solution were used to determine the particle concentration. The surface plasmon resonance peaks were used to determine the amount of Au for optical density, OD = 1. For the conjugation with the fluorescent tag, the gold nanoparticle dispersion (OD=1) was added dropwise into the aqueous solution of FITC-PEG-SH (250 µg/mL) in a 1:1 volume ratio and left under overnight magnetic stirring in the dark. The Au-PEG-FITC NPs (Figure 2-14) was then washed through three cycles of centrifugation (5000 g for 10 min) to remove free FITC-PEG-SH and redispersed in Milli-Q. The particles were characterised using TEM, UV-vis and fluorescence spectroscopy. Dynamic light scattering (DLS) was also employed to measure the hydrodynamic size of the particles (Zetasizer Nano ZSP). The final redispersion was adjusted to OD =1 for further use. MCF7 cells were deformed with 10 nM of the different Au-PEG-FITC NPs at different flow rates (Q = 0 -150 µl/min), washed twice with DPBS and resuspended in DMEM culture medium. Confocal images of the cells with the fluorescent Au NPs were taken in the same manner as the QDs, described in section 2.6.1.

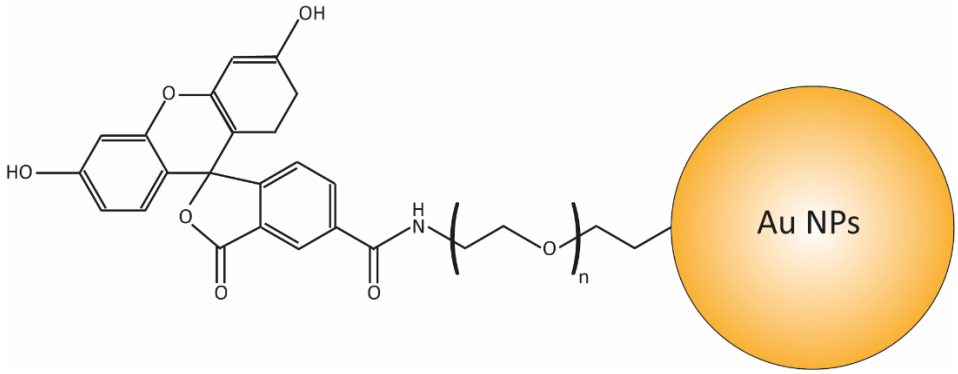

Figure 2-14. Schematic of the Au-PEG-FITC NPs.

2.16. CdSe Quantum rod synthesis and characterisation

2.16.1. The Quantum rod synthesis

The CdSe QRs were synthesised according to the method described by Shieh *et al.* [228]. The cadmium precursor was prepared by dissolving 0.114 g (0.89 mmol) of CdO, 0.43 g (0.155 mmol) of n-tetradecylphosphonic acid (TDPA) in 7 g of trioctylphosphine oxide (TOPO) which melted at 50 ^{o}C, giving a wine-red coloured solution. The mixture was degassed with nitrogen under reflux for 3 h. The mixture was gradually heated to ~300 ^{o}C, where it turned into a clear solution, indicating the formation of the Cd-TDPA complex under reflux as shown in Figure 2-15. The mixture was further heated to 340 ^{o}C to ensure the complete formation of the Cd-TDPA complexes and then gradually cooled and maintained at 260 ^{o}C. The Se-precursor was prepared by dissolving 78.96 g (1 mmol) of Se powder in 5 ml trioctylphosphine (TOP) and heated to 120 ^{o}C. The hot Se-precursor was injected rapidly into the Cd-TDPA complex solution in sequential steps of 0.5 ml, every 3-5 min. The number of injections determined the aspect ratio of the QRs and the duration between injections controlled the overall size. The reaction mixture was rapidly cooled in an ice bath so that the QRs could maintain their shape, preventing the rounding of the particles. The control QDs were also synthesised in the same manner, except the Se-precursor was injected all at once with the same total reaction time. The synthesised QRs were stored at room temperature until further use. The QR solution was cleaned by centrifugation with excess ethanol at 30 ^{o}C at 4000 g for 5 min. The QR pellet was suspended in the desired solvent (chloroform or hexane) for further use and analysis.

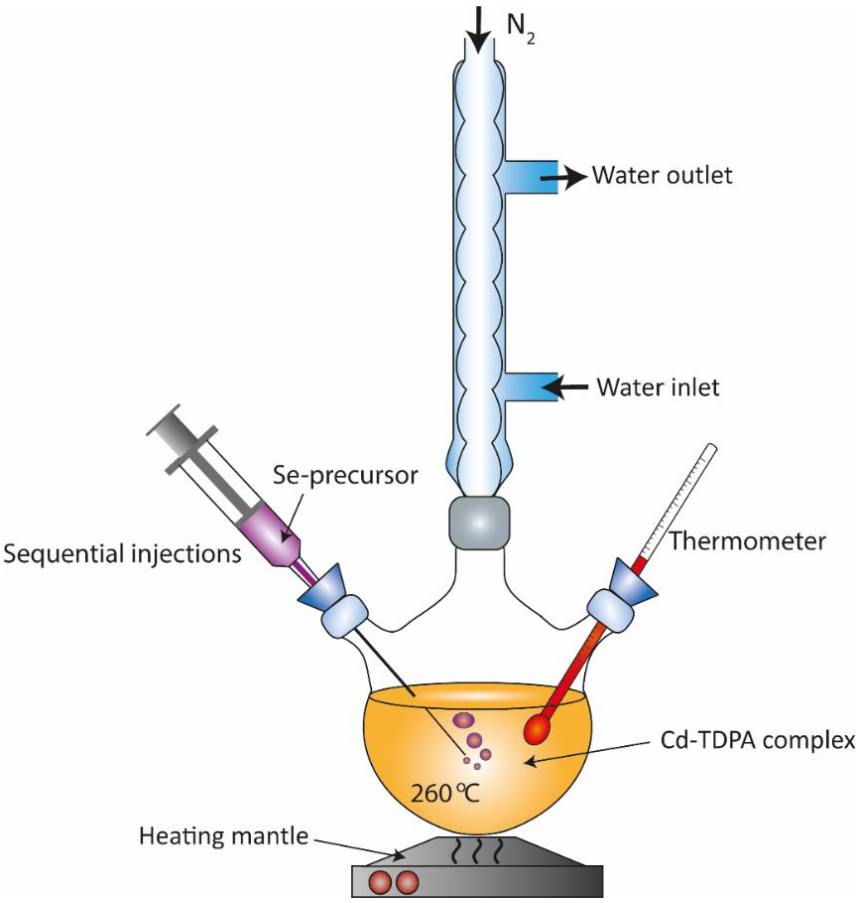

Figure 2-15. Schematic for the experimental apparatus setup for the synthesis of QRs showing the injection of Se-precursor into the hot Cd-TDPA complex.

2.16.2. ZnS shell growth on QRs for surface passivation

1 ml of the QR as-prepared stock solution was cleaned by centrifuging with excess ethanol (ethanol:QR = 10:1 v/v) at 4000 g for 5 min. The pelleted QRs was suspended in 10 ml octadecane and 3 ml TOP. 1 mmol Zinc diethyldithiocarbamate was dissolved in 3 ml oleylamine (keeping the molar ratio between Se and Zn as 1:1). The QR solution and the Zn precursor were mixed and heated to 120 ^{o}C for 2-4 h under reflux. The reaction mixture was gradually cooled to room temperature and cleaned as described earlier in the previous section.

2.16.3. $CdCl_2$ treatment of QRs surface passivation

The QRs were cleaned with excess ethanol (ethanol:QR = 10:1 v/v) by centrifuging at 4000 g for 5 min. The pelleted QRs were suspended in toluene and maintained at 60 °C in a capped vial. The solution was degassed with nitrogen for 1 h. 0.33 M $CdCl_2$ stock solution was made by dissolving 0.3 g (1.64 mmol) of $CdCl_2$ powder and 0.033 g (0.12 mmol) TDPA in 5 ml oleylamine at 100 °C. The solution was degassed for 30 min at 100 °C with nitrogen and gradually cooled to 60 °C (Figure 2-16). The $CdCl_2$ stock solution was added to the QR solution in toluene by rapid injection under stirring (with concentrations calculated to 96 – 192 Cl^- ions/nm^2 of the Q rod surface) in the oxygen-free glove box. The reaction was allowed for 15 min at 60 °C with constant stirring. The mixture was gradually cooled to room temperature and stored in the oxygen-free glovebox. The optical properties of the QRs with the $CdCl_2$ treatment was compared to the negative control in which the Q rods were treated in the same manner with the same volume of oleylamine but without the $CdCl_2$.

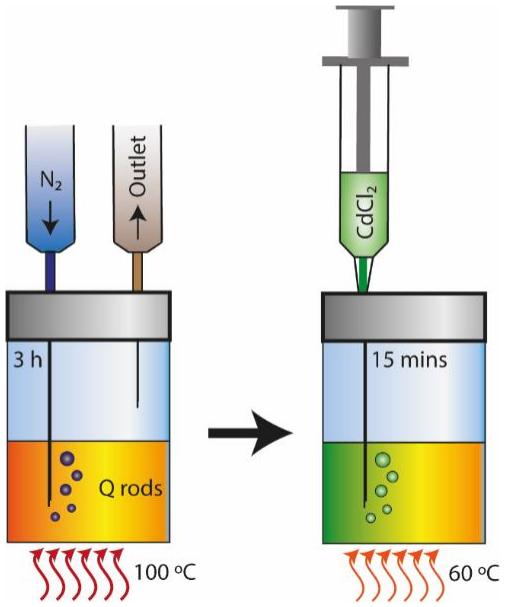

Figure 2-16. Schematic of the experimental setup for the $CdCl_2$ treatment of QRs showing the initial deoxygenation of the QRs at 100°C and the subsequent injection of $CdCl_2$ solution at 60°C.

2.16.4. Characterisation of QRs

The QRs optical characterisation was performed with UV-Vis absorption spectroscopy with Lambda 35, Perkin Elmer and fluorescence spectroscopy were performed using the FLS 980, Edinburgh Instruments using quartz crystal cuvettes. The Fluorescence spectra, lifetime and the PLQY were recorded similarly as described earlier for QDs in section 2.3. The QRs were analysed with respect to solvent blanks for the optical characterisations. A dilute solution of the QRs was drop cast on copper grids with holey carbon film and air-dried. The TEM of the QRs were performed FEI Tecnai TF20 and FEI Titan Themis Cubed 300 TEM.

2.16.5. Transfer into the aqueous phase with amphiphilic polymer

The amphiphilic polymer, poly(maleic anhydride-alt-1-tetradecene), 3-(dimethylamino)-1-propylamine derivative (PMAL) was dissolved in chloroform. The QRs were cleaned as described earlier in section 2.16.1. and dispersed in low concentration in the PMAL containing chloroform at different PMAL: QR ratios (10^3 – $4x10^4$). The mixture was vigorously stirred for 2 h followed by sonication for 1h. The solution was allowed to naturally evaporate overnight with an open cap in the fume hood. Once dry, the precipitate was resuspended in Milli-Q water and sonicated for 30 min (Figure 2-17). The excess unbound PMAL were removed using 20 KDa cut-off ultrafiltration units (CENTRISART-1, Sigma Aldrich) by centrifugation at 2000 g for 1h.

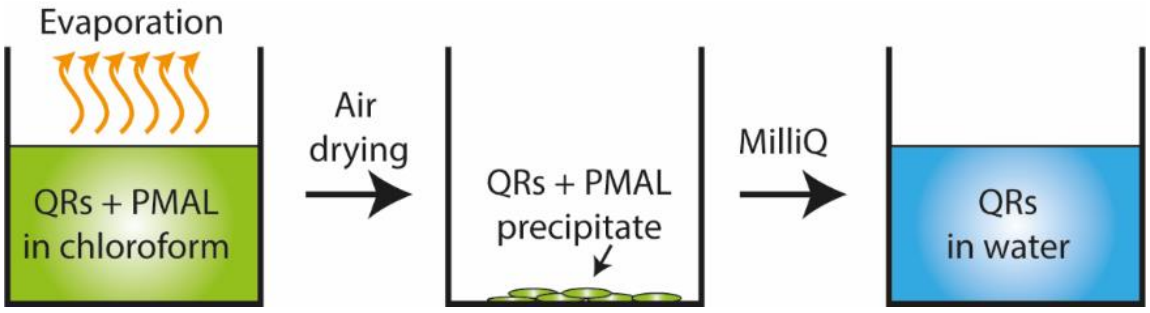

Figure 2-17. Schematic of the steps showing the conversion of hydrophobic QRs in chloroform into hydrophilic QRs in water by the treatment with amphiphilic polymer PMAL.

3. Non-endocytic uptake of QDs by cell deformation

Endocytosis limits the functional capability of NPs in cells, as such, it is essential to seek other effective methods of non-endocytic delivery in live cells. Here, cytosolic delivery of QDs was investigated by shear force-induced hydrodynamic cell deformation of MCF7 cells to produce membrane disruption using the cross-slot microfluidic device.

This chapter contains details on the synthesis and optical characterisations for the CdTe/CdS core/shell QDs. The size of the QDs were determined from the TEM analysis. The toxicity study of QDs for MCF7 cells was performed with MTT assay and the lethal dose at 50 % (LD_{50}) was determined. Deformation index (DI) gives the degree of the stretching of the cells by the shearing forces of the moving fluids and was measured as a function of the flow rate of the cell suspension through the cross-slot microfluidic device. A comparison of cell viability was made for MCF7 cells deformed with and without QDs at different flow rates. The total fluorescence intensity of the QDs from the cells is indicative of the degree of intracellular delivery. The relative total fluorescence intensity was measured using confocal microscopy to investigate the uptake of QDs as a function of flow rate. STEM images of cell sections were analysed for cells deformed with QDs to investigate the nature of the particle uptake.

The non-endocytic QD uptake using the cell deformation technique was subsequently used to introduce the redox-active QDs in the cytoplasm of different cell lines (chapter 4) and to investigate the membrane disruption and leakage of intracellular materials (chapter 5).

3.1. Characterisation of CdTe/CdS QDs

The CdTe/CdS core/shell QDs stabilised with TGA (Figure 2.1) were synthesised according to the methods described in section 2.1. To demonstrate the range of emission of these QDs, the CdTe cores were grown under reflux between 30 min and 24 h which gave a wide range of photoluminescence (PL) emission maxima from 538 to 616 nm (Figure 3-1a). The CdS shell were further grown for 7 h with the final PL emission maxima at 625 nm. This shows that the emission of the QDs is easily tunable to the desired emission. Unlike the hydrophobic CdTe QDs that takes a considerably short time to grow (~1-10 min), the growth of these hydrophilic

particles takes longer [259]. However, the hydrophilic QDs can be readily used for biological applications. The PL emission and the absorption spectra for the QD growth with time are provided in Appendix 9.1. A plot of the PL maxima wavelength and the first excitonic absorbance peak wavelength shows a similar trend in the redshift with growth time (Figure 3-1b). Additionally, it can be observed that with the shell growth, there is a further redshift. Exponential growth curves were applied to fit the core and shell growth separately using: $y = y_0 + A\, e^{-x/\tau}$. The time constant τ for the CdTe core growth were 5.4 ± 0.8 h and 3.0 ± 0.8 h for the emission peak and the first absorbance maxima, respectively (R^2 > 0.98). For the CdS shell growth τ increased to 7.1 ± 3.8 h and 4.4 ± 3.4 h for the respective emission and first absorbance peaks (R^2 >0.95). Here, the data is represented as mean ± standard deviation (S.D). The absorbance and emission spectra for the dataset is provided in appendix 9.1.

It was observed that the longer wavelength emitting QDs showed higher PLQY, which increased significantly with the shell growth (Figure 3-1c). It could be understood that the bigger QDs have fewer surface traps as the larger surface can accommodate more passivating ligands with less spatial hindrance compared to the smaller QDs. The maximum PLQY obtained for these QDs particles was ~57% for particles with the emission peak at 616 nm. It has been previously reported that the larger water-soluble colloidal CdTe QDs stabilised with TGA have higher photoluminescence efficiency of up to 72.6 % for QDs with the emission peak at 651 nm [260].

The full-width-half-maximum (FWHM) of the emission peak initially increased rapidly with QD size and becomes steady. The width of the emission peak is indicative of the polydispersity of the particles, with more polydispersed QDs showing larger emission width. Since the FWHM remains relatively steady at 57 ± 1 nm, it implies that the growth of the particles was uniform and indicated the suppression of the Ostwald ripening (dissolution of smaller particles for deposition on larger ones) with time. Recently, very narrow band (FWHM ~11.7 nm) emission in the red region for CdTe QDs have been obtained by programmed dropwise precursor addition, significantly suppressing the Ostwald ripening [261].

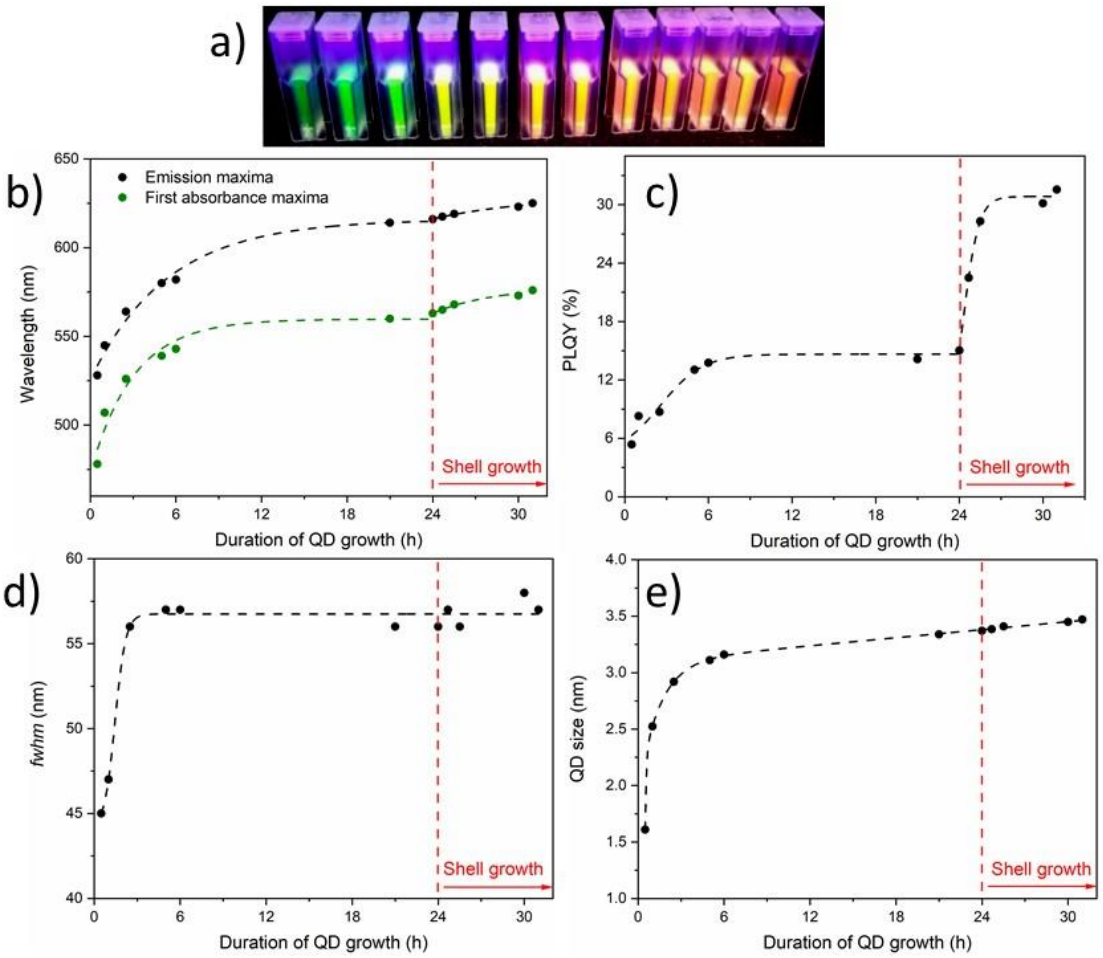

Figure 3-1. Monitoring the growth of the CdTe/CdS QD with TGA capping with the duration of growth under reflux. a) QDs with the duration of growth ranging from 30 min to 31 h showing PL emission from green to red b) the comparative position of PL emission and the first absorbance peaks with growth duration c) PLQY and d) FWHM of the emission peak. e) QD size as a function of growth duration as determined from the first absorbance maxima using the method described by Yu et al [5].

The concentration of the colloidal QD solution was determined from the first excitonic absorbance peak using the empirical relations described by Yu *et al.* [5]. The molar extinction coefficient of the QDs at the first absorbance peak depends strongly on the particle size. The particle size was determined using the empirical fitting function:

$$D = (9.8127 \times 10^{-7})\lambda^3 - (1.7147 \times 10^{-3})\lambda^2 + (1.0064)\lambda - 194.84 \qquad (3.1)$$

where D (nm) is the diameter of the QDs and λ (nm) is the first excitation wavelength. For simplicity, it was approximated that the QDs are only made of CdTe. Figure 3-1e shows the

increase of QDs with time under reflux having exponential growth fitting. The molar extinction coefficient (ε) for the first excitonic transition was determined using:

$$\varepsilon = 10043\ (D)^{2.12} \qquad (3.2)$$

Typically, the ε for the CdTe/CdS QDs ranged between 70,000 to 200,000. Finally, the concentration of the QD solution was obtained by using Lambert-Beer's law

$$A = \varepsilon CL \qquad (3.3)$$

Here, A is the absorbance at the peak position, C is the concentration (moles/L) of the quantum dots in solution and L is the beam path length (1 cm for these experiments).

Typical absorbance and PL emission spectra of the QDs with the core and shell growth of 1 h each is shown in figure 3-2a. The PL emission peak is at 561 nm with an FWHM of ~57 nm. The first exciton absorbance peak is at 527 nm, giving a Stokes shift of 34 nm. The typical transient PL lifetime decay curve of the core/shell QDs show bi-exponential decay behaviour, fitted to equation 2.2 (Figure 3-2b). The time constants from the fit are τ_1 = 6.7 ± 0 .07 ns and τ_2 = 29.2 ± 0.23 ns with corresponding amplitudes of A_1 = 0.57 and A_2 = 0.39 (R^2 >0.998) (exponential decay fits R^2 values- mono: 0.984, bi: >0.998). τ_1 represents the combination of the fast electron capturing processes by the surface traps and defects which leads to non-radiative recombination with valence band holes. The longer time constant τ_2 represents the process of the radiative recombination of the exciton, responsible for the PL emission.

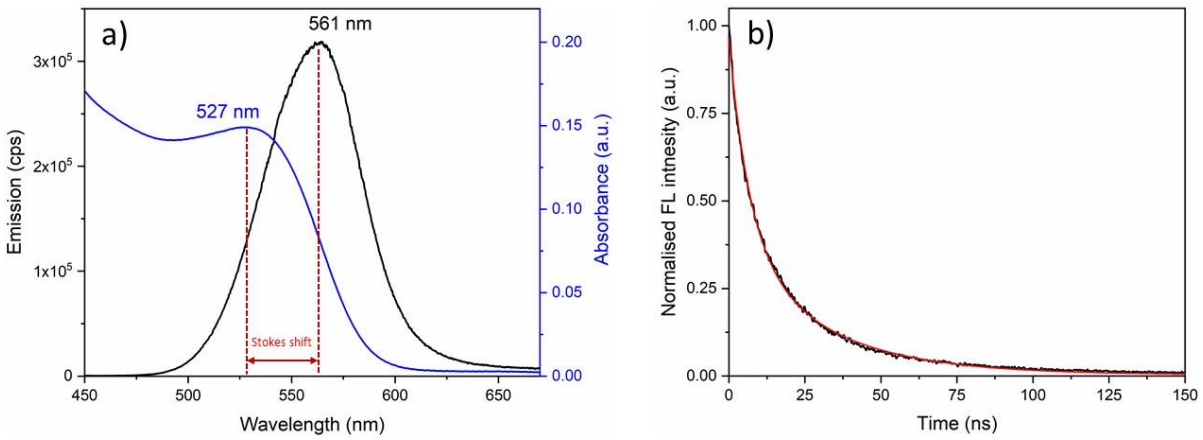

Figure 3-2. Typical optical behaviour of the CdTe/CdS core/shell QDs stabilised with TGA. a) Absorbance and PL emission spectra and (b) PL decay curve with the red line as the biexponential fit (R^2>0.99).

The TEM images show that the CdTe/CdS core/shell QDs (1 h core and 1 h shell growth) are roughly spherical in shape (Figure 3-3). The particles were sized manually using ImageJ by fitting an ellipse to the QDs. Both the major and minor axes were measured and averaged over 200 QDs. The average size of the QDs is 2.9 ± 0.9 nm (mean ± SD) which correlates with the particle size determined from the absorption spectra (~2.8 nm) estimated using the empirical function described by Yu *et al.* as shown above in equation 3.1 [5]. The histogram of QD size from the TEM images was fitted to a normal distribution (Figure 3-3 inset).

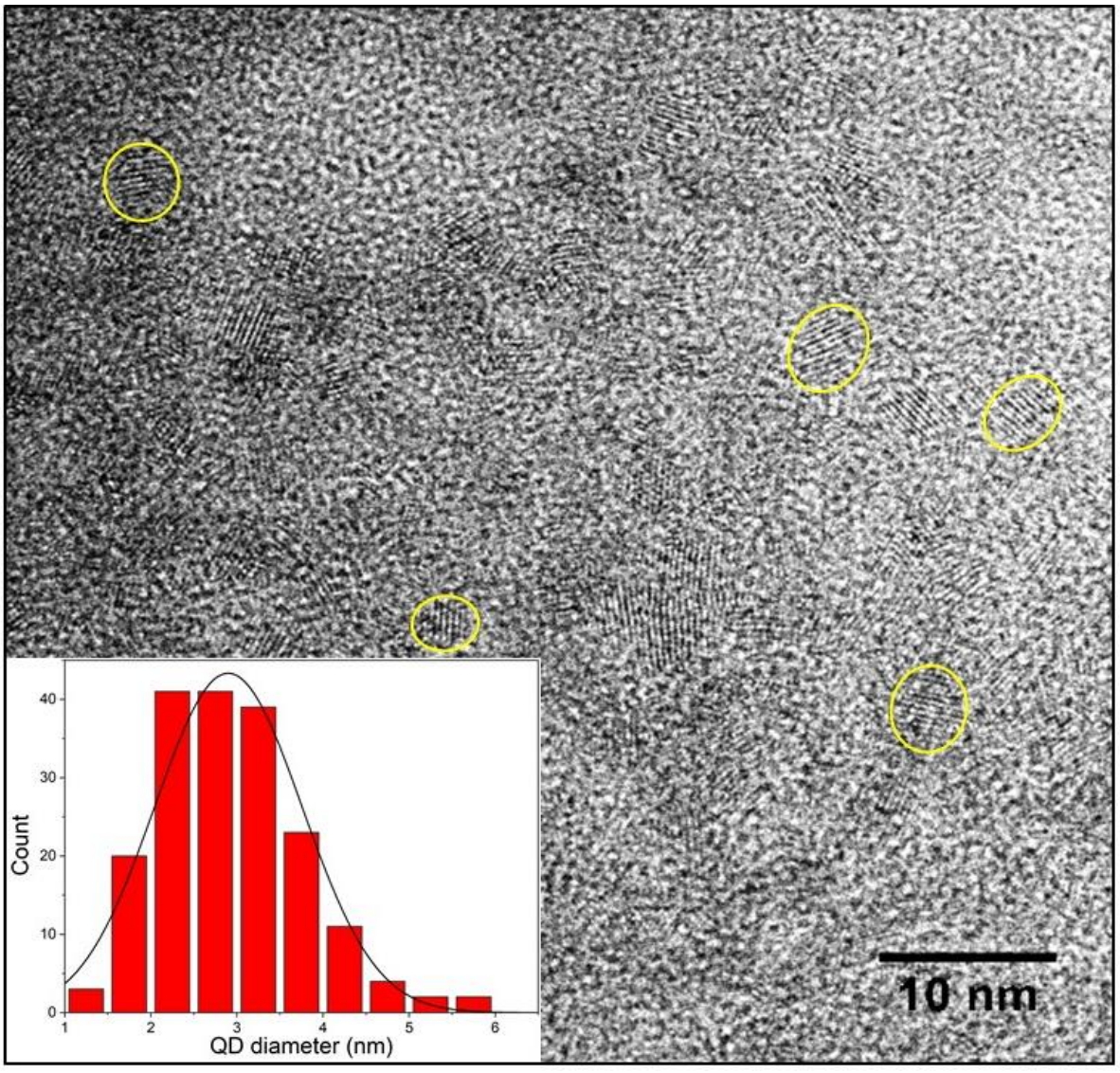

Figure 3-3. Typical TEM images of the CdTe/CdS QDs with inset showing the particle size distribution along with fitted normal curve.

3.2. Toxicity of QDs to MCF7 cells

The toxicity of the MCF7 cells to the treatment of CdTe/CdS QDs stabilised with TGA ligands was performed according to the method described in section 2.5.3. Cells were seeded in 96-well plates and treated with different concentrations of QDs (0-10 µM). After an 18 h incubation, the cells were washed twice with DPBS and the MTT assay was performed as described in section 2.5.3. The viability was measured with respect to the control cells which did not receive any treatment. The study showed that the cells remain viable above 80 % at 100 nM QD concentration. Further increase in the QD concentration caused a drop in the viability with the LD_{50} value at ~670 nM. The cytotoxicity of the CdTe QDs is mainly reported due to ROS production, GSH depletion, formation of TeO_2 and CdO rather than the release of free cadmium [262]. As the viability of the cells decreased rapidly beyond the 500 nM QD concentration, further experiments were performed at 100 nM QDs unless stated otherwise.

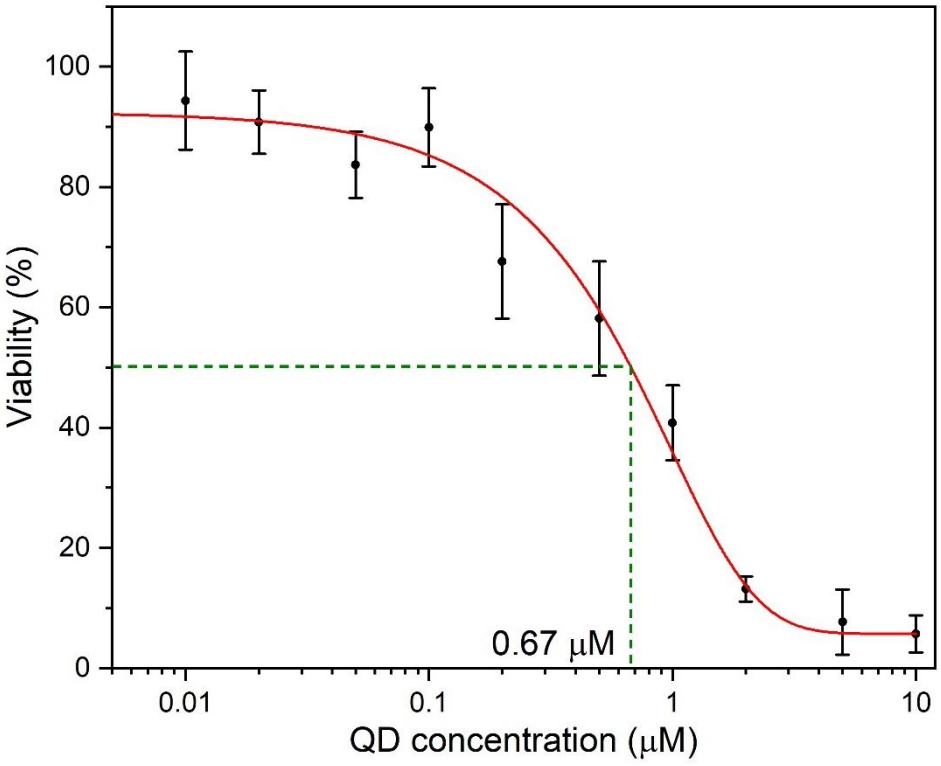

Figure 3-4. The viability of MCF7 cells as a function of CdTe/CdS QD concentration. The cells were incubated with QDs for 18 h and viability was measured using MTT assay in 96-well plates (n = 3 with 5 wells for each sample). The data is expressed with S.E. and the dose-response fitting curve is used (R^2 =0.99).

3.3. Microfluidic cell deformation

The cells were deformed through the cross-slot microfluidic device (Figure 2-8) as described in section 2.5.4. The method was high throughput, by which a few 100s to 1000 cells/min was treated, depending on the flow rate and the concentration of the cells, facilitated by a high-speed camera [181]. The cells suspension in the device maintained a constant speed over the inlet channels (~750 μm) before entering the extensional-flow junction. From the videos captured by the high-speed camera, the cells entering the field of view (FOV) was observed from one of the inlets (Figure 3-5). The cells approached the extensional-flow junction along the straight channel in a partially deformed state, where the cell assumed a bullet shape. This occurs due to the shear viscous forces from the channel walls [263]. At the extension-flow junction, the opposing fluids from the two inlets intersect, slowing on collision and hence generated a stagnation point at the centre of the junction, where the cells temporarily stopped. Here, the cell was under the influence of the compressive inertial force due to the incoming fluid from the inlets and the shearing force due to the fluid moving around the edges (Figure 1-15). The inertial force tends to squeeze the cells at the centre of the motion. The shearing forces around the edges tend to stretch the cells at their peripheries. The combined action of these two forces caused the cells to deform. Depending on the viscosity and the rate of flow of the fluid, one of these forces will dominate. For low viscous fluids, the inertial force dominates, and the high viscosity of the fluid leads to a shear force-dominated regime (Figure 1-16). The degree of deformation of the cells depends upon the balance of these forces [181]. For the inertial dominated regime, the same degree of deformation is obtained at much higher flow rates compared to the shear dominated regime at increased fluid viscosity.

The cells leave the extensional-flow junction through one of the outlets, where they remained partially deformed before regaining their shape. It is important to make a note here that not all cells go to the stagnation point. Some cells (~5-10%) slip around the edges and are not deformed to the same degree as compared to the cells at the stagnation point. However, since we cannot separate these cells for the QD uptake study, all cells were considered for the DI measurements, regardless of them not making it to the stagnation point.

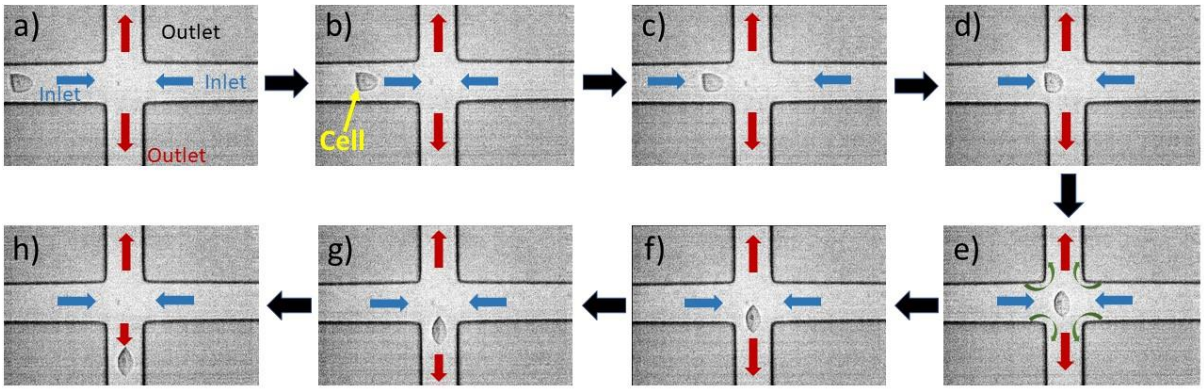

Figure 3-5. High-speed camera Images stages of the MCF7 cells passing through the extensional-flow junction of the cross-slot microfluidic device at 100 µl/min flow rate. (a) The cell enters the FOV from one of the inlets and b-d) maintains a bullet shape. e) The cell deforms by the action of the moving fluid at the stagnation point and f-h) and exits through one of the outlets.

With the introduction of 0.5 % (w/v) methylcellulose (MC) in DPBS, the viscosity of the suspension fluid increases from ~1 cP to 33.0 ± 0.3 cP, as such, the deformation of the cells is in the shear dominated regime (Re <11) [181]. All experiments in this thesis were performed in this condition. The cells at the stagnation point deformed into an ellipsoidal with the cells being stretched by the shearing forces of the moving fluid at the stagnation point. With increasing flow rates, the ellipsoidal shape of the cells became more pointed at the two edges (Figure 3-5e). This suggests that the cells are being more stretched near these points that could potentially lead to greater membrane disruption at these two diametrically opposite regions on the cell membrane, which would require further investigation. The degree of cell deformation as measured through DI steadily increased with the flow rate (Q) initially and then plateaued around 125 µl/min flow rate. From the curve of the mean DI as a function of Q, exponential decay function was fitted (R^2 >0.98) with the maximum DI observed to be ~1.58 for these MCF7 cells at the flow rate of 175 µl/min (Figure 3-6a). The maximum DI from the curve fitting (DI_{max}) was determined using equation 3.4 which is the exponential fit function used for the datasets in Figure 3-6a.

$$DI = A.e^{-Q\tau} + DI_{max} \qquad (3.4)$$

It is a mono-exponential decay function with amplitude A, time constant τ and offset DI_{max}. This was used to find the extrapolated parameter DI_{max} (~1.6) which represents the maximum fitted deformation of the cells as a function of Q. The resistance to greater deformation at

higher flow rates can be attributed to the combined action of the viscoelastic properties of the cells and the cytoskeleton. Actin disruption of the cellular cytoskeleton for SW480 cells with latrunculin-A have shown increased DI in the shear regime, which is indicative of the contribution of actin towards cell stiffness and the consequent resistance to deformation [181].

Assuming that the volume does not change during deformation, and the shape of the cells can be approximated to an ellipsoid, the change in the surface area of the cell was calculated using the measured DI (Figure 3-6b). The ratio of the height and the width of the cells at deformation was obtained from the mean DI for different flow rates, which was used to calculate the mean surface area of the deformed cells. This was compared to the surface area of the undeformed spherical cells with the same volume, to calculate the increase in the cell surface area upon deformation. It was observed that the percentage change in the cell area on deformation increases linearly with the DI. It was also noted that all experimental values of Q, except 25 µl/min show more than a 2 % change in the surface area. There are reports from membrane model-based studies that membrane poration can occur when the surface area of the lipid bilayer membrane is stretched by 2% [264]. Hence, cell deformation using the cross-slot microfluidic device could generate cell membrane pores to allow diffusive uptake of QDs.

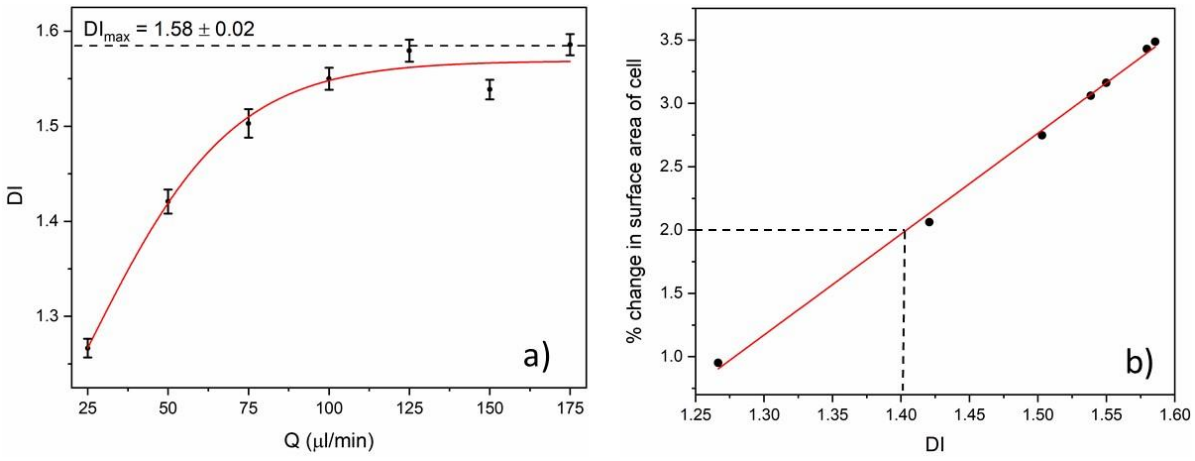

Figure 3-6. Deformation of the MCF7 cells in a cross-slot microfluidic device in the shear regime (µ ~ 33 cP). a) DI as a function of Q with data expressed as mean ± SE averaged for N = 3 repeats with ~200 cell events for each data point. b) percentage change in the surface area of the cell with respect to the measured DI assuming no volume loss and the cell shape can be approximated to an ellipsoid in the deformed state Linear fit is represented with a red line (R^2 >0.99). The dashed lines represent the 2 % change in cell volume with corresponding DI ~1.4.

3.4. Viability of cells on deformation and QD uptake

MCF7 cells were deformed through the cross-slot microfluidic device at different flow rates of up to 175 µl/min, with and without QDs. The viability of the cells was measured using the MTT assay as described in section 2.5.3. For cells deformed without QDs, the viability did not seem to be affected by flow rate and remains above 85%. This suggested that despite the cells being subject to deformation, they are capable of recovery at these flow rates.

When the cells were deformed with 100 nM QDs, the results showed that at lower flow rates (up to 125 µl/min), the viability remained ~80%. However, from Q = 150 µl/min and above, the viability dropped steadily to ~60% for Q = 175 µl/min. It has to be noted that the total exposure time of the cells to the QDs was 30 min for these experiments, in contrast to the toxicity study involving 18 h incubation discussed in section 3.2. This was chosen because the total exposure time of the cells with the QDs was no longer than 30 min for the deformation experiments. This decrease in viability can be attributed to the toxicity caused by the higher uptake of QDs. The CdTe QDs are known to be toxic to the MCF7 cells at higher concentrations [62]. Additionally, it also suggests that there is an increase in the membrane porosity of the cells, hence leading to higher QD uptake. In spite of the deformation index remaining constant at higher flow rates, the cell membrane porosity could be higher to allow greater uptake of QDs. The viability of the cells at Q = 100 µl/min is comparable with and without QDs, as such, this flow rate was chosen for further single flow rate experiments.

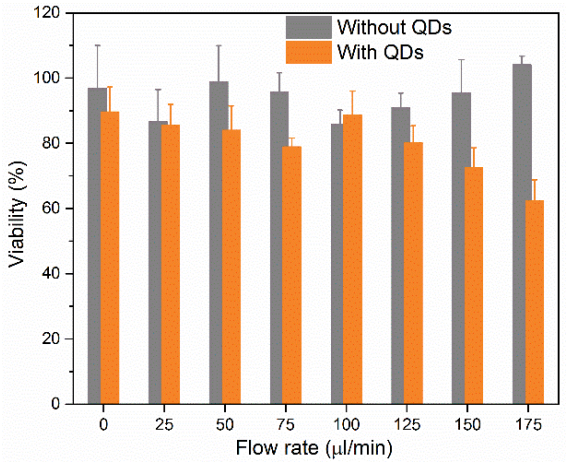

Figure 3-7. The viability of MCF7 cells deformed through the cross-slot microfluidic device with and without 100 nM QDs. The viability was measured using MTT assay in 96-well plates (n = 3 with 5 wells for each sample). The data is expressed with SE.

3.5. Confocal imaging of cells and measurement of fluorescence intensity

The cells were deformed with 100 nM QDs through the cross-slot device at different flow rates as described in section 2.5.4. The cells were washed twice with DPBS to remove the excess QDs and dispersed in DMEM culture medium. Confocal images of the cell suspension (Figure 3-8) in incubation chamber wells (Lab-Tek II, VWR International) were taken and while maintained at 37^{o}C as described in section 2.6.1.

The confocal images were analysed using a customised MATLAB script, using the "imfindcircles" function to trace the cell outline in the bright field images, which identified cells as circles from the bright field images (circularity up to 0.9 was tolerated). The contrast of the bright field images was increased to make the outline of the cells clearly visible against the white background of the bright field images. The range of the size of the circle traces was adjusted to fit in most of the cells in the images (Figure 3-8c and d). It can be seen from the fitted traces that some of the cells with circularity below 0.9 were not fitted by the MATLAB script. Very large cells with radii beyond 15 µm were ignored. It can also be seen from the that the script can identify few regions with circular trace fits in the image which does not contain cells. These artefacts were removed manually as they are easy to identify, since the have no or very little fluorescence (<1% of the typical measurement). The circular traces of the cells from the bright field image were projected onto the corresponding fluorescence image. The MATLAB script now integrated the total fluorescence intensity from each of the circles, which corresponded to the QD uptake in the individual cells. The data was export from the script giving the cell radius and the corresponding total fluorescence intensity from the cell in an excel file.

From the analysis of the confocal images of the MCF7 cells deformed with QDs, it was observed that the total integrated fluorescence intensity from the cells increased with the increase in the flow rate (Figure 3-9). This indicates that with increasing deformation, the QD uptake increases. It was observed that the mean uptake of the QDs increased steadily and slowed down for higher Q values. A $\log_{10}$-dose-response guideline fitting was done using equation 3.2 for the average total PL emission (U) per cell, deformed with 100 nM QDs as a function flow rates for the dataset in Figure 3-9.

$$U = A_1 + \frac{(A_2 - A_1)}{1 + 10^{\log(x_0 - x)p}} \qquad (3.2)$$

here, A_1 and A_2 are the baseline response (bottom) and the maximum response (top) of the curve respectively. $\log(x_0)$ is the Q when the U value is in-between A_1 and A_2, and p is the Hill-slope of the curve ($R^2 > 0.98$).

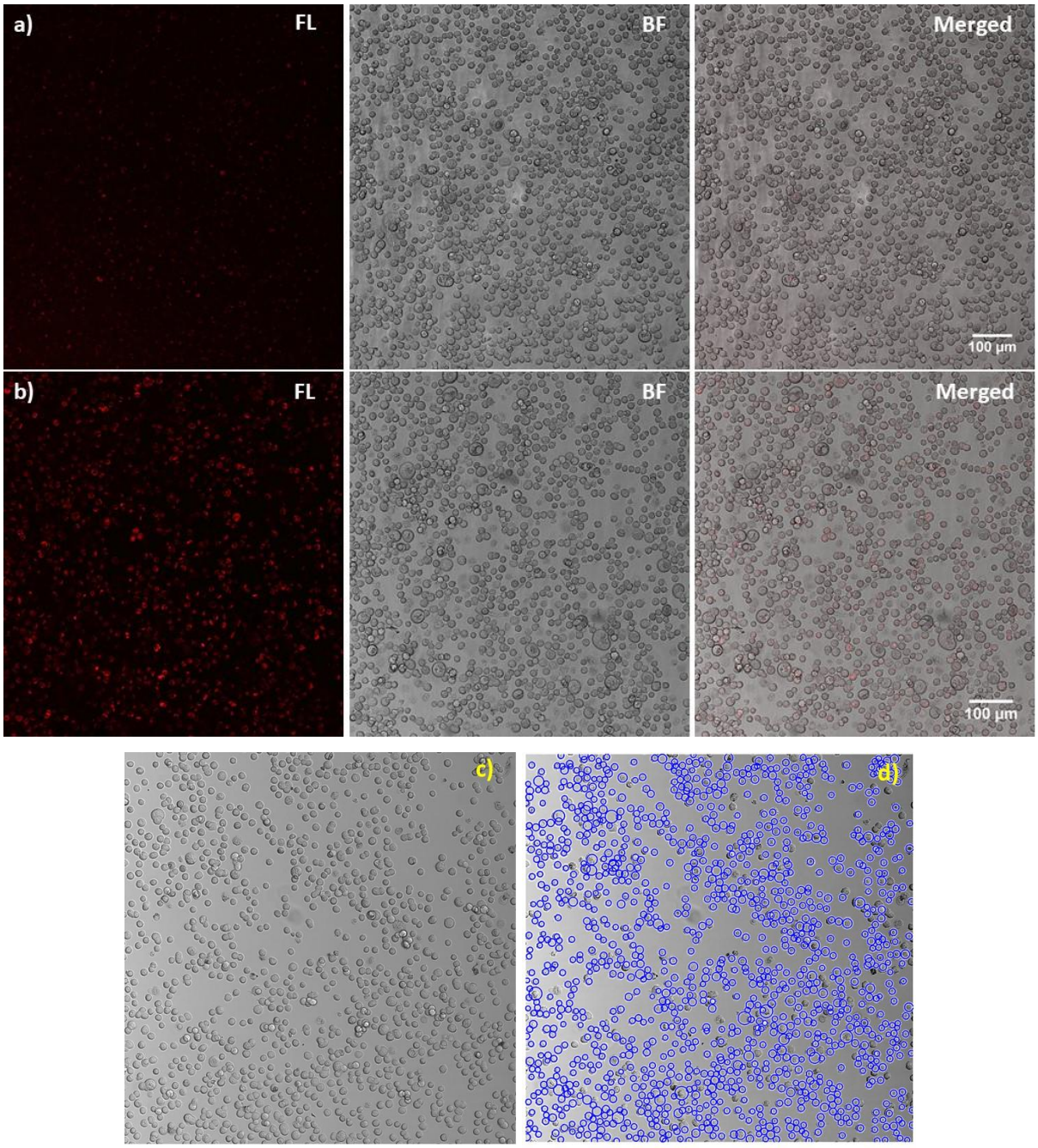

Figure 3-8. Typical confocal images of MCF7 cells used for QD uptake analysis. a) Cells incubated and b) Deformed at Q = 100 µl/min with 100 nM QDs. FL = fluorescence, BF = bright field channels and merged channels using ImageJ. c) A typical BF confocal image of MCF7 cells with the corresponding d) circular trace fits using the MATLAB script for the measurement of the total fluorescence intensity from each cell.

A conventional method of defining delivery efficiency in literature is the fraction of the cells that take up the cargo above a threshold, which is typically the uptake of the top 5 % of the control (incubated) group [163]. This threshold of the top 5 % is estimated to account for the endocytic delivery, surface binding and autofluorescence. Applying this method to analyse the uptake efficiency from the total PL emission of the cells, we obtain a maximum delivery efficiency of ~34 % at the flow rate of 150 µl/min as shown in figure 3-9b (at Re <11). The delivery efficiency increases with the flow rate which correlates with the mean total PL intensity from cells in Figure 3-9a. The Chung group reported ~25 % delivery efficiency for 3-5 kDa dextran in MCF7 cells in the inertial flow regime at Re = 189 using the cross-slot device. They report almost 100 % delivery efficiency of these dextran particles for HEK293 cells at this inertial regime. Lee *et al.* have also reported intracellular delivery efficiency up to 35 % for QDs using the constriction based microfluidic deformation of HeLa cells [163].

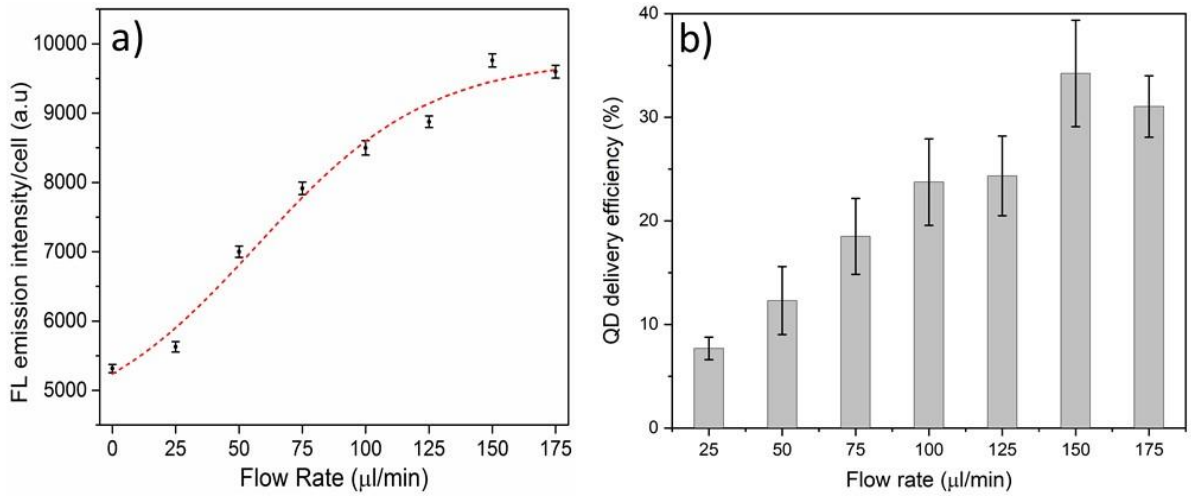

Figure 3-9. a) Mean total fluorescence emission from the cells at different flow rates. The dotted line represents a log_{10}-dose-response guide curve (R^2 > 0.98). b) The intracellular delivery efficiency of QDs with flow rate according to the method described by Lee et. al [163]*. Data is expressed as mean ± SE with N =3 repeats having >4000 cells each in total.*

The cell incubated with the QDs will uptake mostly through the endocytic pathways. According to the scatter plot of the integrated total fluorescence intensity in cells with cell area, it is observed that the distribution of uptake with the cell area is linear (R^2>0.91), suggesting that larger cells tend to uptake more particles (Figure 3-10a). This is because there is potentially more surface area for QDs to interact for larger cells. From the scatter plots it was seen that

the QDs uptake gradually deviated from the linear endocytic uptake behaviour with increasing flow rate (Figure 3-10b-h). From the scatter plot for Q = 50 µl/min, it was observed that there are two different populations of the uptake, indicating the possible presence of the two different uptake mechanisms. There should be a presence of another mechanism of QD uptake in addition to the endocytic processes. Beyond Q = 50 µl/min, the second mechanism of uptake dominated over the endocytic methods. Comparing this to the deformation indices of the cells with flow rates (Figure 3-6a), it was seen that with the increase in the deformation of the cells, the uptake of the QDs increased.

With increasing deformation, there is an increase in the cell surface area that could lead to higher membrane porosity (Figure 3-6b). However, as discussed earlier, the deformation index plateaued after a certain high Q (~125 µl/min), with the same degree of deformation even with increased speed of the cell suspension through the device. The QDs uptake increased even though the DI plateaued. This indicates that there is an increase in the membrane porosity at higher flow rates despite similar deformations. This implies that the membrane disruption is higher with increasing flow rates, irrespective of the DI. As seen earlier, higher uptake of QDs also corroborates the decreased viability of the cells at higher flow rates. Further investigation is necessary to interpret the relation between membrane disruption, flow rate and particle uptake.

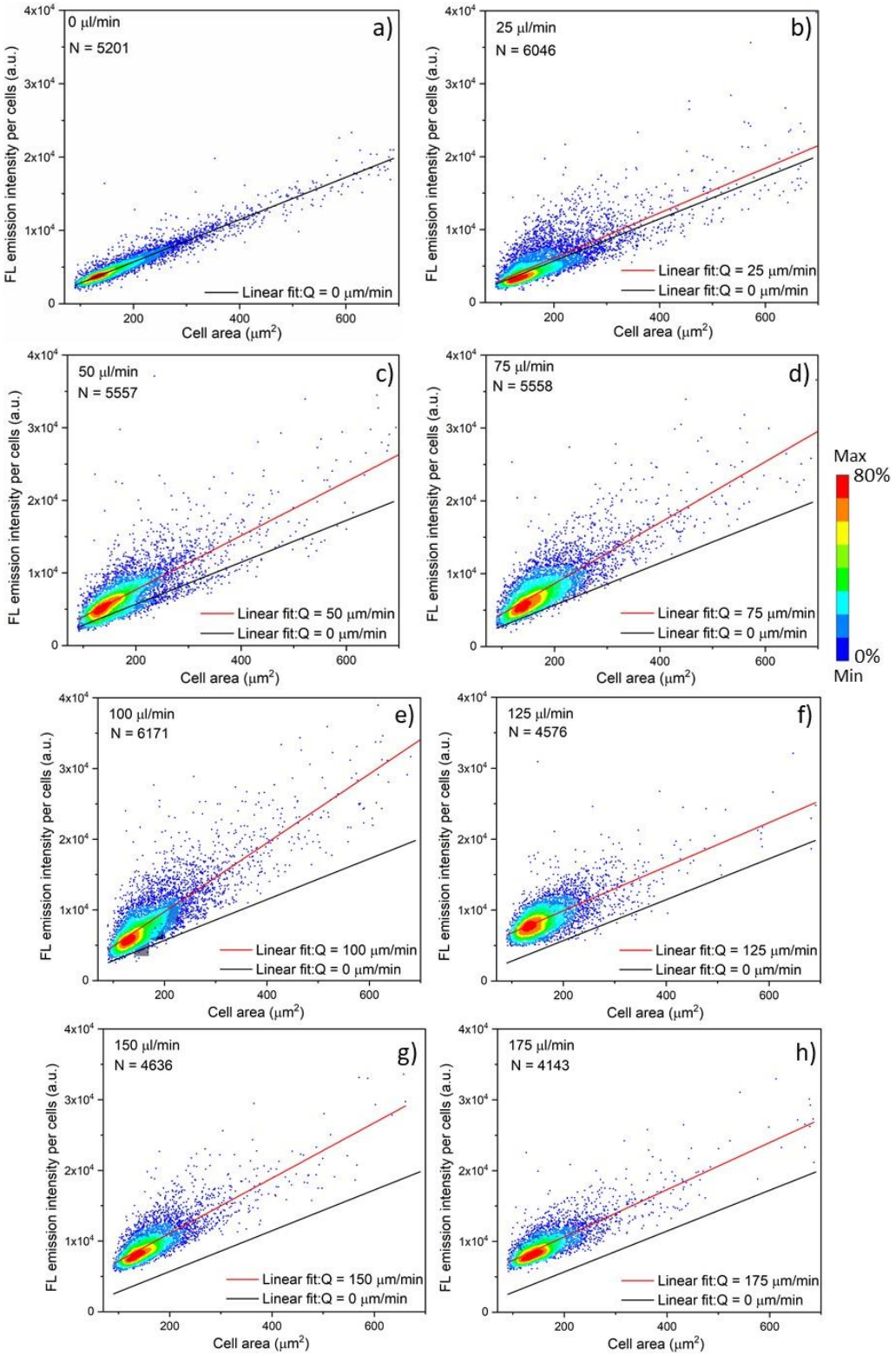

Figure 3-10. Density scatter plots of the Total fluorescence emission intensity from the cells using confocal images, deformed through the cross-slot microfluidic device with 100 nM QDs. a) Cells with no deformation (Q = 0 µl/min, incubated control) with linear fitting represented by the black line (R^2>0.91). b-h) Cells deformed at different flow rate (Q = 25 - 175 µl/min). The black line represents the linear fitting as a guideline for the data set with the red line as the linear fit for Q = 0 µl/min as reference.

3.6. QD quantification in cells using ICP-MS

To estimate the number of QDs delivered to cells with cross-slot microfluidic deformation, the ICP-MS analysis to quantify the cadmium from the cells was performed according to the method described in section 2.9. The calibration curve using the standard cadmium showed linear distribution (R^2 >0.99) with a known amount of cadmium (Figure 3-11a). The cadmium concentration for each of the samples was estimated from this calibration curve. The value of the blank cell sample (no QDs) was subtracted from the dataset to establish a baseline. The number of cells used in each of the samples is given in table 3-1. From the TEM images of these QDs (shown in appendix 9.4), the mean size of the QDs used for this experiment was ~4.0 ± 1.2 nm (48 h CdTe core and 5 h CdS shell growth, emission peak maxima ~625 nm). From the QD size, the mean volume of each QD was determined and this data was used to calculate the mean number of moles of cadmium in each QD as ~$(8.16 \pm 0.1)\times10^{-25}$. Using this value and the data from the ICP-MS measurements, the average number of QDs/cells were calculated as shown in Table 3-1 and Figure 3-11b. The results show that the average uptake due to endocytosis (for 0 µl/min flow rate sample) is ~6.4 ± 2.7 million QDs/cell. This did not change significantly with deformation at a lower flow rate of 50 µl/min. However, at higher flow rates (100 and 150 µl/min) the average number of QDs/cell is >8 million, indicating increased uptake with membrane disruption. The data in Figure 3-11b is expressed with SD, which arises from the distribution of the QD particles size. As the particle size significantly affect the number of moles of Cd per particle, hence the SD is large. Summers *et al.* reported a mean uptake of ~2.4 million QDs/cell for 1 h incubation of 10 mM QDs for U-2 OS (ATCC HTB-96) osteosarcoma cells [265]. They quantified the QDs in cells through a combination of 3-dimensional whole-cell imaging using electron microscopy and fluorescence-based dose quantification using flow cytometry. Hence, the data from the ICP-MS analysis shows that the QD uptake is in the same order of magnitude as previously reported using a different technique. However, there are several differences such as the cell type, QD concentration and incubation period. Since the ICP-MS investigation was performed for a large number of cells for each sample set, the experiment extended over several passages of the MCF7 culture, which can bring some discrepancy in the nature of uptake. The trend of the QD uptake is also not consistent with the confocal image analysis with flow rate (Figure 3-9). Nevertheless, it gives us a broad estimate of the number of QDs delivered to the cells.

Flow rate (µl/min)	Cd concentration (µg/L)	No. of cells (×10^6)	No of QDs/cell (×10^6)
0	1.939	32.9	6.4 ± 2.7
50	1.583	27.1	6.4 ± 2.7
100	3.521	43.7	8.8 ±3.7
150	3.146	41.6	8.3 ± 3.5

Table 3-1. Determination of the number of QDs/cell from ICP-MS for cells deformed with 100 nM QDs at different flow rates.

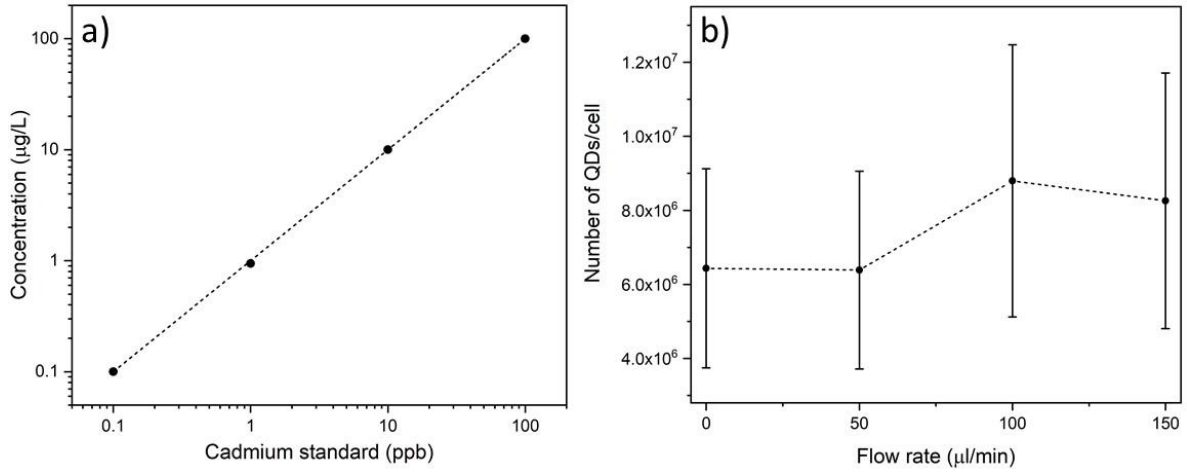

Figure 3-11. ICP-MS analysis for the quantification of QDs delivered into cells by hydrodynamic deformation via cross-slot microfluidic device. a) The calibration curve for the estimation of cadmium concentration using an ICP-MS grade cadmium standard (R^2 >0.99). b) The average number of QDs/cell with flow rate. Data expressed as mean ± SD. SD arises from the distribution of the QD particle size measured from the TEM images (Appendix 9.4).

3.7. STEM images of cell sections

From the confocal image analysis, it was observed that there is an increase in the uptake of the QDs through deformation in comparison to the endocytic uptake. As such, there must be another mechanism in addition to the endocytic entry of the particles into the cells. This could be through the uptake of QDs via diffusion across the membrane pores of the deformed cells. To investigate the nature of the QDs uptake, electron microscopy of the cells with QDs were performed. MCF7 cells were treated with QDs, either incubated or deformed (Q = 100 µl/min) with 100 nM QDs. Cells were fixed and embedded in resin as described in section 2.8. Microtome sections of the cells (~100 nm thick) were placed on copper grids with carbon film and imaged using FEI Tecnai TF20. STEM images were chosen over the TEM images for the cell

sections, as the contrast of the QDs within the cells were superior with the STEM technique (Appendix 9.2 and 9.3). From the images of the deformed cells, it was observed that the QDs are freely dispersed within the cytoplasm, in addition to the endosomal uptake (Figure 3-12). The free dispersion of the particles shows that there is non-endocytic uptake of QDs. There is also the presence of endocytic uptake of QDs in addition to the non-endocytic uptake for the deformed cells (Appendix 9.2). This corroborates well with the presence of two different populations of cells for the integrated total fluorescence intensity as seen in the scatter plots from the analysis of the confocal images (Figure 3-10c). On cell deformation through the cross-slot microfluidic device, the cells were stretched under the shearing force of the moving fluid which generated membrane pores. These membrane pores facilitated the diffusion of the QDs into the cytosol in a non-endocytic manner. From the STEM images of the cell sections incubated with the QDs, we can observe that the particles remain within endosomes in the cell cytoplasm. QDs entrapped in endosomes have limited functional capabilities within the cells as they do not directly interact with the cytoplasm. However, using the cell deformation method, the QDs come in direct contact with the cytosol and will be able to truly bio-sense in live cells. This method opens a potential for vector-free, non-endocytic delivery of nanomaterials to the cytoplasm for intracellular sensing in live cells.

It can be seen from the STEM images that there are aggregates of QDs with the cells (the third panel in Figure 3-12a). However, these aggregates are not enclosed in endosomes. These aggregates were possibly formed in the running buffer prior to the uptake of the particles. Hence, care has to be taken that the QDs are always freshly prepared in the running buffers and the experiments are carried out immediately to minimize the formation of the QD aggregates.

It can also be observed that there are some freely suspended QDs within the nucleus (Appendix 9.2). This suggests that the QDs were able to pass through not only the cell membrane but also the nuclear membrane. It could be understood that during cell deformation, there is also a potential deformation of the nucleus, leading to the formation of pores on the nuclear membrane. However, nuclear membrane disruption studies are challenging and have not been undertaken for microfluidic cell deformation techniques so far. This future study can be crucial in understanding the nuclear membrane behaviour under mechanical stress for potential intra-nucleus sensing and labelling.

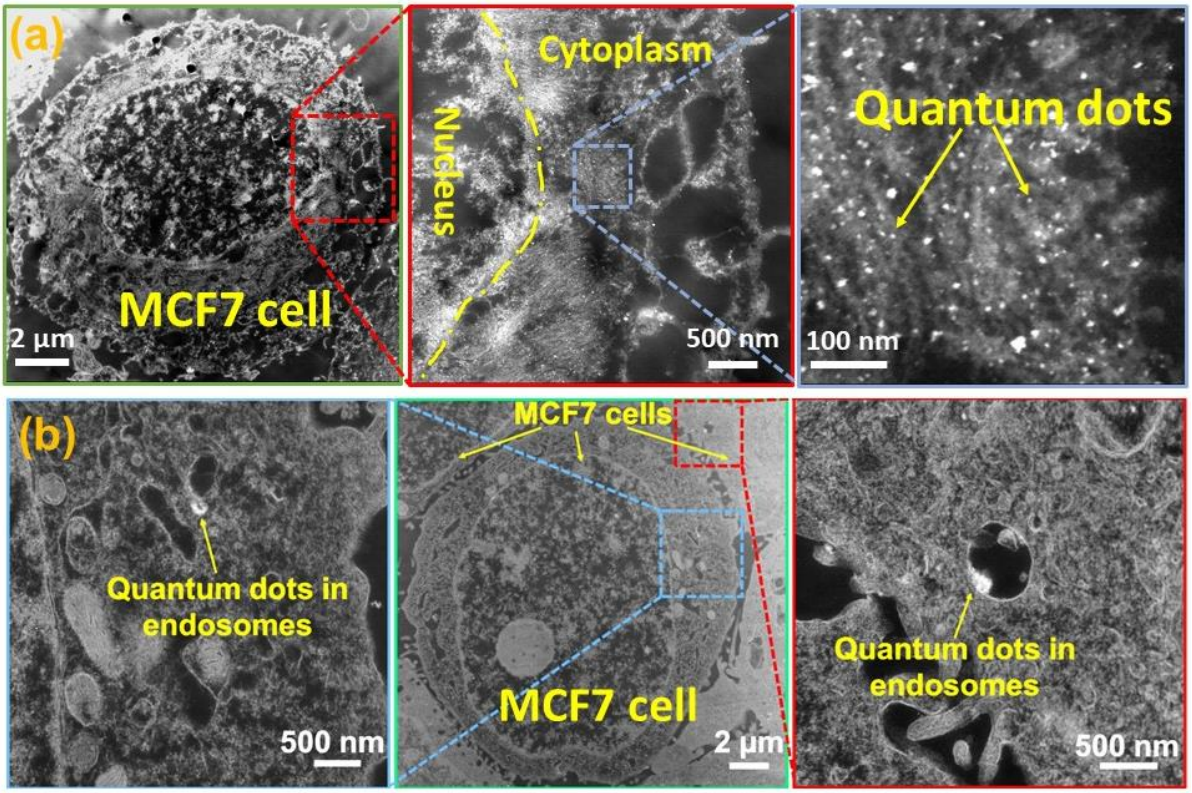

Figure 3-12. STEM images of the microtome sections of MCF7 cells treated with 100 nM QDs and a) deformed through the cross-slot microfluidic device at 100 µl/min flow rate and b) incubated.

3.8. Concluding remarks

The deformation of cells through the cross-slot microfluidic device facilitated the non-endocytic uptake of QDs in the cytoplasm of MCF7 cells. Cell deformation generated transient membrane disruption, which allowed the intracellular diffusion of QDs. The method is high-throughput, vector-free, inexpensive, simple and easily reproducible.

CdTe/CdS core/shell QDs stabilised with TGA were synthesised and the concentration was determined from the first exciton absorbance peak. Their PL emission was highly tunable depending on the duration of the growth. Shell passivation enhanced the PLQY of the QDs significantly. HRTEM images showed that the mean QDs size was ~2.5 nm for 1 h core and 1 h shell growth. MCF7 cells were deformed through the cross-slot device in the shear dominated regime. The high viscosity of the cell suspension (~33 cP) caused the cells to stretch in a controlled manner at the extensional-flow junction at a low Reynolds number (Re <11). The human breast cancer cell line MCF7 cells were chosen for these initial experiments due to its

highly reducing cellular environment, which would be of importance in the redox-sensing, discussed in chapter 4. MCF7 cells remain viable to ~ 85% for flow rates up to 175 µl/min. However, the viability dropped when deformed in the presence of 100 nM QDs at higher flow rates. This suggests that there was increased uptake of QDs at higher flow rates as the particle toxicity increases. With the increasing flow rate, the DI of the cells increased up to Q = 125 µl/min, beyond which the change was insignificant. In spite of increasing the shearing force by the faster motion of the cell suspension, the degree of deformation did not change, which suggests that the cells opposed the deformation due to the shearing forces. This could be attributed to the combined action of the viscoelastic properties and cytoskeletons of the cells [181].

From the confocal images of the cells deformed with 100 nM QDs, it was observed that the uptake depends strongly on the flow rate. The QD uptake increased with the increasing flow rate of the cell suspension through the device. Although the degree of deformation of the MCF7 cells was not seen to change significantly at higher flow rates, the QD uptake increased, suggesting that other factors such as pore size, pore density and/or repair mechanism could be affected, which could be investigated in the future. Scatter plots for QD luminescence from the cells at different flow rates suggests the presence of the second mechanism of particle uptake in addition to the endocytosis.

From the ICP-MS analysis for the quantification of cadmium from the cells deformed with the QDs, it was observed that the average number of QDs delivered to the cells is in the order of a few million. The number of QDs/cell increased for higher flow rates (100 and 150 µl/min) but remained similar to the incubated cells for deformation at a lower flow rate (50 µl/min). The SD arising in the number of QDs/cell from the distribution of QD size was significantly large and the experiment needs to be repeated to have confidence in the data. STEM images of the cell sections confirmed the non-endocytic uptake of the QDs using the deformation in the cross-slot microfluidic device. The QDs diffused through the membrane disruptions and were scattered in the cytoplasm, free from endosomes. This result can be suitable for the non-endosomal delivery of many cytosolic sensors through a method that is vector-free, reliable and reproducible. Additionally, there was evidence of QD dispersed in the nucleus. Hence, there is a potential for intra-nuclear delivery and sensing using the cross-slot microfluidic cell deformation.

4. Redox-sensing in live cells by Quinone conjugated QDs

Many of the cellular processes depend on its redox state. Redox regulation is vital in understanding the health of the cells. In breast cancer cells the redox state is indicative of the degree of malignancy and sensing the redox in live cells can provide information in understanding the progression of the disease. In this chapter, the non-endocytic delivery of redox-sensitive RA-QDs into the cytoplasm of breast cancer cells using deformation by the cross-slot microfluidic device is discussed. The RA-QDs were made by conjugating a quinone ligand on the CdTe/CdS core/shell QD surface. They are found to be PL-quenched in the oxidised form of the quinone (Figure 1-19). However, the quenching is reversed when the quinone is reduced. Hence, the QD emission is sensitive to the oxidation-reduction of the quinone, making it suitable for redox sensing in cells. Breast cancer cells with different reducing cytoplasmic environments (ER+ cells: MCF7 and T47D; ER- cells: MDA-MB-231) were chosen along with a non-malignant breast epithelial cell line, MCF10A. The viability of each of the cell lines was tested for varying concentrations of both QD and RA-QDs. The luminescence of the RA-QDs in the cells was studied in comparison to the cells with QDs having no quinones for uptake at different flow rates through the cross-slot microfluidic device. Using confocal microscopy, a comparison was made between different cell lines on how the RA-QDs can sense the redox states. To investigate the response of the RA-QDs from cells with the chemical alteration of the redox state, the cells were treated with AAPH to generate ROS. This permitted the monitoring of the change in the cells' redox potential in response to external chemical stimuli.

4.1. Redox active QDs

The RA-QDs were prepared according to the method described in section 2-2. The quinone ligand (Figure 2-3) binds to the CdTe/CdS QD surface through the formation of a thiolate bond between the Cd and the S on the ligand. The resultant QD surface has a mixed population of Q2NS and TGA ligands. It is expected that the number of Q2NS molecules per QD follows a Poissonian distribution. The electron-accepting Q2NS ligands in their oxidised state have the capability of capturing the conduction band electron in an ultrafast process (2-8 ps) [45]. The

electron gets excited to the conduction band by the absorption of the sufficiently energetic incident photon. This electron gets rapidly captured by the oxidised quinone, mediated through a surface electron trap state, in a process that can outcompete the band-edge cooling, radiative and non-radiative recombinations (Figure 1-19a). The electron ultimately recombines with the valence band hole in a non-radiative process. As such, the PL emission of the QD is quenched, effectively switching The QD "OFF".

Figure 4-1 shows that the quenching efficiency increased with the increasing Q2NS:QD molar ratio. With Q2NS:QD = 1:1, it was observed that the integrated PL emission dropped to nearly half and a further increase in the Q2NS made quenching more significant. At the 10:1 ratio and beyond, the quenching was >99% and was considered that the QD had been switched 'OFF'. The increasing number of Q2NS on the QD surface improved the chance of electron capture. Further increase in the quinone quantity lowered the QD emission but the difference became smaller. Also, a further addition to the number of quinone ligands to the QDs would be difficult due to the steric hindrance in the arrangement of these ligands on the QD surface as Q2NS are much larger than the TGA ligands. The PL emission peak of the RA-QDs showed a blue shift with increasing Q2NS ligands (Appendix 9.5). This is because the longer wavelength emitting larger QDs can accommodate more Q2NS ligands compared to the smaller QDs. Hence, the quenching of the larger QDs was more efficient.

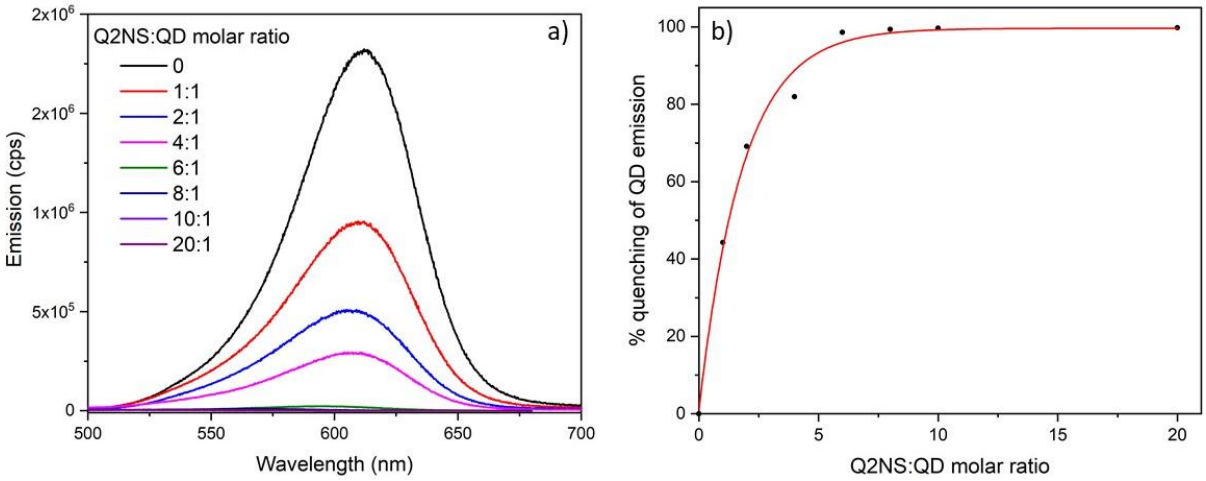

Figure 4-1. The effect on the fluorescence emission of the CdTe/CdS QDs with the increase in the Q2NS ligands. a) PL emission spectra showing a drop in the total emission intensity of the QDs with increasing Q2NS. b) Percentage change in the quenching of the QD emission as a function of the Q2NS:QD molar ratio. The data points are fitted with an exponential decay curve (R^2> 0.99).

The PL lifetime decay curve of the QDs changed significantly with the addition of these quinone ligands (Figure 4-2). The RA-QDs showed a better tri-exponential fitting (τ_1 = 0.37 ± 0.07 ns, τ_2 = 1.9 ± 0.1 ns and τ_3 = 10 ± 1 ns) with the quinones as compared to the biexponential fit for the QDs (τ_1 = 1.7 ± 0.9 ns, τ_2 = 11 ± 1 ns) (Exponential fit R^2 values- QD mono: 0.982, bi: 0.993; RA-QD mono: 0.98, bi: 0.985, tri: 0.999). This shortest lifetime component for the RA-QDs refers to the ultrafast transfer of electrons to the quinones mediated by the 'hot' surface trap states. The remaining longer lifetime decay components correspond to the surface trapping of the electrons and the radiative recombination, which are similar to the case of the QDs without the quinones.

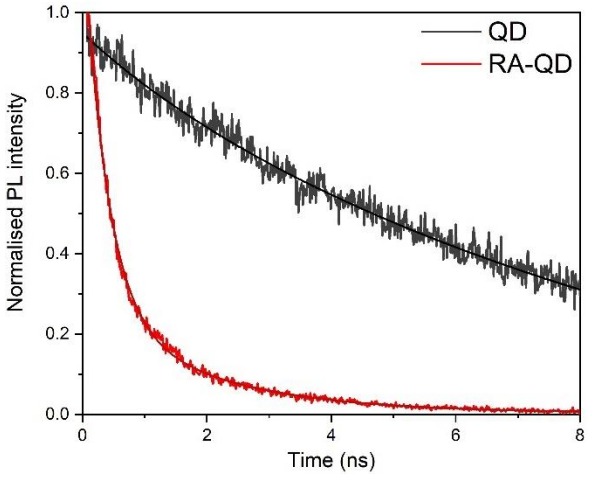

Figure 4-2. PL lifetime decay curves for the QD and redox-sensitive RA-QDs in the oxidised form for Q2NS:QD = 20:1 molar ratio. The black line for the QD curve represents the bi-exponential fit and the red line for the RA-QDs is the tri-exponential fit (R^2 >0.99).

The quenching of the QDs is reversible when the quinones are reduced using a concoction (10% w/v sodium dithionate and 10% w/v sodium ascorbate) of strong reducing agents [45]. In the reduced form of the quinones, the rapid electron trapping mechanism through the hot trap state is no longer available, as such, the radiative electron-hole recombination was restored with PL emission. Hence, effectively the RA-QDs were switched back "ON" (Figure 1-19b). It was also observed that the fluorescence emission intensity of the RA-QDs was higher with a red-shifted peak on reduction. In addition, the lifetime is also longer suggesting that the particle emission is more stable after reduction. This could mean that following the reduction of the quinone ligands, the electron-hole recombination becomes more efficient, suggesting that the quinone ligands have a role in quenching the surface traps. It is difficult to understand

how the different ligands arrange themselves on the RA-QD surface. It could be understood that there is ligand exchange where some of the TGA is replaced with Q2NS. Hence, there is a mutual accommodation of these ligands eliminating more surface traps, which needs to be confirmed with further investigations.

The PL emission switching behaviour of the RA-QDs depending on the redox state of its quinone ligand is suitable for studying the redox state in live cells. For the RA-QDs experiments in cells, Q2NS:QD molar ratio of 20:1 was chosen with >99% PL emission quenching in the oxidised form of the quinone.

4.2. Cyclic Voltammetry of the RA-QDs

The reduction potential of the RA-QDs was measured according to the method described in section 2.10 to estimate the LUMO level of the oxidised Q2NS. Q2NS:QD at a molar ratio of 20:1 sample were prepared in HEPES buffer (pH 7.2, 50 mM) and incubated with the electrode for 1 h. The particles were immobilised on the gold electrode electrostatically due to the interaction of the negatively charged TGA on the QD surface and the net positive charge from the self-assembled monolayer of 6-mercaptohexanol and 6-amino-1-hexanethiol on the electrode (Figure 2-10). The potential was scanned both forward and backward (as seen by the multiple numbers of curves in Figure 4-3a) at a controlled rate (50 mV/s). The chemical reversibility denotes the stability of the particles on reduction and subsequent oxidation [248]. The reduction potential of RA-QD was calculated at -0.59V vs mercury/mercurous sulphate electrode, which corresponds to 50 mV vs SHE. The control QDs having no quinones, prepared in the same manner did not show the presence of the oxidation and reduction peaks, unaffected by the treatment and hence unable to sense the redox state in cells. Converting The redox potential to the vacuum level, the estimated LUMO of the Q2NS is at -4.55 eV. This value lies within the bulk bandgap of both CdTe and CdS as shown in Figure 4-3b. The bandgaps will be wider for QDs compared to the bulk materials. Hence, the Q2NS ligand behaved as the electron-accepting ligand, which captured the excited electrons from the conduction band of the QD donor.

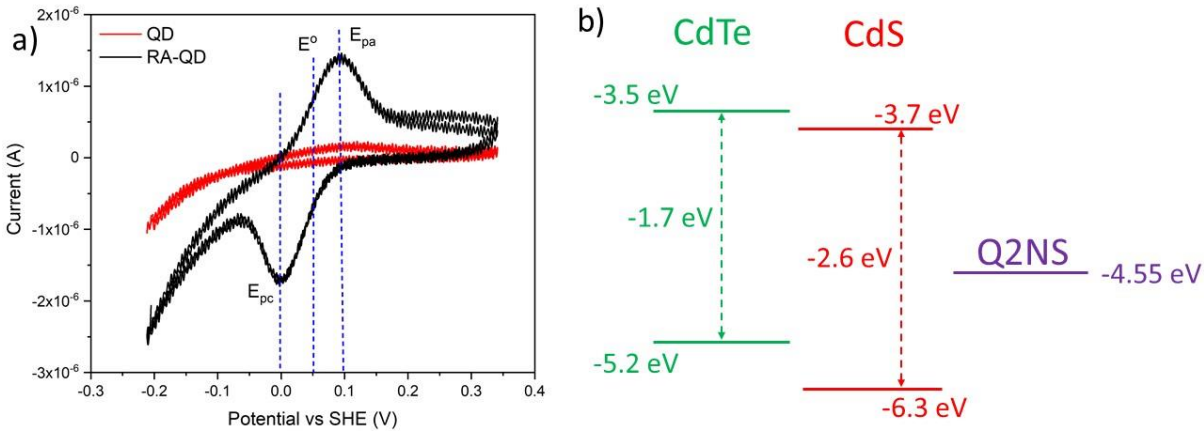

Figure 4-3. a) Cyclic voltammogram of the QDs and RA-QDs (Q2NS:QD = 20:1 molar ratio) obtained vs mercury/mercurous sulphate electrode, shown as vs standard hydrogen electrode. E^o is the reduction potential, E_{pc} and E_{pa} is the cathodic and the anodic peaks, respectively. b) Comparative band structure alignments of the bulk CdTe and CdS with the LUMO of Q2NS.

4.3. Uptake and response to RA-QDs by MCF7 cells

As mentioned before, the MCF7 cells are ER+ breast cancer cells having a higher reducing cytoplasmic environment compared to other breast cancer cells. As such, this cell line was chosen for the preliminary experiments to study the effect on the luminescence of the quenched RA-QDs through non-endocytic microfluidic delivery. These cells should have a higher capacity to reduce the RA-QDs to restore the photoluminescence. RA-QDs were prepared as described before with the molar ratio Q2NS:QD of 20:1. The PL emission of the QDs was quenched with the total intensity dropping by ~99%, confirmed by PL spectroscopy (Figure 4-4a). 100 nM quenched RA-QDs were delivered to the MCF7 cytoplasm by cross-slot microfluidic deformation at a flow rate of Q = 100 µl/min and the confocal images were taken for the cells suspended in DMEM culture medium as described in section 2.5.4.

The images showed that the quenched RA-QDs were switched "ON" inside the cells (Figure 4-4b). This show that the quinone ligands were reduced, preventing the rapid capture of excited electrons from the conduction band by the ligand. This allowed the recombination of the electron-hole pair, restoring the PL emission of the QD. The reduction of the quinone ligand shows that the RA-QDs are interacting with and hence sensing the reducing environment of the cell.

The unquenched QDs without the quinones were also deformed with the cells in the same manner for comparison. The images were analysed using MATLAB as described in section 2.6.1. and 3.5. For the cells incubated (no deformation) with RA-QDs, it was seen that the fluorescence emission from the cells was comparable to the cells with QDs incubated at the same conditions (Figure 4-4c). This implies that the endocytic uptake of the RA-QDs also reduced the quinone ligands. The scatter plots of total integrated PL emission from cells with cell area for this dataset is provided in Appendix 9.7. Studies have shown that the endosomes show acidic pH in live cells [266–268]. As such, the endosomes possess the capability to reduce the quenched RA-QDs. The cells deformed with RA-QDs showed higher luminescence than the incubated cells, suggesting these particles are interacting with the reducing cytosol, in addition to the endosomal reduction. Evidence of both forms of uptake can be seen in the confocal images with the presence of aggregated and diffused emission (figure 4-4b and Appendix 9.8).

It was observed that the quenched RA-QDs appeared more luminescent than the unquenched QDs on cell deformation uptake (Figures 4-4d, Appendix 9.7 and 9.8). This could be due to the enhancement of the fluorescence emission of the RA-QDs on reduction as seen spectroscopically, reported earlier by Harvie *et al.* [45]. Additionally, there could be preferred surface trap passivation in the cellular environment for the RA-QDs, which would need further investigation.

Since the RA-QDs are switched 'ON' inside the cells giving higher luminescence by deformation uptake, this strongly supports that there is non-endosomal interaction of the RA-QDs with the cytosol. This establishes new possibilities for live cell cytoplasmic sensing through deformation uptake of functional nanomaterials. The sensing capability of the RA-QDs in the reducing cellular environment would be suitable to compare between cells having different redox environments.

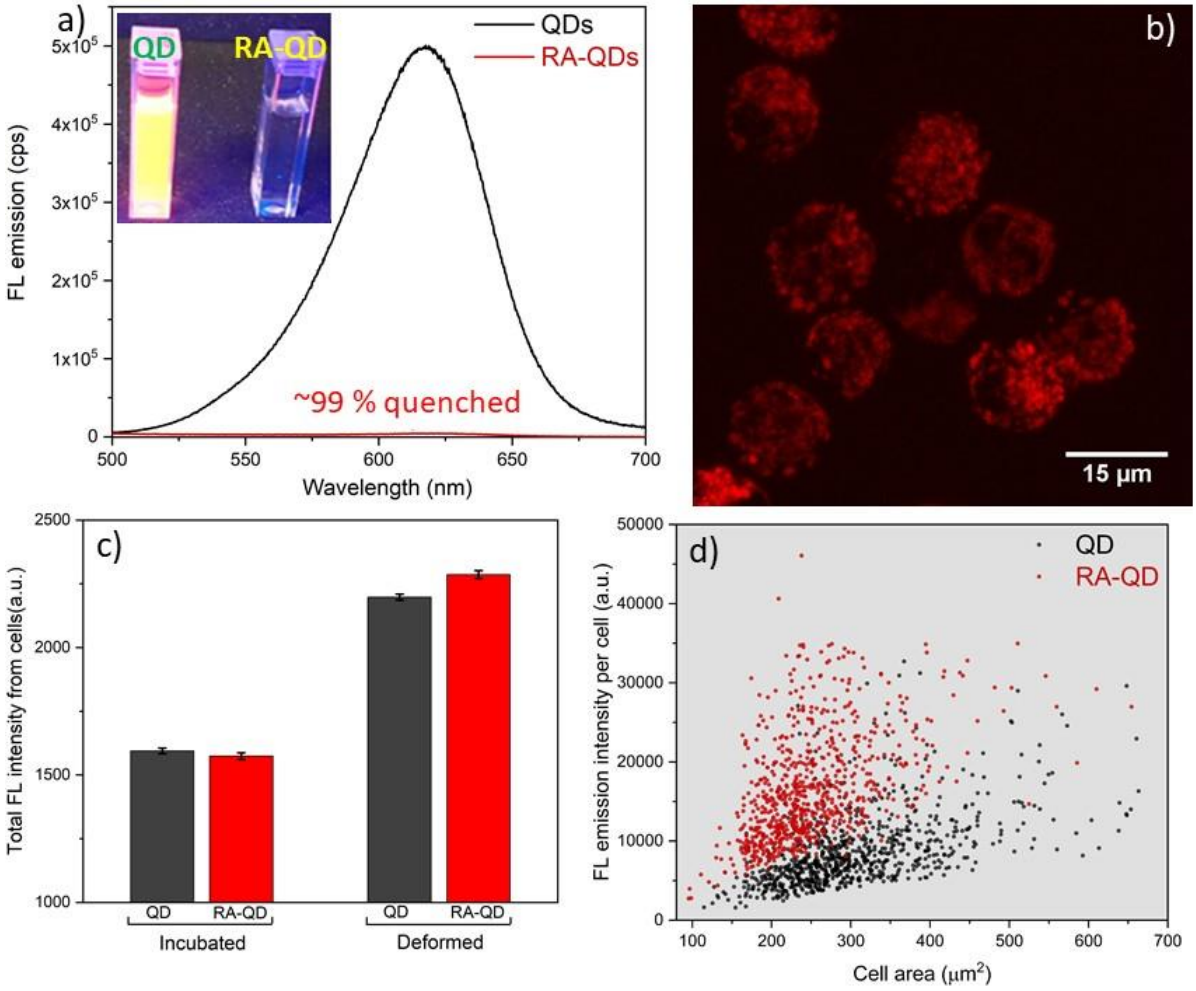

Figure 4-4. The uptake of quenched RA-QDs by MCF7 cells. a) PL emission of QD and RA-QD (molar ratio Q2NS:QD =20:1) with figure inset showing the same under UV light, b) The confocal images of the cells with the quenched RA-QDs showing the restoration of the QD emission after reduction of the quinone ligands in the cells, c) the relative mean PL intensity emission of the cell incubated or deformed with 100 nM QD/RA-QDs (data expressed as mean ± SE) and d) relative scatter plots of the total PL emission intensity from the cells deformed with 100 nM QDs and RA-QDs at Q = 100 µl/min.

4.4. Viability of different cell lines deformed with QDs and RA-QDs

Different cells lines have different levels of redox state in the cytoplasm. Breast cancer cells are of particular interest depending on the presence of estrogen receptors (ER). These proteins bind to the hormone estrogen that could promote the growth of the cells and their presence can affect the reducing environment of the cytosols. ER+ cells such as MCF7 and T47D show higher reducing cytoplasm, whereas ER- cells like MDA-MB-231 show relatively lower reduced state which is regulated by the redox couples (NADH/NAD^+, NADPH/$NADP^+$, and GSSH/2GSH).

In comparison, the non-malignant breast cell line MCF10A have further low reducing cytosol [206]. To investigate the sensing capability of the RA-QDs for the reduced state of the cells, it is essential to observe their photoluminescent behaviour in these different cell lines.

Before proceeding with the redox-sensing of these cells, it was necessary to test the viability of these cell lines with both QD and RA-QD. As controls for each uptake experiment of the RA-QDs, uptake of QDs without the quinones was undertaken. The viability of the cells was tested with these two different QDs for 18 h incubation as a function of concentration (0.001-10 µM) as described in section 2.5.3. All measurements were compared to cells with no treatment, considered to be at 100% viability.

The viability as a function of concentration for both QD and RA-QD for different cell lines are shown in Figure 4-5. A dose-response curve was fitted to all datasets for consistency, with R^2 ranging between 0.88 to 0.98. The comparative LD_{50} of the different cell lines to the QDs and RA-QDs are presented in Table 4-1. For MCF7 cells, the viability remains above 70% for concentrations up to 0.2 µM for both particles, which dropped significantly on further increments. The LD_{50} for QD and RA-QD are 1.19 and 0.41 µM respectively, suggesting that the toxicity increases with the introduction of the quinone ligands for this cell line. However, for T47D cells, which is also an ER+ breast cancer cell line, the viability for RA-QDs was higher compared to the QDs, with LD_{50} = 3.2 µM for RA-QDs compared to 2.6 µM for QDs. Overall, the T47D cells seem to show better viability for both the particles compared to the other cell lines, suggesting it is more resistant to the particle toxicity. At 0.5 µM concentrations of RA-QDs, the viability of the T47D cells remained above 80% which was not observed for other cell lines. For the ER- cell line MDA-MB-231, the RA-QD showed significantly higher viability (>90%) compared to the QDs (~70%) at lower concentrations up to 0.2 µM. However, the viability rapidly dropped for RA-QDs with LD_{50} = 0.93 µM lower than that of QD at ~1.93 µM. The non-malignant MCF10A cells show more toxicity towards both the particles with viability not going over 80% for all concentrations. This cell line was most affected for particle toxicity; however, they are more viable at higher concentrations than the cancer cells (LD_{50} = 1.87 and 2.58 µM for RA-QD and QD, respectively).

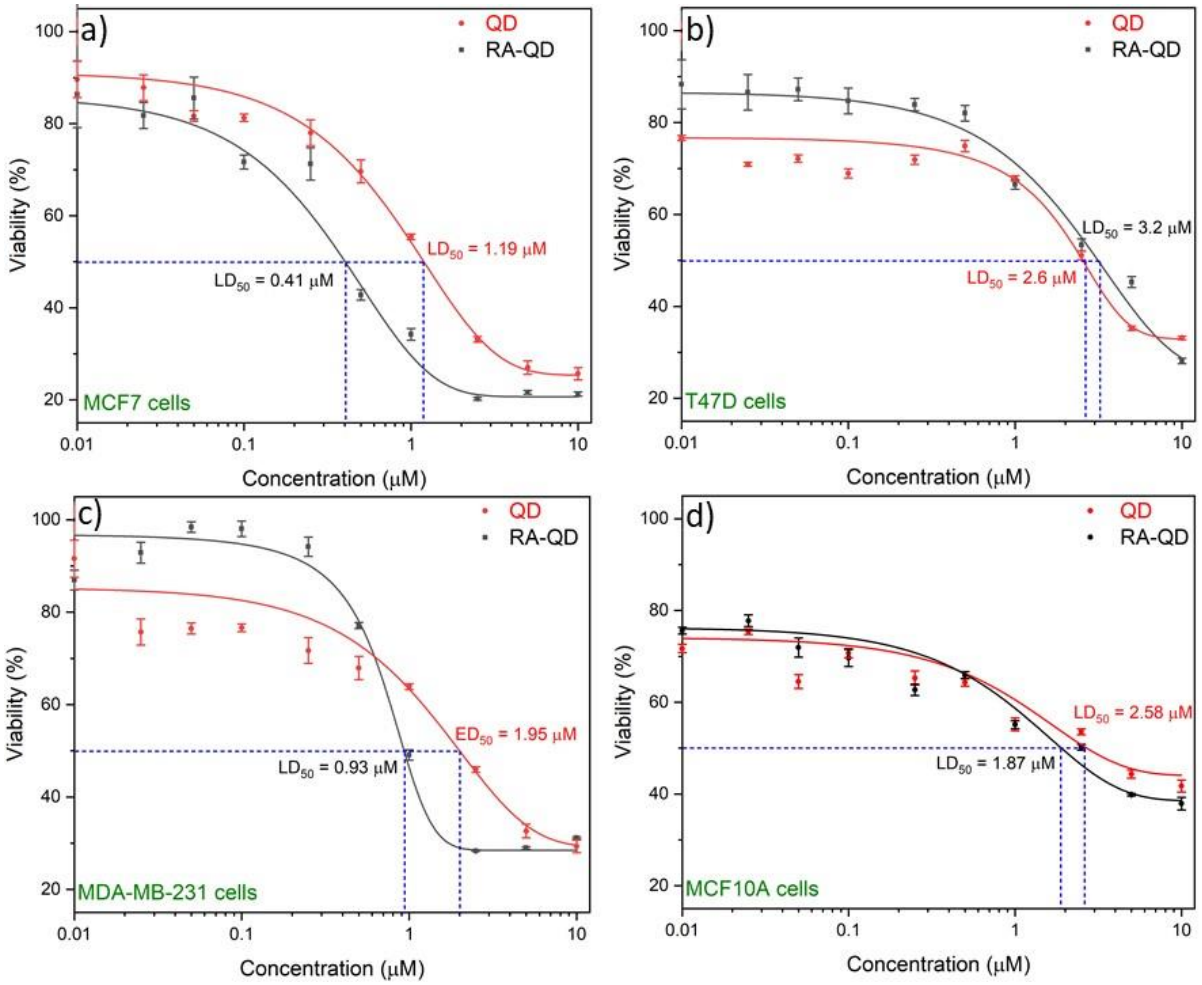

Figure 4-5. Comparative viability of cells as a function of concentrations of QDs and RA-QDs for a) MCF7 (b) T47D (c) MDA-MB-231 and (d) MCF10A cell lines. Data expressed as mean ± SE for N=3 repeats. The LD_{50} was estimated from the dose-response fitting (Red lines for QD and Black like for RA-QD). The R^2 for the fittings varied between 0.95 to 0.986.

Figure 4-6a shows comparative viability curves for all cell lines treated with QDs. The cancer cells show better viability compared to the non-malignant MCF10A cells at lower concentrations. A similar comparison was made for the viability of cells with RA-QDs as shown in Figure 4-6b. The fitted curves are more dispersed compared to the curves for QDs with no particular trend between cell lines. All further experiments with these different cell lines for both the QDs were performed at 100 nM concentration which is well below all the LD_{50} values.

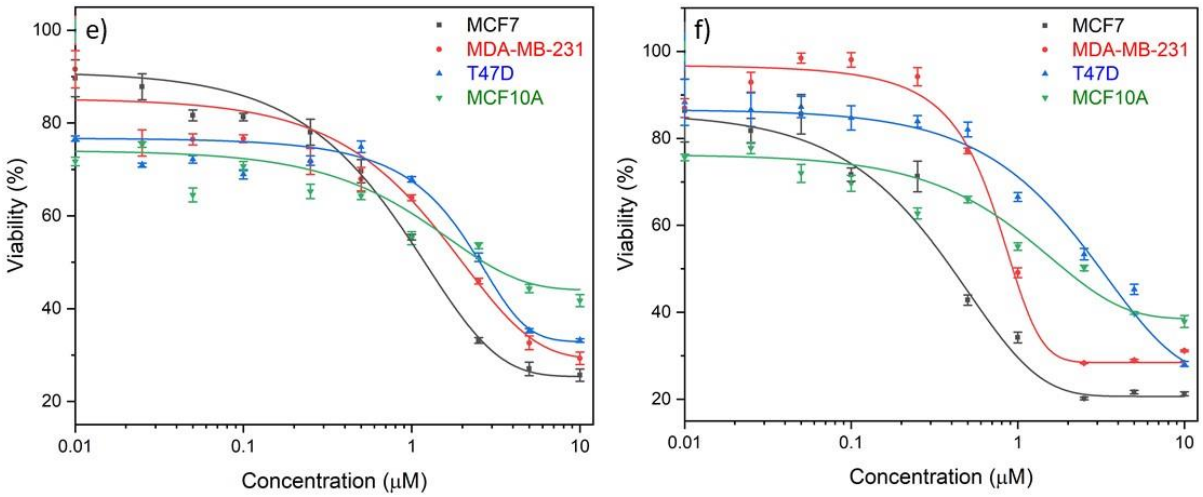

Figure 4-6. Viability of different cells with concentrations of a) QDs and b) RA-QDs Data expressed as mean ± SE for N=3 repeats. The LD_{50} was estimated from the dose-response fitting (Red lines for QD and Black like for RA-QD). The R^2 for the fittings varied between 0.95 to 0.986.

Cell line	LD_{50} (μM)	
	QDs	RA-QDs
MCF7	1.19	0.41
T47D	2.6	3.2
MDA-MB-231	1.95	0.93
MCF10A	2.58	1.87

Table 4-1. LD_{50} of the different breast cell lines for QDs and RA-QDs determined from the dose-response fittings as shown in Figure 4-5.

4.5. DI of the breast cell lines versus flow rate

The degree of deformation of the cells through the cross-slot microfluidic device would determine the degree of membrane disruption and consequently the uptake of particles. Hence, it is crucial to compare the deformations of the different cell lines for a better understanding of the uptake behaviour. The deformation indices of the cell lines were measured according to the method described in section 2.5.4 from the videos captured by the high-speed camera. Cells were deformed between 25 to 175 μl/min flow rate in the running buffer of DPBS with 0.5% (w/v) MC. The high-speed videos of the cells at the extensional-flow junction of the cross-slot microfluidic device revealed that the deformation behaviour of the

cell lines was similar except for the T47D cell line. The DI increased for MCF7, MDA-MB-231 and MCF10A cell lines with flow rate with their values plateauing at higher flow rates (Figure 4-7). Other than MCF7 showing more stiffness at lower flow rates, the exponential decay curve fitting for MCF10A and MCF7 cells suggests very a similar nature of deformations, with DI_{max} of 1.57 and 1.58 respectively (R^2 >0.98). This similarity in deformation is favourable as it helps in comparison of the QD uptake by these cell lines. The MDA-MB-231 cells show similar DI to MCF10A at lower flow rates. However, the DI slightly increases at Q = 175 µl/min with the exponential decay curve fitting showing DI_{max} = 1.63 (R^2 >0.97).

The T47D cell line, however, does not show an exponential growth of the DI at these flow rates. The curve fitting for this dataset is best represented by a linear fit (R^2=0.95). Moreover, the DI of these cells was much higher compared to the other cell lines, suggesting they are more stretchable, potentially leading to higher membrane porosity, subject to further investigations. The DI for T47D could plateau at higher flow rates >175 µl/min which was not undertaken for this current study. Scatter plots of DI as a function of the width (size) of the cells suggest that smaller cells tend to deform more for all cell lines (Figure 4-8). Larger cells show higher resistance to deformation potentially due to a larger cytoskeletal network.

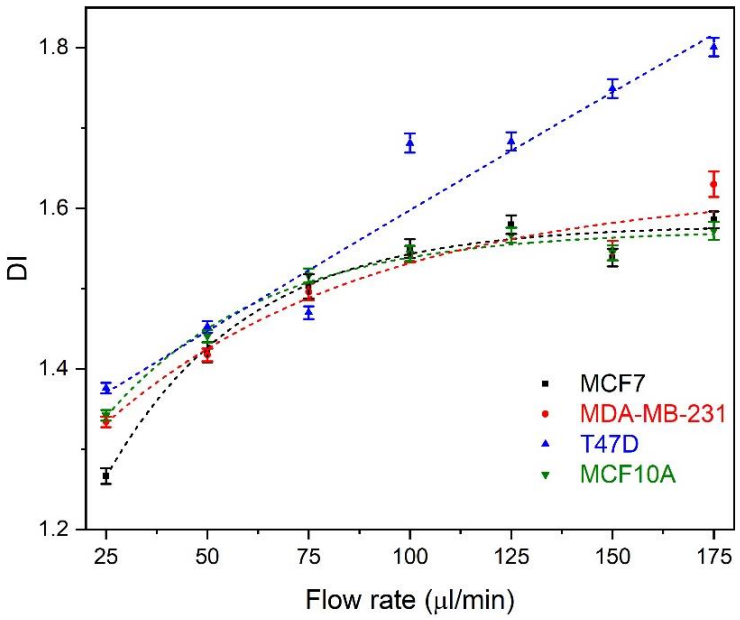

Figure 4-7. DI of the different breast cells lines as a function of the flow rate of the cell suspension through the cross-slot microfluidic device (µ ~33 cP). The curve fittings are exponential decay for MCF7, MCF10A and MDA-MB-231 cells and linear for T47D cells. Data is expressed as mean ± SE with N repeats= 3 and each data point having >200 cells.

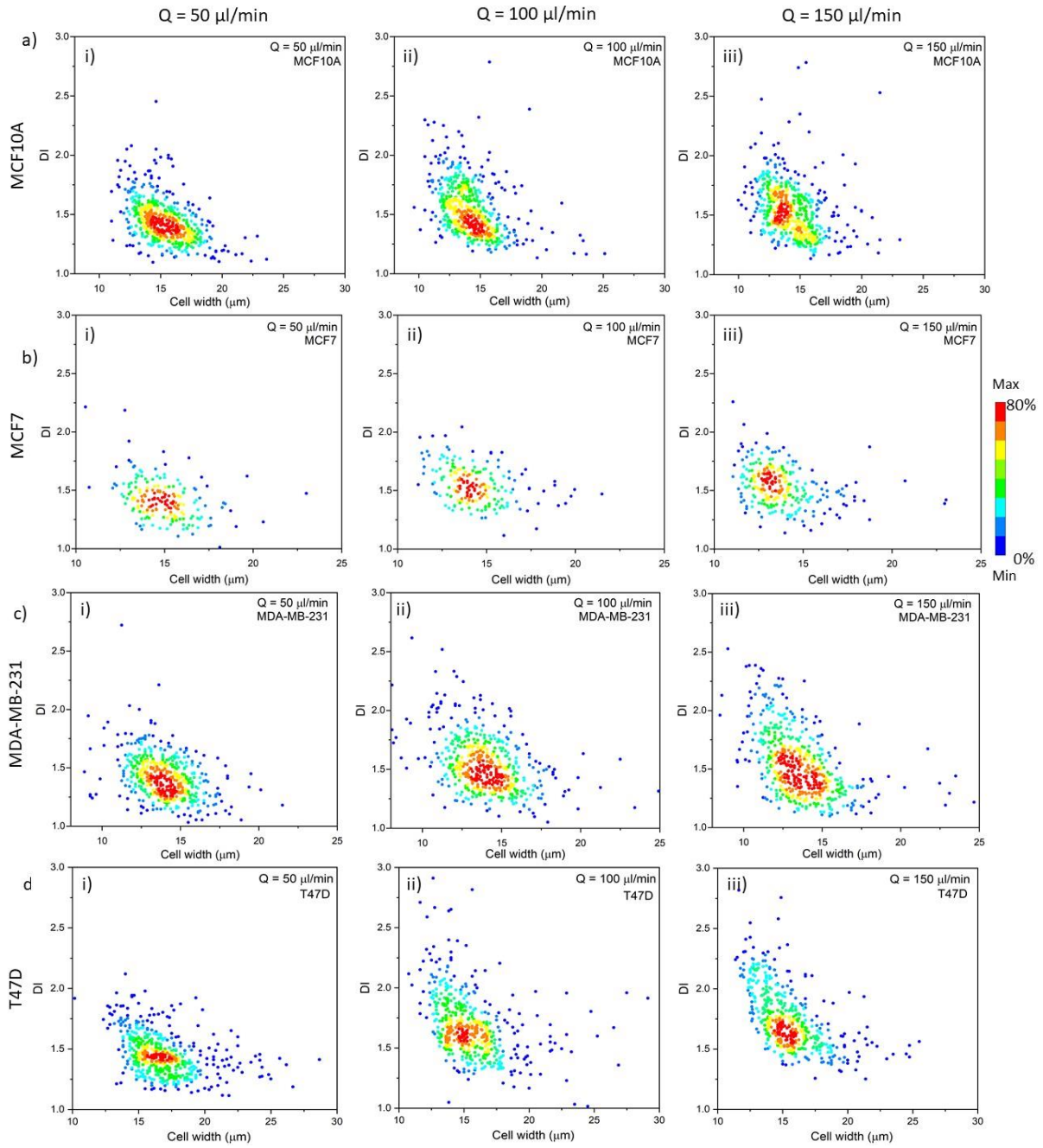

Figure 4-8. Scatter plots for the DI of the different cells lines with the width (size) of the cells for a) MCF10A, b) MCF7, c) MDA-MB-231 and d) T47D cells for Q = i) 50, ii) 100 and iii) 150 µl/min flow rates of the cell suspension through the cross-slot microfluidic device. N = 3 repeats with each sample having >200 cells in total.

4.6. Comparative photoluminescence of Redox QDs from different cell lines

As seen from section 4.3, the quenched RA-QDs are capable of switching "ON" when the Q2NS ligand is reduced, demonstrating that they are sensitive to the redox environment in cells. Here, we put the RA-QDs to test, as to whether it is capable of sensing the difference in the redox states of different live breast cancer and one non-malignant cell lines. To study the luminescent response of RA-QDs in different cells, cross-slot microfluidic deformation was performed at different flow rates in the presence of 100 nM RA-QDs as described in section 2.6.1. The cells in suspension were imaged using the confocal microscope and the total integrated PL emission from the cells were measured using MATLAB as described earlier in section 2.6.1. and 3.5. As a control for the redox response from cells through the uptake of RA-QDs and its photoluminescence, cells were also deformed with QDs having no quinone ligands, imaged, and analysed in the same manner.

In Figures 4.9 and 4.10, luminescence from cells deformed with either QD or RA-QDs have been expressed as the percentage change in the mean total fluorescence intensity, which is the increase in the emission from the cells as compared to the control cells (Q =0 µl/min) incubated with the respective particles for the same duration. The emission of both RA-QDs and QDs increased with the flow rates for all cell lines. This is expected as with the increasing flow rate, the deformation increases leading to an increase in membrane porosity. Higher deformation allows for more particle diffusion into the cells as established from our previous results. The ER+ cell lines (MCF7 and T47D) showed higher relative photoluminescence for the RA-QDs with increasing flow rates, suggesting that the quenched RA-QDs are efficiently switching 'ON' (Figure 4.9). Similar to the observation in section 4.3, the RA-QD displayed higher fluorescence emission compared to their QD counterpart from the MCF7 cells. The other ER+ cell line, T47D also showed similar enhanced photoluminescence for RA-QDs in comparison to the QDs. Hence, the quinones are more efficiently reduced for these ER+ cells and the QD emission was restored. As mentioned earlier, the increase in the RA-QD emission on reduction in comparison to the QDs was also reported spectroscopically [45]. The MCF7 cells show similar uptake and luminescence of RA-QDs and QDs for flow rates up to Q = 100 µl/min (figure 4.10a). However, at Q = 150 µl/min, the RA-QD emission was significantly higher (~48%) compared to the QDs, suggesting that the reduction of the RA-QDs was more efficient at higher shearing stress on

the cells. However, there is not enough evidence to support this theory and require further detailed examination. T47D cells showed significantly higher relative luminescence from the RA-QDs (Figure 4.12b). This correlates with the higher DI of T47D cells compared to other cell lines. This suggests that T47D cells have higher particle uptake potentially due to higher membrane porosity, subject to further investigations.

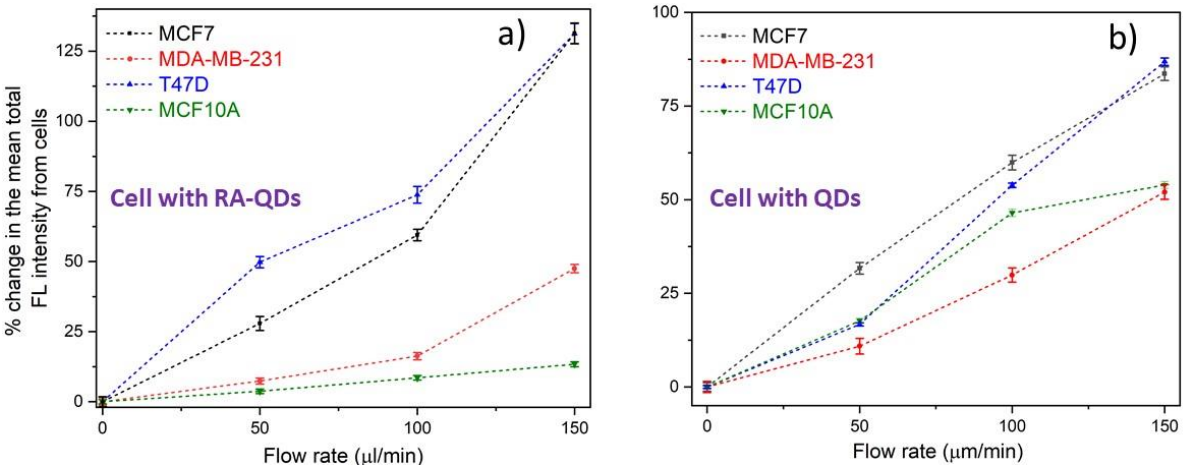

Figure 4-9. Comparative percentage change in the total fluorescence emission intensity using confocal images of the cells in suspension for different cells lines with flow rates through the cross-slot microfluidic device for cells deformed with 100 nM a) RA-QDs and b) QDs. Data represented as mean ± SE for N = 3 repeats for each data point having a total of >5000 cells.

The ER- cell line, MDA-MB-231 showed relatively lower fluorescence emission from the cells with RA-QDs compared to the ER+ cells (figure 4.9). Their luminescence was also lower compared to the same cells deformed with QDs under the same conditions (Figure 4.10c). This suggests that the quinone ligands on the QDs surface are not fully reduced in the MDA-MB-231 cells. The relatively lower reducing environment in these cells compared to the ER+ cells may not be sufficient to efficiently reduce the quinones, as such the RA-QD emissions are not fully restored.

The non-malignant cell line MCF10A showed the lowest PL emission upon deformation uptake of the RA-QDs (Figure 4.9). The cytoplasm of these benign cells is less reducing than that of the cancer cell lines. Hence, their quinone reducing capability is low and the emission of the RA-QDs were not fully restored. MCF10A cells deformed with control QDs showed relatively higher PL emission compared to the RA-QDs under the same conditions, suggesting that the reduced

luminescence of RA-QDs was the consequence of inadequate quinone reduction (Figure 4.10d). From these results, it can be seen that RA-QDs are sensitive to the difference in the redox state of the live cells.

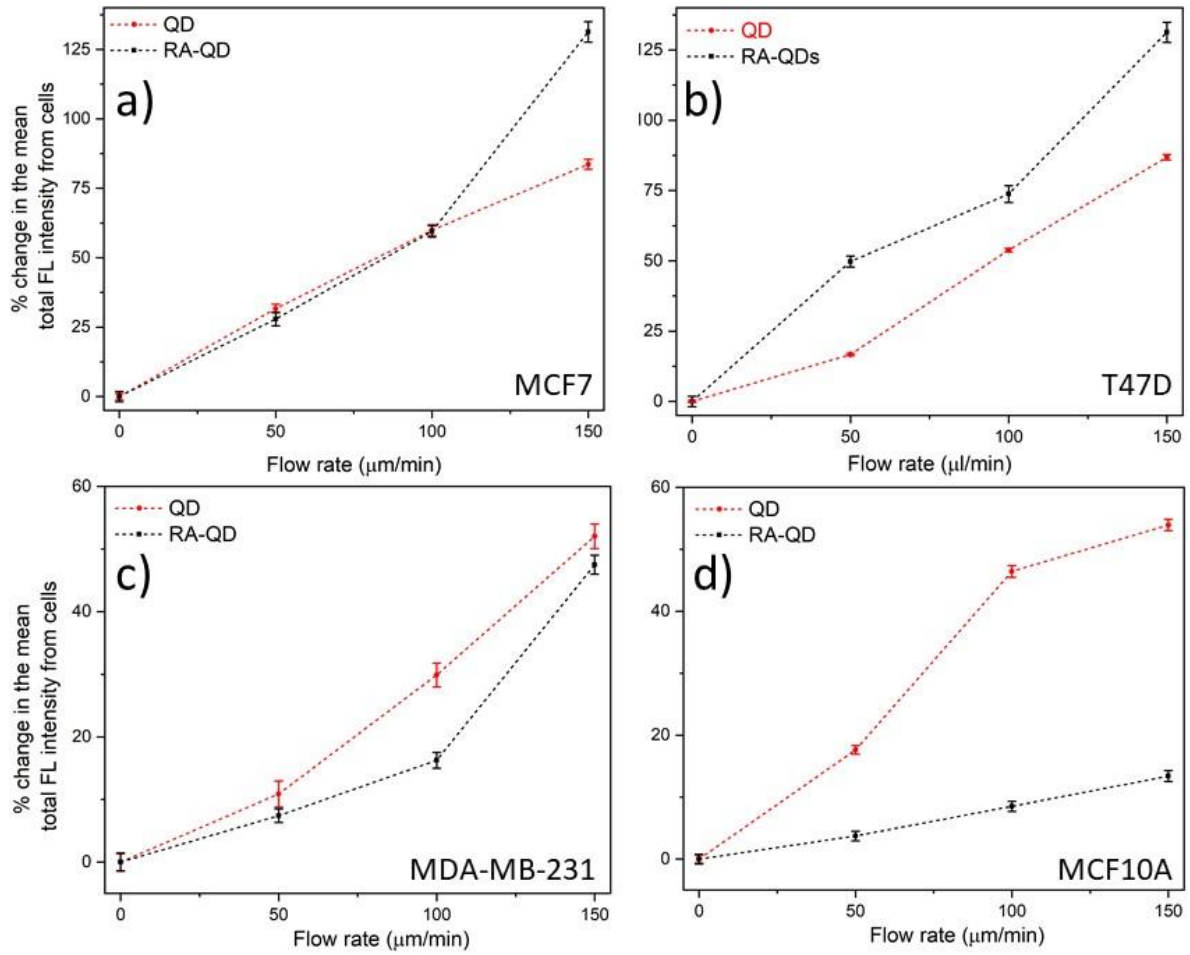

Figure 4-10. Comparative percentage change in the total fluorescence emission intensity using confocal images of the cells in suspension deformed with 100 nM QDs/RA-QDs with flow rates of the cell suspension through the cross-slot microfluidic device for (a) MCF7 (b) T47D (c) MDA-MB-231 and (d) MCF10A cell lines. Data represented as mean ± SE for N = 3 repeats for each data point having a total of >5000 cells.

For imaging adhered cells, the different cell lines were treated with 1µM Hoerscht 33342 (nuclear stain, Thermofisher) and 1 µM mitotracker green (for mitochondria staining, Invitrogen) for 30 min as described in section 2-13. The cells incubated and deformed at 100 µl/min with RA-QDs were washed and adhered in 8-well incubation chamber (Lab-Tek II, VWR International) pre-treated with 1 µM poly-L-lysine. They were incubated for 24 h at 37 ^{o}C with

5 % CO_2 atmosphere with their respective culture media. The confocal images of the cell show the distribution of the RA-QDs in adhered cells with respect to the nucleus and the mitochondria (Appendix 9-10).

4.7. Redox alteration with AAPH treatment

With establishing the efficient sensing of cellular redox state by RA-QDs, delivered through cell deformation, it is now essential to study how these particles respond to the chemically-induced change of the cellular redox state. It is known that the treatment with AAPH induces oxidative stress by generating ROS [269,270]. As such, the cytoplasmic redox potential changes significantly with AAPH treatment, as reported previously using a different nanosensor [271]. The MCF7 cells were deformed with 100 nM RA-QDs at Q = 100 µl/min through the cross-slot device. The cells were imaged using a confocal microscope for 30 min to account for any fluctuation in the PL emission. AAPH was added to the cell suspension to a final concentration of 30 mM and further imaged for ~30 min. The total fluorescence intensity from the cells were measured using the MATLAB script described in section 2.6.1. and 3.5.

With the AAPH treatment, the luminescence of RA-QDs from the cells dropped rapidly (within ~1 min) indicating a significant change in the cytoplasmic redox potential (Figure 4-11a). The total mean PL intensity dropped by ~32% and became steady with time (~15 min post-treatment). For the deformed cells, the drop in the PL emission is attributed to the effect of AAPH on both endosomal and cytoplasmic RA-QDs. As a control to the experiment, MCF7 cells were subjected to the same treatment without deformation, in which they were simply incubated with RA-QDs for the same duration. For these cells, it was observed that the drop in RA-QD luminescence was even higher (~38%). This implied that the AAPH treatment seems to affect the endosomal redox state more significantly than the cytoplasmic redox potential. Also, in both cases, it was observed that the PL-emission dropped in stages which could imply that the ROS generated by the AAPH treatment occurs in stages and can be investigated further in detail.

To confirm that RA-QDs' response to the AAPH treatment is due to the changes in the redox state of the cells, control experiments were performed where the cells were subjected to a

similar treatment using QDs without quinones. We observed that the QD emissions dropped a maximum of 8.6% and 9.55 % for deformed and incubated cells, respectively (Figure 4-11b). Although there is a drop in the photoluminescence of the QDs on AAPH treatment, it is not as significant as in the case of the cells treated with RA-QDs. This suggested that the response in the drop of RA-QDs luminescence from the cells was attributed to the change in the redox potential of the cells. The drop in PL emission of QDs in cells with AAPH treatment could be speculated as the effect of the ROS generated in the cells to alter the passivating capacity of the TGA ligands.

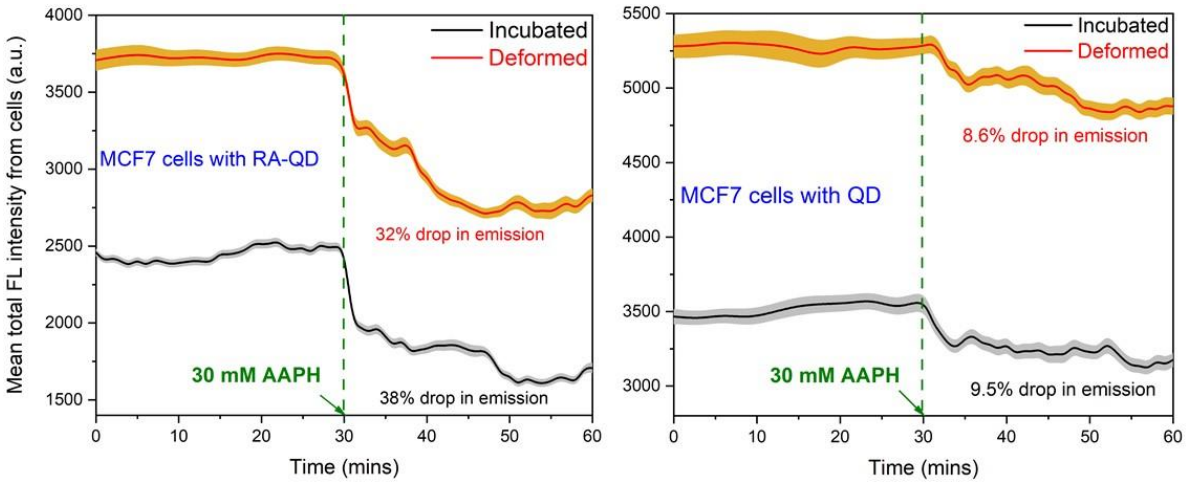

Figure 4-11. Mean fluorescence emission intensity using confocal images of MCF7 cells in suspension over time with 30 mM AAPH treatment for cells treated (deformed/incubated) with 100 nM a) RA-QDs and b) QDs. Data represented as mean ± SE for >1000 cells for each dataset.

To compare the behaviour of RA-QDs in non-malignant cells with cancerous MCF7 cells, MCF10A cells with RA-QDs were subjected to a similar AAPH treatment are described earlier. It was observed as shown in Figure 4-12, that the drop in the emission from the cells was much higher in the deformed cells than the incubated cells (46.8% and 36.9%, respectively). This suggests that the AAPH affects the cytoplasmic redox more than the endosomes of the non-malignant cells. Additionally, the stepwise drop in the PL-emission as seen for the MCF7 cells was not observed in the case of MCF10A cells. Although the cells remained alive, their health was compromised for the observed duration with noticeable blebbing. The non-malignant MCF10A cells are not as robust or resistant to ROS generation by AAPH as the carcinogenic MCF7 cells.

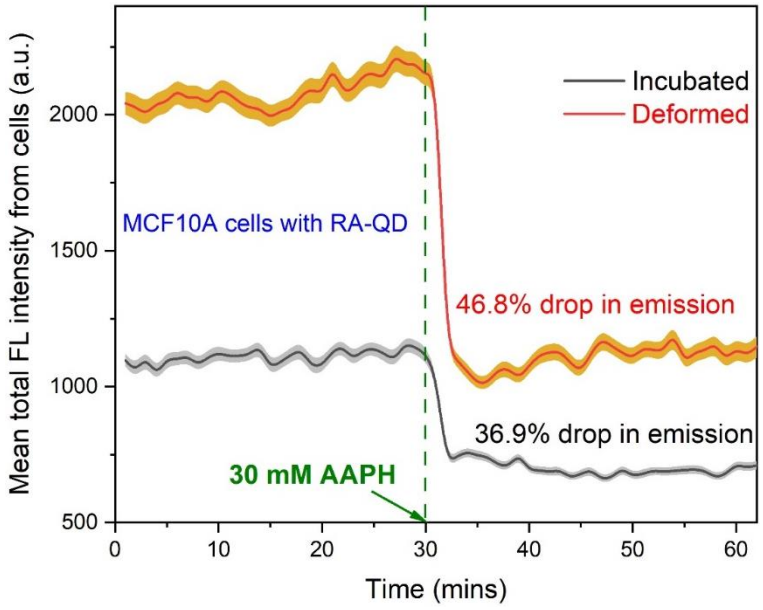

Figure 4-12. Mean fluorescence emission intensity using confocal images of MCF10A cells in suspension over time with 30 mM AAPH treatment for cells treated (deformed/incubated) with 100 nM RA-QDs. Data represented as mean ± SE for >1000 cells for each dataset.

4.8. Concluding remarks

In this chapter, the quinone ligand-based RA-QDs was used for sensing the reducing cellular environment of human breast cells. The RA-QDs delivered in the cytoplasm using the cross-slot microfluidic deformation can effectively make comparisons between the different redox states of various breast cancer and non-malignant breast cell lines. RA-QDs can also detect the chemically-induced change in the cytoplasmic redox state of the cells.

The RA-QDs were prepared by introducing a quinone ligand Q2NS on the QD surface. The Q2NS in the oxidised form can rapidly capture the excited electrons in the conduction band, effectively switching 'OFF' the PL emission of the QDs. The quenching of the QDs depended on the number of quinone molecules on its surface showing ~99% drop in photoluminescence for the molar ratio of Q2NS:QD = 10:1 or higher. The quinone in its oxidised form rapidly captured the excited conduction band electrons via a 'hot' surface trap state. This electron capture process was faster than the radiative recombination, as such quenching of the QD emission occurred. The redox potential of the RA-QDs was 50 mV vs SHE, measured using cyclic voltammogram which is in the range of the cellular redox levels. The LUMO of the oxidised

Q2NS lie within the bandgap of the bulk CdTe and CdS, which established its role as an electron acceptor for the QD quenching. The quenching was, however, reversible and was restored when the quinone was reduced [45]. The reduced form of the quinone no longer had the rapid electron capture mechanism and the RA-QDs is switched back 'ON'. This reversible switching of the RA-QDs was suitable for redox sensing in live cells.

The RA-QDs were delivered into the MCF7 cells through cell deformation in the cross-slot microfluidic device. These quenched QDs were switched 'ON' inside the cells showing that they interact with the reducing cellular environment. Endocytically delivered RA-QDs through incubation also restore their emission, demonstrating that the endosomes have reducing acidic pH. The luminescence was higher for cells that were deformed compared to the cells incubated with RA-QDs which was due to the uptake through non-endocytic diffusion of particles in addition to the endocytic uptake. This shows that the RA-QDs, freely dispersed in the reducing cytoplasm are also switched 'ON'. Hence, cytoplasmic redox sensing was achieved through cell deformation uptake of RA-QDs.

To compare the redox state of different breast cancer cell lines, firstly, the viability of the cells as a function concentration of RA-QDs and control QDs were tested. The non-malignant MCF10A breast cells showed higher toxicity (viability <80%) for the particles at 18 h incubation, however, its LD_{50} (1.87 µM) was higher compared to MCF7 and MDA-MB-231 breast cancer cell lines (0.41 and 0.93 µM, respectively). T47D cells showed high cell viability for both particles suggesting it was comparatively more resistant to QD toxicity. This was performed to confirm that the concentrations of the QDs and RA-QDs used for the investigations are well within the accepted limits of the cell viability. The cellular uptake experiments were conducted within 30 min at 100 nM QD/RA-QD concentration, during which the cells remained healthy.

From the DI measurements of the different cell lines as a function of flow rate through the cross-slot microfluidic device, it was observed that the degree of cell deformations for MCF7, MDA-MB-231 and MCF10A cells were very similar. This could subsequently mean that the degree of membrane porosity is similar and is advantageous in making comparisons for the particle uptake. T47D cells showed higher DI for the same range of flow rates, suggesting a potentially higher degree of membrane disruption and uptake which would require further investigation.

NADH/NAD^+ standard assay was performed to compares the levels of the redox couples in these breast cells (Appendix 9.9). However, the data did not show the expected trend as projected by the literature [213]. This could indicate the inadequacies of the standard measurement of NADH/NAD^+ level in live cell which need to be validated with further repeats and more extensive investigation.

From the confocal microscopy analysis, the relative emission of RA-QDs from the different cells upon uptake through deformation at different flow rates were analysed. It was observed that the ER+ cells (MCF7 and T47D) show higher particle luminescence compared to the ER- (MDA-MB-231) and the non-malignant (MCF10A) breast cells. The difference is greater for the higher flow rates. This is indicative of the higher reducing cellular environment of the ER+ cells producing a more efficient reduction of the quinones on the RA-QDs compared to the ER- and non-malignant cells. In the case of T47D, the higher PL-emission from the cells could also be manifested from its higher DI which needs further investigation. Comparatively, the uptake of QD without quinones do not show this trend, verifying that the RA-QD luminescence from cells was the outcome of the reduction efficiency of the cellular environment. Hence, RA-QDs can operate as redox-sensitive probes in live cells. However, it is necessary to further investigate the correlation between deformation and the degree of membrane disruption for the different cell lines for making more precise conclusions.

MCF7 cells treated with RA-QDs (both deformed and incubated) were put under chemically-induced oxidative stress by AAPH treatment. It showed a rapid drop in the photoluminescence of the RA-QDs from both forms of uptake (incubation and deformation). This is indicative that AAPH affects the redox state in both the cytoplasm and the endosomes of live cells. This showed that the RA-QDs are sensitive to changes in the redox state of the cells. In comparison, the control QDs without quinones did not show a significant change in their luminescence from the cells on AAPH treatment. Similar treatment of the non-malignant MCF10A cells also demonstrated a drop in the RA-QD photoluminescence, with the alteration of the cellular redox state. The RA-QDs can effectively sense the cellular redox potential and its alterations that could have potential applications in stem cells, primary cells and other model cell lines. Additionally, the next challenge would be to separate the PL emission signals from the endosomes and the cytoplasm. This could in theory be achieved by using redox-sensitive

ligands that can switch the PL emission of the QDs within a narrow pH range, capable of differentiating the cytoplasmic and endosomal uptakes.

5. Membrane disruption and fluid motion

The hydrodynamic stretching of the cells using the cross-slot microfluidic device generates short-lived membrane pores that allow the diffusion of QDs into the cytoplasm. To have a deeper insight into how the uptake occurs, it is essential to understand the behaviour of the cell during deformation, particularly the motion of fluids through the pores. In this chapter, the behaviour of the intracellular fluids during and after cell deformation and the direction of fluid motion across the membrane pores, using the high-speed confocal FDM microscope was investigated.

MCF7 cells were stained with calcein which labels the cytoplasm and deformed through the cross-slot microfluidic device at 5 and 10 µl/min flow rates in order to capture a large number of frames per event. High-speed confocal images of cell deformation were taken using an FDM microscope at the extensional flow junction. FDM enabled high-speed imaging of the cells which were used to quantify the change in the calcein fluorescence during the deformation event.

The FDM images were affected by several inherent factors, such as the scan velocity of the laser beams, the lifetime of the fluorophore and the motion of the cells with respect to the scanning beams. These factors cause image distortions and affect the fluorescence output, as such, image corrections were performed to enable quantification of the results. The analysis showed that there was a drop in the total emission intensity from the cells as they deform through the cross-slot device. This implies that there was an outflow of intracellular materials from the transient membrane pores. A simulation was designed to estimate the distortion in the cell images due to its motion with respect to the scanning beams of the FDM and its effect on the fluorescence intensity measurements.

Cells deformed at the higher flow rate (Q = 100 µl/min), were imaged post deformation at different regions along the outlet channel using a static scanning arm and the motion of the cell through the channel. This again showed a drop in the PL intensity, confirming the leakage of intracellular material and a possible drop in cell volume. Therefore, cell deformation causes material flow in both directions across the transient membrane pores, as confirmed by the calcein leakage and QD uptake results. The bi-directional flow of materials across the transient membrane pores on deformation can be crucial in understanding the cellular behaviour under

mechanical stress. It can give more insight for future studies of uptake applications in sensing, imaging and membrane dynamics.

Uptake of Au NPs of different sizes with FITC fluorescent tags showed that there is sized dependent uptake with flow rate. This is indicative of the size of the transient membrane pores through which the particles can diffuse into the cytoplasm.

5.1. FDM microscopy of cells stained with calcein

To understand the uptake mechanism of QDs by cells through cell deformation using the cross-slot microfluidic device, it is important to understand the dynamics of the fluid across the transient membrane pores. The process of cell deformation is high throughput in which thousands of cells are deformed every second. Cells deform very rapidly (~1 ms) at the extensional flow junction and exit through the outlets where they recover. With the FDM microscope, we visualised the cell deformation and track the PL intensity at up to 16,000 frames/s.

MCF7 cells were incubated with 1 µM calcein-AM for 30 min which is a fluorescent dye used to label the cytoplasm of live cells. The quenched calcein-AM is membrane permeable, which is converted to fluorescent calcein by the cleavage of AM group by esterases in the cells. The cells were detached by trypsinisation, resuspended in the running buffer (DPBS + 0.5% MC) and deformed through the cross-slot microfluidic device at flow rates of 5, 10 and 50 µl/min as described in section 2.15. The deformation events were captured with the ultrafast confocal FDM with both bright field and fluorescence imaging.

The event capturing in the FDM was triggered when the fluorescence was detected in the field of view (FOV) by the moving cells. The image capturing was done by an array of 100 scanning beams moving across the FOV from along the x-direction. The scanning beams were incident on the sample by the moving galvanic mirror, which swung back and forth in the FOV. As such, images were captured in alternating directions. As the galvanic mirror oscillated, the beams at rest at one end of the FOV accelerated and gained a maximum velocity at the centre and slowed down before coming to stop at the other end. The direction was reversed in the next

scan. The motion of the scanning mirror was described by its velocity (v_b) and position (x) using the following equations:

$$v_b(t,\,\theta) = v^s_{max}\,\sin(2\pi t \times \mathrm{f} + \theta)\ \ [\mathrm{m/s}] \qquad (5.1)$$

$$x(t,\,\theta) = \int_0^t v(t',\theta)\,dt' \qquad (5.2)$$

Here, t is the time in the scan direction; amplitude scan velocity of the laser beam, v^s_{max} (=2.3 m/s); θ is the initial phase shift in the velocity waveform which describes the position of the scanning beams when the event is triggered and the f is the scanning frequency (7.93×10^3 Hz). The pixel rate in the scan direction for the FDM was 4101562.5 Hz.

Hence, equation (5.1) can be written as:

$$v_b(vertical\,pixel,\,\theta) = 2.3 \times \sin\left(2\pi \frac{pixel\ index}{4101562.5} \times 7.93 \times 10^3 + \theta\right)\ [\mathrm{m/s}] \qquad (5.3)$$

A distortion of the images was produced due to the variation of the scanning speed, the correction of which is described in detail later. An event, which was a series of images taken as the cells moved in the FOV, were captured as binary files (.FIRE) that were converted to 16-bit images (.tiff format) using a MATLAB script. The raw images were generated as long strips of frames joined to each other. The frames were separated into individual images using the MATLAB script, by reading and applying the initial phase θ of the scanning mirror from an excel file, recorded during the event capture with the help of equation 5.3 (Figure 5-1). When an event was triggered by the entry of the cell in the FOV, the scanning mirror could be in any position, which was described by the recorded initial phase angle θ. The positions to extract and cut the individual frames from the joined strips were determined using equation 5.2. The extracted images had 21-22 and 11-12 frames per event for the flow rates Q =5 and 10 µl/min, respectively. The contrast of the images was enhanced to better visualise the cell in the FOV. This format of the MATLAB script could only extract every odd frame from the individual event and needed improvements to obtain all the frames. Artefactual events, which were mostly triggered by fluorescent cell debris or multiple cells in the FOV were removed manually. The first and the last few (1-2) frames were rejected from analysis (depended on individual events) as they only captured the cells partially. For Q = 50 µl/min, it was seen that the number of frames per event was 4-5. On rejecting the frames having partial cell capture, the remaining frames (2-3) were not sufficient enough to give a proper trend in the change of fluorescence

through the passage of cells in the FOV. Hence, this dataset was not considered for analysis. Once the individual frames were separated, several corrections were made to the images which are described in detail below.

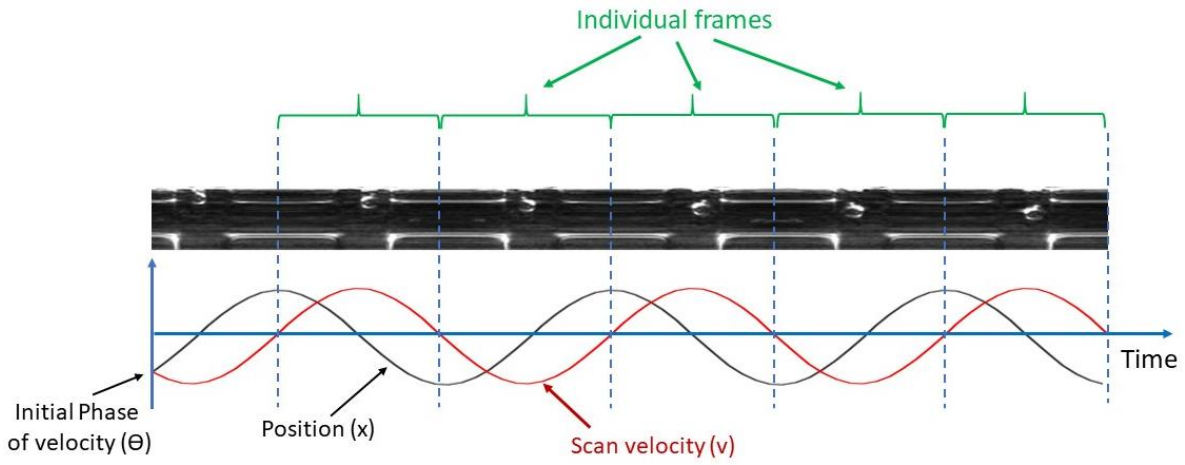

Figure 5-1. Frame extraction of an FDM event from a typical raw image file having multiple frames joined together. Individual frames are extracted from the scan velocity profile and the initial phase (θ) of the velocity when the event was triggered.

5.1.1. Corrections of image distortion due to the nonlinear (sinusoidal) scan

As mentioned in the previous section, the scanning velocity of the laser beam array was controlled by the motion of the galvanic mirror which moved back and forth in the x-direction. This caused distortion to the images generated. The velocity of the laser beam array was lowest at the edges of the field of view (FOV) and maximum at the centre. This caused the pixel to be elongated at the edges and compressed at the centre. Figure 5-2a shows a raw uncorrected frame of a typical event, after the frame separation from the merged strip, for the cell in the extensional flow junction. It can be seen that the channels appear wider along the x-direction, clearly depicting the distortion.

Using a Python code, the cells were detected from the images by grey-scaling, filtering, thresholding, finding the contours (using cv2 python module). A bilateral filter (cv2.bilateralFilter) was applied to the image to smooth out the random noise and make the cell detection more reliable. Adaptive threshold was applied to calculate the threshold based on the average intensities across the multiple regions of the image. This means the code found

areas in the FOV that are brighter than the area directly surrounding it. This was helpful in determining the edge of the cell. Now, an ellipse was fitted to the contour (a basic check for size and circularity was applied to prevent fitting artefacts). The ellipse was generated by fitting a polygon with number of sides >10 and smoothening the edges. The fitting was performed on each frame to track the cell throughout the event. The ellipse was fitted for both bright field and fluorescence images and the average position and size of the cells were determined from the fits of both channels (Appendix 9.15). The total PL intensity (from the fluorescent channel) of the calcein emission from inside the fitted ellipse was measured by masking the image and summing the pixel intensity.

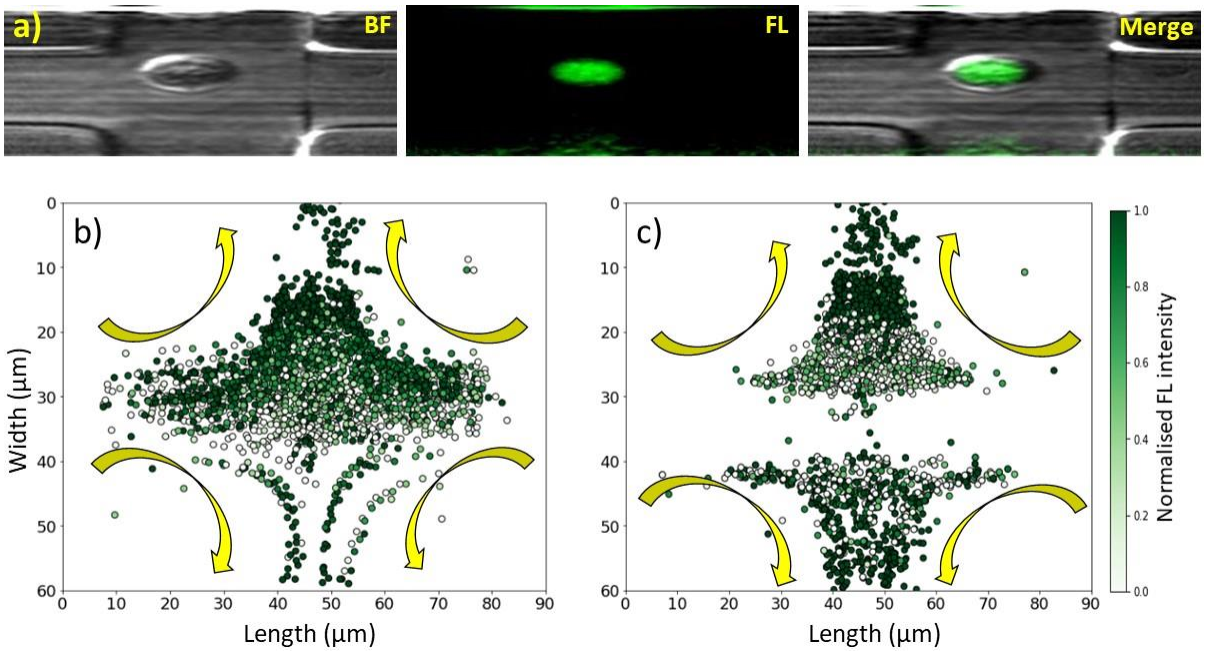

Figure 5-2. a) A typical FDM uncorrected raw image of MCF7 cells stained with calcein at the extensional flow junction of the cross-slot microfluidic device (bright field (BF), fluorescent (FL) and merged channels). The normalised total fluorescence intensity scatter trace plots from the cells before the corrections for b) 5 and c) 10 µl/min flow rates. Each point represents the position of the cell during its motion in the FOV. The colour of the point represents the normalised total PL-intensity from the cells with respect to the scale bar on the bottom right of the figure. The arrows indicate the direction of flow.

The PL intensity scatter trace plots for Q = 5 and 10 µl/min are shown in Figure 5-2a and b respectively for the uncorrected raw images. The distortion of the images was clearly visible as the channel widths appeared wider along the x-direction compared to that along the y-

direction. The scatter trace for each event was constructed by measuring the PL intensity from the fitted ellipse for the cell at every alternative frame with a position assigned to the centre of the fit. We observe the cells enter the FOV from the inlets with high PL intensity and as the cells moved through the junction, the intensity dropped for both the flow rates. The pixels distortion can contribute towards this fluorescence drop effect as the ellipse tracking the cells would predict more pixels at the edges and fewer at the centre. Hence, the pixel distortion correction was necessary.

Additionally, it is to be noted that more cells are entering from the upper inlet compared to the lower one. This discrepancy could have occurred purely due to the statistical distribution of events or the slight preferential flow from the upper inlet which was not detectable during the experiments.

The correction of the images due to the distortion caused by the scan velocity profile is termed as 'squaring of the pixels'. To perform this, an image of a graticule was taken with the FDM to measure the degree of distortion as a function of position. A graticule had equidistant parallel lines and the distortion of the distance between the lines at different regions on the FOV gave the degrees to which the images are distorted. The distortion was measured and a spline function was fitted (smoothening the fitting to avoid discontinuities) for the correction which was applied to all images for squaring of the pixels, using the same MATLAB script as mentioned earlier in section 5.1. Figure 5-3a shows the same images as in Figure 5-2a after the correction has been applied to 'square the pixels'. It was observed from the corrected image that all channels are of similar widths. The pixel count for the corrected images was 110 pixels along the x-direction and 100 in the y-direction, instead of the 259×100 pixels for the FOV in the uncorrected images. Additionally, improvements were made to the MATLAB code such that all frames were extracted instead of only the odd frames in the previous version of the code. With the extraction of all the frames, it was observed that the odd numbered frames were flipped by 180^{o} compared to the even numbered frames. This is because the direction of the scan is reversed for alternating frames. The MATLAB script inverted the odd numbered frames along the x-direction, such that, all the frames had the same orientation. The images for the event were saved as .tiff files which was also converted to .csv files by merging the different frames to produce a video of the event.

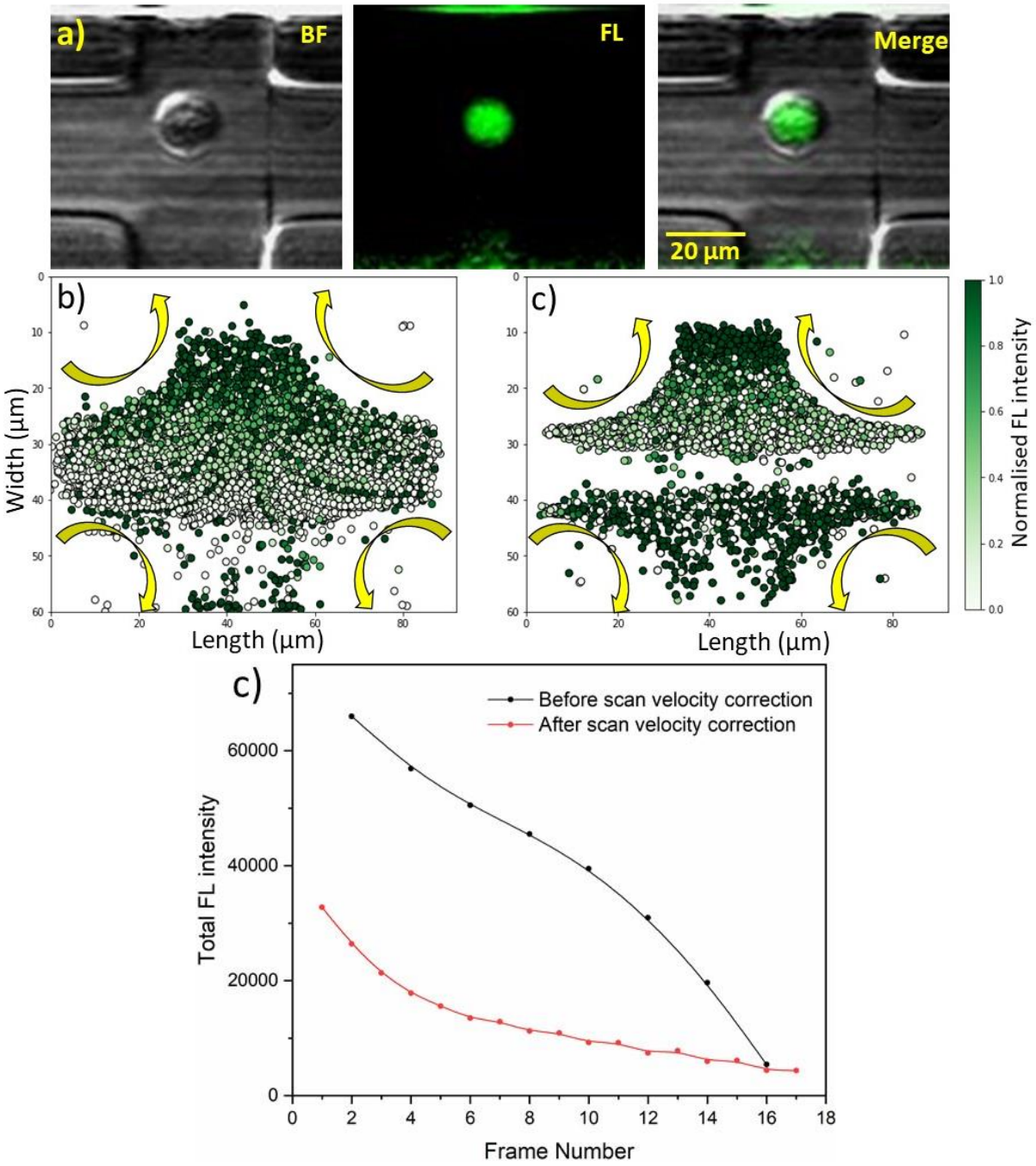

Figure 5-3. a) A typical FDM image of MCF7 cells stained with calcein after the scan velocity profile related distortion correction of a cell at the extensional flow junction of the cross-slot microfluidic device (bright field (BF), fluorescent (FL) and merged channels). The corrected normalised total fluorescence intensity scatter trace plots from the cells for b) 5 and c) 10 µl/min flow rates. Each point represents the position of the cell during its motion in the FOV. The colour of the point represents the normalised total PL-intensity from the cells with respect to the scale bar on the bottom right of the figure. The arrows indicate the direction of flow. d) Comparative normalised total fluorescence intensity from a typical event before and after the scan velocity related distortion correction.

Figure 5-3b and c show the normalised total fluorescence intensity scatter trace plots for Q = 5 and 10 µl/min, respectively after the correction to the scan velocity related distortion. It can be observed that the cell positions are significantly more spread through the FOV compared to the uncorrected plots. The cells showed a significant drop in the total PL intensity measured for a single event in comparison to the uncorrected image (Figure 5-3d). However, it was observed that there is a decrease in the PL intensity down the y-direction for the cells entering from the upper inlet. This trend is not observed for the cells entering from the lower inlet. This discrepancy relates to the spatial effect on the FDM images from the lifetime of the fluorophore, the correction of which is described in the following section.

5.1.2. Corrections to PL intensity due to the lifetime effect of the fluorophore

If the fluorescence lifetime of the fluorophore is comparable to the dwell time of the pixels, there is a decrease in the signal-to-noise ratio (SNR) from the images. The majority of the fluorescence emission occurs after the dwell time and would not contribute to the image contrast. The FDM is capable of very fast fluorescence imaging (~16,000 frames/s). However, in spite of the fast scans, the pixel dwell time is longer than that of the conventional confocal fluorescence microscopy, as the imaging speed is characterised by the QAM-SDC beam modulation bandwidth, described in section 2.14. The FDM gives an improved SNR and hence compensate for the decreased fluorescent signal due to the fluorescence-lifetime limit. However, the frequency bandwidth is limited by the fluorescence lifetime which is characterised by the spatial frequency response function as [251]:

$$R(y) = \frac{e^{i \arg(1-2\pi i v \tau y)}}{\sqrt{1+(2\pi v \tau y)^2}} \qquad (5.4)$$

Here, τ is the fluorescence lifetime of the fluorophore and v is the modulated frequency of the scanning laser beam. Equation 5.4 indicates that $R(y)$ degrades the optical transfer function along the y-direction. v varies from ~4 to ~400 MHz which were in one-to-one correspondence with the 100 pixels along the y-direction. In other words, the n^{th} laser beam had a frequency of (4 + 4n) MHz (Figure 5-4a). Figure 5-4b shows the absolute value of the $R(y)$ for calcein with fluorescence lifetime τ =2.9 ns. Using the same Python code as mentioned earlier in section

5.1.1., the correction function was applied across the FOV along the y-direction by multiplying the measured fluorescence intensity with the corresponding amplitude of the absolute value of $R(y)$ for all images.

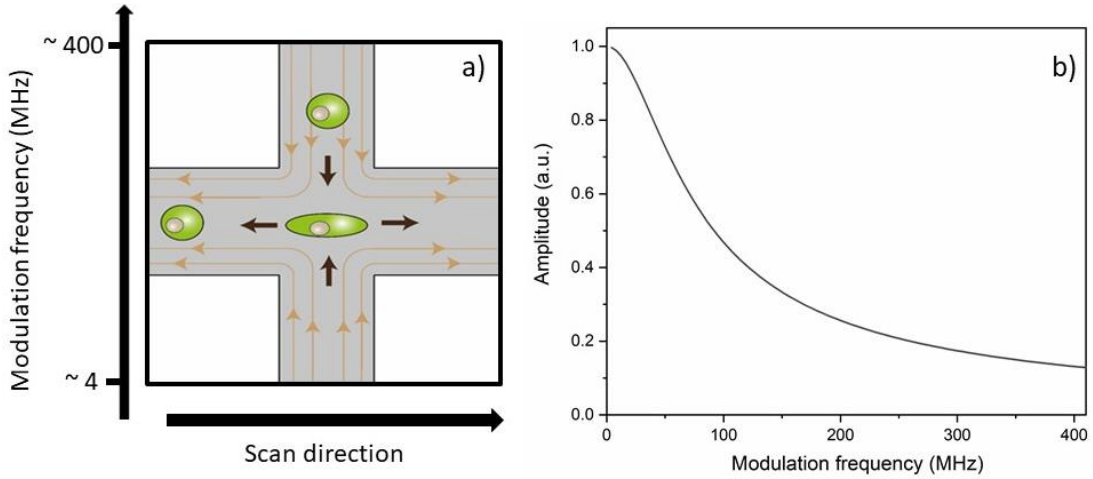

Figure 5-4. Correction on the FDM microscope images due to the lifetime effect of the fluorophore. a) Schematic of the FOV with cell in the extensional flow region of the cross-slot microfluidic device as a function of modulation frequency along the y-direction. b) The amplitude of function $R(y)$, which is the correction functions curve for the FDM images as a function of the modulation frequency for calcein (τ = 2.9 ns).

Figures 5-5a and b represent the scatter trace plots (Q = 5 and 10 µl/min, respectively) for the total photoluminescence from the deformed cells after applying the correction to the intensity due to the fluorescence lifetime effect of the fluorophore. This correction was applied in addition to the previously corrected images for the distortion (squaring of the pixels) due to the effect of the scanning velocity profile. Here, the drop in PL intensity from the cells entering from the upper inlet was not as significant as without the lifetime correction (Figure 5-3). However, for the cells entering from the lower inlet, there was a drop in the PL intensity as the cells move through the extensional flow region. This is consistent with the trend observed for the cells entering from the upper inlet. If the fluorescence intensity of the calcein from the cells should change with deformation, it should have the same trend regardless of the port of entry. Hence from this correction, the consistency with the expected result can be observed. However, the actual trend will only be clear after all the corrections have been made to the dataset, which is described in the following section.

Additionally, several further modifications and improvements were made to the Python code for better detection and tracking of the cells. From the previous scatter trace plots shown in Figure 5-3, it was observed that there is a presence of artefacts detected by the code, such as objects from the no-flow regions. These were the regions in the FOV where the PDMS channel walls are located. These artefacts were removed from detection by imposing spatial restrictions and thus disregarding any data in the regions that are not within the channels. From the trace of a typical single event, as shown in Figure 5-5c with the fluorophore induced lifetime correction, we observed that there was an overall drop in the total PL intensity measured from the cells in addition to the drop observed after the scan velocity profile correction.

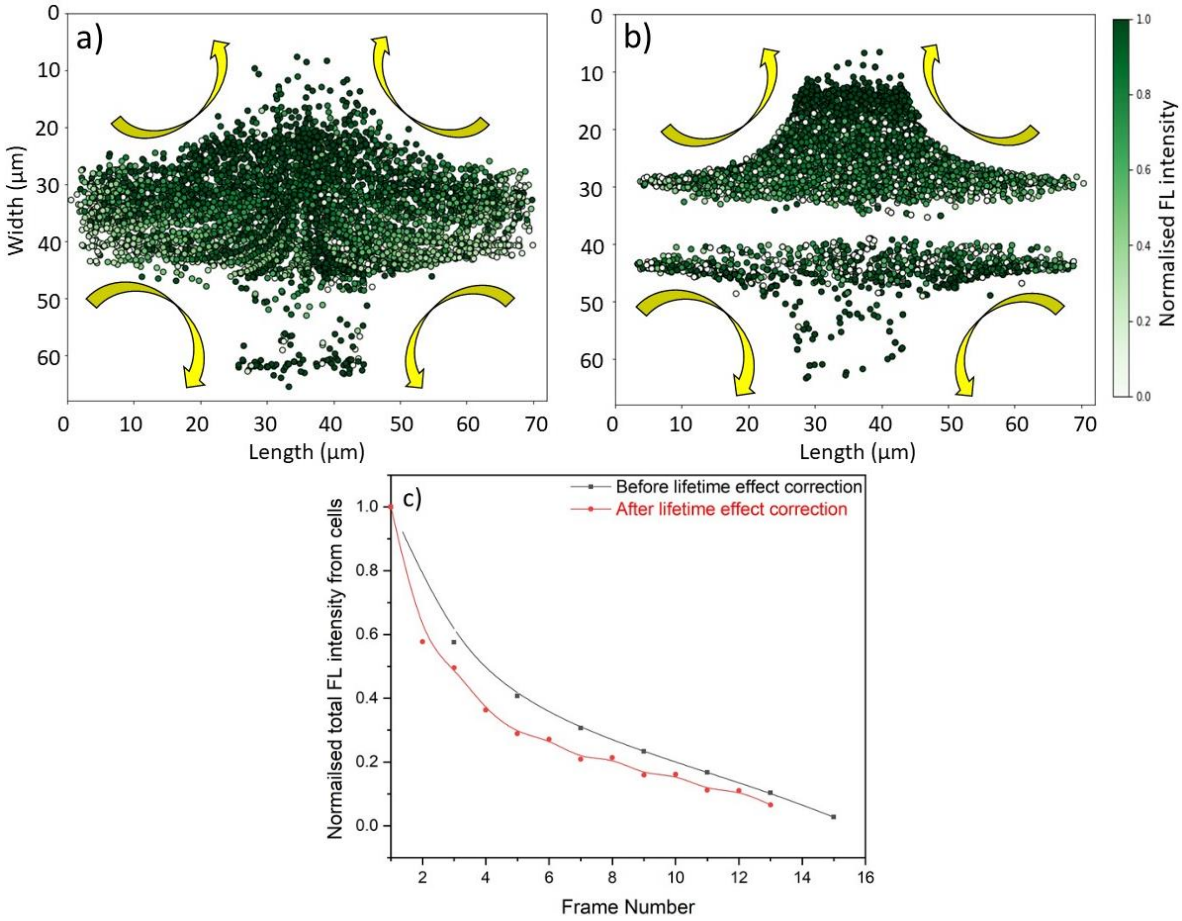

Figure 5-5. The normalised total fluorescence intensity scatter trace plots for the FDM images of MCF7 cells stained with calcein with the scan velocity profile correction and the lifetime effect of the fluorophore correction from the cells deformed through the cross-slot microfluidic device for a) 5 and b) 10 µl/min flow rates. Each point represents the position of the cell during its motion in the FOV. The colour of the point represents the normalised total PL-intensity from the cells with respect to the scale bar on the right of the figure. The arrows indicate the direction of flow. c) Comparative normalised total fluorescence intensity from a typical event before and after the lifetime effect correction for calcein (τ = 2.9 ns).

Typical normalised total fluorescence intensity traces of the cells at Q = 5 and 10 µl/min are shown in Figure 5-6. The photoluminescence steadily dropped for both the flow rates as the cells deform through the extensional flow region. This implies there is an outflow of intracellular fluid from the transient membrane pores generated by the hydrodynamic deformation.

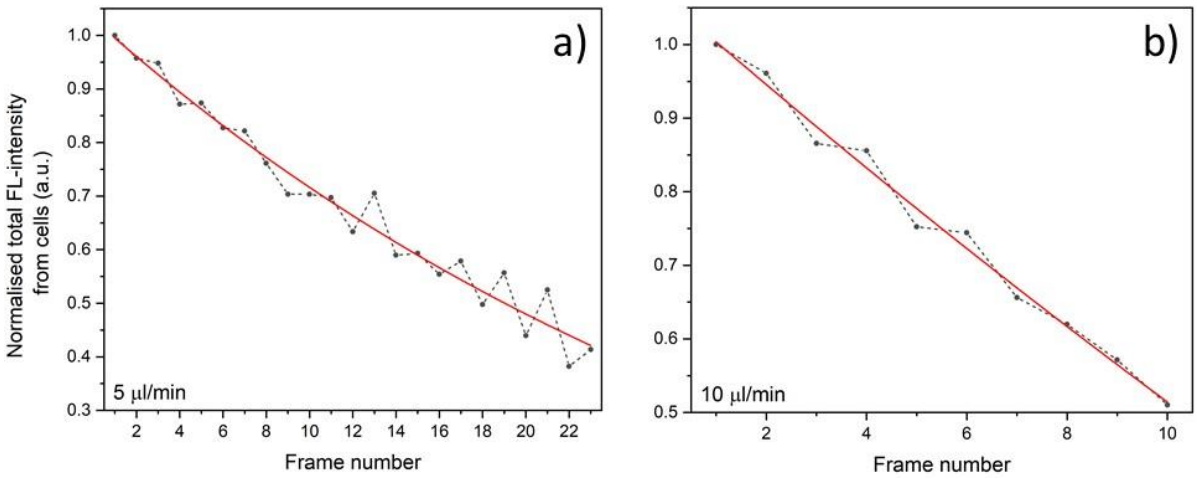

Figure 5-6. Normalized total fluorescence intensity from a typical single-cell event as observed through the FDM at the extensional flow region of the cross-slot microfluidic device with stained with calcein at a) 5 ul/min and b) 10 ul/min flow rates. The solid red lines represent exponential decay fits (R^2 > 0.96).

5.1.3. Corrections to cell distortion due to cell motion

The final corrections to the FDM images for the cells deformed through the cross-slot microfluidic device were due to the motion of the cells with respect to the scanning beam. As the cells move through the extensional flow junction, the velocity of the cells changes as it enters and exits the FOV according to the velocity profile (Figure 1-8) described by Armistead et. al [181]. The cells initially have a constant velocity in the straight inlet channels and slow down at the extensional flow junction where they deform. After coming to a stop at the stagnation point, the cells accelerate again towards the outlets and maintain a constant velocity through the straight outlet channels. The velocity of the fluid along the straight channels depends on the flow rate of injection (~0.05 and ~0.1 m/s for Q = 5 and 10 µl/min, respectively). The relative motion between the FDM scanning beams and the moving cells distorts the cell shape. As described earlier, the velocity of the scanning beam (v_b) also changes

with respect to the position on the FOV as described in equation 5.3. The scanner velocity is at a maximum at the centre of the FOV (v_b= 2.3 m/s) and decreases at the edges (simple harmonic oscillator). As the scanning velocity slows down at the edges of the FOV, the cell velocity becomes comparable to the scanning beam velocity. Hence, the cell distortion was highest at the left and right edges of the FOV.

The distortion of the cells depended on the relative direction of the cell motion and the scanning beam. For the cells moving perpendicular to the beams, the distortions can be described by the illustrations in Figure 5-7a and b. As the array of laser beams scan across the x-direction, the cell in motion would have travelled along the y-direction. As a result, any motion along the y-direction stretched the cells. If the cells are moving along the direction of the scanning beams (x-direction), they appeared to be either elongated or compressed in the same direction depending upon the direction of the scan. If the cell moved in the same direction of the scan, they appear elongated (Figure 5-7c). If the motion of the cell was opposite to the scanning beam, the cells appeared compressed (Figure 5-7d). The total distortion of the cell in the FOV would be a combination of both the distortions in x- and y-directions.

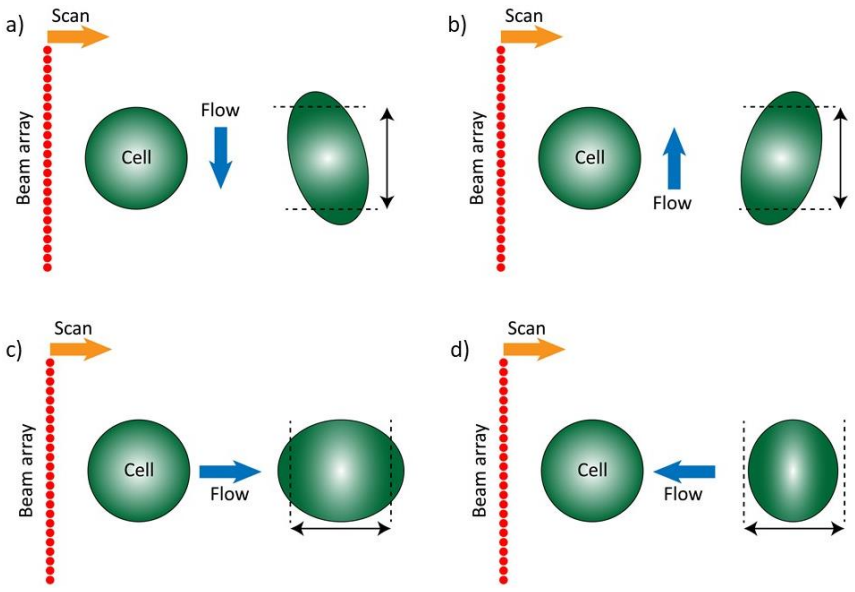

Figure 5-7. Schematic of the FDM image distortion due to cell motion with respect to the scan directions when the cells move a) perpendicular and down, b) perpendicular and up, (c) parallel and left, and d) parallel and right to the scan direction (the dashed lines showing the actual cell size).

The corrections for the cell distortions due to the relative motion of the cells with respect to the scanning laser beams was approximated using the following expressions:

$$D_{x_i} = D_{x_i}^m \times \left[1 - \left(\frac{v_{x_i}}{v_b(x)}\right)\right] \quad (5.5)$$

$$D_{y_i} = D_{y_i}^m - \left(\frac{v_{y_i} \times D_{x_i}^m}{v_b(x)}\right) \quad (5.6)$$

Here, D_{x_i} and D_{y_i} are the corrected cell diameters, $D_{x_i}^m$ and $D_{y_i}^m$ are the measured cell diameters along the x- and y-directions, respectively for the (i+1)th frame of the event. $v_b(x)$ was the scanning beam velocity profile with respect to the position, x on the FOV as described in equation 5.3. v_{x_i} and v_{y_i} represented the cell velocity components along x- and y-directions for the (i+1)th frame. In equation 5.6, the second term is always positive because whether moving up or down along the y-axis, and the scanner left to right, all caused the cell to be elongated in the y-direction. In the case when $|v_b(x)|$ is much greater than the modulus of the cell speed, the measured diameters tend towards the actual cell diameter. The cell velocities were determined by the change in the cell's position between ith and (i+1)th frames and the time between them.

As mentioned earlier, the scanning beams moved and captured in both +x and -x directions, as such, the cell distortion correction along the direction of the beam will also depend on the direction of the scanner; however, this has to be is accounted for both v_b and v_{x_i} because they are vectors. The direction of the scanning beam was determined for the first frame of every event from the initial phase (θ) and substituting this value into equation 5.1 to determine the scanner direction (positive or negative) at t =0 s. A positive scanner velocity means the scanning beam direction is left to right for the first frame; and if v_b <0, this means the scanning beam is moving the right to left (negative) for the first frame. From this knowledge, the direction of the scanner was determined for each subsequent frame and it is trivial to ensure the sign of the scanner velocity is in the correct direction. If the scanning beam and the cell are moving in the same direction (Figure 5-7c), the distortion would result in the elongation of the cell, and thus the second term in equation 5.5 would be subtracted from the measured diameter. Similarly, if the cell and the scanning beams are moving opposite to each other (Figure 5-7d), the cells

would be contracted, but the second term in equation 5.5 would be negative and thus would increase the measured diameter. Equation 5.6 takes the modulus of the second term because regardless of the direction of motion of either the cell or the scanner, the cells will be elongated in the y-direction. The image distortion corrections in both x- and y-directions were applied to all images which had already been corrected for the image distortion due to the scanning velocity profile and fluorophore lifetime effect correction.

Figures 5-8 show the normalised fluorescence scatter trace plots (Q = 5 and 10 µl/min) before and after the correction to the distortion due to cell motion with respect to the scanning laser beam. It can be observed that the overall trend to the decrease in the emission intensity from the cells does not change significantly with the distortion correction. However, due to the corrections, the scatter points are much more compact and closer to each other in the FOV. In addition, with the improvements to the detection of cells, there are more points in the FOV and the events at the edges with partial cells have been removed. It must be noted that the images have also been corrected for velocity profile distortion and the fluorophore lifetime effects. Hence, Figure 5-8b are the final corrected scatter trace plots for the MCF7 cells stained with calcein, deformed through the cross-slot microfluidic device and imaged using the FDM. The plots show a decrease in the fluorescence intensity as the cell deform at the extensional-flow junction due to the leakage of intracellular materials from the transient membrane pores.

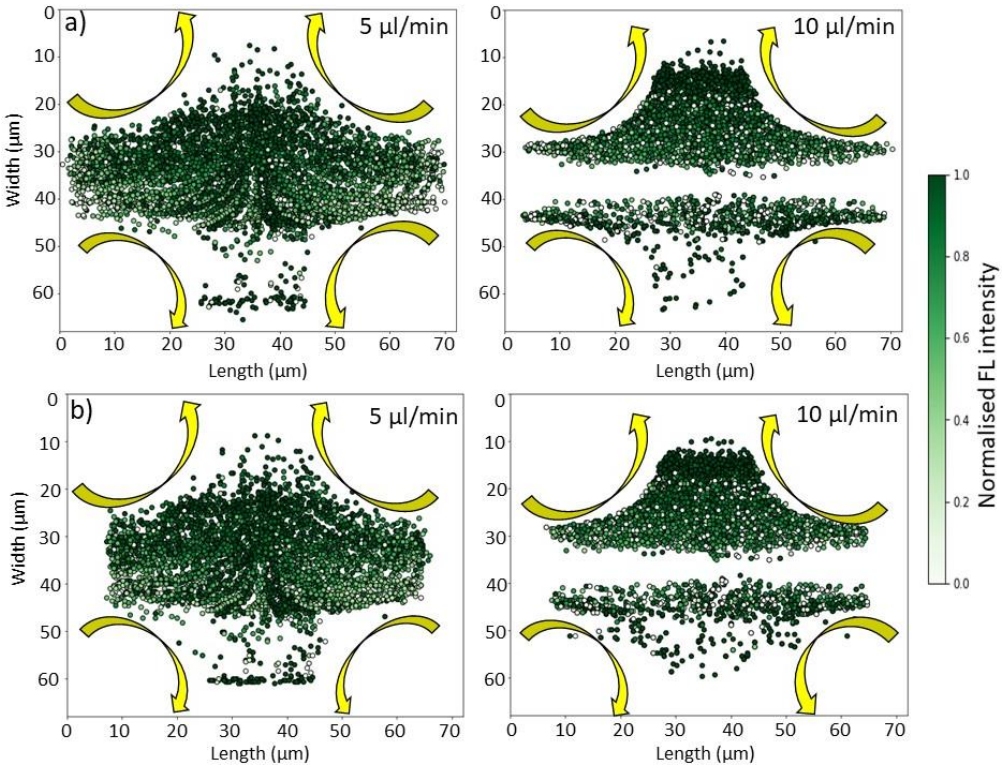

Figure 5-8. The comparative normalised total fluorescence intensity scatter trace plots for the FDM images of MCF7 cells stained with calcein, before and after the cell motion distortion corrections. The scan velocity profile correction and the lifetime effect of the fluorophore corrections were performed for all plots prior to the analysis. a) The uncorrected and b) corrected scatter plots for distortion due to cell motion for Q = 5 and 10 µl/min, respectively. Each point represents the position of the cell during its motion in the FOV. Each point represents the position of the cell during its motion in the FOV. The colour of the point represents the normalised total PL-intensity from the cells with respect to the scale bar on the right of the figure. The arrows indicate the direction of flow.

Typical events of cell deformation captured using the FDM is shown in Figure 5-9 (Q = 5 and 10 µl/min), with and without the distortion correction due to cell motion. The cell area without correction (A^m) was determined using:

$$A^m = \frac{\pi}{4} \times D_{x_i}^m \times D_{y_i}^m \qquad (5.7)$$

Similarly, the cell area after the distortion correction (A) due to cell motion was determined as:

$$A = \frac{\pi}{4} \times D_{x_i} \times D_{y_i} \qquad (5.8)$$

With the correction to the distortion due to cell velocity with respect to the scanning beam velocity, it was seen that the fluctuations in the cell area between alternative frames have been

reduced for both Q =5 and 10 µl/min. The fluctuations arise due to the distortion of the cell which is dependent on the direction of the scanning beam as demonstrated in Figure 5-7c and d. Since the direction of the scanning beam alternates, the fluctuations in the measured cell area also fluctuates between alternating frames. Although the distortion corrections have not completely removed the fluctuations, they have been reduced. The normalised integrated fluorescence from the cell for this particular event at Q = 5 µl/min was not affected by the corrections. However, for Q = 10 µl/min events, the PL intensity from the cell shows reduced fluctuations, much like the cell area with the corrections. The distortion corrections are theoretically expected to have a higher impact on the events at a higher flow rate (Q =10 µl/min) as the distortion will be much larger with the increased speed of the cell through the FOV.

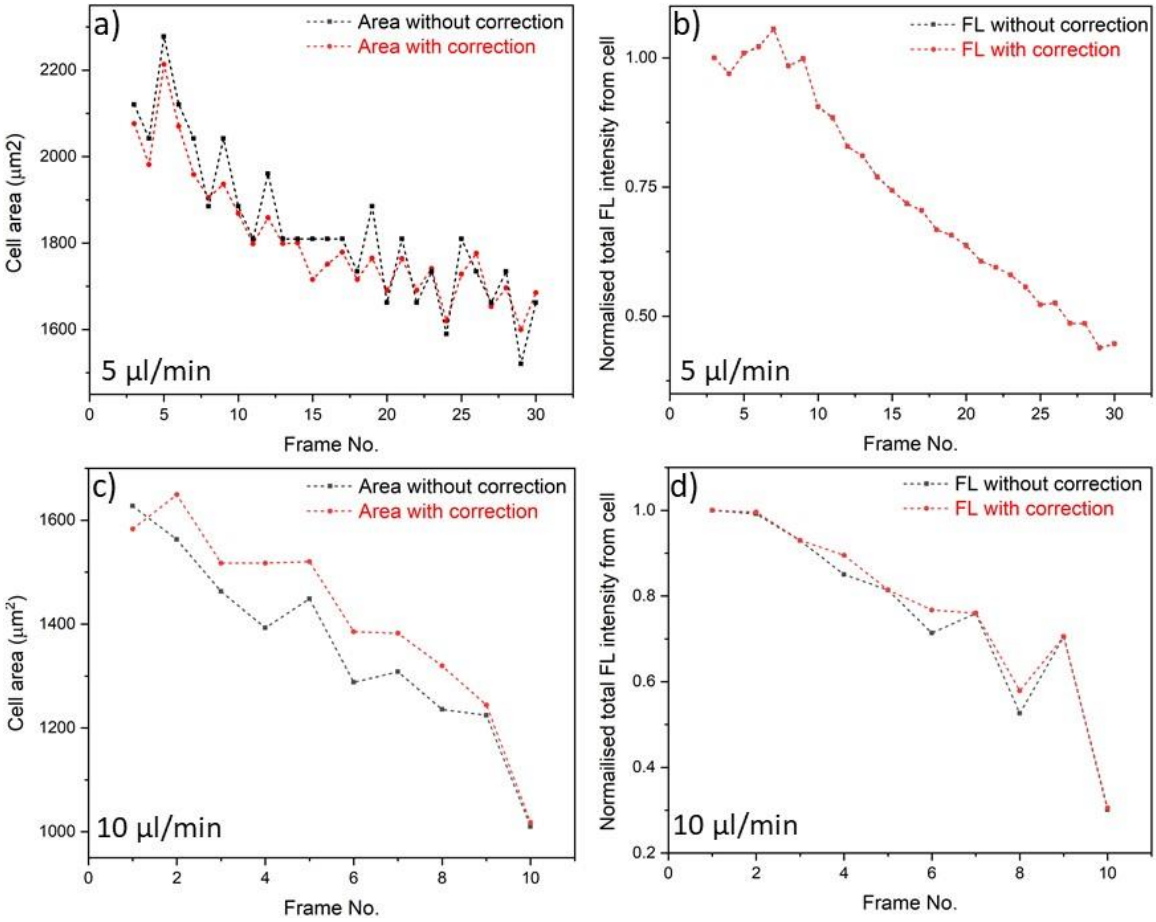

Figure 5-9. Typical events of cell deformation captured using FDM, with and without the cell motion distortion correction for MCF7 cells stained with 1 µM calcein, deformed through the cross-slot microfluidic device. Plots for Q =5 µl/min with the frame number showing a) the change in the cell area, b) the normalised fluorescence intensity and for Q =10 µl/min with c) change in cell area and d) the normalised fluorescence intensity, with and without the correction to distortion due to cell motion.

The comparative normalised fluorescence intensity for the entire dataset, with and without the correction to distortion due to cell motion, as a function of the distance travelled in the FOV is given in Figure 5-10. It is the combined overall fluorescence intensity of the cells though the FOV for the same datasets that has been described in the scatter trace plots in Figure 5-8. For both flow rates, the distortion correction lowered the overall rate of drop of the normalised fluorescence measured. For Q = 5 µl/min events, the mean drop in measured fluorescence changed from 2.26 %/µm to 1.72 %/µm with the correction over the distance travelled by the cells in the FOV (~23.9 % change). The change was more significant (~45.2 %) for the Q = 10 µl/min events, with the mean drop rate in the normalised fluorescence intensity from the cells changing from 3.23 %/µm to 1.77 %/µm after distortion corrections. The greater change for the faster flow rate with the distortion corrections correlates with the theoretical understanding that the distortion would be higher for faster moving cells.

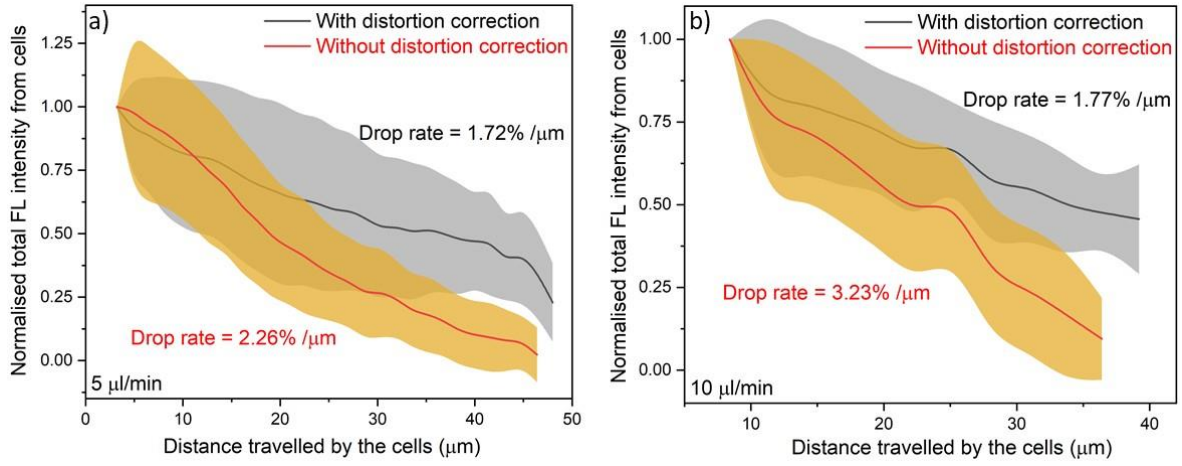

Figure 5-10. Normalised mean total fluorescence intensity of Calcein luminescence from MCF7 cells from the FDM images as a function of distance travelled in the extensional flow region of the cross-slot microfluidic device for a) 5 µl/min and b) 10 µl/min flow rates, with and without the correction for the distortion due to cell motion. Data expressed as mean ± SD (N >350 events). These plots are derived from the scatter trace plots shown in Figure 5-8.

The overall change in the final corrected normalised fluorescence intensity for the MCF7 cells stained with calcein captured using the FDM, deformed through the cross-slot device, as a function of the distance travelled in the FOV is given in Figure 5-11. The cells deformed at Q = 5 µl/min can be imaged closer to the edges of the FOV as compared to that at Q = 10 µl/min

due to the slower motion of the cells. The mean rate of drop of fluorescence intensity with distance was similar for the two flow rates (1.72 and 1.77 %/μm for Q = 5 and 10 μl/min, respectively). This suggests that the degree of poration of the cells at these flow rates were similar, leading to a similar outflow of intracellular materials from the transient membrane pores. Additionally, it also confirmed that the drop in the luminescence intensity of calcein from cells was not dominated by photobleaching. If photobleaching was dominant, then the drop in the intensity would be much higher for the slower flow rate as they have a longer laser exposure time. The hydrodynamic deformation of cells in the cross-slot microfluidic device rapidly generates transient membrane pores through which there is a leakage of intracellular material. There will be a volume loss incurred by the cells on deformation, which is recovered by taking up the surrounding fluid. As seen from the earlier results (Chapter 3), the uptake of the surrounding fluids leads to the non-endocytic delivery of QDs. These findings are indicative of the bi-directional model of diffusion across the transient membrane pores.

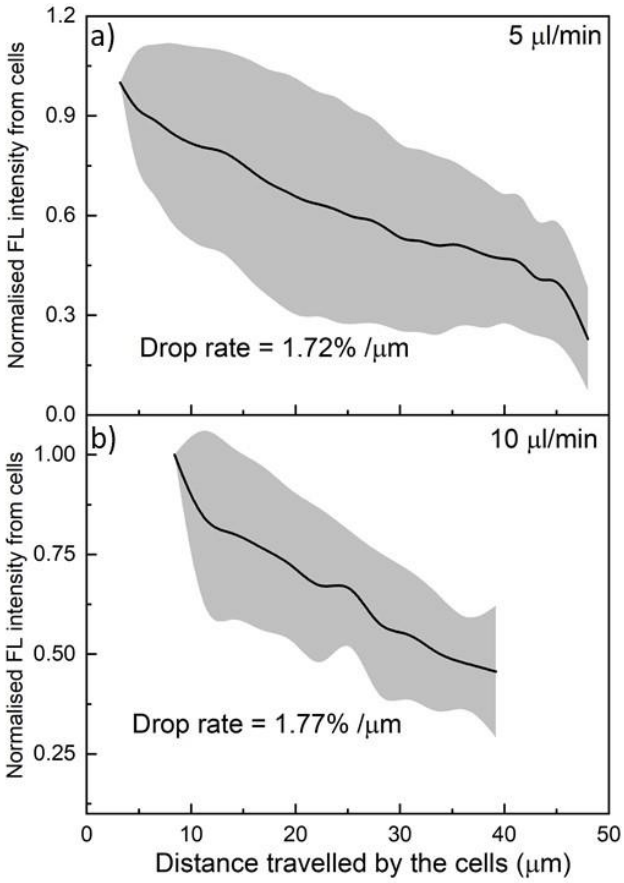

Figure 5-11. Comparative normalised mean total fluorescence intensity from MCF7 cells stained with calcein as a function of distance travelled in the extensional flow region of the cross-slot microfluidic device from the FDM images for a) 5 μl/min and b) 10 μl/min flow rates. Data expressed as mean ± SD (N >350 events).

5.1.4. Simulation to measure the distortion due to cell motion in FDM

To have a better understanding of the distortions produced by the cell motion, a simulation was designed using Python code to visualise the motion of the cell in relation to the variable scanning beam velocity. The code simulated the cell motion from the inlet to the extensional flow junction and exit from the outlet. This was achieved by constructing a circle and analysing its distortion for varying cell speed against the scanning beams. The scanning of the circle was done in both directions along the x-axis to replicate the FDM imaging conditions; however, for simplicity the cell speed was kept constant. In this simulation, the circle's position is determined with respect to time (t) from its centroid coordinate by stepping the time t by a uniform step, Δt. The simulated scanner moved across the FOV using Equation 5.9.

$$x(t) = \frac{x_{max}}{2} + \frac{x_{max}}{2} \sin(\omega t + \varphi) \qquad (5.9)$$

Here, x_{max} was the FOV width (in pixels) to give the centre and amplitude of the scanning line. The position of the scanner in the x-direction can be determined by the time t, and the angular velocity of the scanner. For each time point, the scan line position is determined and if that line passed through the edge of the circle the pixels passing through the circle were coloured green. This is simple to achieve as the equation of a circle along with its central position can be determined with a few lines of code. The simulation steps forward one-time point (which moves the circle) and the scanner x-position (using Equation 5.9) and again tests whether the scanner line and the circle (cell) intersect- if they do those pixels are coloured green (line top to bottom of the circle). A frame was completed when $\omega t + \phi = n\pi$, where n is a positive integer, and was saved. The image of the distorted circle formally underwent thresholding, contouring, and fitting to an ellipse. The speed and direction of the cell, the time step and the scanner frequency (speed) could all be modified. The simulation was conducted for a 'cell' radius of 14 pixels. The time step was calculated to ensure the scanner 'scans' each line of the image (all 100 pixels). Distortions around the edges were omitted when the entire cell was not visible in the FOV. Importunately the simulation models the scanning as an oscillator and can allow the 'cell' motion to follow any path defined.

For Q =5 µl/min, the maximum cell velocity is ~0.05 m/s, which is ~2% of the scanning beam velocity (2.3 m/s). The pixel distortion from the simulation measured a maximum of ~7%

distortion in the cell area. The change in the pixel size of the circle with the scan along with the cell position in the FOV are shown in figure 5-12a and b. Similarly, for the maximum cell velocity of ~0.1 m/s which is for Q =10 µl/min (~4% velocity of the scanning beam), the maximum distortion in the cell area was ~8.2%. It was noted that as the cell enters the stagnation point and towards the outlet, the cell radius fluctuates along the x-direction. This is the effect of the change in the direction of the scanning beams. From the plots for the position of the cells in the FOV, we observe that the frame number decreased with the increasing flow rate as expected (Figure 5-12b and d). It is our understanding that these distortions are for the maximum cell velocities which occur in the straight channels of the device (inlets and the outlets). However, at the extensional flow junction, which is the FOV for the FDM experiments, the cells slow down considerably coming to stop at the stagnation point and exits through the outlet. Hence, the cell speed was a lot lower in the FOV, as such the distortions will be smaller.

From the simulations, when the circle goes to the centre of the FOV and begin to move along the '+' x-directions, the radius of the circle fluctuates along the x-direction as seen in Figure 5-12 a and b. This oscillation occurs due to the relative motion between the scan direction and the circle (cell) motion. If the scan is along the '+' x-direction and the cell also moves in the same direction along x-axis, the image of the circle elongate. On the other hand, if the motion of the circles remains along '+' x-direction, however, the scan is along '–' x-direction, the circle becomes compressed. This is similar to the imaging conditions of the cells in the FDM.

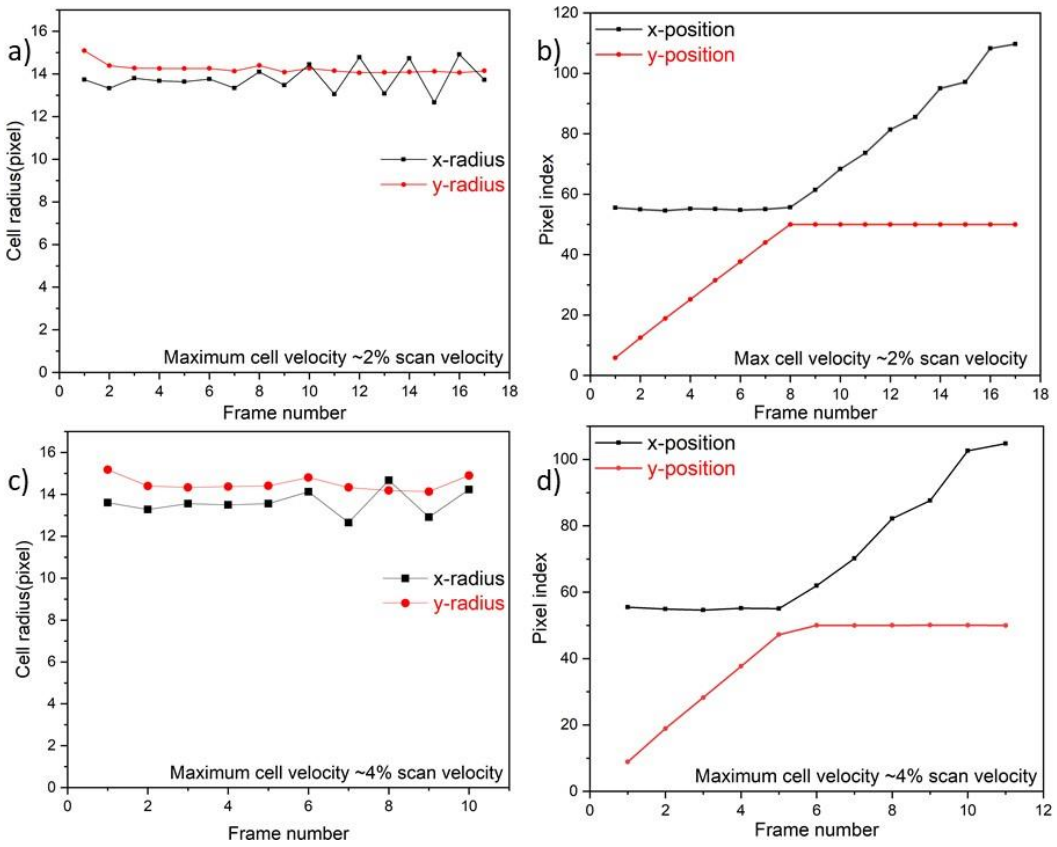

Figure 5-12. Results of the simulation of the cell distortion due to the motion of the cells with respect to the scanning beam velocity for a circle of radius 14 µm. a) the radii in x- and y-direction and b) the position of the circle for a maximum cell speed ~ 2% of the scan velocity which is equivalent to the Q = 5 µl/min data. c) the radii and d) the position of the circle in the FOV for maximum cell speed ~4% of the scan velocity, equivalent to Q = 10 µl/min data.

To further observe the extent of the distortion for higher flow rates, the simulation was conducted for cell speeds equivalent to 7, 10 and 20 % of the scanning beam velocity. These correspond to Q = 17, 24 and 48 µl/min flow rates, respectively. Figure 5-13 show the cell radii in both x- and y-directions in the FOV for the simulations. We observed that the fluctuation in the cell size became greater for these flow rates compared to that in Figure 5-12. The cell area distortion showed exponential growth with the increasing flow rates under this simulation (Figure 5-13d). Hence, it implies from the simulation that at lower flow rates of the FDM experiments (Q = 5 and 10 µl/min) the distortion is relatively lower as corroborated from the actual experimental data.

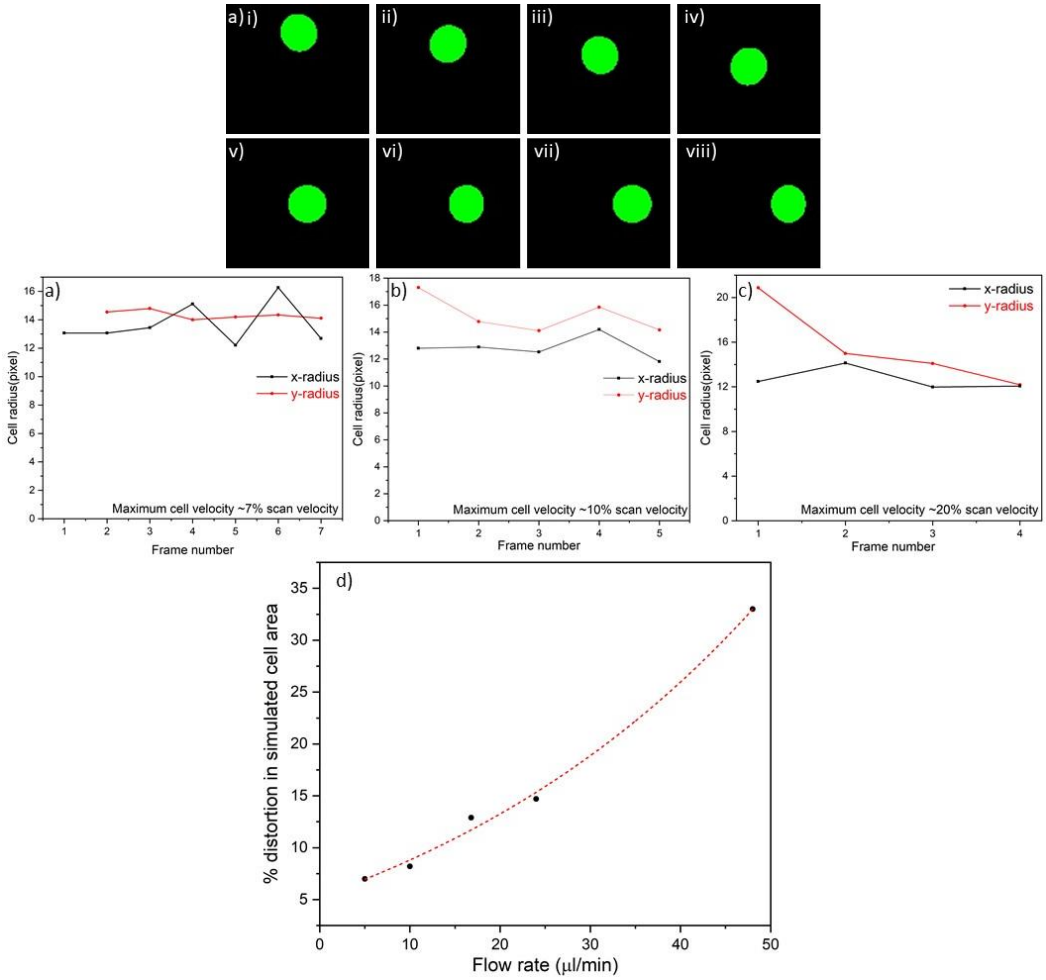

Figure 5-13. Results of the simulation of the cell distortion due to the motion of the cells with respect to the scanning beam velocity for a circle of radius 14 μm. a) Typical images of the simulated circle showing distortion, moving at a cell speed of 7 % of the scan velocity. The cells move downwards for images i-iv and across towards the right for images v-viii. The cell radii in x- and y-directions for cell speed equal to b) 7, c) 10 and d) 20 % of the scanning beam speed. e) the percentage distortion in the area of the cell as measured by the simulation of cell distortion with respect to the flow rate. The fitting curve(red line) is an exponential growth with $R^2 > 0.99$.

5.2. FDM of Calcein intensity in cells post-deformation

We have seen that there was a leakage of intracellular material on hydrodynamic deformation of the cells at the extensional flow junction of the cross-slot microfluidic device. The deformation generates transient membrane pores very rapidly through which the diffusion occurs. However, the membrane pores should remain active post-deformation as it facilitated the uptake of QDs. To understand the membrane pore dynamics with time and its effect on the leakage of intracellular material, MCF7 cells stained with 1 μM calcein were imaged using

the FDM microscope post-deformation at the outlet channel at Q = 100 µl/min as described in section 2.16.2.

This experiment was performed by imaging cells immediately after the deformation at the extensional flow junction along one of the outlet channels at regions 1 and 2 separated by 750 µm (end-to-end) as shown in Figure 2-11. The imaging process was triggered by the fluorescence in the FOV and single images of a large number of cells (>2800 cells each) were taken at these two regions. Here, the beams scan in only one direction giving raw bright field and fluorescent images for the cells with calcein as shown in Figure 5-14.

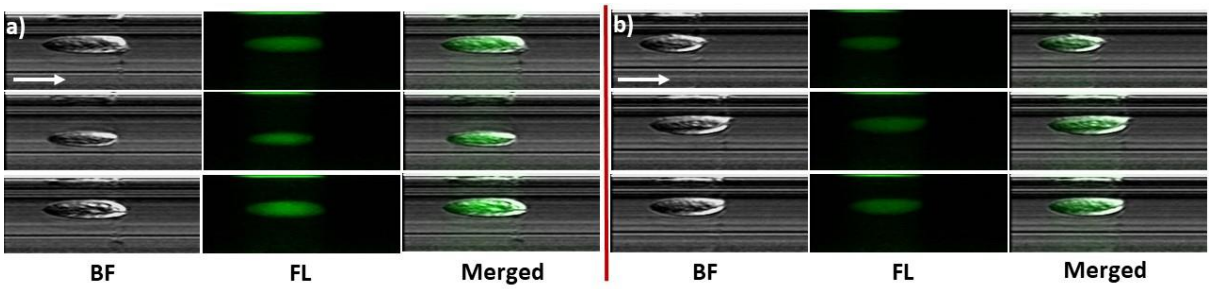

Figure 5-14. Typical FDM images of the MCF7 stained with calcein cells without distortion corrections (Bright field, FL channel and merged) post deformation at a) region 1 and b) region 2. The arrows represent the direction of flow.

The images were generated assuming the flow speed was constant (0.952 m/s). Artefacts such as multiple cells in an image and image capture due to fluorescent cell debris were removed manually before analysis. Similar to the raw images as seen in the extensional flow junction, these single snapshot images are also distorted due to the scanning beam velocity profile and the luminescence was affected by the fluorophore lifetime. Here, since the cell flow speed was constant, these image dimensions were corrected by simply using the following equations:

$$Horizontal\ FOV\ (\mu m) = \frac{Horizontal\ pixel\ nimber \times flow\ speed\ (^{m}/_{s})}{pixel\ scan\ rate\ (MHz)} \quad (5.11)$$

$$Veritical\ FOV\ (\mu m) = 0.84\ (\mu m) \times vertical\ pixel\ number \quad (5.12)$$

Here, Horizontal FOV refers to the direction of the cell flow (x-direction) and the vertical FOV is the direction of the beam alignment (y-direction). The pixel scan rate of the FDM during these experiments was 4.1015625 MHz. For the raw images, the number of pixels was 252 and 100 in x- and y-directions, respectively. Hence, the dimensions of the FOV were 58.5 µm and

84 µm in the x- and y- directions, respectively. Figure 5-15 show the images of the cells in Figure 5-14 after these corrections were made.

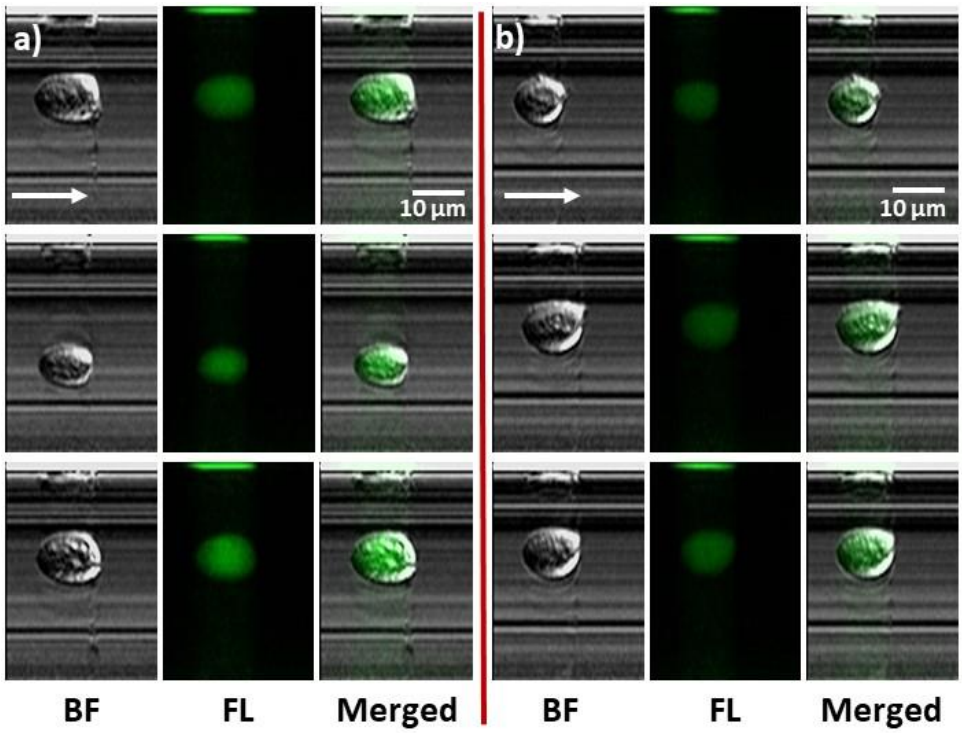

Figure 5-15. Typical FDM images of the MCF7 stained with calcein cells with the distortion corrections (Bright field, FL channel and merged) post deformation at a) region 1 and b) region 2. The arrows represent the direction of flow.

With the pixel distortion corrections, the cells appear to be more rounded. However, for region 1, which is closer to the stagnation point, we can see the reminiscence of the deformation as the cells have not fully recovered. The DI of the cells was measured by considering an elliptical fit for the cells using a phyton code. The DI was calculated from the ratio of the major and the minor axes of the fitted ellipse. From figure 5-16a, we observe that the DI of the cells at region 1 is ~1.25 and become more circular with DI ~1.14 at region 2, where they showed more recovery of their shape.

The correction due to the fluorescence lifetime effect of the fluorophore was also performed for these images as described earlier using equation 5.4. The raw fluorescence intensity of the images was multiplied with the amplitude of the function $R(y)$ in correspondence to the pixel index along y-direction for a lifetime value of τ = 2.9 ns for calcein. The total fluorescent

intensity from the cells was measured using the same python code at these two regions by assuming elliptical fitting for the cell in the bright field image, tracing the ellipse to the corresponding fluorescent image and measuring the total intensity.

The distance between these regions on the microfluidic device is ~750 µm and the time taken to travel between them would be ~0.8 ms for Q =100 µl/min. From Figure 5-16b, there is a drop in the mean total fluorescence intensity from the cells between region 1 to region 2 of 4.73 %. This implies that there is leakage of calcein from the cells post-deformation. The membrane pore remains active after the deformation and continuing leakage of intracellular material. This shows that although the formation of membrane pores is rapid during deformation, they do not immediately close and remain active for a period of time. The scatter plots of the total PL intensity from the cells with respect to cell size show more scattered size distribution in region 1 (Figure 5-16c and d). This could be due to the higher deformed state of the cells in region 1 as compared to region 2, where the cells regain their spherical shape.

It could be understood that the majority of the uptake could take place when the cell regains its volume post deformation by the uptake of the extracellular fluid. The cell suffers a loss of volume at deformation due to the expulsion of intracellular material. The cells subsequently recover in volume by the uptake of the suspension fluid through the pores which have been described as volume exchange in previous studies of microfluidic cell deformation [272].

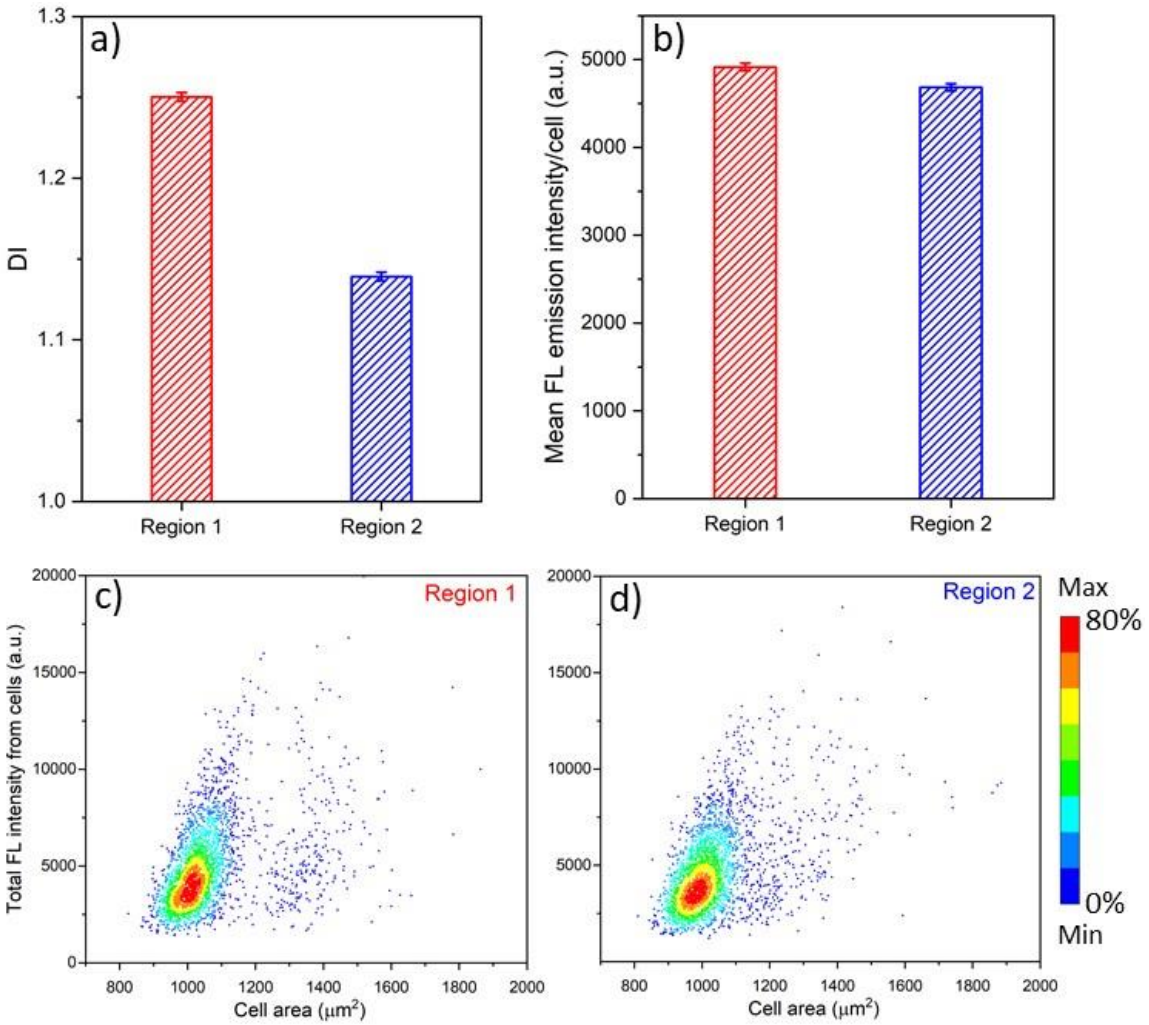

Figure 5-16. FDM analysis of MCF7 cells stained with calcein, post deformation at regions 1 and 2 (Q = 100 µl/min). Comparative a) DI, b) mean total fluorescence emission intensity from the cells for the two regions (Data expressed as mean ± SE). The 2-sample t-test showed the p-values for the pair were <0.001. The scatter plots show the total fluorescence intensity from the cells as a function of cell area for regions c) 1 and d) 2.

5.3. Uptake of Au-FITC particles by cell deformation

To have insight into the nature of membrane poration by hydrodynamic deformation of cells using the cross-slot microfluidic device, it is essential to know the size of the pores through the uptake of larger particles. Uptake of differently sized particles by the cells as a function of the flow rate through the device would give indications of the pore size. A previous study has shown uptake of dextran-FITC particles of various sizes by deformation through the cross-slot microfluidic device [170]. However, the uptake of inorganic NPs, which can have the

advantages of easily tunable size and surface functionalisation, had not been demonstrated [273–275].

Colloidal Au-PEG-FITC NPs of different sizes were synthesised according to the methods described in section 2.17. The smallest Au NPs for the uptake experiments (Batch A) were synthesised by the rapid injection of the reducing agent, $NaBH_4$ into a mixture of sodium citrate and $HAuCl_4.3H_2O$ in Milli-Q water under vigorous stirring [253–255]. Larger Au NPs (Batches B and C) were synthesised using the well-known Turkevich method as described in section 2.16.2 [256–258]. By varying the amount of sodium citrate added dropwise to the boiling Au-precursor ($HAuCl_4.3H_2O$), the size of the particles can be controlled. Table 5-1 gives the molar ratio of the Au-precursor to sodium citrate used for the synthesis of these batches of Au NPs. The Au NPs were pelleted by centrifugation at 15,000 g, the supernatant was removed and the particles were redispersed in Milli-Q water. The absorbance spectra of the ×10 diluted colloidal solution were used to determine the particle concentration (Figure 5-17a). The surface plasmon resonance peaks were used to determine the amount of Au for absorbance =1. To conjugate the Au NPs with the fluorescent PEG-FITC, 1 ml of 250 µg/ml PEG-FITC was added to the colloidal Au NPs solution with an amount equivalent to an absorbance of 1 and incubated overnight under stirring in the dark. Excess unbound PEG-FITC were removed by centrifugation at 15,000 g which remained in the supernatant. The pelleted Au-PEG-FITC NPs were resuspended in Milli-Q water. The wavelength (λ_m) of the surface plasmon resonance peak is also indicative of the size of the particles [276]. Batch A shows the lowest λ_m at 506 nm, with 528 nm for batch B and highest for batch C at 548 nm, showing the difference in the size among batches.

Batch	$HAuCl_4$:Sodium Citrate Molar Ratio	Hydrodynamic size from DLS (nm)	Particle diameter from TEM (nm)	Absorbance Peak (nm)
A	1:0.66	16 ± 6	4.3 ± 1.6	506
B	1:1.94	55 ± 14	43.3 ± 8.6	529
C	1:1	79 ± 23	77.5 ± 11.8	548

Table 5-1. Comparative table of the Au-FITC particles used for the uptake study in MCF7 cells using microfluidic deformation experiments showing the ratio $HAuCl_4$:sodium citrate during the synthesis to control the particle size, hydrodynamic size from DLS, particle diameter from TEM (mean ± SD.) with the corresponding wavelength for absorbance peak maxima.

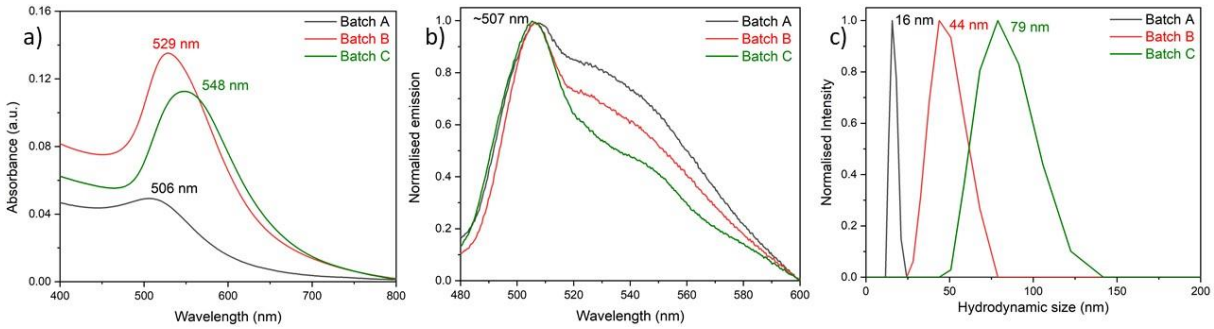

Figure 5-17. Optical characterisation of Au-FITC NPs. a) The absorbance spectra, b) the emission spectra and c) hydrodynamic size measured using DLS of the Au-FITC NPs for different batches having different sizes.

The normalised fluorescence emission spectra of the Au-PEG-FITC NPs are shown in Figure 5-17b. The emission peak wavelength was observed ~507 nm for all the batches. The PL emission of the particles will depend on the number of PEG-FITC ligands on the particle surface. Since Batch A was significantly smaller, it will be accommodating fewer fluorescent ligands as compared to batches B and C. Hence, the PL emission per particle would depend on the number of the ligand attached to the NPs surface. As such, over the population of particles, Batch C would be the brightest, followed by Batch B and finally Batch A.

The hydrodynamic particle size was determined using the DLS as shown in Figure 5-17c. Batch A shows a hydrodynamic size with maxima at ~16 nm and having a narrow distribution peak compared to its TEM images giving a mean size of ~4.3 ± 1.6 nm (Figure 5-18a). This showed that the conjugation of PEG-FITC ligands increases the hydrodynamic radius of these particles significantly. Batches B and C show the hydrodynamic size peaks from DLS at ~55 and ~79 nm, respectively. The peak width for the size distribution increased with the particle size between different batches.

The particle size of the different batches of Au-PEG-FITC was determined from the TEM images (Figure 5-18). The particles are not perfect spheres, a such, the diameter was measured in two perpendicular directions for each particle and averaged over a large number of NPs. The size distribution histogram fitting curves (log-normal) shown in Figure 5-18d gives the average size of the NPs ~ 4.3 nm, 43.3 nm and 77.5 nm for Batches A, B and C respectively (Table 5-1). The size distribution was significantly narrow for Batch A as compared to Batches B and C. This correlates with the size distribution as seen from the DLS measurements. The DLS

measurements show a larger particle size for all the batches in comparison to the TEM analysis. This is due to the presence of the PEG-FITC ligand which increases the hydrodynamic size of the particles.

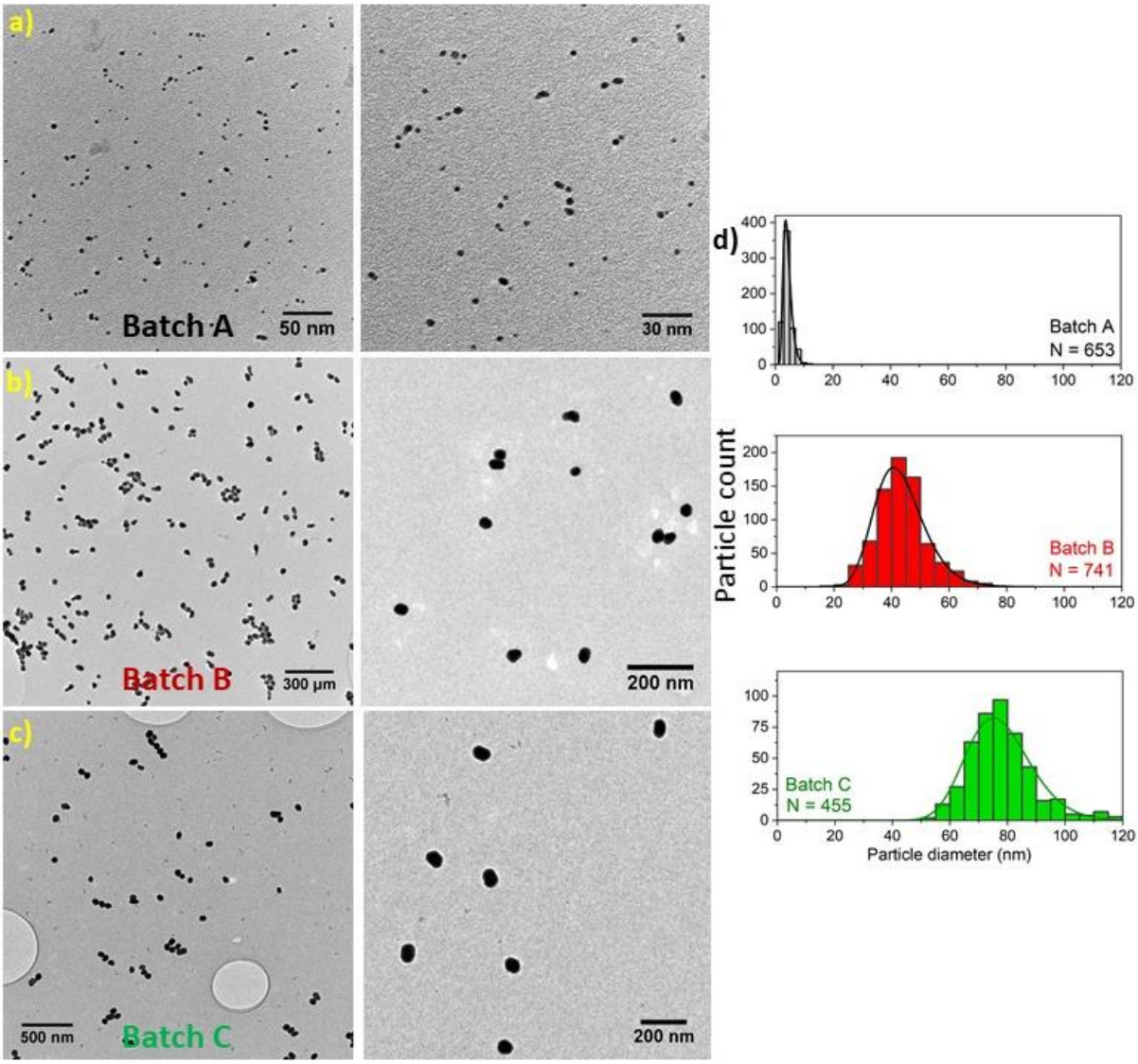

Figure 5-18. TEM images of the Au-FITC NPs of different sizes used for the uptake study in MCF7 cells using microfluidic deformation experiments for a) batch 'A', b) batch 'B' and c) batch 'C'. d) Size distribution histogram of the Au-FITC NPs from the TEM images with log-normal fitting curves.

MCF7 cells were treated with different sized 10 nM number concentration of Au-PEG-FITC NPs (Batches A, B and C) in buffer (DPBS + 0.5% MC w/v) as described in section 2.15. The cells were deformed through the cross-slot microfluidic device at different flow rates (Q =0-150

µl/min), washed twice with DPBS to remove the excess NPs and suspended in DMEM culture media. 8-well incubation chambers (Lab-Tek II, VWR International) were used to image the cells using the confocal microscope. The typical confocal images of cells deformed hydrodynamically through the cross-slot microfluidic device with the different sized Au-PEG-FITC NPs are shown in Figure 5-19 in comparison with the control cells which were incubated without deformation for the same duration. The images showed uptake of the NPs of different sizes for the control incubated cells (Q =0 µl/min) which is through the endocytic pathways. For the deformed cells, the smallest Au-PEG-FITC particles (Batch A), show increasing PL-intensity with flow rate through the microfluidic device (Figure 5-19a). However, the change in the PL-intensity for the other NPs (Batches B and C) from the cells with deformation was not evident from the visual inspection of the confocal images (Figure 5-19b, c).

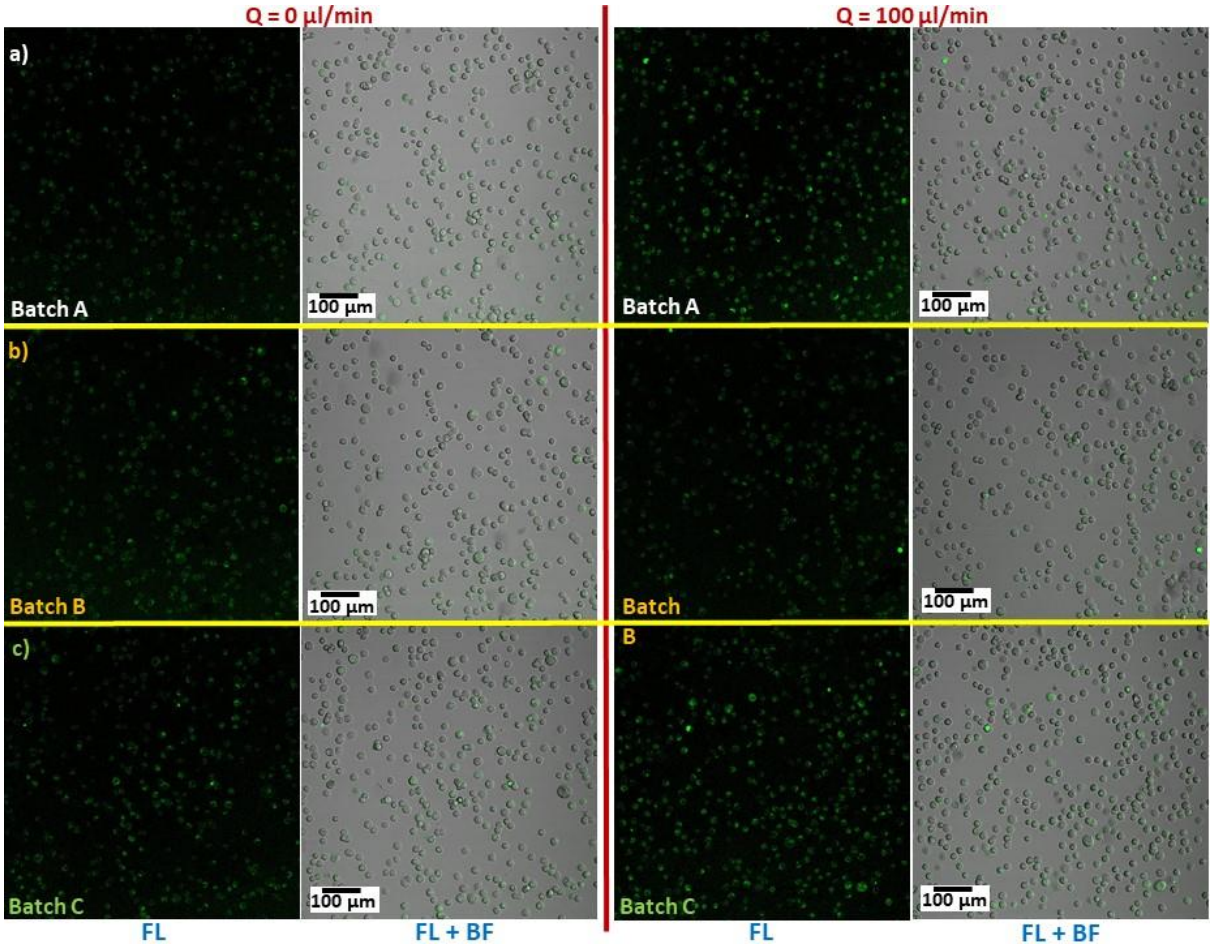

Figure 5-19. Typical confocal images of MCF7 cells deformed with 10 nM number concentration Au-PEG-FITC NPs at Q = 0 µl/min (incubated control) and 100 µl/min flow rates through the cross-slot microfluidic device for different sized NPs at a) 4.3 nm (Batch A), b) 43.3 nm (Batch B) and c) 77.5 nm (Batch C) particle sizes.

The comparative analysis of the confocal images to measure the PL intensity from the cells deformed with Au-PEG-FITC NPs of different sizes using MATLAB code (Section 2.6.1) is shown in Figure 5-20. From the percentage change in the mean PL intensity as a function of flow rate, it was observed that the uptake of the smallest NPs (Batch A) followed a similar trend as the QDs with the increase in uptake with flow rate. However, the rate of percentage increase of PL intensity from cells for the Batch A NPs (~33% at Q = 150 µl/min) was much lower than the QDs (~83% at Q = 150 µl/min). The hydrodynamic size of the QDs could be much smaller than these NPs (~16 nm), as such, the uptake of QDs across the membrane pores can be higher. It is important to note that the DLS measurement of QDs was not carried out due to their small size (~2.5 nm), which would result in improper scattering results. In addition, the wavelength of the incident laser (633 nm) used to study scattering in DLS overlaps with the PL-emission wavelength of the QDs (500-700 nm), as such, the results would not have been reliable.

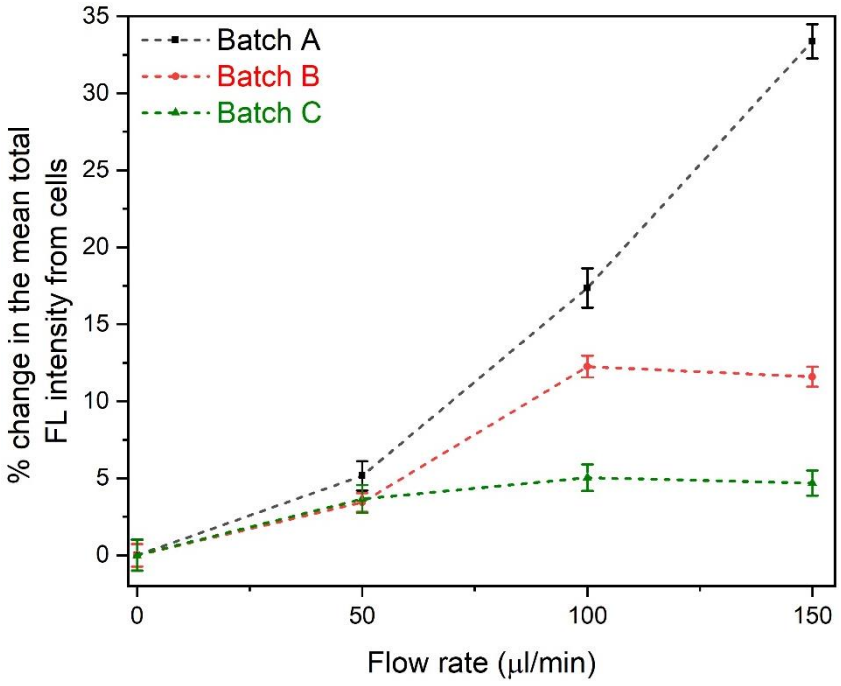

Figure 5-20. Comparative percentage change in the total PL emission intensity from confocal images of MCF7 cells with flow rate through the cross-slot microfluidic device for cells deformed with 10 nM number concentration AU-FITC NPs of different sizes (Batch A = 4.3 nm, Batch B = 43.3 nm and batch C =77.5 nm). Data represented as mean ± SE for N = 2 repeats for each data point having a total of >3200 cells.

For the Au-PEG-FITC NPs with bigger sizes (Batch B and C), the increasing trend in uptake with increasing flow rate was not observed. Batch B showed a small increase in the particle uptake up to Q = 100 µl/min, beyond which there was no significant change with increasing flow rate. For batch C, which was the largest NPs used for the experiments (~79 nm hydrodynamic radius), the increase in the uptake with flow rate was less than 5% even at higher flow rates. As such, the larger particles did not show a significant increase in the uptake with the deformation of cells through the cross-slot microfluidic device. This implies that the membrane pores are not large enough to allow significant diffusion and non-endocytic uptake of these larger NPs. For the same flow rate, uptake of smaller particles was higher which is attributed to the size of the membrane pores. Larger particles were not able to diffuse through the smaller pores into the cell cytoplasm. For the larger NPs (Batch B and C), the uptake increases up to Q = 100 µl/min flow rate, beyond which there is no notable increase. This implies that the size of the pore at different flow rates/deformation has a certain maximum value, which could be investigated in greater detail in future studies.

From the scatter plots of the fluorescence emission intensity from the cells deformed with Au-PEG-FITC NPs (Figure 5-21) as a function of cell area, larger cells tend to uptake more particles which were also observed for the QDs (Figure 3-10). The scatter plot for the emission intensity for cells deformed with Batch A NPs showed an increasing trend with flow rate (Figure 5-21). For Batch B, the scatter plot showed a less significant change with increasing flow rates. The incubated control scatter plot (Q = 100 µl/min) for this sample showed a small population deviation (~5%) from the normal uptake trend, which could be an anomaly. The scatter plots for Batch C did not show any significant change from the control incubated samples, implying that the change in uptake was not significant with cell deformation. Overall, more evidence is needed to support the findings with more repeats and the inclusion of a wider range of particles sizes in the study.

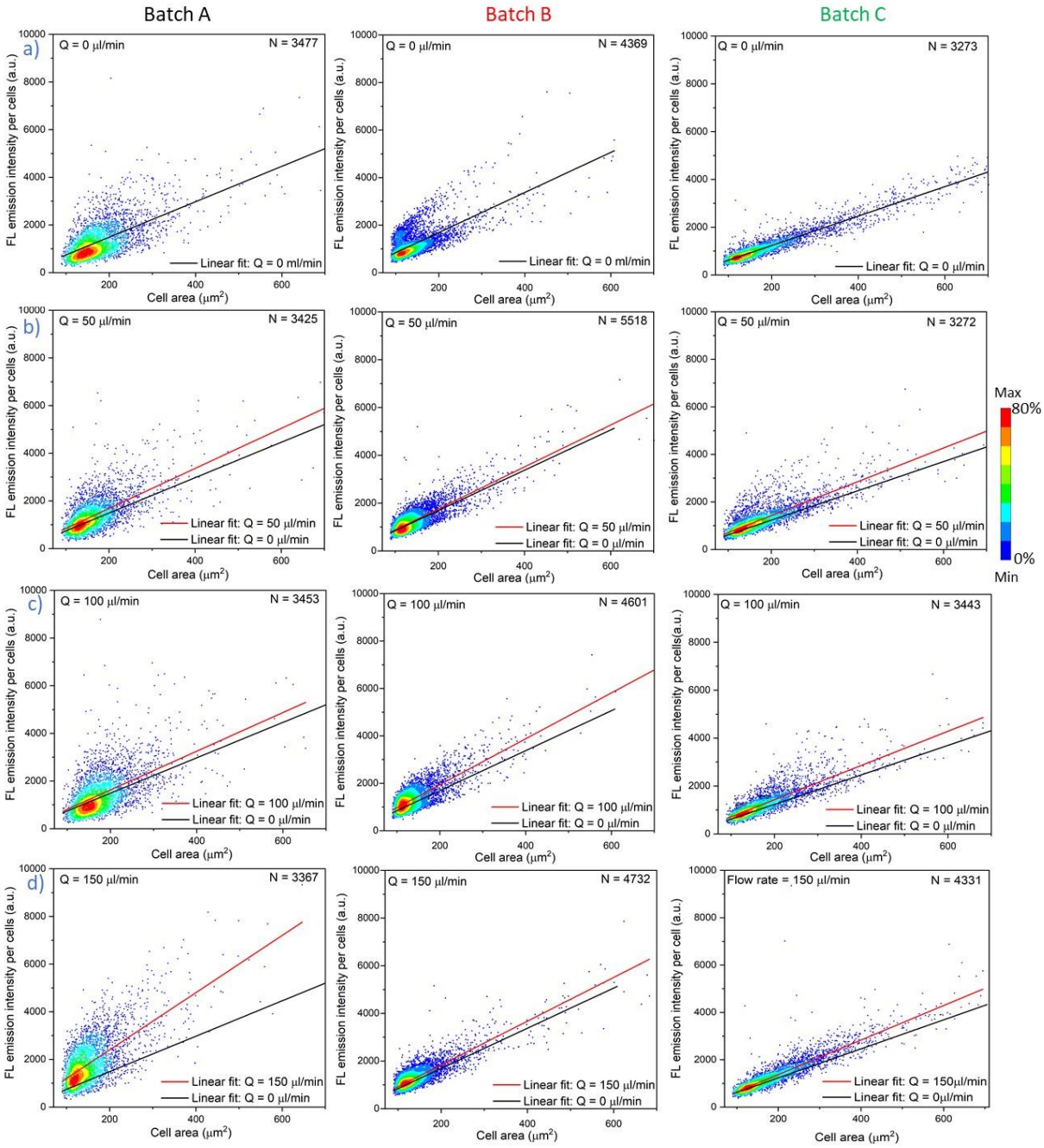

Figure 5-21. Density scatter plots of the Total fluorescence emission intensity from the confocal images of MCF7 cells deformed through the cross-slot microfluidic device with 10 nM number concentration Au-FITC NPs of various sizes (Batch A= 4.3 nm, Batch B= 43.3 nm and batch C= 77.5 nm) at Q = a) 0 µl/min (incubated control) b) 50, c) 100 and d) 150 µl/min flow rates.

5.4. Concluding remarks

In this chapter, we have investigated the membrane poration by hydrodynamic deformation of cells in the cross-slot microfluidic device through the outflow of intracellular materials from the transient membrane disruptions. Membrane poration by cell deformation is a rapid process and an ultrafast confocal FDM microscope was used to study the leakage of the cellular materials from the transient pores. MCF7 cells were stained with the cytoplasm label calcein and deformed through the cross-slot microfluidic device at low flow rates of Q = 5 and 10 µl/min. The deformation events were imaged at the extensional-flow junction with the FDM for both bright field and fluorescence channels. The slower flow rate (Q = 5 µl/min) gave 30-31 frames for the deformation events, whereas 10-12 frames were obtained for the deformation events at Q = 10 µl/min.

The FDM images needed corrections due to the inherent properties in the operation of the microscope. The images are procured by an array of laser beams which scans the FOV to-and-fro along the x-direction. The scanning beam had a simple harmonic oscillator velocity profile, with the scan rate faster at the centre of the FOV and slower at the edges. This caused image distortion along the x-direction with pixels being compressed at the centre and elongated at the edges. This correction termed as 'squaring of the pixels' were performed with the help of an FDM image of a graticule that has evenly spaced parallel lines. The distortion on the FDM image of the graticule was fitted with a spline function and applied all the images of the cells to square the pixel using a custom MATLAB script. The correction results in the decrease in the total PL intensity measured from the cells.

The fluorescence lifetime of the fluorophore limits the frequency bandwidth of the signal of the image, which is characterised by the spatial frequency response function as shown in equation 5.4. To correct the fluorescence image for this effect due to the lifetime of the fluorophore, the measured fluorescence was multiplied with the amplitude of the decay function in equation 5.4 along the y-direction using a custom Python code. The lifetime effect correction also lowered the total PL intensity measured from the cells.

The final correction to the FDM images was for the distortion produced in the cell shape due to the relative motion of the cells with respect to the scanning laser beams. Cells get elongated along the y-direction due to their motion perpendicular to the scanning beams. The cells will

get elongated or contracted along the x-direction depending on whether they move in the same direction as the scanning beams or against them. The corrections to these distortions were approximated according to equations 5.5 and 5.6 in both x- and y-directions respectively and applied to all images using the same Python code. The corrections showed that the fluctuations in the cell area and the fluorescence measured dependent on the direction of the scans, were reduced. There was also a reduction in the rate of drop of fluorescence intensity with the corrections with respect to the distance travelled by the cells in the FOV. A simulation was also designed to mimic the cell deformation and it showed that the maximum cell deformation is ~8.2% for the higher flow rate (Q = 10 µl/min) which correlates with the experimental results.

Finally, with all the corrections made to the FDM images of cells at the extensional-flow junction of the cross-slot device, it was observed that there was a drop in the fluorescence intensity from the cells with deformation. The calcein luminescence dropped from the cells on deformation, suggesting there was an outflow of intracellular materials from the transient membrane pores, generated by the hydrodynamic cell stretching. The transient membrane pores, which caused the uptake of QDs as seen in the earlier chapters, also allowed the leakage of cytoplasmic materials. Hence, the flow of materials across the membrane pores is bi-directional which supports the diffusion model. It is also indicative of combined actions of diffusion and convectional flow via solution exchange about the transient membrane pores as proposed by Kizer *et al.* [170]. The cells initially undergo volume loss during deformation with the expulsion of the cytoplasmic materials from the transient membrane pores. As the cells recover their original volume with the influx of extracellular surrounding fluid, through which non-endocytic uptake of NPs was facilitated through the diffusion and convection-driven delivery [272].

To further demonstrate the loss of intracellular material through the transient membrane pores by hydrodynamic deformation in the cross-slot microfluidic device, single images of MCF7 cells post-deformation along the outlet channel were taken using the FDM. Cells stained with calcein and deformed at Q = 100 µl/min were imaged at two regions in the outlet channel separated by 750 µm. The images were corrected for the distortion due to the scanning velocity profile and the effect of the fluorophore lifetime similar to the events at the extensional-flow junction. It was seen that there was a drop of ~4.73% in the integrated

fluorescence intensity from the cells between regions separated by less than 0.8 ms duration, suggesting that there was a volume loss by the outflow of intracellular materials from the transient pores. The volume loss occurs rapidly and continues post-deformation even though the cells begin to regain their original shape. This indicates that the membrane pores remain active post deformation which can facilitate the intracellular delivery of nanomaterials. For future FDM studies, cells could be imaged at more regions further away from the extensional flow junction, post-deformation to understand the longevity and the repair kinetics of the membrane pores.

To have an understanding of the size of the membrane pores, MCF7 cells were deformed in the presence Au-PEG-FITC NPs of different sizes as a function of flow rate in the cross-slot microfluidic device. Smaller NPs (hydrodynamic size ~16 nm) exhibited linear uptake with flow rate, indicating that the size of the pores did not have any effect on the particle delivery. This result showed that the majority of the membrane pores are larger than these particles. However, the uptake of larger particles (hydrodynamic sizes ~55 and ~80 nm) did not increase with the flow rate beyond Q =100 µl/min. This indicates that the pores have a size distribution that decreased for larger size, hence preventing the uptake of bigger particles. As the uptake did not increase with the higher flow rate (Q =150 µl/min), this suggested that the increase in the deforming shear force did not have an effect on the maximum pore size. This also correlates with the results of the deformation index measurements which does not increase at higher flow rates for MCF7 cells. Hence, for similar DI, regardless of the flow rate of the cell suspension, the maximum pore size remains fairly constant. However, we have observed that the QD and smaller NPs uptake increases with flow rate (Figures 3-9 and 5-20). This implies that there are other factors governing membrane poration and hence the uptake of particles. It can be speculated that these factors can be the longevity of the pores and the average number of membrane pores on the cells. Additionally, the PL intensity could have distribution for the Au NPs in the same batch, which can affect the total fluorescence measured. The basis of a model to describe the mechanism of membrane poration and uptake of particles was attempted which is described in future works (section 8.1).

6. Enhancement of quantum yield of CdSe QRs

6.1. Background

QRs have optical properties which can be advantageous for biosensing and bioimaging such as linearly polarised emission, wider absorption cross-section, narrow emission spectra and higher extinction coefficient compared to their spherical QD counterparts. However, due to their large surface-to-volume ratio, the PLQY of QRs are very low (~1%) owing to the presence of a large number of surface traps. This chapter focuses on the enhancement of the photoluminescence efficiency of CdSe QRs with the potential for application as biological probes.

CdSe QRs stabilised with the hydrophobic TDPA ligands were synthesised by rapid sequential injections of Se-precursor into the hot Cd-TDPA complex mixture. The aspect ratio of the rods increased with the increasing number of injections. Two approaches were considered for enhancing the PLQY of the rods: epitaxial ZnS shell growth and chloride ion treatment. The surface trap passivation by ZnS shell was performed using a single-molecule precursor $Zn(DDTC)_2$, in a safe and simple method at a relatively low temperature of 120 ^{o}C. The PLQY significantly increased up to ~79% for the CdSe/ZnS and remained stable in storage. The chloride ion treatment to passivate the surface traps of the CdSe QRs was performed using $CdCl_2$ giving a maximum PLQY of ~75%, However, these chloride ions treated QRs did not show photoluminescence stability over time.

The CdSe/ZnS QRs were made hydrophilic by encapsulation with an amphiphilic polymer, a PMAL derivative. Successful transfer of the rods from chloroform to aqueous phase was demonstrated. Although optimisation and complete characterisation of these hydrophilic CdSe/ZnS QRs remains incomplete, they have the potential for biological applications which can be explored in the future.

6.2. Quantum Rod Synthesis and characterisation

The CdSe QRs were synthesised according to the method reported by Shieh *et al.* and described in section 2.17.1. [228]. The Cd-TDPA complex in the organic solvent TOPO was formed by heating the precursor mixture above 320^{o}C in a three-neck flask under a nitrogen atmosphere. The formation of the Cd-TDPA complex was indicated by the change in the colour of the mixture from opaque deep wine red to clear transparent light yellow. The precursor was cooled down to 260^{o}C gradually over 1.5 h and maintained at this temperature for the rest of the synthesis. The Se -precursor was made by dissolving 1 mmol Se in 5 ml of TOP. The solution was maintained at 120^{o}C which facilitated the dissolving of the Se. Sequential injections of 0.5 ml Se -precursor was added to the Cd-TDPA complex rapidly every 3-5 min. The formation of the CdSe seed was indicated by the change in the colour of the mixture from clear light yellow to opaque dark red. The first injection forms the spherical seeds of CdSe and with the limited Se -precursor available at every subsequent injection, the growth of the wurtzite CdSe nanocrystals was favoured in the ⟨002⟩ direction, leading to the formation of rods.

The total growth time for the rods ranged between 18 to 35 min depending on the interval between each injection (3 to 5 min) and the number of injections (6 to 7). For a typical synthesis, samples were extracted before every injection to monitor the growth of the rods. All samples including the final QR solution was rapidly quenched in an ice bath to prevent rounding of the particles. The QRs were cleaned by centrifugation by two cycles of washing with ethanol and suspended in hexane or chloroform for analysis. The samples show a visible change in colour with every injection as it goes from orange to deep red (Figure 6-1a). Under UV-light, the emission of the samples shows a significant redshift with every injection from yellow to deep red (Figure 6-1b).

6.2.1. Optical characterisation of CdSe QRs

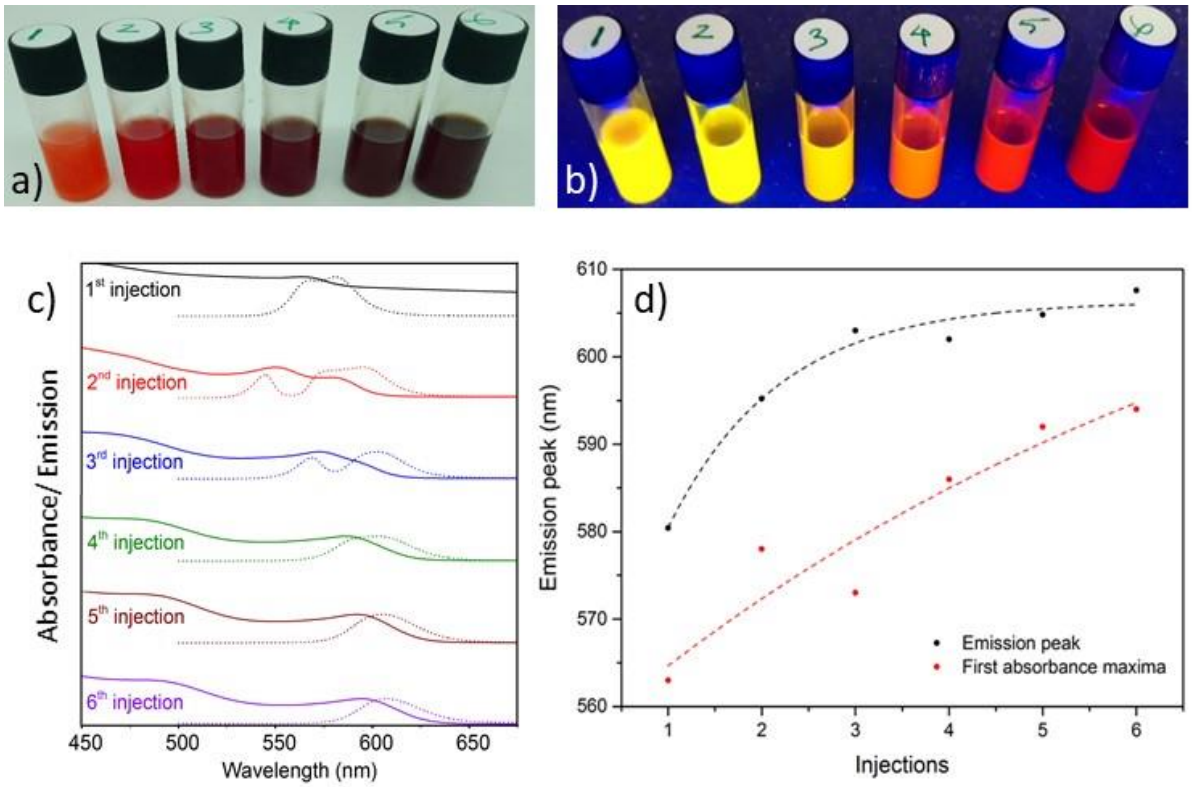

Figure 6-1. QRs at different stages of Se -precursor injections under a) visible light and b) UV-light. c) PL and the UV-vis spectra of the QRs at different stages of growth. Solid lines and dotted lines represent absorbance and emission spectra, respectively. d) the wavelength of the lowest energy fluorescence emission peak and the first absorbance maxima with the number of Se-precursor injections (the guidelines for the data are exponential decay curves).

From the PL emission spectra of the QR with 3 min injection intervals, it was observed that there was a presence of two peaks (569 and 581 nm) after the first injection. This suggested that there was variation in the seed sizes at this stage of the synthesis. Also, from the UV-vis absorption spectra after the first injection, high baseline absorbance was observed which indicates the presence of aggregates. Further, it was seen from the PL spectra that there were multiple peaks between the 2nd and the 3rd injections, suggesting that there are particles of different sizes at the different stages of the formation of the rods (Figure 6-1c). The injections were producing new seeds in addition to the elongation of the existing ones at this stage. However, the peaks merge into one after the 4th injection, which indicated the process of Ostwald ripening, which is the disintegration of the smaller particles contributing to the growth of the larger ones within the reaction mixture. By the 5th and 6th injections, the particles

showed a narrow emission peak (FWHM = 36 nm after the 6th injection) with Gaussian distribution suggesting the presence of monodispersed particles. The lowest energy emission peak maxima show significant initial redshift with Se-precursor injections which slowed down for a higher number of injections (Figure 6-1d). From the UV-Vis spectra, it was observed that there is a redshift in the position of the first absorbance maxima with the increasing number of Se -precursor injections.

The PL lifetime decay curves for the QR samples at different stages of Se-precursor injection were taken (Figure 6-2a) and the normalised PL-intensity was fitted to a bi-exponential decay function:

$$I = y_0 + A_1 e^{-t/\tau_1} + A_2 e^{-t/\tau_2} \qquad (6.1)$$

τ_1 and τ_2 are the time constants with A_1 and A_2 as the corresponding amplitudes. The results of the exponential fits (R^2 values for mono and bi-exponential fits are given in Appendix 9.18, Table 9-1). The time constants are plotted in Figure 6-2b as a function of the number of Se-precursor injections. The shorter time constant (τ_1) is indicative of the excited electron capturing event from the conduction band by the surface traps on the QR surface. The surface traps rapidly take away the electrons which ultimately make their way to the valence band to recombine with the holes in a non-radiative process. τ_1 recorded at the first injection (~6.4 ± 0.1 ns) was relatively high due to the different seeding sizes and the scattering events also observed in the UV-vis spectra. This value dropped to ~4.3 ± 0.1 ns for the 2nd and the 3rd injections which are contributed by QRs of different sizes as seen previously from the PL emission spectra (Figure 6-1a). τ_1 finally settled at ~ 2.4 ± 0.3 ns as the particles become more monodispersed. The longer time constant (τ_2) represents radiative recombination of the exciton pair. The τ_2 values decreased similar to the case of τ_1 from ~34.9 ± 0.3 ns at 1st injection to 25.9 ± 0.2 ns for the 3rd injection. Although the τ_2 keep decreasing slightly with the increasing number of injections, they remained fairly constant ~18.5 ± 0.9 ns after the 4th injection. From Figure 6-2c which shows the decay amplitudes with the number of injections, A_1 fluctuated initially due to the reasons mentioned above and after the 4th injection, when the particles become more monodispersed, it had an increasing trend. This is due to the increase in the surface defects with the increasing aspect ratio of the QRs. As the QRs elongated, the higher number of surface defects promoted more non-radiative capture of

excited electrons. Overall, τ_1 was significantly quicker than τ_2 which indicates that the electron capture by the surface traps is a faster process compared to the radiative recombination. Also, A_1 (~0.62) for the final QR product was larger than A_2 (~0.38) which showed that the electron capture by the surface traps was a more favoured process.

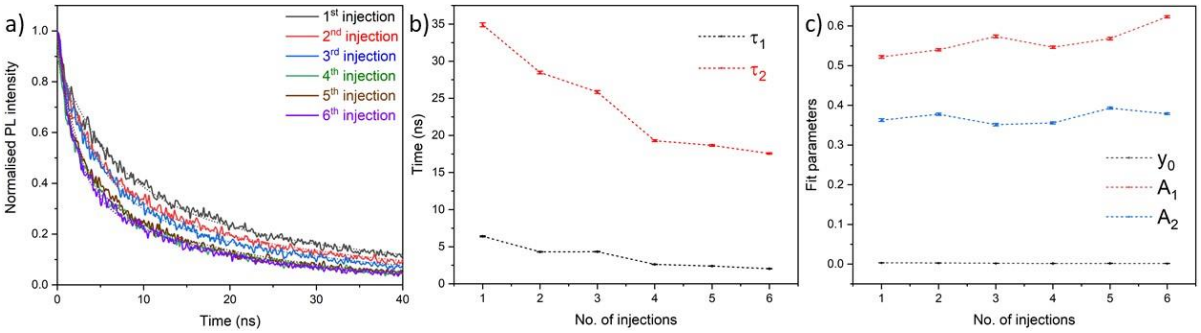

Figure 6-2. a) The normalised PL decay traces of the QRs at different stages of Se-precursor injections. The solid lines represent the actual traces and the dotted lines represents the bi-exponential decay fits (R^2 >0.99 for all cases). b) Lifetime decay constants and c) decay amplitudes of the bi-exponential fits with the number of Se-precursor injections. Data expressed as mean ± SD.

Similar to the QRs synthesised with sequential Se-precursor injections at every 3 min as shown in Figure 6-1, QRs were also synthesised at 5 min injection intervals with the typical final UV-vis and PL emission spectra shown in Figure 6-3. The emission peak was very narrow (FWHM = 31 nm) with Gaussian distribution (R^2 >0.99) which also suggests that the particles are very monodispersed. From the photoluminescence efficiency analysis of the QRs using the integrating sphere as described in section 2.3.3., we observe that the PLQY of all the QRs was <1%. This low PLQY of the CdSe suggests that it is not a suitable practical use unless the surface traps are passivated.

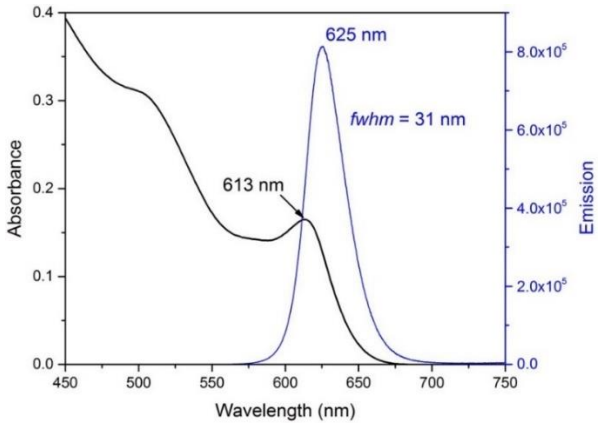

Figure 6-3. Typical UV-Vis and PL emission spectra of CdSe QRs synthetised with six rapid injections of the Se-precursors every 5 min.

6.2.2. TEM analysis of QRs

The TEM images taken using FEI Tecnai TF20 as seen in Figure 6-4 show monodispersed CdSe QRs in two different syntheses. From the analysis of the images, it was observed that the growth of the rods was controlled mainly by the number of Se-precursor injections into the Cd-TDPA complex and the interval between the injections. The number of injections controls the aspect ratio of the QDs and the intervals between the injections determine their overall size. The change in the aspect ratio of the QRs with a different number of injections was demonstrated in the next section (6.3.1).

For the two different QRs synthesised with the same number of injections (6), the size of the rods was seen to be affected by the injection intervals which is summarised in Table 6-1. The rods are thicker for the longer intervals between injections which indicates that the initial seeds in the first few injections are larger compared to the shorter intervals. However, the aspect ratio of the rods remains the same for these two different syntheses. Hence, the size and the aspect ratio of the QRs can be controlled easily, implying that this method is very consistent and the particle size and shape can be tuned as desired. The presence of tripods and tetrapods can also be seen in the TEM images amidst the QRs, but their number is very small (<2 %). Elemental mapping using the HAADF-STEM/EDX shown in Figure 6-4c exhibited an even distribution of Cd and Se throughout the rods.

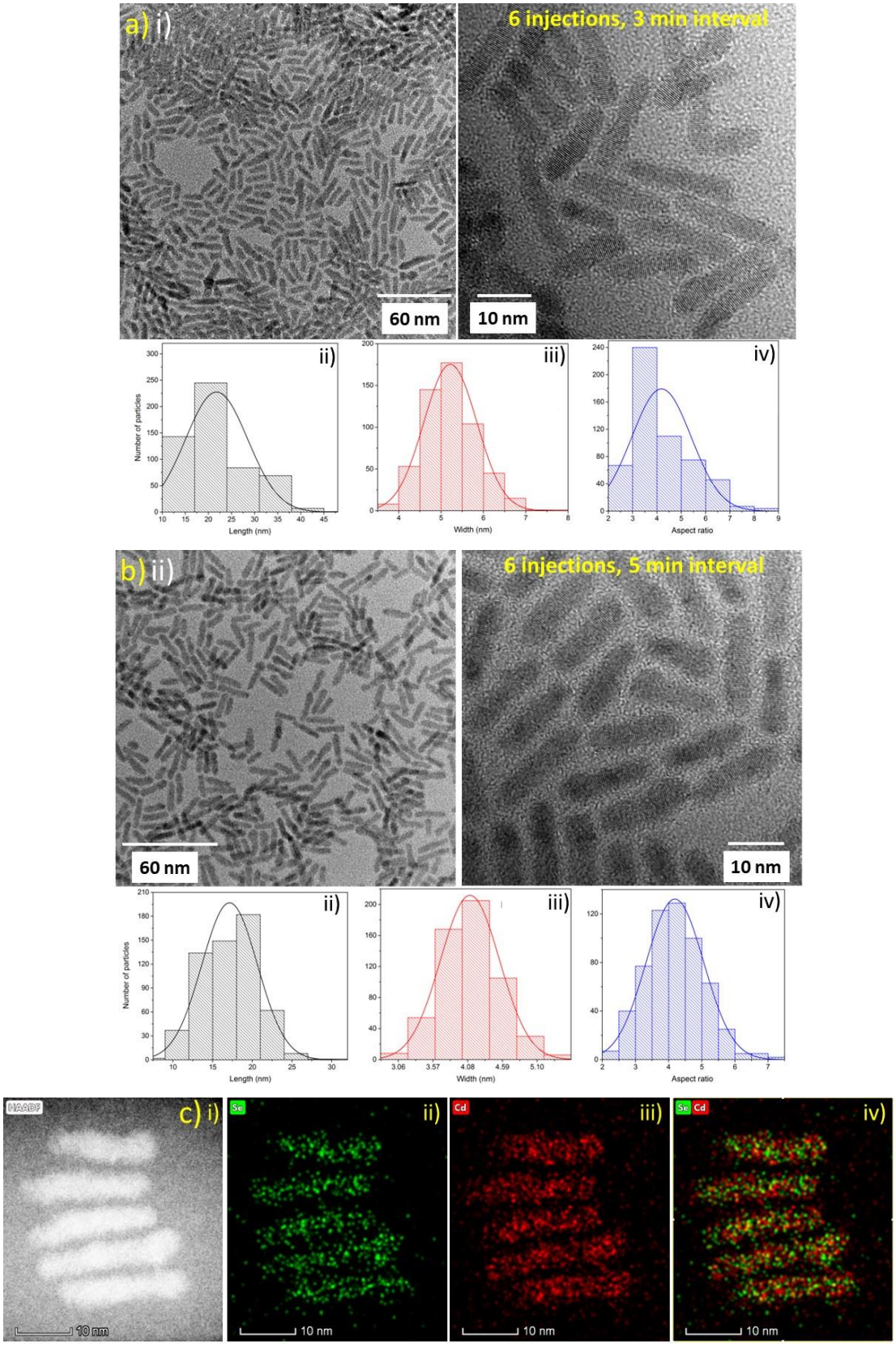

Figure 6-4. TEM images of CdSe QRs for six Se-precursor injections at intervals of a) 3 min and b) 5 min with i) dark field images, histograms of the ii) length, iii) width and iv) aspect ratio of the rods (N >500 each). c) Elemental mapping of the QRs with i) bright field and the corresponding ii) Se, iii) Cd and iv) merged maps.

No. of particles analysed	Se injection intervals (min)	No. of injections	Length (nm)	Width (nm)	Aspect ratio
576	3	6	17.1 ± 3.5	4.1 ± 0.4	4.2 ± 0.9
549	5	6	21.8 ± 6.7	5.2 ± 0.6	4.2 ± 1.2

Table 6-1. Analysis of the TEM images of CdSe QRs for six Se-precursor injections at intervals of 3 min and 5 min. Data represented as mean ± SD.

6.3. Enhancement of the fluorescence yield of the QRs

As mentioned in section 6.2.1, the PLQY of the CdSe QRs are very low (<1%), making them inefficient for practical use. This is due to the presence of a large number of surface traps that rapidly capture the electrons in the conduction band, prohibiting the radiative recombination. The spherical CdSe QDs synthesised using the same protocol but with a single injection of the total Se-precursor showed higher PLQY (~5.6%) compared to that of the QRs (0.7%) for the same duration of particle growth. The comparative optical characterisation between these CdSe QDs and QRs are given in Appendix 9.17. This was because the QRs have a much higher surface-to-volume ratio compared to the QDs, as such, more surface traps are available for the excited electrons. However, with unique optical properties of the rods over the dots, such as linearly polarised emission and wider absorption cross-section make them highly desirable for many applications. Hence, it is essential to enhance the quantum yield of the QRs to make them more attractive for practical applications. Two different methods for the quantum yield enhancement of the CdSe QRs were attempted which are described in detail below. For the purpose of demonstrating the use of QRs of different aspect ratios, the PLQY enhancement investigations were performed on rods grown for a total of 21 min with 7 Se-precursor injections administered every 3 min.

6.3.1. ZnS Shell Passivation

The epitaxial growth of the ZnS shell on the CdSe QRs was performed according to the method described in section 2.17.2 (Figure 6-6). $Zn(DDTC)_2$ was used as a single-molecule precursor in a method that is simple and safe. Assuming that the initial QR synthesis is 100% efficient, the concentration of the QRs were determined by using the mean particle size obtained from the TEM analysis. The surface area of the QRs was estimated and enough $Zn(DDTC)_2$ was used for

the shell growth to give two monolayers on the QR surface. $Zn(DDTC)_2$ was added to the as-prepared CdSe QR solution under a nitrogen atmosphere and maintained at 120°C. It was observed that the colour of the reaction mixture began to change from dull dark red to very bright red within ~15-20 min. Sample extractions were made every 30 min to track the growth of the ZnS shell. At the end of the growth (3 h), the sample was cooled to room temperature and stored in the as-prepared solution. The CdSe/ZnS core/shell QRs were cleaned by two cycles of washing with ethanol and dissolving in hexane/chloroform for further use.

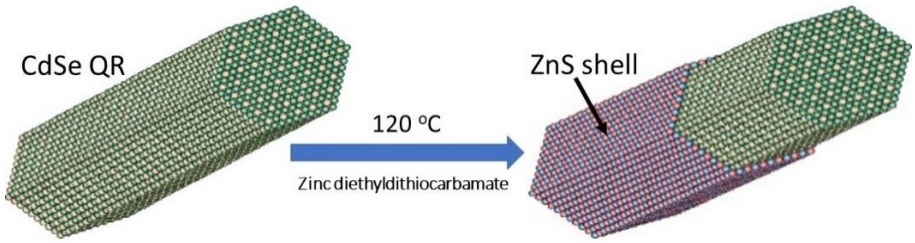

Figure 6-5. Schematic showing the ZnS shell growth on the CdSe QRs using zinc diethyldithiocarbamate.

From the PL emission spectra, it was observed that the emission intensity of the QRs increased significantly with the ZnS shell growth (Figure 6-7a). The increment in the total emission for the first 30 min itself was >2000% compared to the core CdSe QRs. With further shell growth, there was a gradual increase in the PL emission intensity up to ~2349 % compared to the untreated rods. This indicated that the majority of the surface traps are passivated within the first 30 min of shell growth. Additionally, there is a redshift for the emission peak maxima from 620 nm to 630 nm with the shell growth. However, the emission peaks do not show any broadening by shell passivation, with the FWHM (~37 nm) remaining constant throughout the shell growth. Hence, the particle monodispersity was not affected by the addition of the ZnS shell. The PLQY of the QRs show significant improvement with the ZnS shell, from 1.7 % for the CdSe cores to ~79 % for the 3 h shell growth sample (figure 6-7b). Furthermore, the PLQY of the CdSe/ZnS QRs was measured at ~53 % after six months of storage in the as-prepared solution. Although there was a drop in the photoluminescence efficiency of the core/shell QRs in long term storage, the PLQY value remained relatively high. This drop could be caused by the gradual loss of the passivating surface ligands with time, which could be investigated in the future.

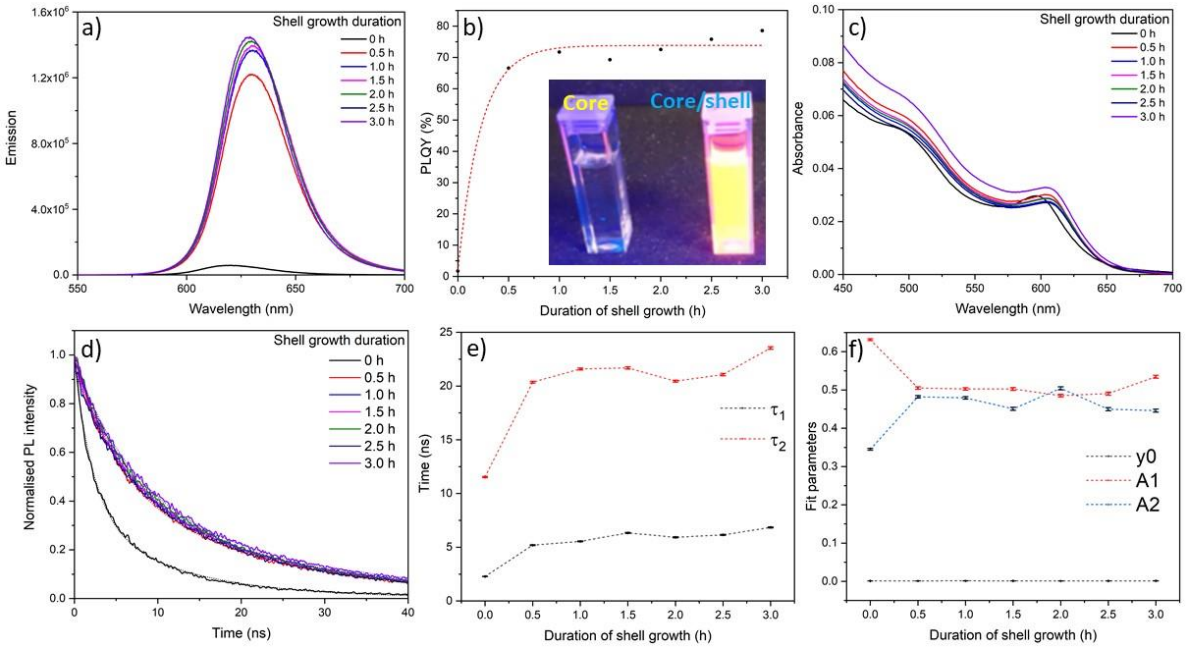

Figure 6-6. ZnS shell growth on the CdSe QRs. a) PL emission spectra, b) PLQY, c) UV-Vis absorbance spectra and d) normalised PL decay traces of the CdSe/ZnS core/shell QRs with the duration of shell growth. In b) the points are fitted to exponential decay curve (R^2 > 0.988) and the inset shows the CdSe core and CdSe/ZnS (3h shell growth) QRs under UV illumination. In d) the solid lines represent the actual traces and the dotted lines represents the bi-exponential decay fits (R^2 >0.99 for all cases). e) Lifetime decay constants and f) decay amplitudes of the bi-exponential fits with the number of Se-precursor injections. Data expressed as mean ± S.D.

Figure 6-7d represents the PL intensity decay traces with the growth of the ZnS shell on the CdSe QRs. The decay traces were fitted to bi-exponential decay curves as shown in equation 6.1 with R^2 >0.99 for all the datasets (R^2 values for mono and bi-exponential fits are given in Appendix 9.18, Table 9-2). The traces show a much slower decay trend with the addition of the ZnS shell. τ_1 which represents the capture of excited electrons from the conduction band by the surface traps, increased from ~2.3 ns for the CdSe cores to ~6.0 ± 0.6 ns for the CdSe/ZnS core/shells (Figure 6-7e). This suggests that the surface trapping process becomes much slower with the addition of the ZnS shell. Additionally, the drop in the amplitude A_1 and the consequent increase of A_2 with the shell growth indicated that the surface trapping was less favoured in comparison to the radiative recombination (Figure 6-7f). The radiative recombination time constant τ_2 also increased with the shell growth from ~11.5 ns of the cores to ~22 ± 1 ns for the core/shells. This increase can be attributed to the charge separation by

the localisation of excited electron in the ZnS shell and the overall increase in the size of the QRs [277].

From the TEM images of the CdSe and CdSe/ZnS QRs as seen in Figure 6-7, it was observed that the rods maintained their overall morphology with the shell growth. The CdSe core QRs were synthesised with seven Se-precursor injections at 3 min intervals, as such the aspect ratio is higher (5.7 ± 0.9 ns) compared to the rods discussed in the previous section with six injections (4.2 ± 0.9 ns). With the shell growth, the aspect ratio on average did not change (5.7 ± 0.9 ns) as seen in table 6-2. The mean width of the rods increased by 0.4 nm suggesting that the ZnS deposition on the side of the rods cannot be more than a single monolayer. However, the mean length increased by ~2.7 nm, indicating that there was a preferential growth of the ZnS shell at the ends of the QRs. In some cases, the rods appeared to be more bulging at the ends which could indicate the partial rounding of the particles at the ends on shell growth. However, since the QRs were not perfectly smooth rods and tend to be undulating. It is possible that a form of annealing is required to create a smooth shell or perhaps a higher shell growth temperature, these would require further studies.

Sample	No. of particles analysed	No. of injections	Length (nm)	Width (nm)	Aspect ratio
CdSe core	413	7	21.4 ± 2.7	3.8 ± 0.4	5.7 ± 0.9
CdSe/ZnS core/shell	336	7	24.1 ± 2.8	4.2 ± 0.4	5.7 ± 0.9

Table 6-2. Analysis of the TEM images of CdSe QRs synthesised with seven Se-precursor injections at 3 min intervals, with and without the ZnS shell. Data represented as mean ± SD.

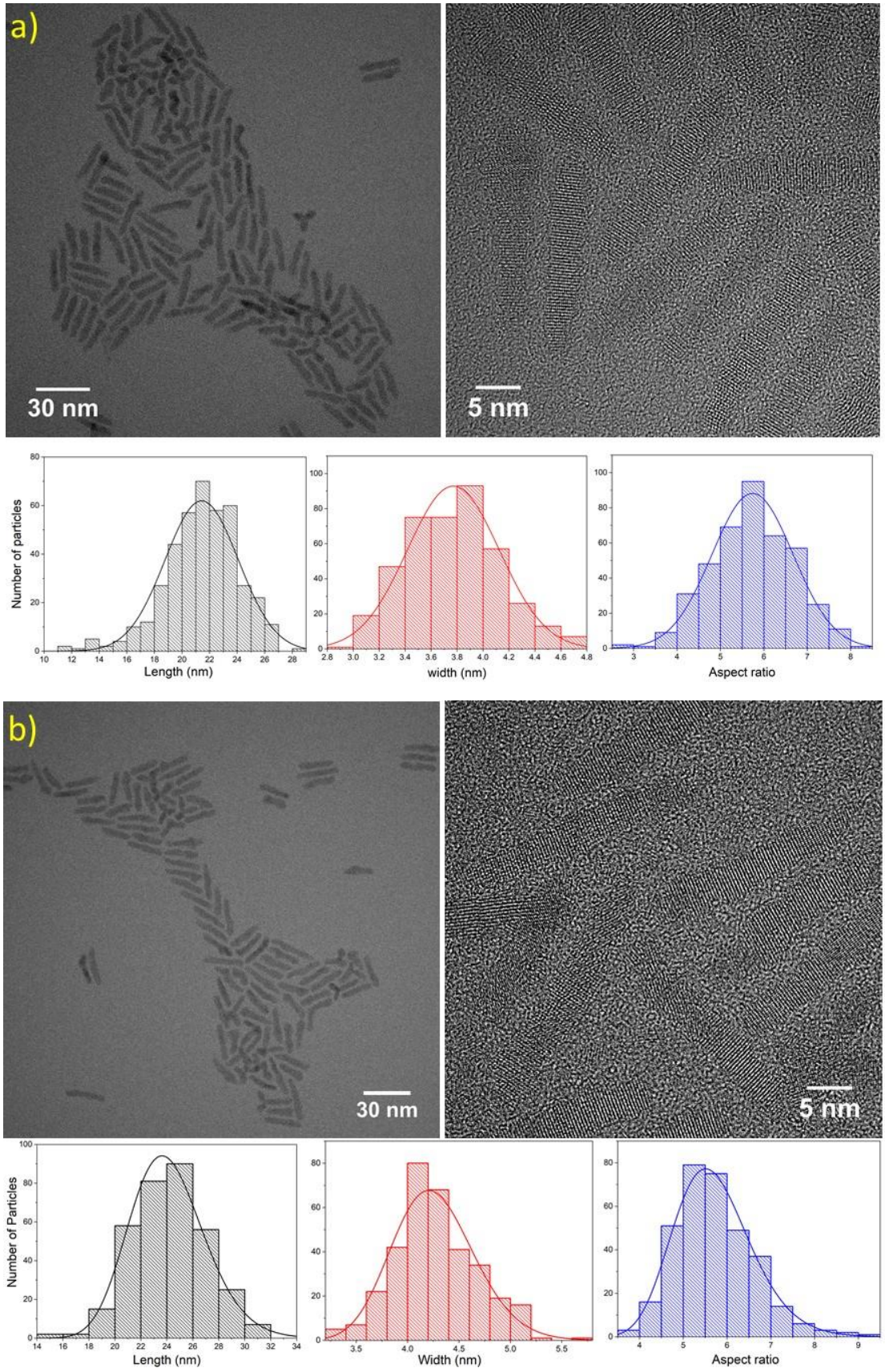

Figure 6-7. TEM images of a)CdSe core QRs and b) CdSe/ZnS core/shell QRs with histograms of length, width and aspect ratio (N >300 each). The histograms are presented with normal distribution.

6.3.2. Cl^- ion Passivation

An efficient method of passivating the surface traps for the excited valence band electrons is by treatment of the particles with chloride ions [238]. The halide ions occupy the positively charged electron traps on the particle surface through electrostatic and ionic interactions, as such, the non-radiative decay pathway becomes suppressed. The QRs were treated with $CdCl_2$ in combination with TDPA (Figure 6-8) according to the method described in section 2.18.3. The dual action of the chloride ions and the TDPA ligand efficiently passivated the surface traps. Two different concentrations of Cl^- ions in oleylamine (96 and 192 Cl^- ions/nm^2 of the QR surface) were used to investigate the surface passivation. Similar to the approximation described in the previous section, the concentration and the mean surface area of the CdSe QRs were calculated by assuming the synthesis of the rods is 100 % efficient with the help of the TEM image analysis. The total surface area of the QRs in solution was calculated and was treated with 96 or 192 Cl^- ions/nm^2 of the QR surface. The control samples were treated in the same manner with the same solvent composition but without the $CdCl_2$.

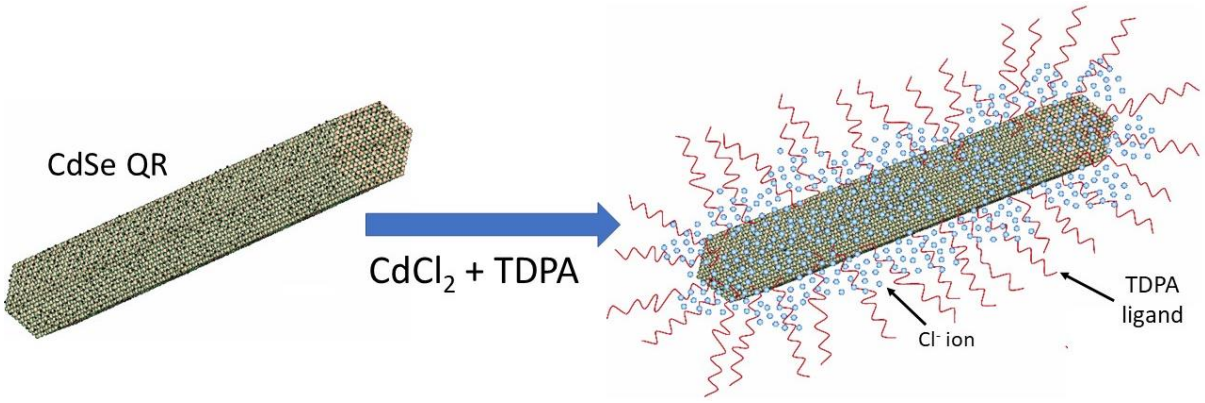

Figure 6-8. Schematic showing the passivation of the surface traps on the CdSe QRs with the TDPA-$CdCl_2$ treatment.

From the PL emission spectra, it was seen that the emission of the CdSe QDs was significantly enhanced by the treatment of $CdCl_2$-TDPA (Figure 6-9a). Higher Cl^- ion concentration showed a greater increase in the PL intensity with >1500 % and >2600 % increase for 96 and 192 Cl^- ions/nm^2 of the QR surface, respectively compared to the untreated rods. There is a blue shift in the emission peak maxima with the chloride ion treatment from ~612 nm to ~606 nm. The

PLQY of the rods also increased significantly with a maximum attained at ~75 % for the 192 Cl^- ions/nm^2 of the QR surface sample (Figure 6-9c). For the 96 Cl^- ions/nm^2 treatment of QRs with and without TDPA, the PLQY increased to ~48 % and 43 %, respectively. This suggests that there was a combined action of both the Cl^- ions and the TDPA ligands in the passivation of the surface traps. Hence, the halide surface passivation of the QRs gave significant enhancement in the photoluminescence. Further increase in the chloride ion concentration could enhance the PLQY but the difficulty in cleaning the QRs post-treatment to remove the excess $CdCl_2$ would be cumbersome. The PLQY of these treated QRs dropped significantly when exposed to the atmosphere from ~75 % to ~27 % within 24 h. The Cl^- ions oxidised readily with atmospheric exposure and suppressed their capacity to passivate the QR surface traps. It was also observed that the cleaning of the Cl^- ions treated QRs show a drop in the photoluminescence efficiency compared to the as-prepared solution (Figure 6-9d). This is due to the removal of the Cl^- ions and the TDPA ligands during the cleaning process, which lowers the passivated state of surface traps.

From the normalised PL intensity decay curves shown in Figure 6-9e, it was observed that the Cl^- ions treatment of the CdSe QRs gave a much slower decay trend compared to the untreated rods (R^2 values for mono and bi-exponential fits are given in Appendix 9.18, Table 9-3). τ_1 increased from ~1.5 ns for untreated QDs to ~7.4 ns for 192 Cl^- ions/nm^2 of QR surface, suggesting the slowing down of the non-radiative electron capturing process by the surface traps (Figure 6-9f). The increase in τ_2 with the chloride ion treatment can also be attributed to the trap passivation. Similar to the ZnS shell passivation, the amplitudes associated with the decay time constants, A_1 and A_2 are also affected by the treatment. A_1 decreases and A_2 increase with increasing chloride ions which indicates that the recombination becomes more favourable compared to the surface trapping of charge. From the TEM images as shown in Figure 6-10, the Cl^- ions did not have a considerable effect on the general morphology of the CdSe QRs.

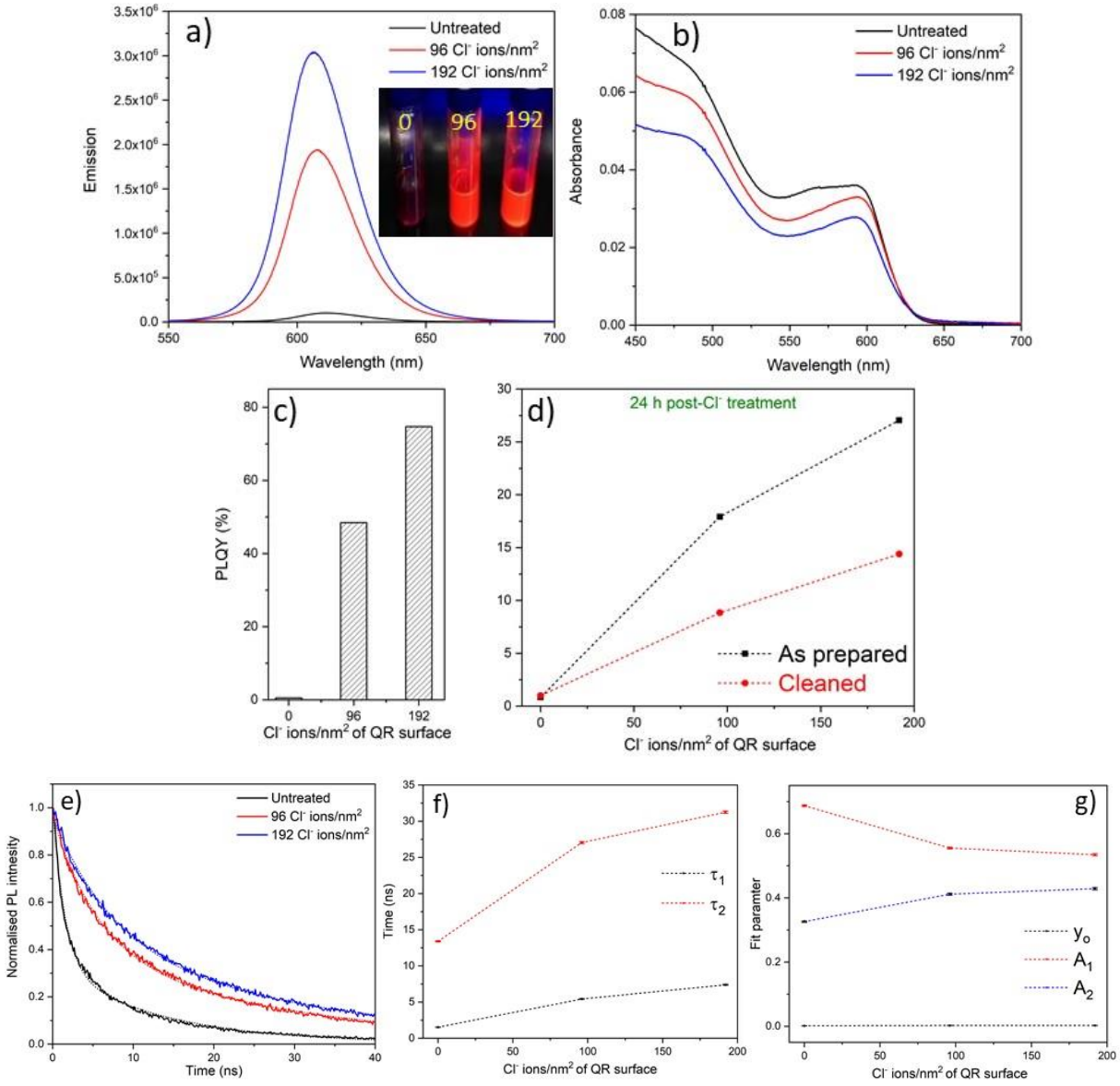

Figure 6-9. Cl^- ion treatment of the CdSe QRs. a) PL emission spectra (inset: QRs under UV-light), b) UV-Vis absorbance spectra and c) PLQY of the untreated, 96 and 192 Cl^- ions/nm^2 of QR surface. d) PLQY of the Cl^- treated CdSe rods 24 h post-treatment with and without cleaning. e) Normalised PL intensity decay traces of the Cl^- treated QRs. The solid lines represent the actual traces and the dotted lines are the bi-exponential fits ($R^2 > 0.99$ each). e) Lifetime decay constants and f) decay amplitudes of the bi-exponential fits with the number of Se-precursor injections. Data expressed as mean ± SD.

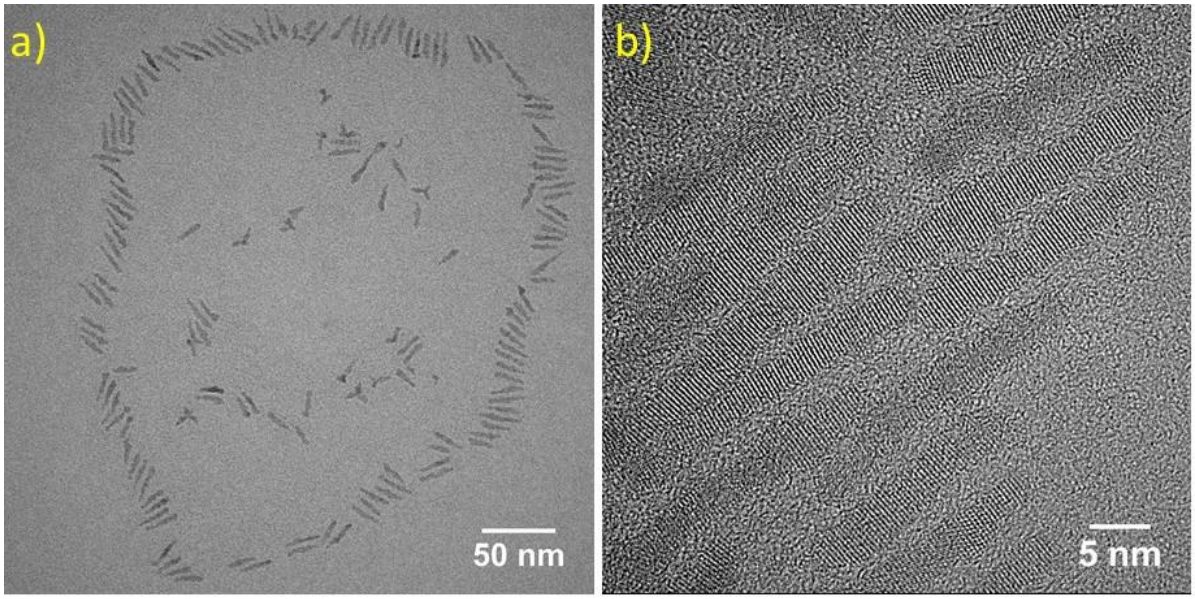

Figure 6-10. TEM images of CdSe QRs treated with 192 Cl^- ions/nm2 of QR surface.

6.4. Phase transfer in water

The transfer of the QRs into the aqueous phase is essential for any potential biological application. The CdSe/ZnS core/shell QRs were chosen for the conversion from hydrophobic into hydrophilic rods, due to their superior stability when exposed to the atmosphere as compared to the chloride ion treated QRs as shown in the above sections. These CdSe/ZnS QRs were treated with different concentrations of the amphiphilic polymer PMAL (Figure 6-11) according to the method described in section 2.18.4. The air-dried QRs after the PMAL treatment was dispersed in Milli-Q water, sonicated for 30 min and filtered before analysis.

The PMAL monomers have amphiphilic domains, which arrange themselves around the QRs such that the hydrophobic chains organise themselves towards QRs and the hydrophilic domains orient outwards. It was observed that the transition into the aqueous phase by the PMAL wrapping of the CdSe QRs was successful with the highest PL emission obtained for PMAL:QR molar ratio of 10,000:1 (Figure 6-12). From the PL emission spectra, it was observed that the total PL intensity of the QRs decreased with the increasing PMAL beyond the PMAL:QR ratio of 10,000. This could be indicative of the formation of larger aggregates that tend to self-quench or the formation of multilayers of PMAL surrounding the QRs, which would need further investigations. Additionally, there was a blue shift with the PMAL addition to the

emission peak of the QRs, which could be indicative of the loss of larger particles due to aggregation.

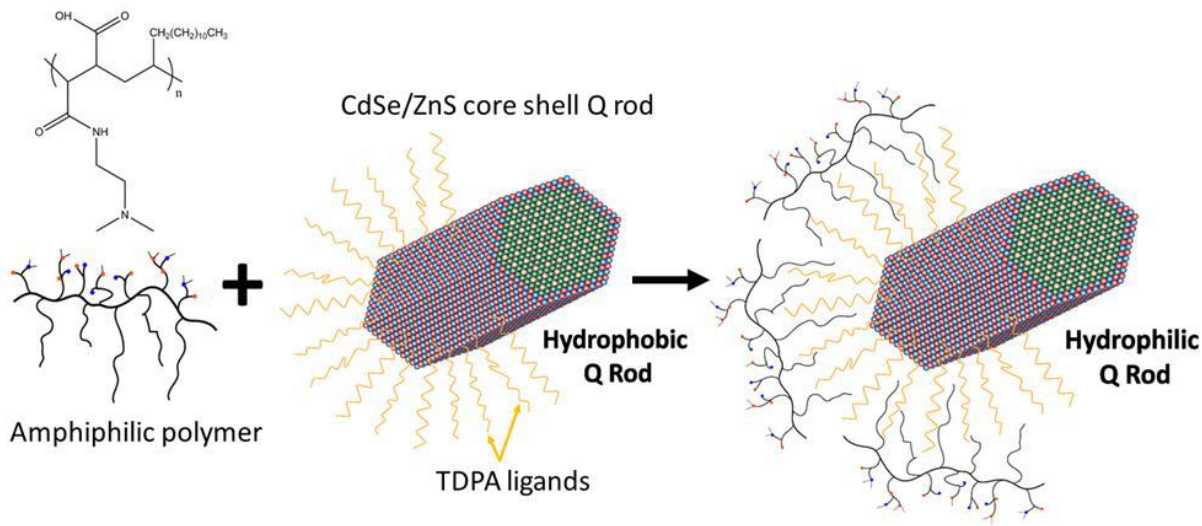

Figure 6-11. Schematic showing the encapsulation of the CdSe/ZnS core/shell QRs with the amphiphilic PMAL to convert from hydrophobic to hydrophilic particles.

The PLQY of the QRs with 10,000:1 PMAL to QR molar ratio was ~14 % which was a drop from the control QRs (~41 %) in chloroform which were treated in the same manner without the polymer. The overall PLQY of the QRs dropped from ~74% of the hydrophobic QRs during this treatment. This decrease in the photoluminescence efficiency of the CdSe/ZnS QRs could occur due to the rigorous treatment during the polymer encapsulation process that could lead to ligand loss and surface oxidation. Regardless, the QRs are transformed into the aqueous phase as shown in the insets of Figure 6-12b and c. The transition from the hydrophobic state of the QRs in chloroform into the aqueous phase was demonstrated under the UV light (Inset of Figure 6-12c), although the method would need improvements.

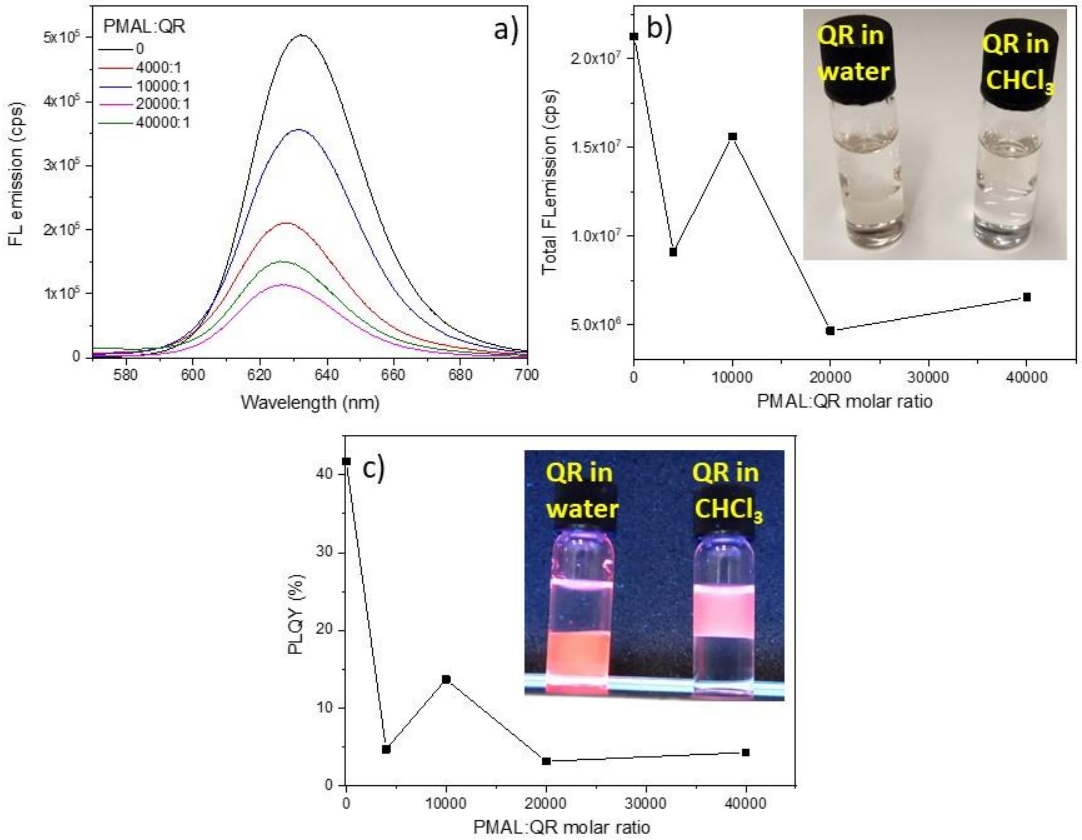

Figure 6-12. Conversion of hydrophobic CdSe/ZnS QRs in chloroform into and hydrophilic rods. a) The fluorescence emission spectra (b) total integrated emission and (c) PLQY of the hydrophilic QRs with different PMAL:QR ratios. The control QRs with PMAL:QR = 0 represents the hydrophobic QRs in chloroform for comparison. The insets of b) and c) show the transition of the QRs from the hydrophobic state in chloroform to aqueous phase in white and UV-light, respectively.

6.5. Concluding remarks

In this chapter, CdSe QRs were synthesised and characterised using optical spectroscopies and TEM. The aspect ratio of the rods could be controlled by introducing limited Se-precursor sequentially into the reaction mixture containing the Cd-TDPA complex. Limiting the amount of Se in the reaction mixture allows the preferential growth of the particles along the ⟨002⟩ direction post-nucleation. From the initial nucleation of the CdSe seeds in the first few Se-injections, there was polydispersity observed in the particle growth as seen by the presence of multiple PL emission peaks. However, with the increasing number of injections, the rods became more monodispersed with the final product showing a narrow emission peak (FWHM

~31-35 nm), which also corroborated from the TEM image analysis. The aspect ratio of the QRs was controlled by the number of Se-precursor injections, while the thickness was controlled by the intervals between these injections, with longer intervals resulting in thicker rods.

Since the PLQY of these CdSe rods is very low (~1 %), two methods to enhance the photoluminescence efficiency was adopted. The epitaxial ZnS shell growth using a single-molecule precursor $Zn(DDTC)_2$ was simple, easy and safe compared to the use of other zinc precursors such as diethylzinc. The PLQY of the CdSe/ZnS core/shell QRs significantly increased with a maximum of ~79 % obtained for 3 h shell growth. PL intensity lifetime decay traces also indicated that the non-radiative capture of excited electrons from the conduction band was suppressed with the ZnS shell passivation. These particles were stable in storage and with atmospheric exposure. The other method of surface passivation attempted was the chloride ion treatment of the rods. These negatively charged ions can occupy the positive surface electron trap sites, which suppresses the non-radiative electron capture. A PLQY of up to ~75 % was obtained with the Cl^- ion treatment. However, the value dropped significantly (~27 %) within 24 h when exposed to the atmosphere. Additionally, the cleaning of the rods post-treatment also lowered the light conversion efficiency. The cleaning of the Cl^- ions treated rods and handling in atmospheric conditions could be improved in future studies.

CdSe/ZnS core/shell QRs were chosen for conversion into aqueous phase due to their better performance under atmospheric exposure compared to the Cl^- ions treated rods. These QRs were treated with an amphiphilic polymer PMAL which rendered these hydrophobic rods into hydrophilic by encapsulation. The hydrophobic chains of the PMAL arrange themselves towards the rods while the hydrophilic ends arrange outwardly towards the water. QRs were successfully transformed from chloroform into the water with the best result obtained for PMAL:QR = 10,000:1 molar ratio. This is promising from the perspective of biological applications of these QRs. However, there was a drop in the PLQY with this conversion which could be due to loss of particles via aggregation, loss in surface passivation due to rigorous treatment or the role of the polymer in suppressing the emission which could be investigated in the future.

7. Conclusion

The aim of this project was to investigate the membrane disruption by shear force induced hydrodynamic cell deformation in a cross-slot microfluidic device to enable cytosolic uptake of QDs for live cell redox sensing. The work was split into three key sections: investigating the nature of QD uptake with cell deformation, redox sensing in live breast cells using the deformation method for delivery of redox-sensitive QDs and investigating the behaviour of cellular fluids and uptake of larger particles with deformation. Additionally, efforts were made to enhance the photoluminescence efficiency of QRs with the potential for biological applications.

In chapter 3, the preliminary focus was given to establishing the relationship between QD uptake and the degree of cell deformation in the cross-slot microfluidic device. CdTe/CdS core/shell QD passivated with TGA was used for the uptake experiments. The QDs show highly tunable emission, photostability and high PLQY of up to ~57 %. The cell deformation was performed using the cross-slot microfluidic device operated in the viscous force-dominated shear-regime. The Reynolds number for the flow of cell suspension fluid was kept low (Re <11) to have controlled cell deformation at increased viscosity (~33 cP). The human breast cancer cell line MCF7 cells were chosen for establishing the deformation-induced QD uptake in consideration for its particularly high reduced cellular environment, which would be of importance in the redox-sensing aspect. The viability of these cells remained high (~85 %) even at a large flow rate (175 µl/min) of the cell suspension through the device. The DI of the MCF7 cells increased with the flow rate and plateaued at higher flow rates. This suggests that even with the increasing shearing force to deform the cells at higher flow rates, the cells resist opposes its stretching due to its viscoelastic properties and the action of the cytoskeleton [181].

From the confocal images of the cells deformed at different flow rates with QDs, it was observed that the PL emission from the cells increased with flow rate. This suggests that there is an increase in the membrane disruption which allowed higher particle diffusion into the cytoplasm. Hence, there is a presence of another mechanism of particle uptake in addition to the endocytosis. Additionally, there was also a drop in the cell viability at higher flow rates

when deformed with QDs. This is also evidence of enhanced uptake as the QD toxicity increases.

ICP-MS analysis to quantify the amount of cadmium for the cells with the QDs showed that the uptake of the QDs by endocytosis was in the order of a few million QDs per cell, which increased with deformation at higher flow rates (100 and 150 µl/min). However, the deviation in the result was significant and the experiment needs to be repeated to have confidence in the data.

From the STEM images, it was clear that the delivery of QDs through the cross-slot cell deformation was non-endocytic. The QDs were freely dispersed in the cytoplasm which suggests passive diffusion of the QDs through the transient membrane disruptions in addition to the endocytosed particles. Establishing the non-endocytic nature of QD delivery was key for further application of the method in live cell redox sensing. The hydrodynamic shear force-induced method of cell deformation for the non-endocytic uptake of QDs using the cross-slot microfluidic device was high-throughput, vector-free, inexpensive, simple and reproducible.

Chapter 4 was dedicated to investigating the redox sensing in different human breast cells using the quinone modified RA-QDs, delivered via cross-slot microfluidic cell deformation. The redox-sensitive RA-QDs were prepared by the introduction of the electron-accepting quinone-based Q2NS ligands which showed quenching of the QD emission by ~99 % for Q2NS:QD molar ratio of 10:1 and higher. The quenching transpired by the ultrafast capture of the excited conduction band electron by the quinone ligand via a 'hot' surface trap state [45]. This electron capture was faster than the radiative electron-hole recombination. However, in the reduced form of the Q2NS, the electron capture mechanism is suppressed and led to the restoration of the QD PL emission. This reversible quenching of the RA-QDs makes it suitable for sensing the reduced cellular environment. Cyclic voltammetry analysis showed that the LUMO of the Q2NS in the oxidised state lies within the bandgap of the CdTe and CdS bulk materials, making it capable of electron capture from the conduction band of the QD.

The RA-QDs were delivered into the MCF7 cells by membrane disruption produced by cross-slot microfluidic cell deformation. From the confocal microscopy, the quenched RA-QDs showed PL emission from within the cells, suggesting that the Q2NS ligands were reduced in the cellular environment. Endocytic delivery of the oxidised RA-QDs also showed restoration

of the PL emission which demonstrated the reducing capabilities of the low pH endosomes. However, the emission from the deformed cells was higher due to the additional uptake of endosome-free RA-QDs.

The viability of the different human breast cancer cells (MCF7, T47D and MDA-MB-231) along with a non-malignant human breast cell MCF10A were tested for different concentrations of the QDs and RA-QDs. This was to ensure that the RA-QD concentration used for the investigations was within the acceptable limits of cell viability. DI measurements showed that the MCF7, MDA-MB-231 and the MCF10A cells had similar deformations with flow rates. T47D had higher DIs compared to the other cell lines, which could reflect on the difference in the degree of membrane disruption, which could be investigated in the future.

From the confocal microscopy images of cells deformed with RA-QDs, it was observed that the ER+ cells (MCF7 and T47D) showed higher PL emission compared to the ER- (MDA-MB-231) and the non-malignant (MCF10A) cells. This was indicative of the higher reducing cellular environment of the ER+ cells compared to the other cell lines. This trend was not observed for the QDs without the quinones. Hence, it shows that the difference in the PL emission of the RA-QDs was the outcome of the degree of reduction efficiency by the cellular environment. However, in the case of T47D the increased PL emission could arise from the higher DI of the cells, which could lead to higher membrane disruption. It would be important to investigate the correlation between cell stiffness, membrane porosity and the corresponding particle uptake with deformation of different cell lines.

To observe the response on the RA-QDs from the cells upon change of the redox state, MCF7 cells deformed with RA-QDs were treated with AAPH, which generates ROS. A drop in the PL emission of the RA-QDs was observed which showed that they are sensitive to the change in the redox state of the cells. The drop in photoluminescence was seen for both incubated and deformed cells, which was indicative of the effect of AAPH on both cytoplasm and the endosomes. MCF10A cells treated in the same manner also showed the drop in the PL emission of the RA-QDs.

From the results obtained in chapters 3 and 4, it is clear that there is non-endocytic delivery of QDs using cell deformation via the cross-slot microfluidic device. The deformation generates transient membrane disruption which allows the QDs to enter the cytoplasm free from

endosomes which strongly suggest passive diffusion of particles across the membrane pores. Hence, there should be evidence of bi-directional flow across the membrane pores to support the diffusion-based uptake argument. Hence in Chapter 5, we investigated the outflow of intracellular materials on deformation using the high-speed confocal fluorescence FDM microscope. The MCF7 cells were stained with calcein which is a membrane-permeable dye capable of staining the whole cell. The cells were deformed through the cross-slot device at 5 and 10 µl/min flow rates and high-speed images of the cell deformation were captured using the FDM were captured. Several corrections to the acquired FDM images were made for the removal of pixel distortion due to the inherent scanning velocity profile of the FDM laser, the effect of the fluorescence lifetime of the fluorophore on the photoluminescent output with respect to the position on the FOV, and finally due to the relative motion between the cell and the scanning beams. The corrected images revealed a drop in the PL intensity of calcein from the cells as they deform. This was indicative of the outflow of intracellular fluid from the transient membrane disruptions generated by the hydrodynamic cell deformation. This result along with the non-endocytic uptake of QDs support the bi-directional flow across the membrane pores according to the diffusion process. Cells undergo volume loss during deformation by the leakage of intracellular fluids and ultimately regains their volume by the uptake of suspension fluid which also facilitates the non-endocytic QD delivery.

Cells were also imaged post-deformation using the FDM at two different regions of the microfluidic device outlet. The comparison of the PL-intensity showed a drop in the fluorescent intensity (~4.7 %) at the region further away from the extensional flow junction. This suggests that the membrane disruptions are actively leaking intracellular fluids post-deformation. The membrane pores remain active even after the cells have regained their shape which enables the particle uptake.

Delivery of NPs (Au-PEG-FITC) of different sizes was attempted by hydrodynamic deformation of MCF7 cells in the cross-slot device. The smaller NPs (hydrodynamic size ~16 nm) were readily delivered into the cells, with a linear increase in measured PL intensity from cells with increasing flow rate. However, the larger particles (hydrodynamic size ~55 and ~80 nm) did not show a significant increase in uptake with increasing flow rates, suggesting that the mean membrane pore size has an upper limit close to the size of these larger particles. There could be other factors governing the uptake and the consequent photoluminescence measured from

the cells, such as the distribution of PL intensity among the NPs in the same batch, pore size and density distribution. Further investigation is necessary to make appropriate conclusions regarding the nature of uptake of larger NPs and the membrane pore size. An attempt to model the membrane poration and uptake of particles was made, which is described in future works (section 8.1).

In Chapter 6, the enhancement of the PLQY of the CdSe QRs was investigated by epitaxial ZnS shell growth and chloride ion treatment. Some of the unique properties of the QRs such as linearly polarised emission, wide absorption cross-section and narrow emission spectra make them highly desirable for various applications. However, the QRs have a very low photoluminescence efficiency (< 1%) due to the presence of a large number of surface traps as the surface-to-volume ratio of the rods are high compared to the QDs. Hence, for the purpose of the application, it is essential to improve the PL efficiency. For the ZnS shell growth for passivation of the surface traps, enhancement in the PLQY of up to ~79 % was obtained for the CdSe/ZnS core/shell QRs. The particles showed stability over time with exposure to the atmosphere. TEM images show the undulating surface of the QRs on shell growth which could be smoothened in future investigations by annealing the rods at a high temperature. The chloride ion treatment of the CdSe QRs resulted in the PLQY enhancement of up to ~75 %. However, the particles could not sustain their photoluminescence efficiency with exposure to the atmosphere.

The hydrophilic conversion of the CdSe/ZnS core/shell QRs was performed using an amphiphilic polymer PMAL. These polymers can organise themselves around the QRs with the hydrophilic ends outwardly arranged. The transfer to the aqueous phase was demonstrated by the treatment of QRs in chloroform with PMAL and ultimately redispersing them in water. A loss in the photoluminescence efficiency was observed during this transfer which can arise due to the rigorous treatment of the particles during the exchange. Hence, there is much scope for further optimisation and improvement in the quality of the hydrophilic QRs, which have the potential for biological applications. They could be utilised in a study to investigate the uptake of particles of different shapes and size using the microfluidic cross-slot device.

8. Future works

8.1. Model for membrane disruption and particle uptake via cross-slot microfluidics

We have demonstrated the intracellular uptake of QD and Au-FITC NPs via membrane disruption by hydrodynamic deformation of cells by the shearing force of the moving fluid in the cross-slot microfluidic device. Additionally, we have also shown that there is an outflow of intracellular materials from these pores using the high-speed confocal images captured by the FDM microscope to visualise the drop in calcein PL intensity from the cells. Since there is the motion of fluids and particles across the membrane in both directions, diffusion is likely to be the mechanism of uptake across these transient membrane pores. Here, an attempt to use the diffusion model to mathematically understand the uptake of NPs has been made.

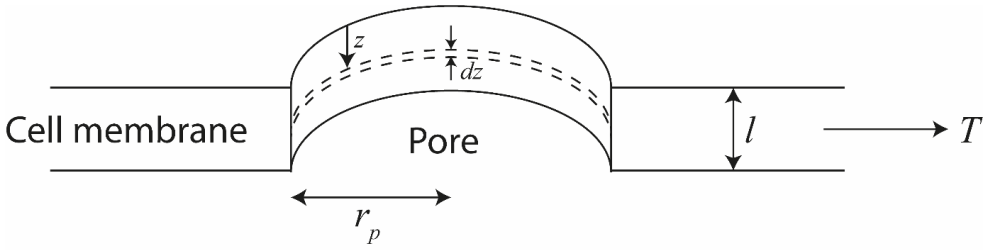

Figure 8-1. Schematic showing a membrane pore of radius r_p generated by the applied tension T for the membrane with thickness l. z is an arbitrary distance through the membrane from the outer surface.

Let us assume that membrane pores are generated when the cells are deformed hydrodynamically in a cross-slot microfluidic device and the QD uptake in the cells take place through passive diffusion across the cell membrane pores. Let us consider a pore on the cell membrane of radius r_p formed due to the tension T caused by the hydrodynamic stress on the cell at the cross-slot junction. Let l be the cell membrane thickness and z be distance through the membrane pore from the outer cell surface. Assuming that the diffusion is in a steady state and there is no accumulation of the QDs in the dz layer:

Diffusion rate of QDs, $J = A(j|_z - j|_{z+dz}) = 0$ (8.1)

where, A is the area of the pore, j = diffusion flux of QDs. Also, A is a function of time since the pores will be repaired by the cells in due time.

Dividing equation 8.1 by the volume of the section:

$$\frac{A((j|_z - j|_{z+dz})}{A[(z+dz)-z]} = 0$$

$$-\frac{\partial j}{\partial z} = 0 \qquad (8.2)$$

We know, from Flick's first law of diffusion, the rate of diffusion is proportional to the particle concentration gradient, as: $-j = D\frac{dc}{dz}$ (8.3)

Where, c is the concentration of QDs and D is the diffusion coefficient of the QDs across the membrane

Therefore, from equation 8.2 and 8.3:

$$D\frac{d^2c}{dz^2} = 0 \qquad (8.4)$$

Integrating equation 8.4:

$c = a + bz$ (a, b are constants of integration)

Boundary conditions: at $z = 0$ (outside the cell) $c = c_0$

at $z = l$ (inside the cell) $c = c_l$

Hence, $c = c_0 + (c_l - c_0)\frac{z}{l}$ (8.5)

Substituting in equation 8.3:

$$j = \frac{D}{l}(c_0 - c_l) \qquad (8.6)$$

Considering that the QD concentration inside the cell is time dependent:

$$c_l = c_l(t)$$

Using the expression of concentration derived for the diffusion of magnesium ions through membrane pores by electroporation described by Bier *et al.*, the differential equation of $c_l(t)$ as a function of time can be written as [278]:

$$V\frac{\partial c_l(t)}{\partial t} = A_s P_m(c_o - c_l(t)) \quad (8.7)$$

Where, A_s and V is the surface area and the Volume of cell, $P_m = P_o e^{\frac{-t}{\tau}}$ is the membrane permeability. Here, P_o is the membrane permeability at $t = 0$ (at deformation). τ is the characteristics time for pore closure (time for 63% of the pores to seal)

Integrating equation 8.7:

$$\int \frac{dc_l(t)}{c_l(t)-c_o} = -\frac{A_c P_m}{V}\int dt$$

$$c_l(t) - c_o = e^{-\frac{A_c P_m}{V}t}$$

Let us consider $$\tau_L = \frac{V}{A_c P_m} \quad (8.8)$$

Which is relaxation time for intracellular QD concentration if no pore sealing were to take place. Hence:

$$c_l(t) = c_o + e^{-t/\tau_L} \quad (8.9)$$

Now, flux of QDs through a pore, $$J = j.A(t)$$

Hence, total uptake of QDs through this pore, $g = \int_0^{t_t} j.A(t)dt$ (8.10)

where, t_t is the pore duration. Let there be N number of pores generated on the cell membrane on deformation. Also, let us consider the mean pore area on the cell membrane be $\bar{A}(t)$. Therefore, the total QD uptake through the cell membrane on deformation:

$$G = N\int_0^{t_t} j.\bar{A}(t)\,dt \quad (8.11)$$

From equation 8.6:

$$G = N\frac{D}{l}\int_0^{t_t}(c_0 - c_l(t))\,\bar{A}(t)\,dt$$

From equation 8.8:

$$G = N\frac{D}{l}\int_0^{t_t}(c_0 - c_0 + e^{-t/\tau_L})\,\bar{A}(t)\,dt$$

$$G = N\frac{D}{l}\int_0^{t_t} e^{-t/\tau_L}\bar{A}(t)\,dt \quad (8.12)$$

Boundary conditions: at $t = 0$ $\bar{A}(t) = \bar{A}_{max}$; pore size is maximum at deformation

at $t = t_t$ $\bar{A}(t) = 0$; cells completely repair pores at time t

From Stoke-Einstein's equation for passive diffusion of large solutes in continuous solvents:

$$D = \frac{KT}{6\pi\mu r_{QD}} \tag{8.13}$$

Where, K is the Boltzmann's constant, T the Absolute temperature, μ is the dynamic viscosity and r_{QD} is the mean radius of QDs.

Hence:

$$G = \frac{NKT}{6\pi\mu l r_{QD}} \int_0^{t_t} e^{-t/\tau_L} \bar{A}(t)\, dt \tag{8.14}$$

For simplicity, let us assume that the pores are circular. Therefore:

$$\bar{A}(t) = \pi \bar{r_p}(t)^2 \tag{8.15}$$

where, $\bar{r_p}(t)$ is the mean pore radius on the membrane at time t.

Hence equation 8.14 can be written as:

$$G = \frac{NKT}{6\mu l r_{QD}} \int_0^{t_t} e^{-t/\tau_L} \bar{r_p}(t)^2\, dt \tag{8.16}$$

Equation 8.16 was simplified by using the following conditions:

at $t = 0$ $\bar{r}_p = \bar{r}_{pmax}$; maximum pore radius at deformation

at $t = t_t$ $\bar{r}_p = 0$; pores are repaired at time t_t

$G = 0$ when $r_{QD} > \bar{r}_{pmax}$; no uptake of particles larger than the pores.

Let us now consider the two different conditions of the pore closure dynamics. Firstly, the cell radius decreases linearly with time and secondly, there is an exponential drop in the pore size for simplicity.

Case I: Assuming $\bar{r}_p$ decreases linearly with time:

Let $\bar{r_p}(t) = \bar{r}_{pmax} - mt$ (8.17)

where, $\bar{r_p}(t) = 0$ at $t = t_t$

Hence: $m = \frac{\bar{r}_{pmax}}{t_t}$ (8.18)

Substituting this in equation 8.16:

$$G = \frac{NKT}{6\mu l r_{QD}} \int_0^{t_t} e^{-t/\tau_L} (\bar{r}_{pmax} - mt)^2 \, dt$$

$$G = \frac{NKT}{6\mu l r_{QD}} \bar{r}_{pmax}{}^2 \int_0^{t_t} e^{-t/\tau_L} (1 - \frac{t}{t_t})^2 \, dt$$

$$G = \frac{NKT}{3\mu l r_{QD}} \frac{\bar{r}_{pmax}{}^2}{t_t^2} e^{-t/\tau_L} [t_t(1 + \tau_L^2) + \tau_L^3] \quad (8.19)$$

Now from equation 8.8:

$$\tau_L = \frac{V}{A_c P} = \frac{4/3 \pi r_c^3}{4\pi r_c^2} = \frac{r_c}{3P} \quad (8.20)$$

where r_c=radius of cell

$$G = \frac{NKT}{3\mu l r_{QD}} \frac{\bar{r}_{pmax}{}^2 e^{-3Pt_t/r_c}}{t_t^2} [\frac{r_c^3}{P^3} + \frac{3t_t r_c^3}{P^2} + 27t_t] \quad (8.21)$$

Let N$\pi \bar{r}_{pmax}{}^2$ =N$\bar{A}_{max} = A_T$ (total pore area on cell membrane at deformation)

Therefore: $G = \frac{KTc_0}{3\pi\mu l r_{QD}} A_T \frac{e^{-3Pt_t/r_c}}{t_t^2} \left[\frac{r_c^3}{P^3} + \frac{3t_t r_c^3}{P^2} + 27t_t\right]$ (8.22)

Case II: Assuming $\bar{r}_p$ decreases exponentially with time

Let $\bar{r}_p(t) = \bar{r}_{pmax} e^{-\alpha t}$ (8.23)

Substituting in equation 8.16:

$$G = \frac{NKT}{6\mu l r_{QD}} \bar{r}_{pmax}{}^2 \int_0^{t_t} e^{-t/\tau_L} e^{-2\alpha t} \, dt$$

$$G = \frac{NKT}{6\mu l r_{QD}} \frac{\bar{r}_{pmax}{}^2}{2\alpha + \frac{1}{\tau_L}} e^{-(2\alpha + 1/\tau_L)t_t} \quad (8.24)$$

Substituting from equation 8.8:

$$G = \frac{NKT}{6\mu l r_{QD}} \frac{\bar{r}_{pmax}{}^2 r_c}{2\alpha r_c + 3P} e^{-(2\alpha + 3P/r_c)t_t} \quad (8.25)$$

Or, $$G = \frac{KT}{6\pi\mu l r_{QD}} \frac{A_T r_c}{2\alpha r_c + 3P} e^{-(2\alpha+3P/r_c)t_t} \quad (8.26)$$

This mathematical concept for the uptake of QDs and NPs need to be tested and improved. Additionally, for the total uptake of particles, we have to consider the delivery through the endocytic pathways. This would give an additional term added to the right-hand side of the uptake equations of G. Several factors have not been considered in this hypothesis, such as the initial volume loss of the cells during deformation, the role of viscosity, the effect of the surface charge of the cargo NPs, the extensive contribution of endocytosis on the uptake, distribution in the pore density and size at different regions of the cell and many more. Not to mention, there could be flaws in the assumptions and overlooking of errors in the mathematics. Nevertheless, building upon this model could be an elegant piece of work.

8.2. Microfluidic device optimisation and additional features

Further optimisation in the design of the microfluidic device would ensure a more efficient delivery of particles. As mentioned in Chapter 3, all cells did not go through the centre of the extensional flow junction as some of the cells (5-10%) tend to follow the slipstream around the edges of the cross-slot. This creates a discrepancy in the measurement of the DI as these cells passing around the edges were not properly deformed like the ones at the stagnation point. However, they could not be avoided from analysis, as the cells collected had a population of both cells entering the stagnation point and those which did not. To ensure that all cells enter the stagnation point of the extensional flow junction, viscoelastic or inertial flow focusing could be introduced in the design of the device [279]. However, the flow-focussing could be flow rate dependent in the cross-slot device, as such, it could be tedious to design devices for each flow rate. Additionally, more features could be added to the device, such as cell trapping or sorting sections after the deformation in the cross-slot. These features could enable further treatment of the cells post-deformation, which can be useful in understanding the cellular recovery and behaviour.

8.3. Applications of non-endocytic delivery by hydrodynamic cell deformation

The cross-slot microfluidic based-method to generate membrane disruption via the shearing force of the moving fluids can be used for the non-endocytic delivery of various functional NPs and macromolecules. The work based on the delivery of Au-PEG-FITC NPs investigated in Chapter 6 remains incomplete. Further investigation on the nature of the uptake via STEM imaging of cell sections is necessary to establish the non-endocytic delivery of NPs larger than QDs. Chung group has demonstrated the delivery of DNA nanostructures in the inertial regime using the cross-slot device [170]. Due to the low Reynolds number, there would be more control over the deformation and the membrane disruption of the cells in the shear dominated regime. Transfection, which is the delivery of DNA and RNA could be attempted through this method in a more controlled manner. Other cargo could include protein complexes, macromolecules, antibodies and NPs with varying morphology and compositions. The applications of these deliveries could lead to live cell sensing, imaging, intracellular targeting, therapies, gene control and editing [128]. It is also necessary to investigate the correlation between the degree of cell deformation and membrane disruption for the different cell lines. Higher deformation does not translate to a higher degree of membrane disruption as it could differ between cell lines and experimental conditions.

8.4. Insight on cellular mechanics and membrane disruption

Cytoskeleton disruption is known to alter the deformation of the cells through the cross-slot microfluidic device [181]. Consequently, the membrane disruption and the particle uptake will be affected. It would be interesting to investigate the change in the membrane porosity with deformation with disruption of the actin, microtubule and the intermediate filaments. Latrunculin-A, which is an actin-disrupting drug produced more deformation in SW480 cells compared to the untreated cells in the cross-slot device in the shear regime [181]. This could indicate generation of larger membrane pores or higher pore density with the cytoskeleton disruption, hence leading to enhanced particle uptake.

Calcium ions play an important role in the repair of the membrane pores and consequently the uptake of NPs [165]. The modification of the microfluidic cross-slot device (with cell traps) to

accommodate controlled exposure to NPs and calcium ions post-deformation can help understand the kinetics of the membrane repair mechanisms and uptake.

Deformation of the nucleus using hydrodynamic forces have generated interest in understanding its behaviour with respect to the whole cell deformation [183]. The nucleus is stiffer than the rest of the cells, as such, the disruption of the nuclear membrane for delivery of functional NPs is a challenge and generating interest. From the STEM images shown in Figures 3-12 and 9-2, there is evidence of intracellular delivery if the QDs in the nucleus. Hence, the cross-slot microfluidic deformation of the cells can potentially cause nuclear membrane disruption, allowing the particle diffusion. A thorough investigation is necessary to characterise the uptake of NPs by the nucleus via cell deformation. High resolution electron microscopy combined with high-speed confocal fluorescence FDM microscopy could be the key in determining the deformation and uptake in the nucleus through cell deformation.

8.5. RA-QDs for redox sensing

The Q2NS can successfully quench the QD emission, which is restored upon its reduction in breast cancer and non-malignant cells. The data suggests that it is sensitive to the different reducing environments of the ER+, ER- and the benign cells. This redox sensing capability of the RA-QDs could be applied to investigate the other known cell line models, stem cells and primary cell lines. For example, the colorectal cancer cell lines SW480, HT29 and SW620, which are cells at different stages of carcinoma from primary, advanced primary to metastasised, obtained from a single patient represent an ideal model to study the disease progression through the redox states [183,279]. Quantification of the redox potential in the cytoplasm of the live cells using the Q2NS can be possible via Raman spectroscopy with the effective conjugation of Q2NS on Au-NPs for surface-enhanced Raman signalling [281].

Cellular spheroids and on-chip vasculatures models can represent solid tumours for microfluidics experiments [282]. The redox state can vary significantly in cellular spheroids depending on the location of the cell. The cells in the interior of the spheroids are oxygen and nutrients deprived compared to the cells on the surface, which can affect their redox state. RA-QDs could be suitable probes for monitoring the 3-dimensional redox state of the cells in

these structures. The challenge would be the effective delivery of the RA-QDs to the interior of spheroids.

Since the RA-QDs were being reduced in both the cytoplasm and the endosomes, the next step in designing the redox-sensitive ligands would be to make them sensitive to the small changes in the pH, so that the PL emission from the cytoplasm and the endosome can be differentiated.

8.6. High PLQY QRs

The photoluminescence efficiency CdSe QRs were enhanced significantly with the ZnS epitaxial shell growth and chloride ion treatment. However, the optimisation of the surface trap passivation using these methods would require further investigation and improvements can be made for both techniques. For the ZnS shell growth, the surface of the QRs could be smoothened by annealing the particles at a high temperature. The growth of multiple ZnS monolayers layers and its effect on the PLQY can be further investigated. For the chloride ion passivation of the QR surface traps, the main challenge would be to sustain the photoluminescence efficiency with time in the presence of the atmosphere. This could require optimising the chloride ion and TDPA ligands population on the QR surface that would give a stable configuration.

The high PLQY QRs can have potential use in optoelectronics for solar cells and lasing devices. Their ability to form superstructures and superlattices can be utilised to obtain highly polarised emissions. They could be used in LED displays for their ability to form an aligned state with the liquid crystal molecules [283]. The hydrophilic QRs could be ideal for investigating directional emissions from biological systems using polarisation microscopy. The study of the excited state dynamics of these highly photoluminescent QRs can generate experimental and theoretical interests.

9. Appendix

9.1. QD characterisation

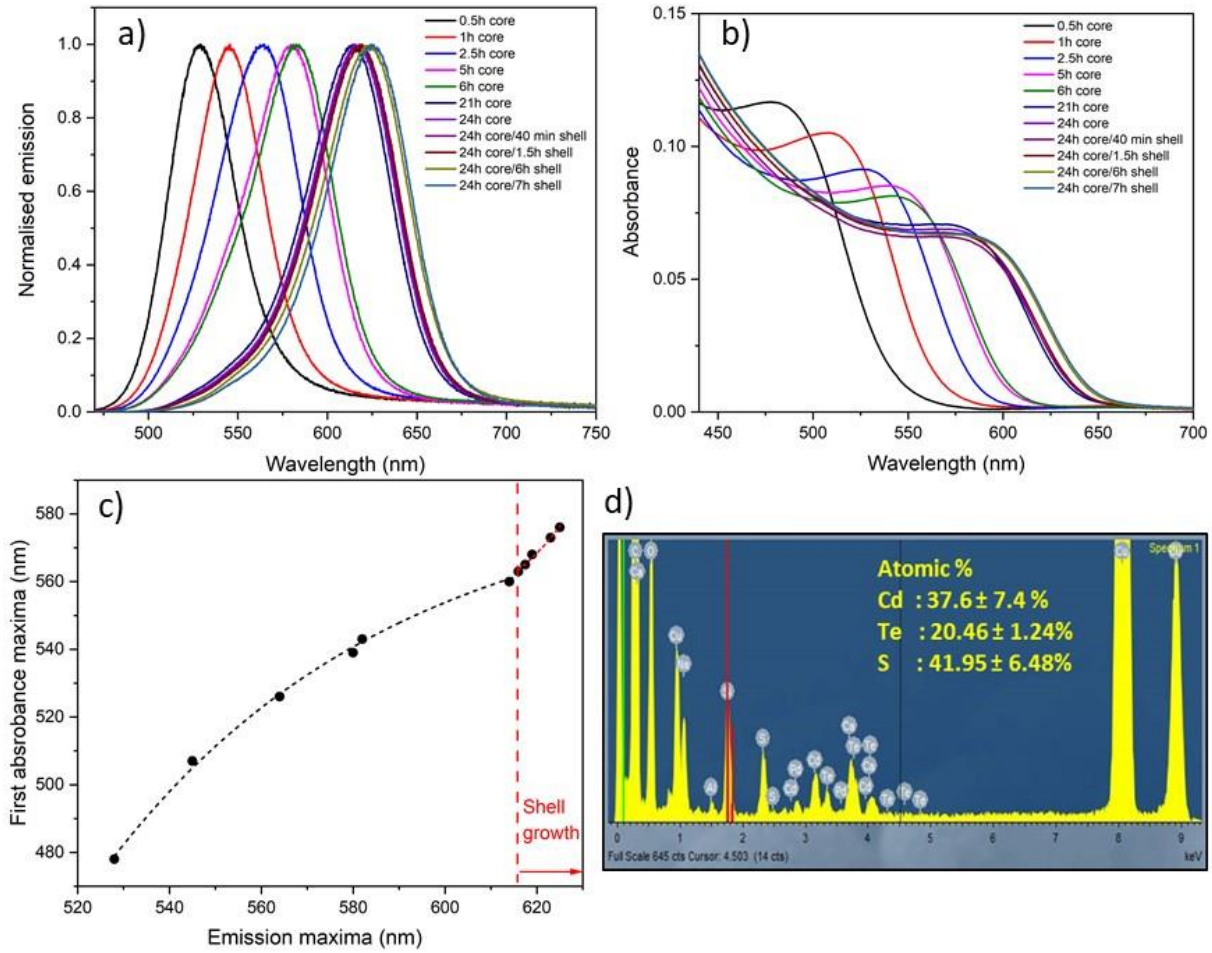

Figure 9-1. a) PL emission spectra, b) absorbance spectra and c) The first absorbance maxima as a function of the PL emission maxima for the growth of CdTe/CdS QDs under reflux for the data expressed in Figure 3-1. d) Energy dispersive X-ray spectrum of the CdTe/CdS QDs.

9.2. STEM images of MCF7 cells deformed QDs

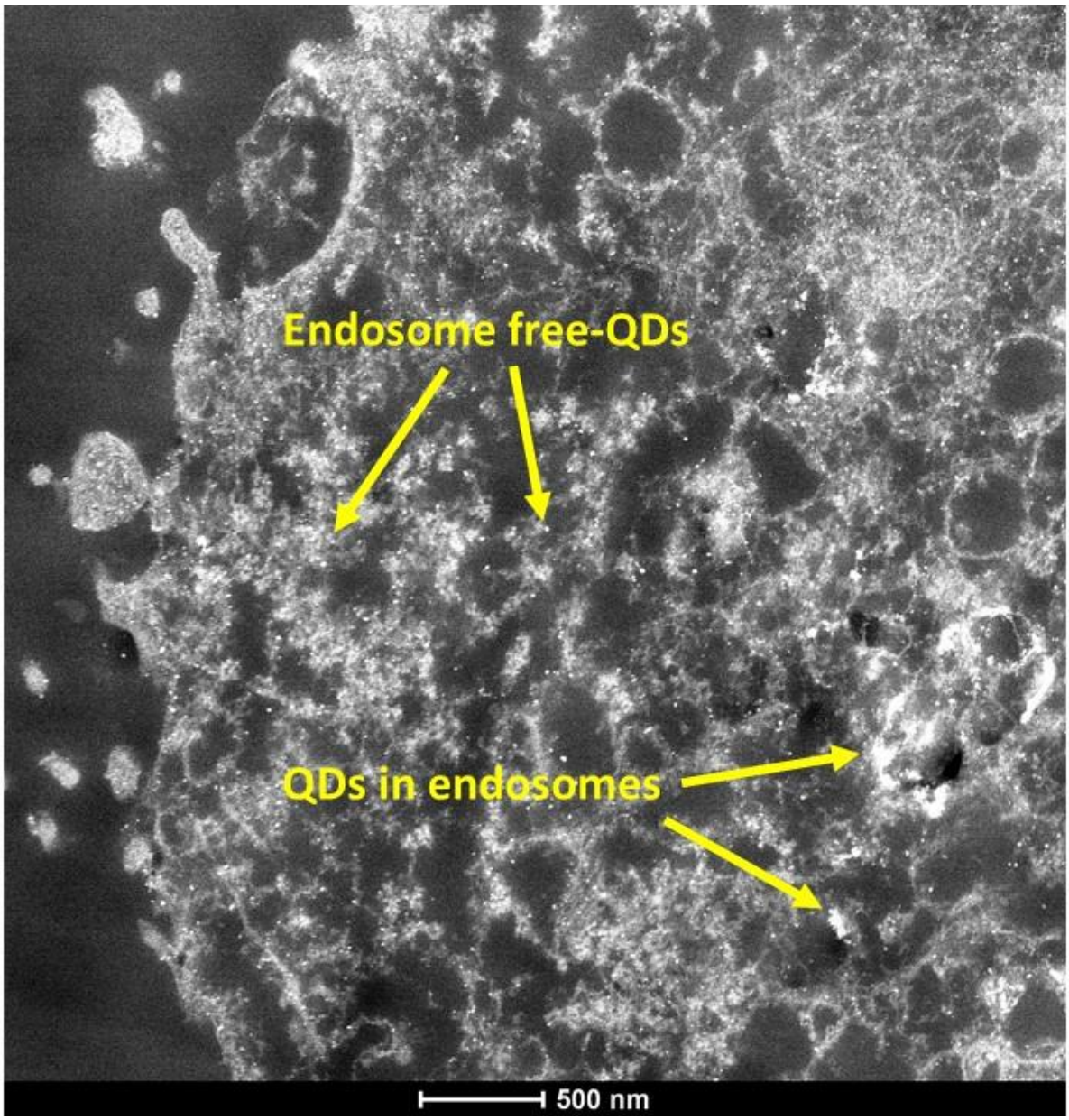

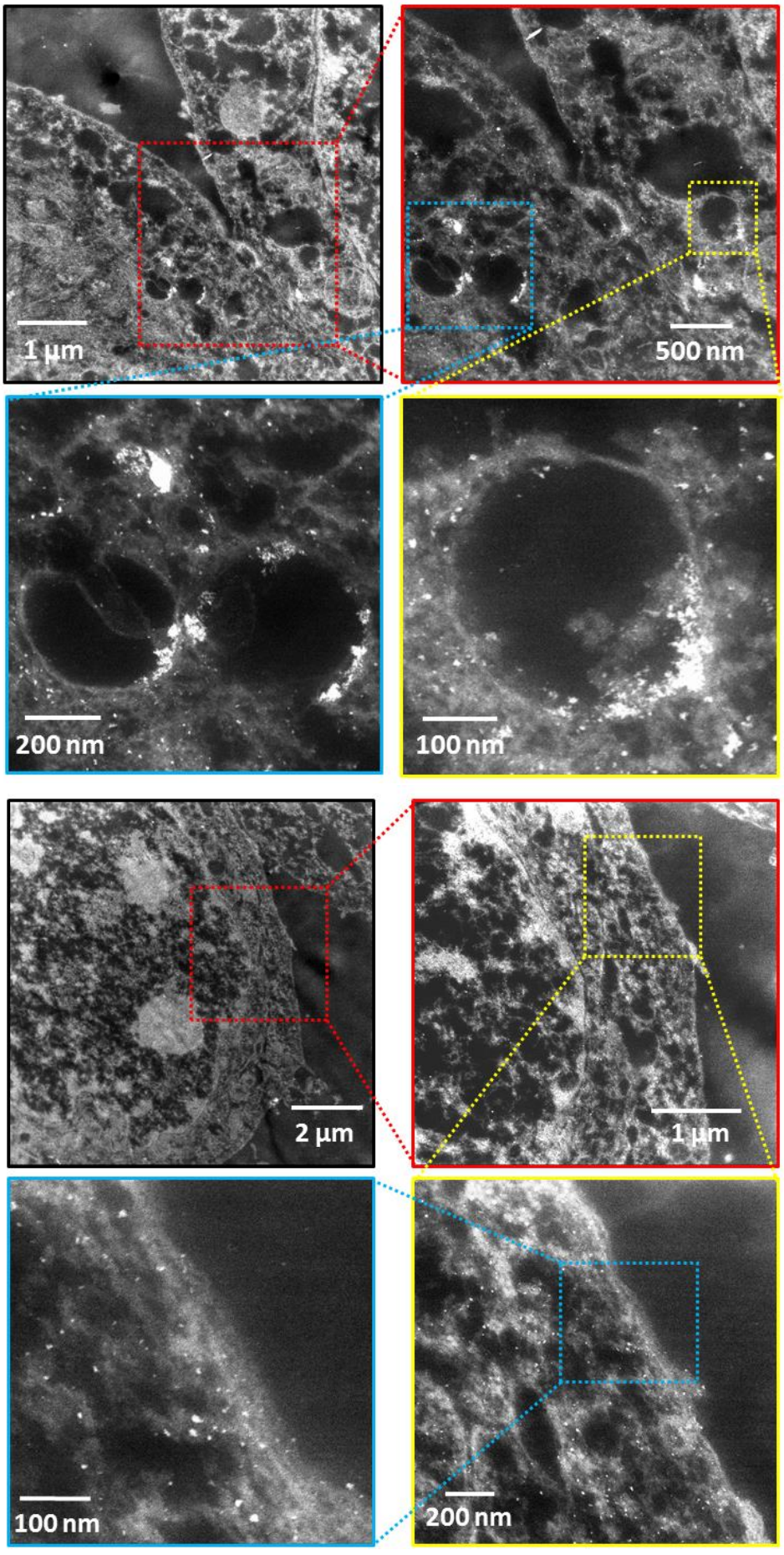
1 µm
500 nm
200 nm
100 nm
2 µm
1 µm
100 nm
200 nm

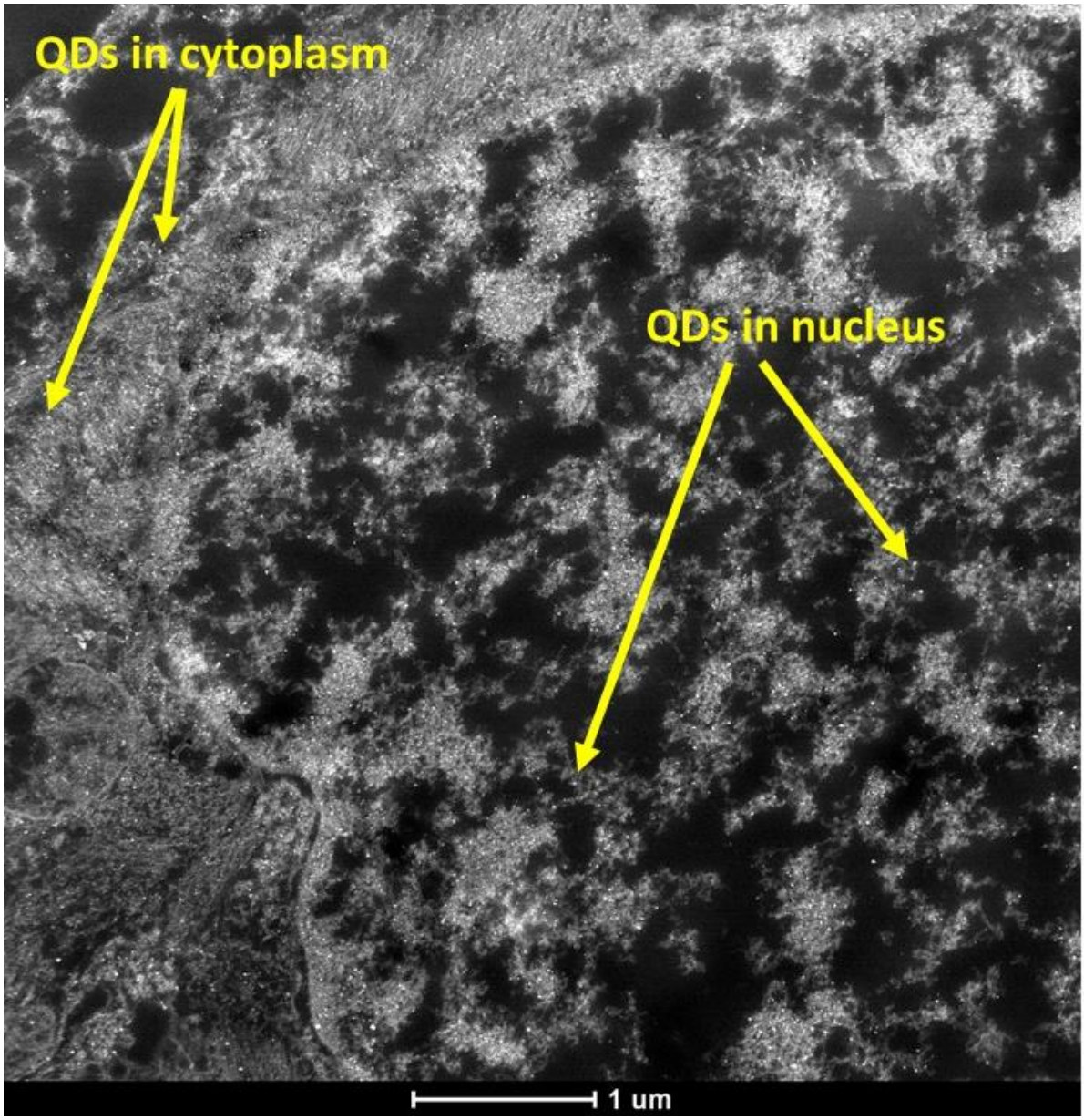

Figure 9-2. STEM images of MCF7 cells deformed with 100 nM CdTe/CdS QDs through the cross-slot microfluidic device at 100 µl/min flow rate, with evidence of QDs dispersed in the nucleus.

9.3. TEM images of MCF7 cells deformed with QDs

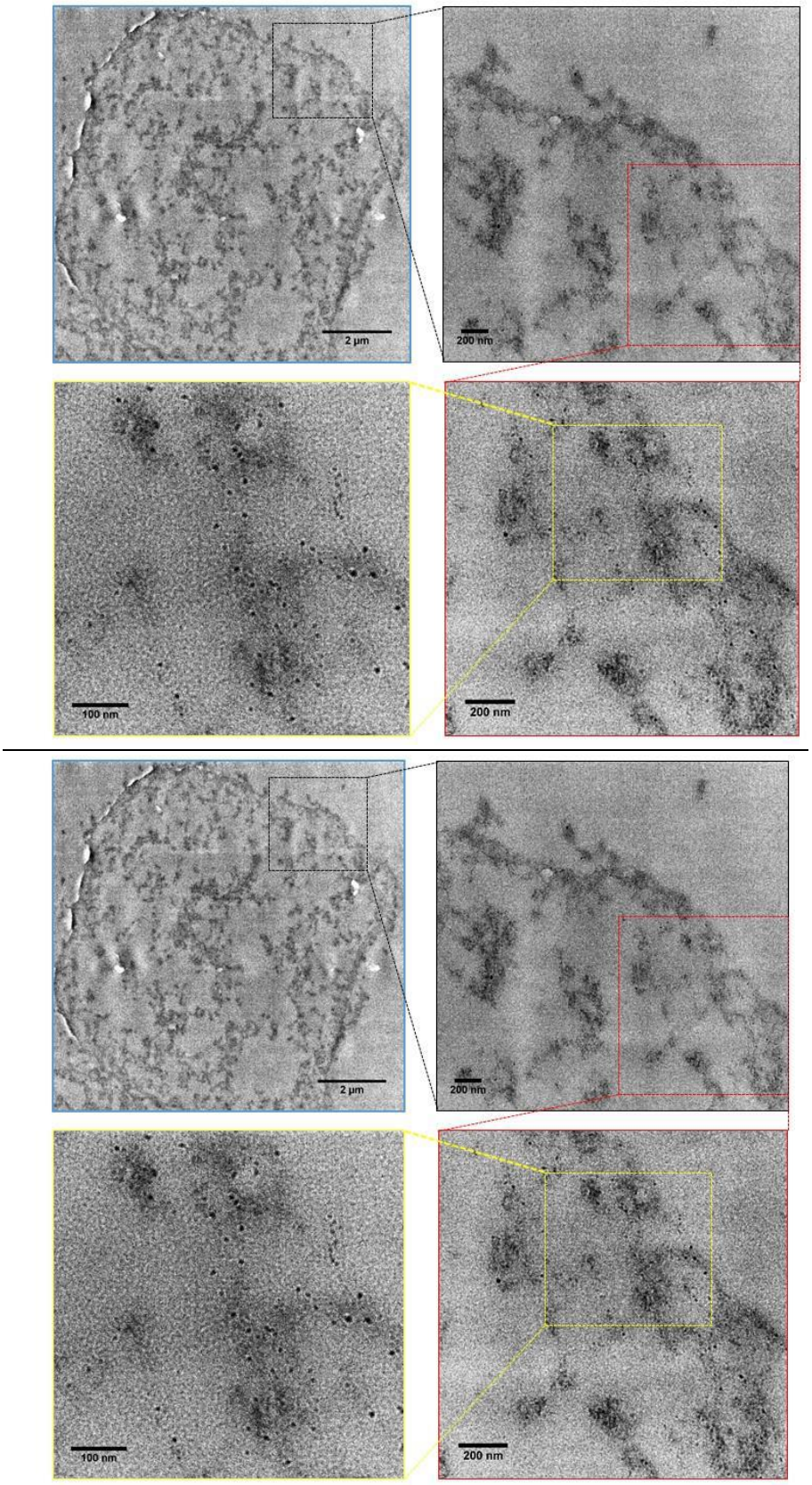

Figure 9-3. Bright field TEM images of MCF7 cells deformed with 100 nM CdTe/CdS QDs through the cross-slot microfluidic device at 100 µl/min flow rate.

9.4. TEM images of QDs used for the quantification in cells using ICP-MS

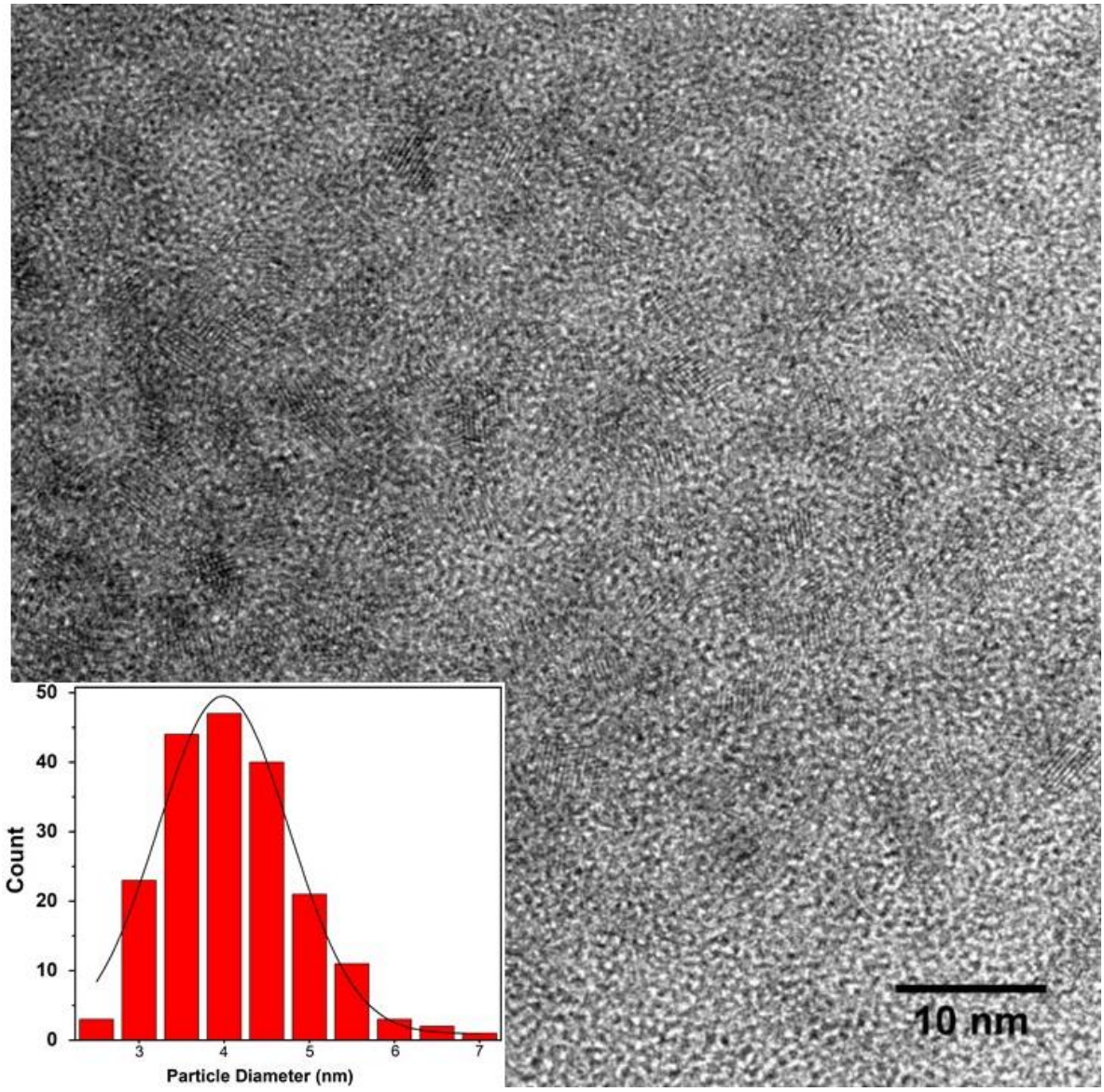

Figure 9-4. A typical TEM image of the CdTe/CdS core/shell QDs used for cellular delivery quantification through ICP-MS via hydrodynamic deformation using the cross-slot microfluidic device.

9.5. Blue shift of the PL emission peak of RA-QDs

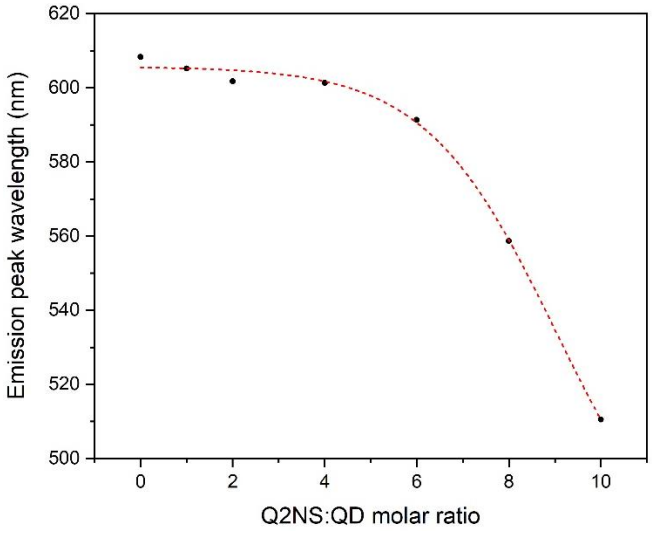

Figure 9-5. The PL emission peak of the RA-QDs with different Q2NS:QD molar ratios

The PL emission of the RA-QDs with different Q2NS:QD molar ratio fitted to a Gaussian peak shows a blue shift with increasing quinone. The fitted guideline (R^2 >0.99) is the dose-response curve given as:

$$y = A_1 + \frac{(A_2 - A_1)}{1 + 10^{\log(x_0 - x)p}}$$

9.6. Fixing cells with Glutaraldehyde deformed with RA-QDs

MCF7 cells deformed through the cross-slot microfluidic device at 100 µl/min flow rate with 100 nM RA-QDs were fixed with the treatment of 2.5 % glutaraldehyde with 30 min of incubation. Confocal images of the cells were taken before and after the fixing as shown in Figure 9-4. The images show that on the treatment of glutaraldehyde the PL emission of the RA-QDs in the cells increased. This is due to the further reduction of the RA-QDs by the glutaraldehyde. This indicates that the RA-QDs are not fully reduced in the MCF7 cytoplasm and would need further investigation to enhance their emission within the cells by chemically enhancing the reducing environment of the cells.

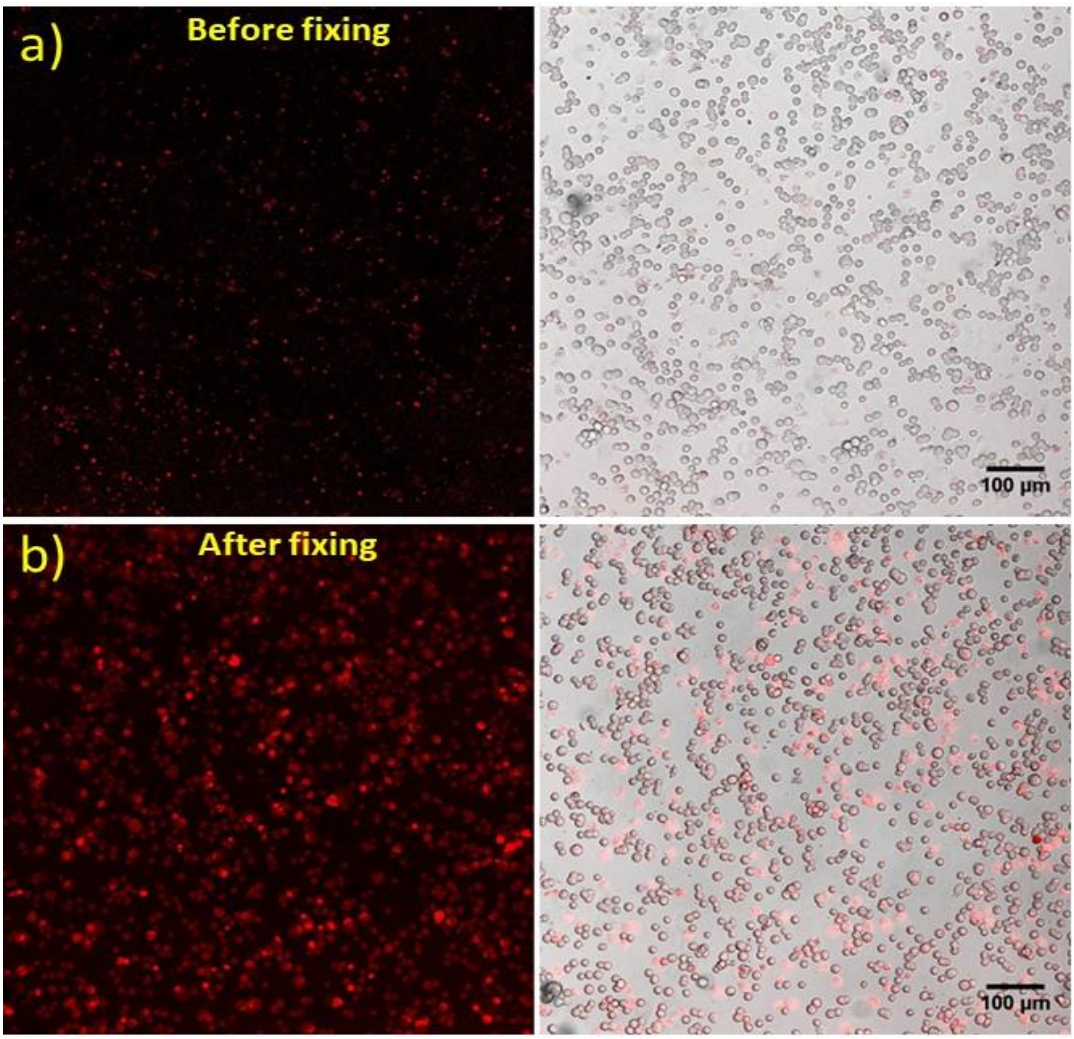

Figure 9-6. Confocal images (FL and merged FL-bright field) of MCF7 cells a) before and b) after fixing with 2.5 % glutaraldehyde treatment.

9.7. Scatter plots for the cells incubated and deformed with QDs and RA-QDs

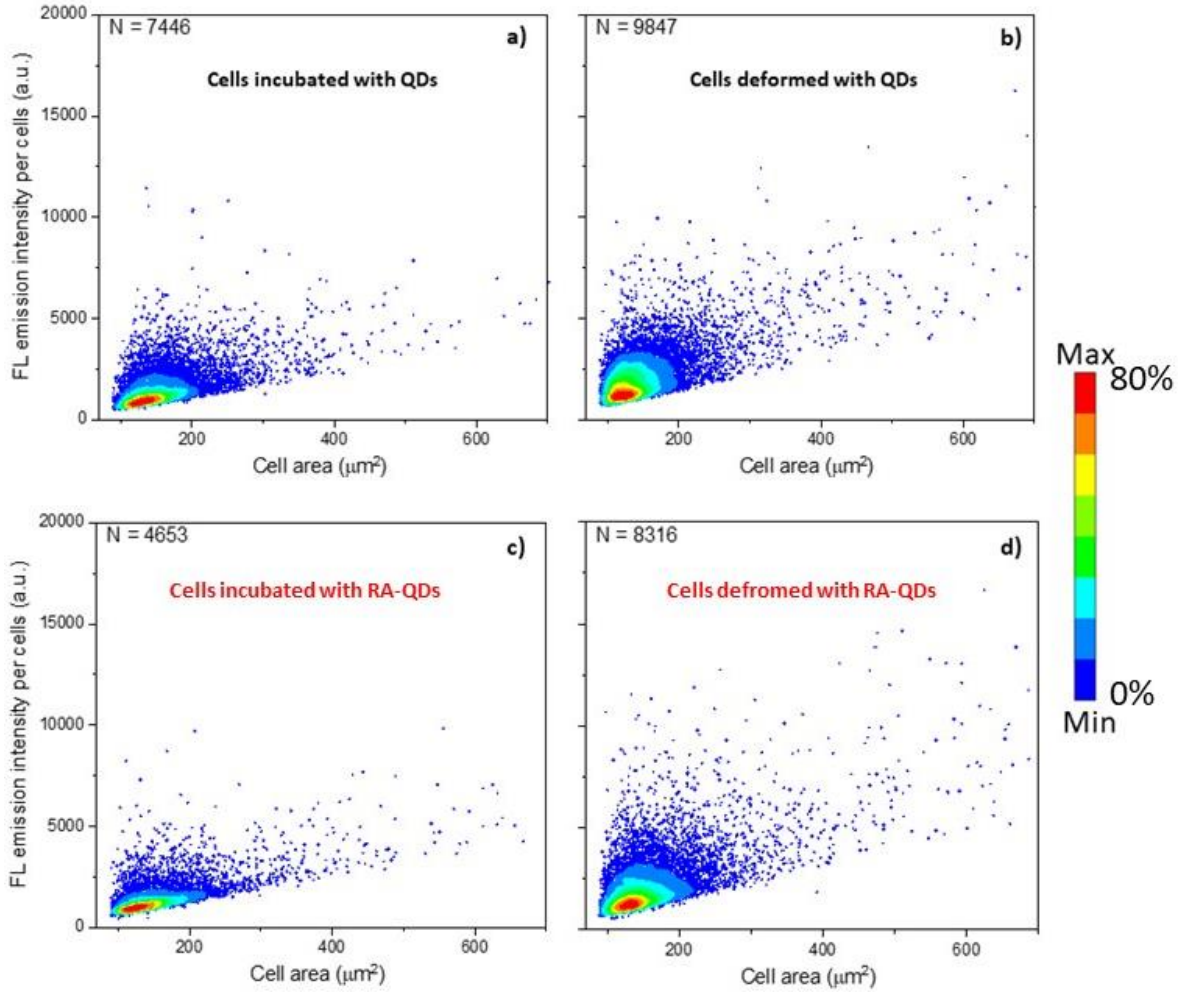

Figure 9-7. Scatter plots for the total PL emission intensity from the MCF7 cells when (a) incubated with 100 nM QDs (b) deformed at 100 µl/min with 100 nM QDs (c) incubated with 100 nM RA-QDs and (d) deformed at 100 µl/min with 100 nM RA-QDs for the data represented in Figure 4-4. molar ratio Q2NS:QD for RA-QDs= 20:1.

9.8. Confocal fluorescence images of cells with RA-QDs

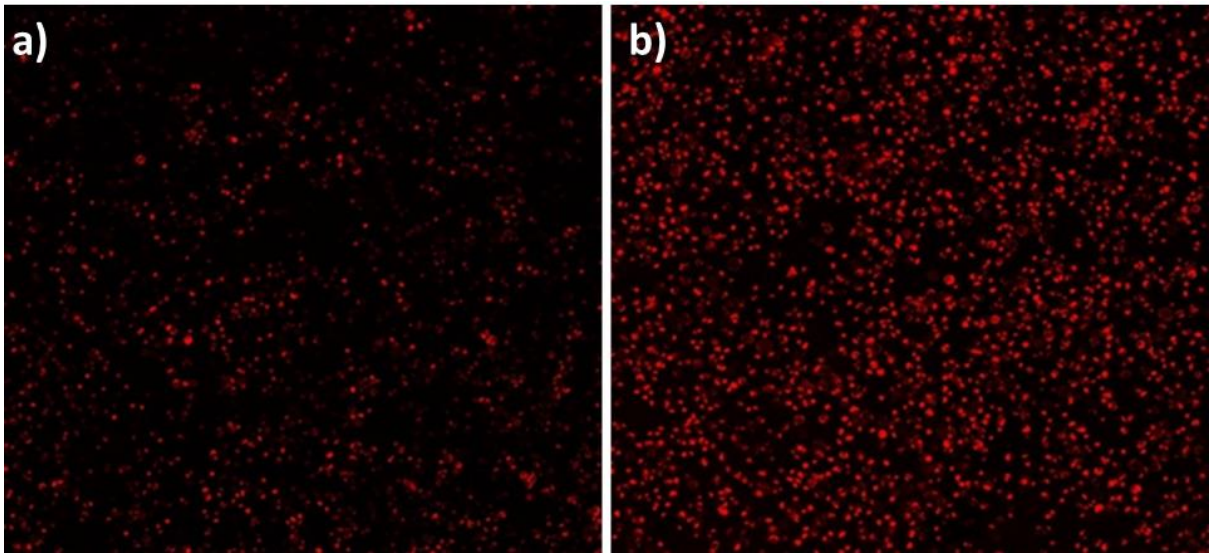

Figure 9-8. Confocal fluorescence images of MCF7 in suspension deformed through the cross-slot microfluidic device at 100 µl/min flow rate with 100 nM of a) QDs and b) RA-QDs for the data represented in Figure 4.4.

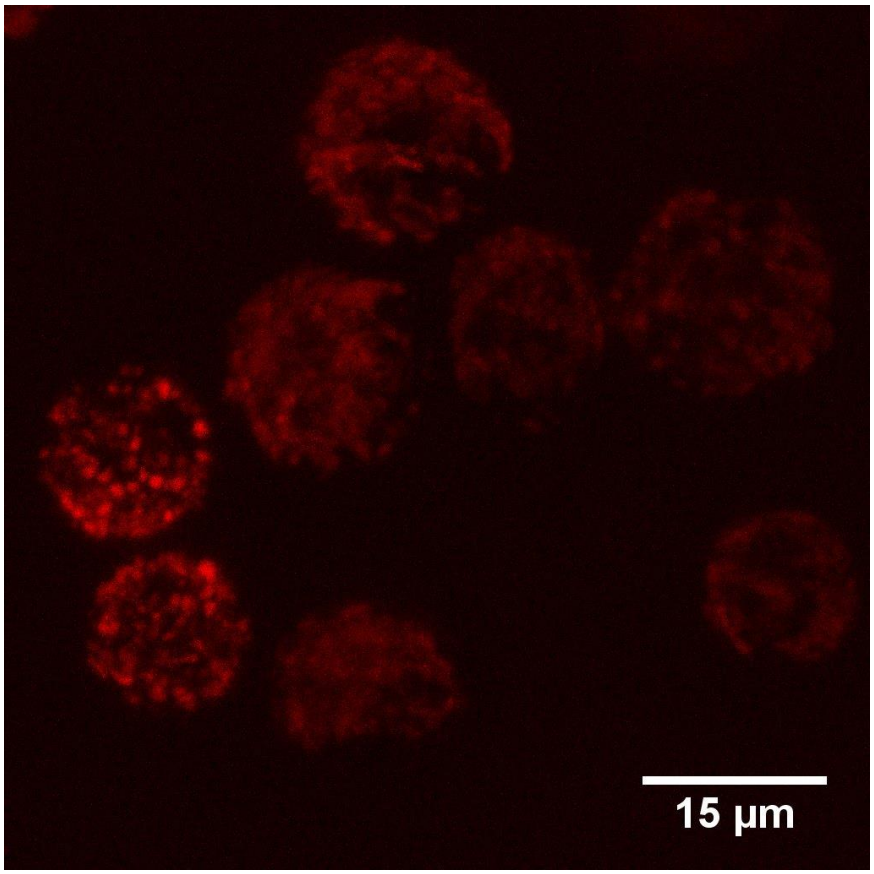

Figure 9-9. Confocal fluorescence images of MCF7 in suspension deformed through the cross-slot microfluidic device at 100 µl/min flow rate with 100 nM RA-QDs.

9.9. Comparison of breast cells for NADH/ NAD^+ using standard assay

The NADH/NAD^+ ratio in the cytoplasm is highly influenced by glycolysis, which is the primary mechanism of energy production in cancer cells. NAD^+/NADH along with the other redox couples as mentioned in sections 1.7.2 and 1.7.3 are responsible for the reducing environment of the cells.

As described earlier in section 2.11, the colorimetric method to quantify NADH along with NADH/NAD^+ ratio using the standard assay was performed against the calibration curve with standard NADH (Figure 9-10). The standard NADH at different concentrations (0-100 pmole) was treated in the sample manner as to the cell samples in 96-well plates as described earlier. The calibration curve from the endpoint reaction for standard NADH shows that the absorbance increases linearly with concentration as shown in Figure 4-9 (R^2>0.99). The quantification of NADH for the different breast cell lines was calculated against the calibration curve.

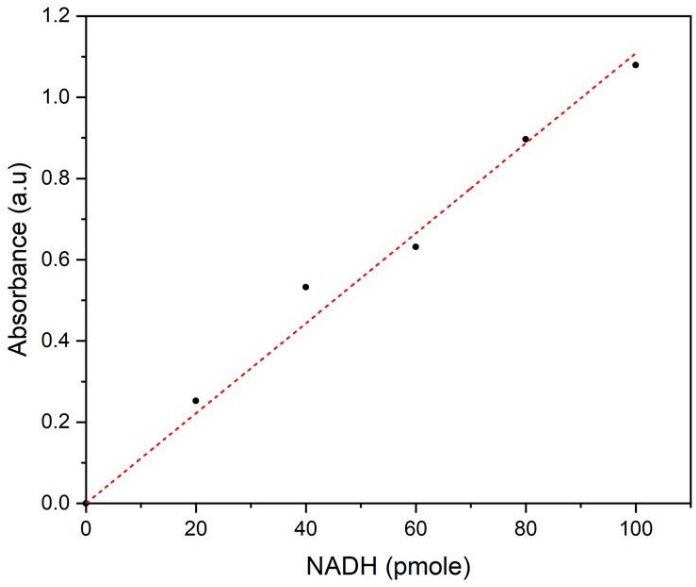

Figure 9-10. Calibration curves for the absorbance of the standard NADH with concentration with linear data fitting (R^2> 0.99).

From Figure 9-11 it was observed that for all the breast cell lines investigated, similar levels of the NADH/NAD+ ratio was measured using the standard assay [206]. Additionally, the NADH levels in the ER+ cells are expected to be higher compared to the ER- and the non-malignant

cells. However, it was seen that the NADH levels for the cells were also similar with the exception of T47D cells, show a lower value (Figure 9-11b). These results do not correlate with the overall findings in the literature and could point to the inadequacy of the standard assay [213]. However, repeats of the experiment are necessary to validate this claim.

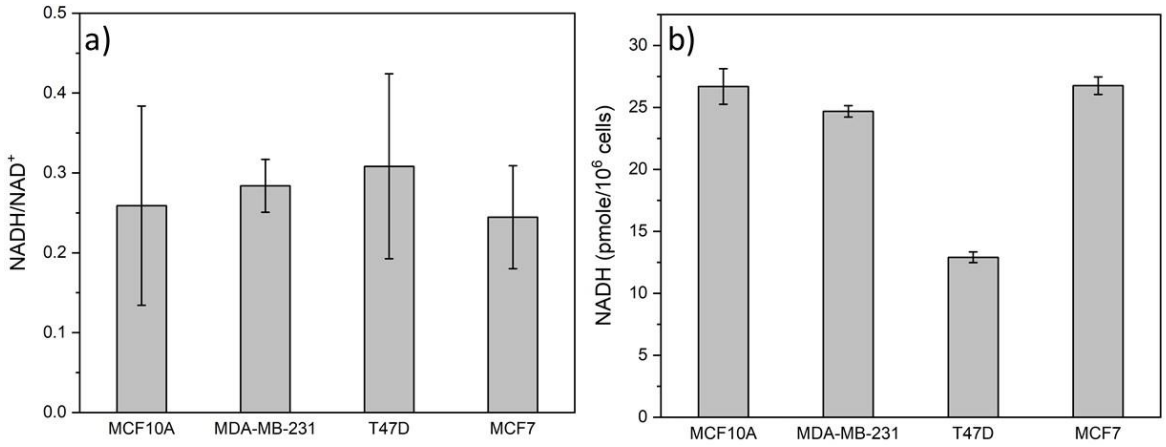

Figure 9-11. The standard assay measurement of a) NADH/NAD⁺ ratio and b) NADH for the different cell lines. Data expressed as mean ± SD with N = 5 wells per sample.

9.10. Confocal Images of cells adhered with RA-QDs

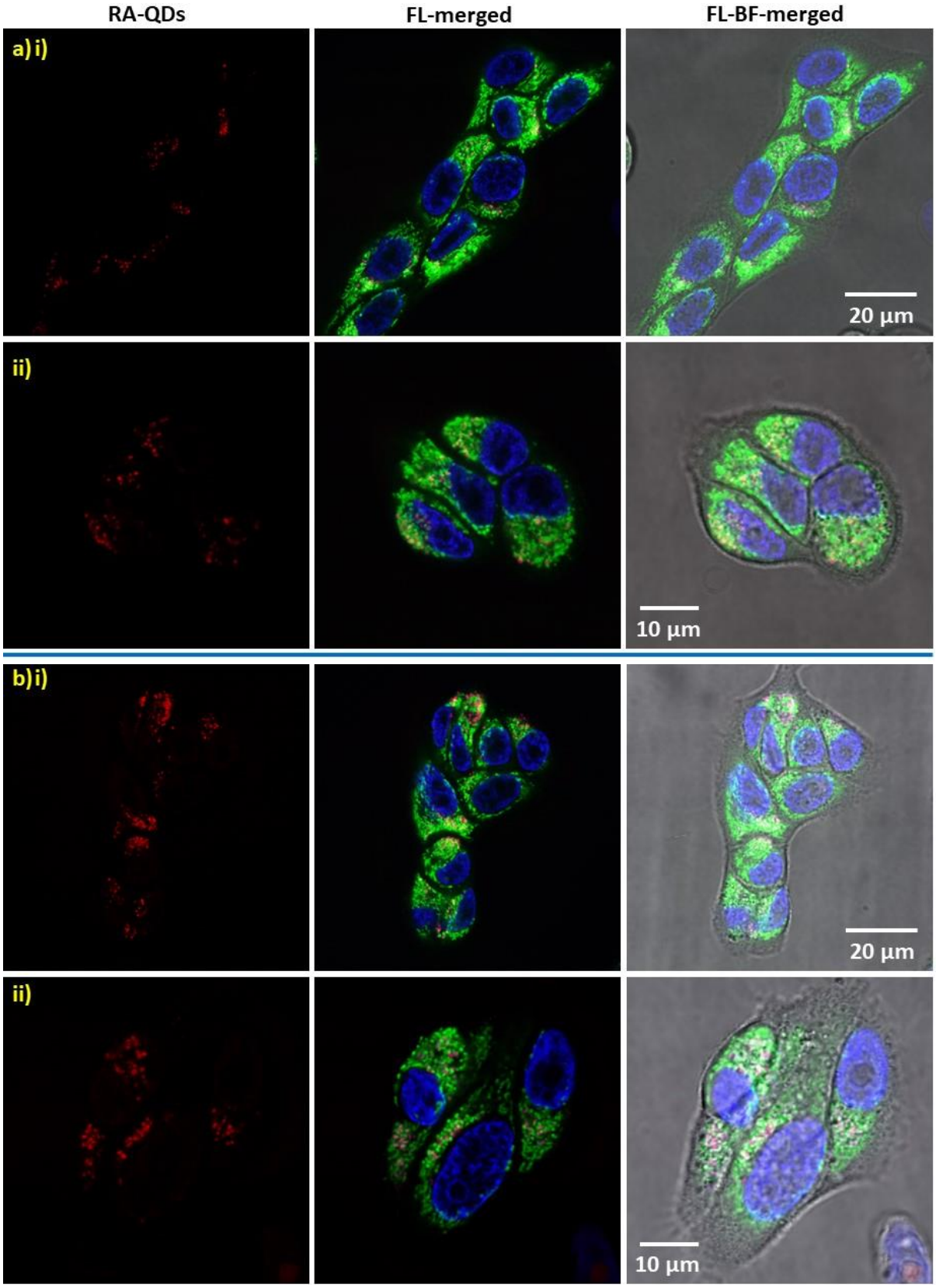

Figure 9-12. Confocal images of adhered MCF10A cells a) Incubated and b) deformed with 100 nM RA-QDs at 100 µl/min flow rate. Red channel: RA-QDs, green channel: mitotracker and blue channel: Hoechst 33342 nuclear stain.

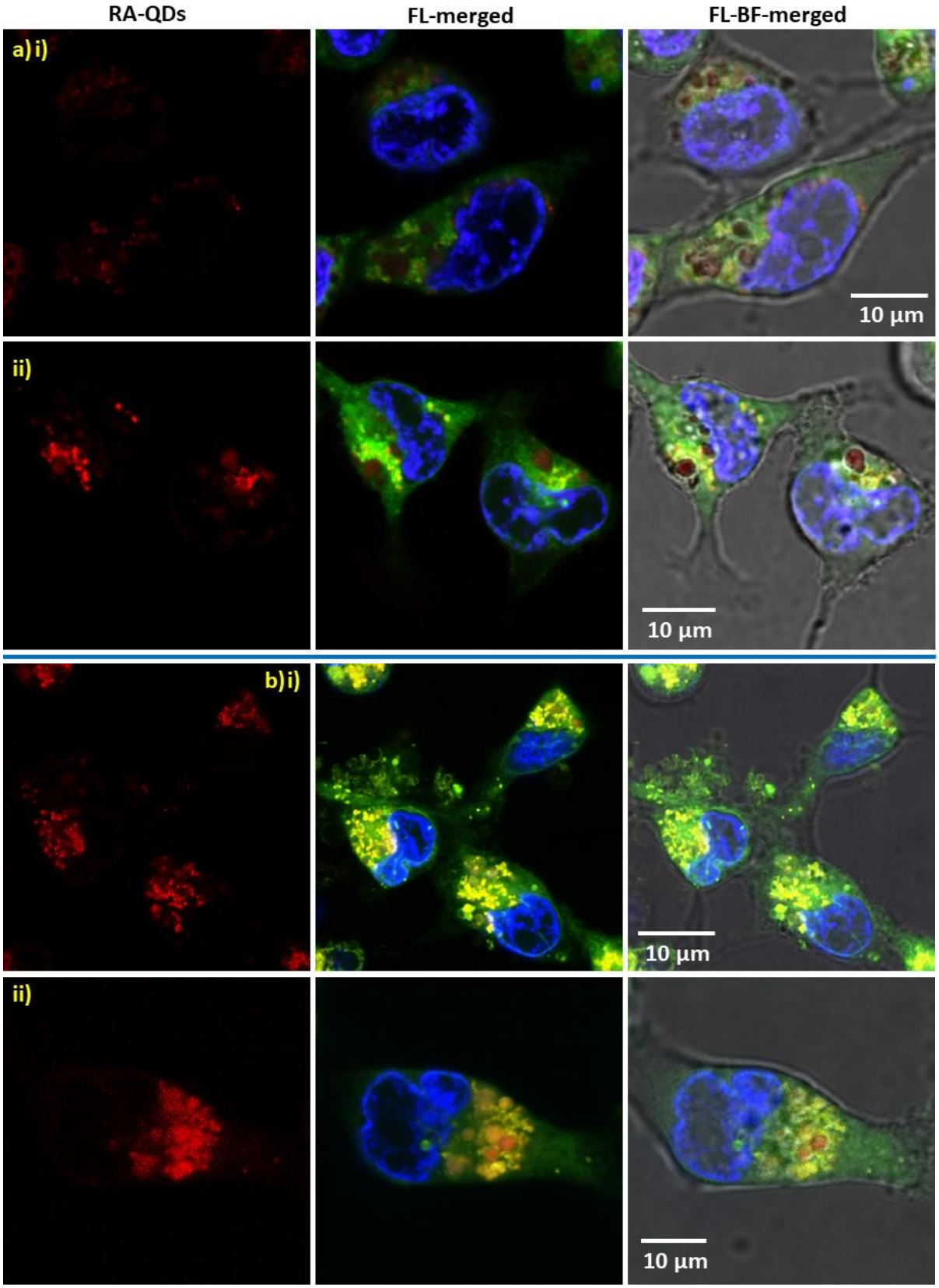

Figure 9-13. Confocal images of adhered MDA-MB-231 cells a) Incubated and b) deformed with 100 nM RA-QDs at 100 µl/min flow rate. Red channel: RA-QDs, green channel: mitotracker and blue channel: Hoechst 33342 nuclear stain.

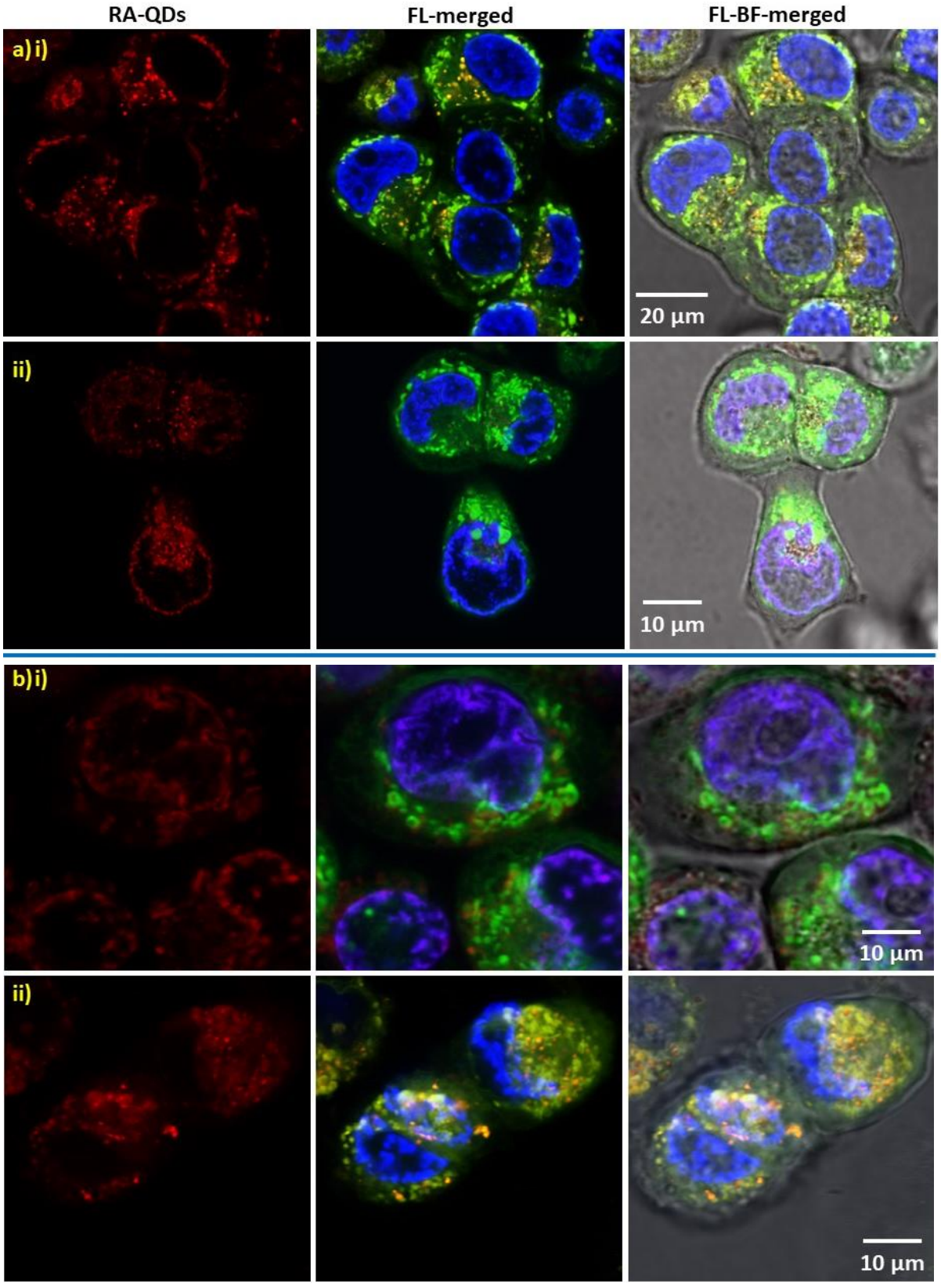

Figure 9-14. Confocal images of adhered T47D cells a) Incubated and b) deformed with 100 nM RA-QDs at 100 µl/min flow rate. Red channel: RA-QDs, green channel: mitotracker and blue channel: Hoechst 33342 nuclear stain.

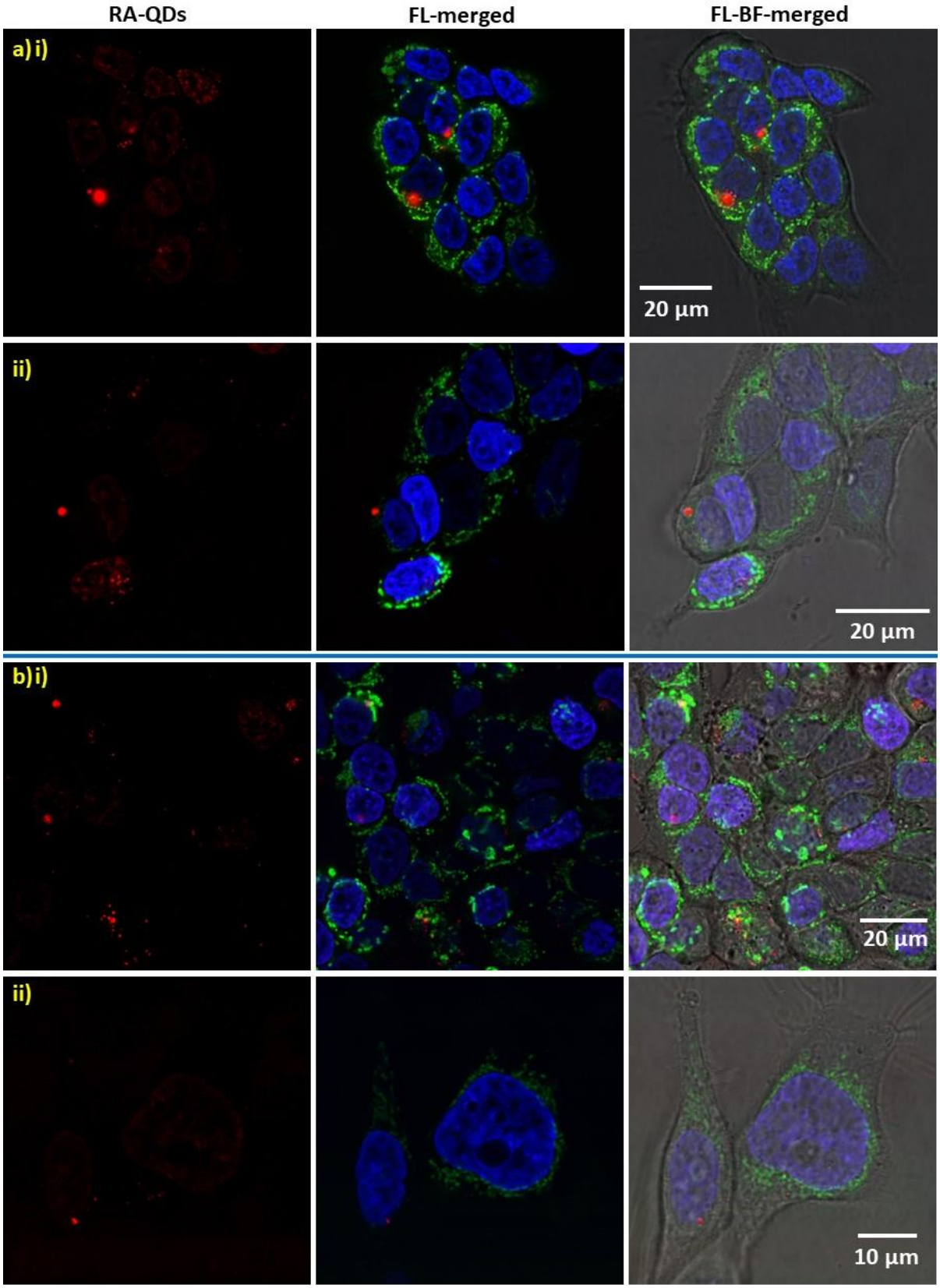

Figure 9-15. Confocal images of adhered MCF7 cells a) Incubated and b) deformed with 100 nM RA-QDs at 100 µl/min flow rate. Red channel: RA-QDs, green channel: mitotracker and blue channel: Hoechst 33342 nuclear stain.

9.11. AAPH treatment of adhered MCF10A cells with RA-QDs

MCF10A cells were pre-treated with mitotracker and Hoechst 33342 for the staining of the mitochondria and the nucleus, respectively. The cells were treated with 100 nM RA-QDs either by incubation or deformation through the cross-slot microfluidic device at 100 µl/min. The cells were further incubated for 15 min and washed twice with DPBS. They were adhered to 8 chamber LABTEK-II which were pre-treated with poly-L-lysine. The cells were incubated for 24 h at 37 ^{o}C under 5 % CO_2 atmosphere. The cells were imaged using the confocal microscope. Regions of interest (ROIs) were identified (Figure 9-16) which showed photoluminescence from the reduced RA-QDs. The cells were treated with 30 mM AAPH which generates oxidative stress in the cells. The cells were monitored for the next 30 min and the integrated fluorescence intensity from the ROIs were measured with time using ImageJ.

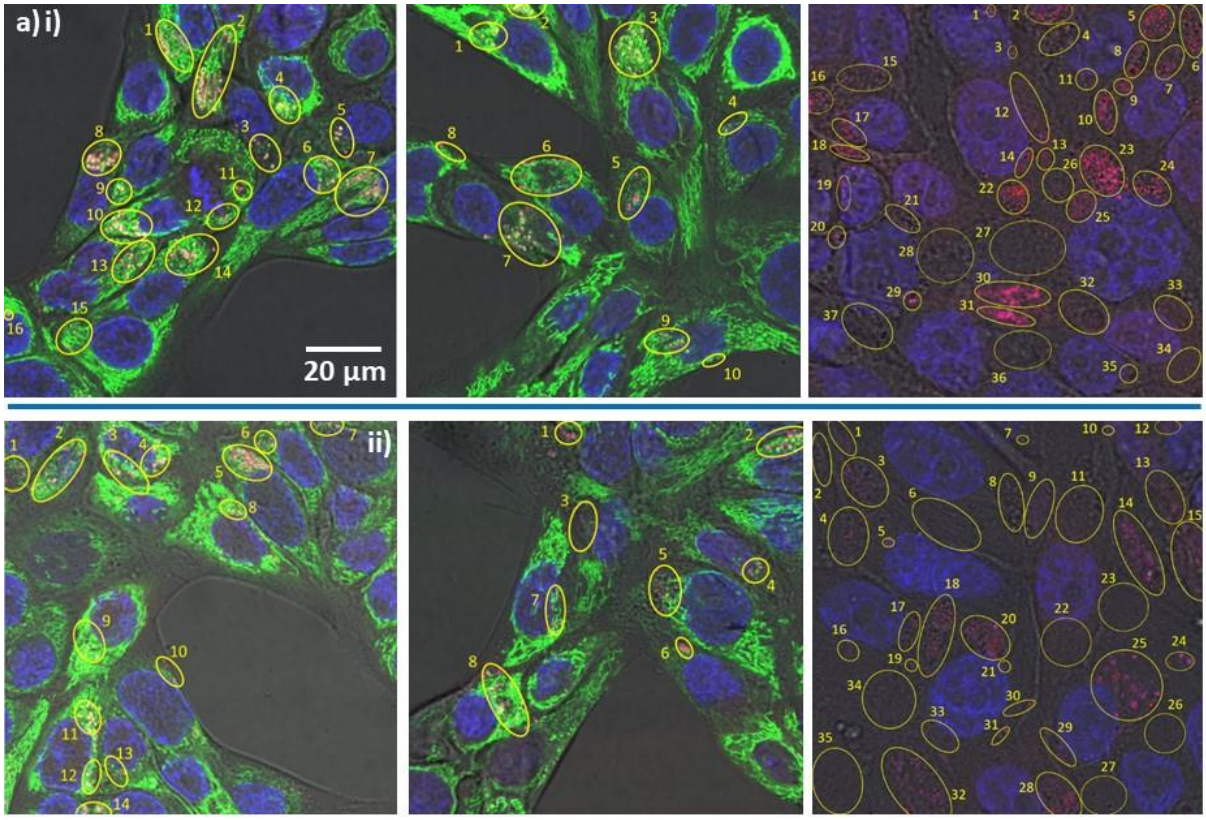

Figure 9-16. Confocal images of adhered MCF10A cells treated with 30 mM AAPH a) Incubated and b) deformed with 100 nM RA-QDs at 100 µl/min flow rate. Red channel: RA-QDs, green channel: mitotracker and blue channel: hoechst 33342 nuclear stain. The scale bar applies to all images. The labelled circles represent the region of interest where the integrated PL-intensity was measured before and after the AAPH treatment.

It was observed that the photoluminescence of the RA-QDs dropped for the ROIs with the addition of AAPH with time due to the increasing oxidative environment of the cells (Figure 9.17). The intensity kept dropping with time, indicating that there was increasing ROS generation with the cells struggling to recover its redox state. However, the overall drop in intensity showed that there is no significant difference in the emission of the RA-QDs from the incubated and the deformed cells. This could perhaps suggest that the RA-QDs dispersed in the cytoplasm for the deformed cells became enclosed in endosomal vesicles during the 24 h incubation. A more in-depth analysis would be interesting to understand the fate of the particles post-cytosolic delivery.

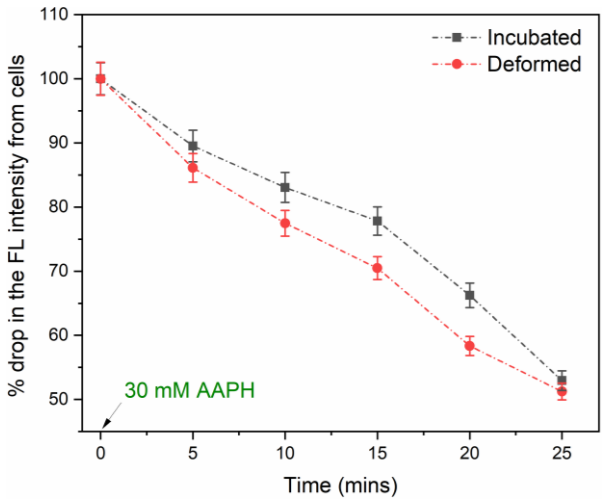

Figure 9-17. The mean percentage drop in the RA-QD integrated fluorescence intensity from the region of interests (labelled in Figure 9-14) from the adhered MCF10A cells incubated and deformed (100 µl/min flow rate) with 100 nM RA-QDs.

9.12. Optical spectroscopy of cells with calcein

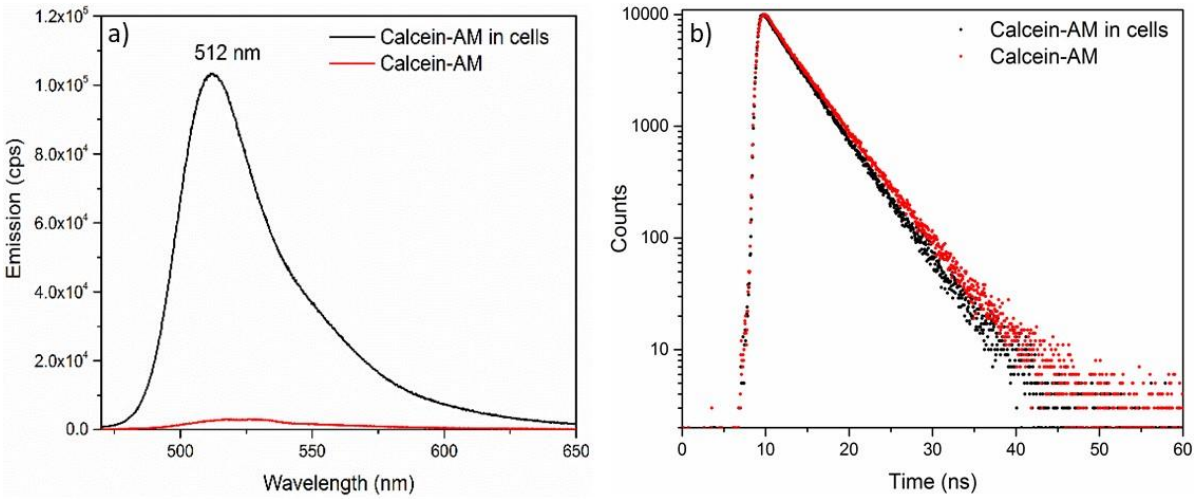

Figure 9-18. Fluorescence a) emission spectra and b) lifetime time decay traces of Calcein-AM in DPBS solution and from the MCF7 cells (1×10^6 cells/ml) incubated with 1 µM calcein-AM for 30 min and dispersed in DPBS.

9.13. Cell deformation with calcein

MCF7 cells were stained with 1 µM calcein and deformed through the cross-slot device at 100 µl/min. The cells (200 µl cell suspension) were collected in the incubation chambers (8 chamber LABTEK-II) and immediately imaged with the confocal microscope at the end of 3 min to the onset of cell collection. Cells were imaged every minute for 35 min or more. Control cells with Calcein but not deformed were also imaged for the same length of time. The fluorescence intensity from the cells was measured using the customised MATLAB as described in section 2.6.1. We observed that initially there are fewer cells at the bottom of the incubation chamber as most of them are still in suspension. The cells settle down to the bottom in about 3 min and the number of cells in the FOV remains fairly constant over the duration of observation. We observe that the PL intensity from the deformed cells is much lower than the control cells, which suggests that there is leakage of intracellular material from the deformed cells (Figure 9-19). However, as time progresses, the deformed cells regain their fluorescence intensity but not quite reaching the level of the control cells. This could be due to the recovery of the redox state in the cell cytoplasm and cleaving of the unreacted calcein-AM within the cells, which could be investigated in the future.

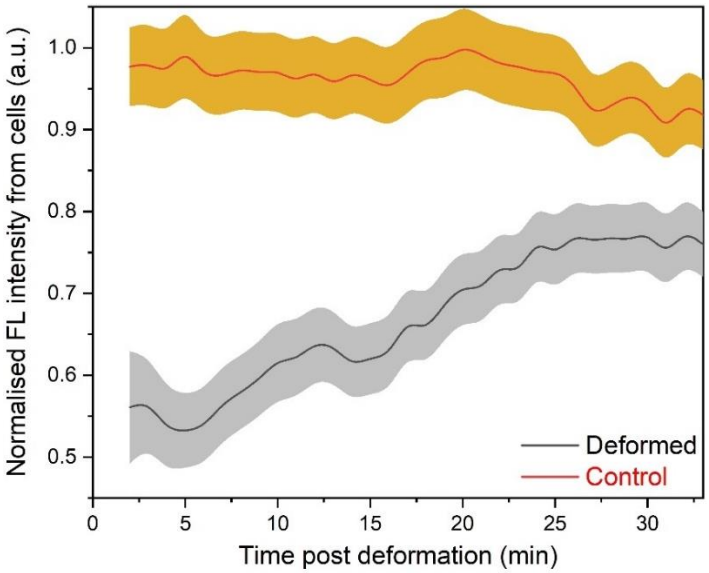

Figure 9-19. Normalised mean total fluorescence intensity from MCF7 cells stained with 1 µM calcein as a function of time post-deformation though the cross-slot microfluidic device at Q = 100 µl/min (Black line) in comparison with the cells without deformation (red line). The data expressed as mean ± SE for with >200 cells each and N =3 repeats.

9.14. Multiple deformation of cells stained with calcein

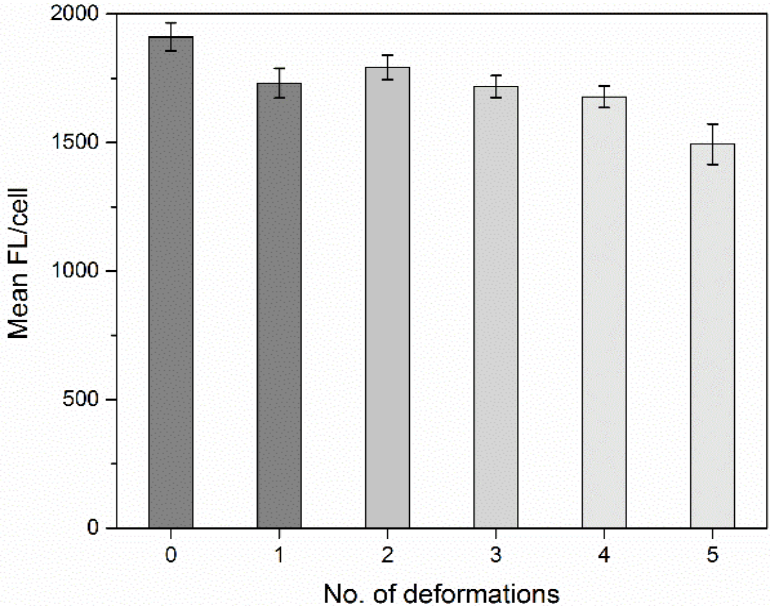

Figure 9-20. Mean integrated total fluorescence intensity from MCF7 cells stained with 1 µM calcein over multiple deformations through the cross-slot microfluidic device at 100 µl/min flow rate. Data expressed as mean ± SE.

9.15. Determination of calcein FL intensity from cells by analysing FDM images

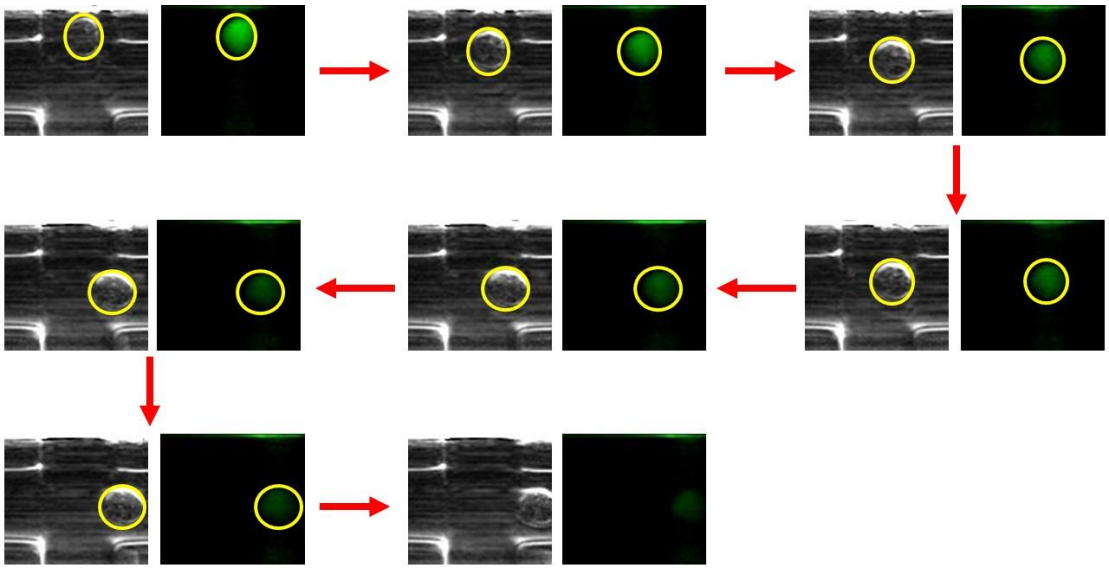

Figure 9-21. FDM images (bright field and fluorescence) of a typical event with MCF7 cells stained with 1 µM calcein passing through the FOV. The traces detected by fitting an ellipse to the average cell position in the bright field and the fluorescence images were projected onto the corresponding fluorescence image and the total fluorescence intensity was measured.

9.16. Distribution of calcein intensity from MCF7 cells in regions 1 and 2 using FDM

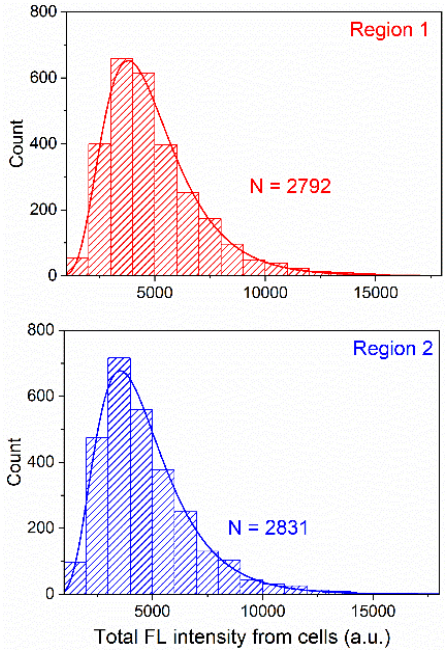

Figure 9-22. Histograms for the total integrated Fluorescence intensity of MCF7 cells stained with 1 µM calcein measured from the FDM images at regions 1 and 2 post-deformation (100 µl/min) for the datasets presented in Figure 5-16.

9.17. Comparison of CdSe QDs and QRs

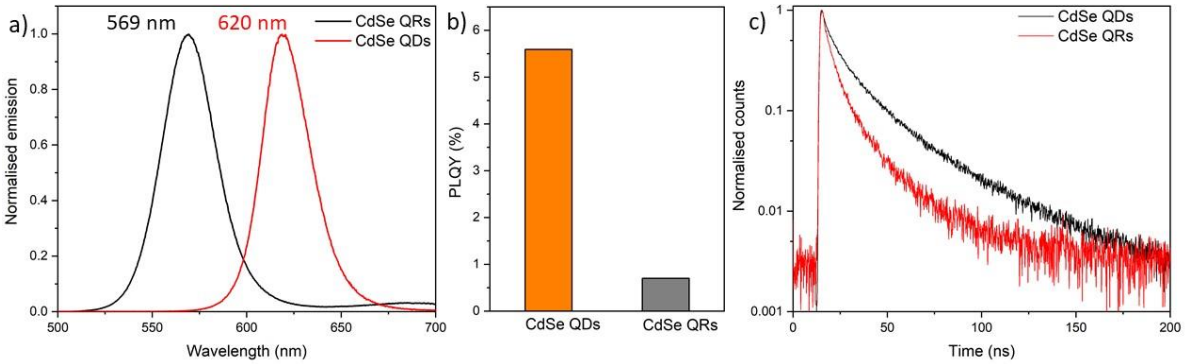

Figure 9-23. Comparative fluorescence (a) emission spectra (normalised) b) PLQY and c) lifetime time decay curves of CdSe QDs and QRs (6-sequetail injections of Se-precursor every 3 min) with the same total duration of growth (18 min).

9.18 Exponential decay fits for the QRs

R^2 values	1st injection	2nd injection	3rd injection	4th injection	5th injection	6th injection
Monoexponential fit	0.97384	0.96686	0.96825	0.95975	0.95937	0.95134
Biexponential fit	0.99485	0.99492	0.99442	0.99324	0.99335	0.99434

Table 9-1: The R^2 values for mono- and bi-exponential decay fits for the fluorescence lifetime decay curves of the CdSe QRs with the number of Se-precursor injections.

R^2 values/Shell growth	0 h	1 h	2 h	3 h	4 h	5 h	6 h
Monoexponential fit	0.97842	0.98548	0.98551	0.98681	0.98691	0.99682	0.99668
Biexponential fit	0.99930	0.99961	0.99928	0.99973	0.99983	0.99993	0.99991

Table 9-2: The R^2 values for mono- and bi-exponential decay fits for the fluorescence lifetime decay curves of the CdSe/ZnS QRs with duration of ZnS shell growth.

R^2 values/ Cl^- ions per nm^2 QR surface	0	96	192
Monoexponential fit	0.96452	0.98105	0.99388
Biexponential fit	0.99938	0.99963	0.99998

Table 9-3. The R^2 values for mono- and bi-exponential decay fits for the fluorescence lifetime decay curves of the CdSe QRs with Cl^- ion treatment.

10. References

1. X. Michalet, Quantum Dots for Live Cells. *Science*, **538** (2013) 538–545. https://doi.org/10.1126/science.1104274.

2. D. Gammon, Electrons in artificial atoms. *Nature*, **405** (2000) 899–900. https://doi.org/10.1038/35016189.

3. T. Kippeny, L. A. Swafford, & S. J. Rosenthal, Semiconductor nanocrystals: A powerful visual aid for introducing the particle in a box. *Journal of Chemical Education*, **79** (2002) 1094–1100. https://doi.org/10.1021/ed079p1094.

4. A. P. Alivisatos, Perspectives on the physical chemistry of semiconductor nanocrystals. *Journal of Physical Chemistry*, **100** (1996) 13226–13239. https://doi.org/10.1021/jp9535506.

5. W. W. Yu, L. Qu, W. Guo, & X. Peng, Experimental determination of the extinction coefficient of CdTe, CdSe, and CdS nanocrystals. *Chemistry of Materials*, **15** (2003) 2854–2860. https://doi.org/10.1021/cm034081k.

6. L. E. Brus, Electron-electron and electron-hole interactions in small semiconductor crystallites: The size dependence of the lowest excited electronic state. *The Journal of Chemical Physics*, **80** (1984) 4403–4409. https://doi.org/10.1063/1.447218.

7. D. E. Ram, A. P. Reyes-cruzaley, G. Dominguez, F. Paraguay-delgado, A. Tirado-gu, & G. Pina-luis, CdTe Quantum Dots Modified with Cysteamine : A New Efficient Nanosensor for the Determination of Folic Acid. *Sensors*, **19** (2019) 4548.

8. A. J. Harvie, Quantum Dot Redox Sensors : Understanding Excited State Dynamics. (2018) 1–164.

9. M. Califano & A. Zunger, Efficient Inverse Auger Recombination at Threshold in CdSe Nanocrystals. *Nano Letters*, **4** (2004) 525–531.

10. I. Takeshi & H. Sakaki, Electron relaxation in a quantum dot: Significance of multiphonon processes. *Physical Review B*, **46** (1992) 7260–7263.

11. C. T. Smith, M. A. Leontiadou, R. Page, P. O. Brien, & D. J. Binks, Ultrafast Charge

Dynamics in Trap-Free and Surface- Trapping Colloidal Quantum Dots. (2015) 1–7. https://doi.org/10.1002/advs.201500088.

12. C. Giansante & I. Infante, Surface Traps in Colloidal Quantum Dots: A Combined Experimental and Theoretical Perspective. *The Journal of Physical Chemistry Letters*, **8** (2017) 5209–5215. https://doi.org/10.1021/acs.jpclett.7b02193.

13. M. A. Boles, D. Ling, T. Hyeon, & D. V. Talapin, The surface science of nanocrystals. *Nature Materials*, **15** (2016) 141–153. https://doi.org/10.1038/nmat4526.

14. Z. J. Zhu, Y. C. Yeh, R. Tang, B. Yan, J. Tamayo, R. W. Vachet, & V. M. Rotello, Stability of quantum dots in live cells. *Nature Chemistry*, **3** (2011) 963–968. https://doi.org/10.1038/nchem.1177.

15. M. J. Choi, R. Pierson, Y. Chang, H. Guo, & I. K. Kang, Enhanced intracellular uptake of CdTe quantum dots by conjugation of oligopeptides. *Journal of Nanomaterials*, **2013** (2013), 14. https://doi.org/10.1155/2013/291020.

16. E. Oh, R. Liu, A. Nel, K. B. Gemill, M. Bilal, Y. Cohen, & I. L. Medintz, Meta-analysis of cellular toxicity for cadmium-containing quantum dots. *Nature Nanotechnology*, **11** (2016) 479–486. https://doi.org/10.1038/nnano.2015.338.

17. M. Green, The nature of quantum dot capping ligands. (2010) 5797–5809. https://doi.org/10.1039/c0jm00007h.

18. J. Breger, J. B. Delehanty, & I. L. Medintz, Continuing progress toward controlled intracellular delivery of semiconductor quantum dots. *Wiley Interdisciplinary Reviews: Nanomedicine and Nanobiotechnology*, **7** (2015) 131–151. https://doi.org/10.1002/wnan.1281.

19. E. R. Goldman & H. Mattoussi, Quantum dot bioconjugates for imaging , labelling and sensing. *Nature Materials*, **4** (2005) 435–446.

20. C. Guhrenz, V. Sayevich, F. Weigert, E. Hollinger, A. Reichhelm, U. Resch-Genger, N. Gaponik, & A. Eychmüller, Transfer of Inorganic-Capped Nanocrystals into Aqueous Media. *Journal of Physical Chemistry Letters*, **8** (2017) 5573–5578. https://doi.org/10.1021/acs.jpclett.7b02319.

21. S. Tamang, G. Beaune, I. Texier, & P. Reiss, Aqueous phase transfer of InP/ZnS nanocrystals conserving fluorescence and high colloidal stability. *ACS Nano*, **5** (2011) 9392–9402. https://doi.org/10.1021/nn203598c.

22. F. Dubois, B. Mahler, B. Dubertret, E. Doris, & C. Mioskowski, A versatile strategy for quantum dot ligand exchange. *Journal of the American Chemical Society*, **129** (2007) 482–483. https://doi.org/10.1021/ja067742y.

23. B. K. Pong, B. L. Trout, & J. Y. Lee, Modified ligand-exchange for efficient solubilization of CdSe/ZnS quantum dots in water: A procedure guided by computational studies. *Langmuir*, **24** (2008) 5270–5276. https://doi.org/10.1021/la703431j.

24. M. Booth, R. Peel, R. Partanen, N. Hondow, V. Vasilca, L. J. C. Jeuken, & K. Critchley, Amphipol-encapsulated CuInS2/ZnS quantum dots with excellent colloidal stability. *RSC Advances*, **3** (2013) 20559–20566. https://doi.org/10.1039/c3ra43846e.

25. L. Huang, M. Liao, S. Chen, V. G. Demillo, S. A. Dupre, X. Zhu, N. G. Publicover, & K. W. Hunter, A polymer encapsulation approach to prepare zwitterion-like, biocompatible quantum dots with wide pH and ionic stability. *Journal of Nanoparticle Research*, **16** (2014), 1-9. https://doi.org/10.1007/s11051-014-2555-3.

26. C. Fowley, B. Mc Caughan, A. Devlin, I. Yildiz, F. M. Raymo, & J. F. Callan, Highly luminescent biocompatible carbon quantum dots by encapsulation with an amphiphilic polymer. *Chemical Communications*, **48** (2012) 9361–9363. https://doi.org/10.1039/c2cc34962k.

27. J. F. Galloway, A. Winter, K. H. Lee, J. H. Park, C. M. Dvoracek, P. Devreotes, & P. C. Searson, Quantitative characterization of the lipid encapsulation of quantum dots for biomedical applications. *Nanomedicine: Nanotechnology, Biology, and Medicine*, **8** (2012) 1190–1199. https://doi.org/10.1016/j.nano.2011.12.002.

28. H. Fan, E. W. Leve, C. Scullin, J. Gabaldon, D. Tallant, S. Bunge, T. Boyle, M. C. Wilson, & C. J. Brinker, Surfactant-assisted synthesis of water-soluble and biocompatible semiconductor quantum dot micelles. *Nano Letters*, **5** (2005) 645–648. https://doi.org/10.1021/nl050017l.

29. W. C. Law, K. T. Yong, I. Roy, H. Ding, R. Hu, W. Zhao, & P. N. Prasad, Aqueous-phase

synthesis of highly luminescent CdTe/ZnTe core/shell quantum dots optimized for targeted bioimaging. *Small*, **5** (2009) 1302–1310. https://doi.org/10.1002/smll.200801555.

30. N. Gaponik, D. V. Talapin, A. L. Rogach, K. Hoppe, E. V. Shevchenko, A. Kornowski, A. Eychmüller, & H. Weller, Thiol-capping of CDTe nanocrystals: An alternative to organometallic synthetic routes. *Journal of Physical Chemistry B*, **106** (2002) 7177–7185. https://doi.org/10.1021/jp025541k.

31. M. Ulusoy, J. G. Walter, A. Lavrentieva, I. Kretschmer, L. Sandiford, A. Le Marois, R. Bongartz, P. Aliuos, K. Suhling, F. Stahl, M. Green, & T. Scheper, One-pot aqueous synthesis of highly strained CdTe/CdS/ZnS nanocrystals and their interactions with cells. *RSC Advances*, **5** (2015) 7485–7494. https://doi.org/10.1039/c4ra13386b.

32. S. Kini, S. D. Kulkarni, V. Ganiga, T. K. Nagarakshit, & S. Chidangil, Dual functionalized, stable and water dispersible CdTe quantum dots: Facile, one-pot aqueous synthesis, optical tuning and energy transfer applications. *Materials Research Bulletin*, **110** (2019) 57–66. https://doi.org/10.1016/j.materresbull.2018.10.013.

33. T. Zeng, Y. Hu, N. Wang, C. Xia, S. Li, Y. Zu, L. Liu, Z. Yao, Y. Zhao, & H. C. Wu, Effects of different metal ions on the fluorescence of CdSe/ZnS quantum dots capped with various thiolate ligands. *Physical Chemistry Chemical Physics*, **15** (2013) 18710–18715. https://doi.org/10.1039/c3cp52666f.

34. H. Zhu, M. Z. Hu, L. Shao, K. Yu, R. Dabestani, M. B. Zaman, & S. Liao, Synthesis and optical properties of thiol functionalized CdSe/ZnS (Core/Shell) quantum dots by ligand exchange. *Journal of Nanomaterials*, **2014** (2014) 1-14. https://doi.org/10.1155/2014/324972.

35. A. Shavel, N. Gaponik, & A. Eychmüller, Factors governing the quality of aqueous CdTe nanocrystals: Calculations and experiment. *Journal of Physical Chemistry B*, **110** (2006) 19280–19284. https://doi.org/10.1021/jp063351u.

36. M. D. Peterson, L. C. Cass, R. D. Harris, K. Edme, K. Sung, & E. A. Weiss, The role of ligands in determining the exciton relaxation dynamics in semiconductor quantum dots. *Annual Review of Physical Chemistry*, **65** (2014) 317–339.

https://doi.org/10.1146/annurev-physchem-040513-103649.

37. K. Virzbickas, L. Rimkute, A. J. Harvie, & K. Critchley, Surfactant-dependent photoluminescence of CdTe/CdS nanocrystals. *Journal of Experimental Nanoscience*, 12 (2017) 94–103. https://doi.org/10.1080/17458080.2016.1273553.

38. A. L. Rogach, T. Franzl, T. A. Klar, J. Feldmann, N. Gaponik, V. Lesnyak, A. Shavel, A. Eychmüller, Y. P. Rakovich, & J. F. Donegan, Aqueous synthesis of thiol-capped CdTe nanocrystals: State-of-the-art. *Journal of Physical Chemistry C*, 111 (2007) 14628–14637. https://doi.org/10.1021/jp072463y.

39. D. Bera, L. Qian, T. Tseng, & P. H. Holloway, Quantum Dots and Their Multimodal Applications: A Review. (2010) 2260–2345. https://doi.org/10.3390/ma3042260.

40. D. Vasudevan, R. Ranganathan, A. Trinchi, & I. Cole, Core – shell quantum dots : Properties and applications. *JOURNAL OF ALLOYS AND COMPOUNDS*, 636 (2015) 395–404. https://doi.org/10.1016/j.jallcom.2015.02.102.

41. S. Jain, S. Bharti, G. Kaur, & S. K. Tripathi, I-III-VI core / shell QDs : Synthesis , characterizations and applications. *Journal of Luminescence*, 219 (2020) 116912. https://doi.org/10.1016/j.jlumin.2019.116912.

42. B. O. Dabbousi, F. V Mikulec, J. R. Heine, H. Mattoussi, R. Ober, K. F. Jensen, & M. G. Bawendi, (CdSe) ZnS Core - Shell Quantum Dots : Synthesis and Characterization of a Size Series of Highly Luminescent Nanocrystallites. 9463 (1997) 9463–9475.

43. X. Huang, X. Tong, & Z. Wang, Journal of Electronic Science and Technology Rational design of colloidal core / shell quantum dots for optoelectronic applications. *Journal of Electronic Science and Technology*, 18 (2020) 100018. https://doi.org/10.1016/j.jnlest.2020.100018.

44. S. Kim, B. Fisher, & M. Bawendi, Type-II Quantum Dots : CdTe / CdSe (Core / Shell) and CdSe / ZnTe (Core / Shell) Heterostructures. *Journal of American Chemical Society*, 125 (2003) 11466–11467.

45. A. J. Harvie, C. T. Smith, R. Ahumada-Lazo, L. J. C. Jeuken, M. Califano, R. S. Bon, S. J. O. Hardman, D. J. Binks, & K. Critchley, Ultrafast Trap State-Mediated Electron Transfer

for Quantum Dot Redox Sensing. *Journal of Physical Chemistry C*, **122** (2018) 10173–10180. https://doi.org/10.1021/acs.jpcc.8b02551.

46. R. Ghosh Chaudhuri & S. Paria, Core/shell nanoparticles: Classes, properties, synthesis mechanisms, characterization, and applications. *Chemical Reviews*, **112** (2012) 2373–2433. https://doi.org/10.1021/cr100449n.

47. I. V. Martynenko, A. P. Litvin, F. Purcell-Milton, A. V. Baranov, A. V. Fedorov, & Y. K. Gun'Ko, Application of semiconductor quantum dots in bioimaging and biosensing. *Journal of Materials Chemistry B*, **5** (2017) 6701–6727. https://doi.org/10.1039/c7tb01425b.

48. P. Zrazhevskiy, M. Sena, & X. Gao, Designing multifunctional quantum dots for bioimaging, detection, and drug delivery. *Chemical Society Reviews*, **39** (2010) 4326–4354. https://doi.org/10.1039/b915139g.

49. L. . Michalet, X., Pinaud, F.F., Bentolila, Quantum_dots_for_live_cells__i.PDF. *Science*, **307** (2005) 538–544.

50. X. Gao, Y. Cui, R. M. Levenson, L. W. K. Chung, & S. Nie, In vivo cancer targeting and imaging with semiconductor quantum dots. *Nature Biotechnology*, **22** (2004) 969–976. https://doi.org/10.1038/nbt994.

51. J. K. Jaiswal, H. Mattoussi, J. M. Mauro, & S. M. Simon, Long-term multiple color imaging of live cells using quantum dot bioconjugates. *Nature Biotechnology*, **21** (2003) 47–51. https://doi.org/10.1038/nbt767.

52. L. J. Zhang, L. Xia, H. Y. Xie, Z. L. Zhang, & D. W. Pang, Quantum Dot Based Biotracking and Biodetection. *Analytical Chemistry*, **91** (2019) 532–547. https://doi.org/10.1021/acs.analchem.8b04721.

53. X. Wu, H. Liu, J. Liu, K. N. Haley, J. A. Treadway, J. P. Larson, N. Ge, F. Peale, & M. P. Bruchez, Immunofluorescent labeling of cancer marker Her2 and other cellular targets with semiconductor quantum dots. *Nature Biotechnology*, **21** (2003) 41–46. https://doi.org/10.1038/nbt764.

54. F. Chen & D. Gerion, Fluorescent CdSe/ZnS nanocrystal-peptide conjugates for long-

term, nontoxic imaging and nuclear targeting in living cells. *Nano Letters*, **4** (2004) 1827–1832. https://doi.org/10.1021/nl049170q.

55. B. Y. S. Kim, W. Jiang, J. Oreopoulos, C. M. Yip, J. T. Rutka, & W. C. W. Chan, Biodegradable quantum dot nanocomposites enable live cell labeling and imaging of cytoplasmic targets. *Nano Letters*, **8** (2008) 3887–3892. https://doi.org/10.1021/nl802311t.

56. V. Biju, T. Itoh, & M. Ishikawa, Delivering quantum dots to cells: Bioconjugated quantum dots for targeted and nonspecific extracellular and intracellular imaging. *Chemical Society Reviews*, **39** (2010) 3031–3056. https://doi.org/10.1039/b926512k.

57. K. Bruun & C. Hille, Study on intracellular delivery of liposome encapsulated quantum dots using advanced fluorescence microscopy. *Scientific Reports*, **9** (2019) 1–15. https://doi.org/10.1038/s41598-019-46732-5.

58. D. S. Lidke, P. Nagy, T. M. Jovin, & D. J. Arndt-Jovin, *Biotin-ligand complexes with St reptavidin quantum dots for in vivo cell labeling of membrane receptors* (2007). https://doi.org/10.1385/1-59745-369-2:69.

59. I. L. Medintz, M. H. Stewart, S. A. Trammell, K. Susumu, J. B. Delehanty, B. C. Mei, J. S. Melinger, J. B. Blanco-Canosa, P. E. Dawson, & H. Mattoussi, Quantum-dot/dopamine bioconjugates function as redox coupled assemblies for in vitro and intracellular pH sensing. *Nature Materials*, **9** (2010) 676–684. https://doi.org/10.1038/nmat2811.

60. N. Li, A. Than, C. Sun, J. Tian, J. Chen, K. Pu, X. Dong, & P. Chen, Monitoring Dynamic Cellular Redox Homeostasis Using Fluorescence-Switchable Graphene Quantum Dots. *ACS Nano*, **10** (2016) 11475–11482. https://doi.org/10.1021/acsnano.6b07237.

61. L. X. Qin, W. Ma, D. W. Li, Y. Li, X. Chen, H. B. Kraatz, T. D. James, & Y. T. Long, Coenzyme Q functionalized CdTe/ZnS quantum dots for reactive oxygen species (ROS) imaging. *Chemistry - A European Journal*, **17** (2011) 5262–5271. https://doi.org/10.1002/chem.201003749.

62. M. Bottrill & M. Green, Some aspects of quantum dot toxicity. *Chemical Communications*, **47** (2011) 7039–7050. https://doi.org/10.1039/c1cc10692a.

63. S. Nikazar, V. S. Sivasankarapillai, A. Rahdar, S. Gasmi, P. S. Anumol, & M. S. Shanavas, Revisiting the cytotoxicity of quantum dots: an in-depth overview. *Biophysical Reviews*, **12** (2020) 703–718. https://doi.org/10.1007/s12551-020-00653-0.

64. Y. Wang & M. Tang, Review of in vitro toxicological research of quantum dot and potentially involved mechanisms. *Science of the Total Environment*, **625** (2018) 940–962. https://doi.org/10.1016/j.scitotenv.2017.12.334.

65. R. Hardman, A toxicologic review of quantum dots: Toxicity depends on physicochemical and environmental factors. *Environmental Health Perspectives*, **114** (2006) 165–172. https://doi.org/10.1289/ehp.8284.

66. M. J. D. Clift, J. Varet, S. M. Hankin, B. Brownlee, A. M. Davidson, C. Brandenberger, B. Rothen-Rutishauser, D. M. Brown, & V. Stone, Quantum dot cytotoxicity in vitro: An investigation into the cytotoxic effects of a series of different surface chemistries and their core/shell materials. *Nanotoxicology*, **5** (2011) 664–674. https://doi.org/10.3109/17435390.2010.534196.

67. C. Maksoudian, S. J. Soenen, K. Susumu, E. Oh, I. L. Medintz, & B. B. Manshian, A Multiparametric Evaluation of Quantum Dot Size and Surface-Grafted Peptide Density on Cellular Uptake and Cytotoxicity. *Bioconjugate Chemistry*, **31** (2020) 1077–1087. https://doi.org/10.1021/acs.bioconjchem.0c00078.

68. O. Gladkovskaya, P. Greaney, Y. K. Gun'Ko, G. M. O'Connor, M. Meere, & Y. Rochev, An experimental and theoretical assessment of quantum dot cytotoxicity. *Toxicology Research*, **4** (2015) 1409–1415. https://doi.org/10.1039/c5tx00149h.

69. E. Chang, N. Thekkek, W. W. Yu, V. L. Colvin, & R. Drezek, Evaluation of quantum dot cytotoxicity based on intracellular uptake. *Small*, **2** (2006) 1412–1417. https://doi.org/10.1002/smll.200600218.

70. N. Chen, Y. He, Y. Su, X. Li, Q. Huang, H. Wang, X. Zhang, R. Tai, & C. Fan, The cytotoxicity of cadmium-based quantum dots. *Biomaterials*, **33** (2012) 1238–1244. https://doi.org/10.1016/j.biomaterials.2011.10.070.

71. Y. Su, Y. He, H. Lu, L. Sai, Q. Li, W. Li, L. Wang, P. Shen, Q. Huang, & C. Fan, The cytotoxicity of cadmium based, aqueous phase - Synthesized, quantum dots and its

modulation by surface coating. *Biomaterials*, 30 (2009) 19–25. https://doi.org/10.1016/j.biomaterials.2008.09.029.

72. A. Cuypers, M. Plusquin, T. Remans, M. Jozefczak, E. Keunen, H. Gielen, K. Opdenakker, A. R. Nair, E. Munters, T. J. Artois, T. Nawrot, J. Vangronsveld, & K. Smeets, Cadmium stress: An oxidative challenge. *BioMetals*, 23 (2010) 927–940. https://doi.org/10.1007/s10534-010-9329-x.

73. B. A. Rzigalinski & J. S. Strobl, Cadmium-containing nanoparticles: Perspectives on pharmacology and toxicology of quantum dots. *Toxicology and Applied Pharmacology*, 238 (2009) 280–288. https://doi.org/10.1016/j.taap.2009.04.010.

74. C. Kirchner, T. Liedl, S. Kudera, T. Pellegrino, A. M. Javier, H. E. Gaub, S. Stölzle, N. Fertig, & W. J. Parak, Cytotoxicity of colloidal CdSe and CdSe/ZnS nanoparticles. *Nano Letters*, 5 (2005) 331–338. https://doi.org/10.1021/nl047996m.

75. S. Behzadi, V. Serpooshan, W. Tao, M. A. Hamaly, M. Y. Alkawareek, E. C. Dreaden, D. Brown, A. M. Alkilany, O. C. Farokhzad, & M. Mahmoudi, Cellular uptake of nanoparticles: Journey inside the cell. *Chemical Society Reviews*, 46 (2017) 4218–4244. https://doi.org/10.1039/c6cs00636a.

76. V. Raicu & A. Popescu, Cell Membrane: Structure and Physical Properties. *Integrated Molecular and Cellular Biophysics*, (2008) 73–99. https://doi.org/10.1007/978-1-4020-8268-9_3.

77. F. Khalili-Araghi, J. Gumbart, P. C. Wen, M. Sotomayor, E. Tajkhorshid, & K. Schulten, Molecular dynamics simulations of membrane channels and transporters. *Current Opinion in Structural Biology*, 19 (2009) 128–137. https://doi.org/10.1016/j.sbi.2009.02.011.

78. B. Roux & K. Schulten, Computational studies of membrane channels. *Structure*, 12 (2004) 1343–1351. https://doi.org/10.1016/j.str.2004.06.013.

79. Y. Wang, J. Cohen, W. F. Boron, K. Schulten, & E. Tajkhorshid, Exploring gas permeability of cellular membranes and membrane channels with molecular dynamics. *Journal of Structural Biology*, 157 (2007) 534–544. https://doi.org/10.1016/j.jsb.2006.11.008.

80. M. A. Cooper, Advances in membrane receptor screening and analysis. *Journal of Molecular Recognition*, **17** (2004) 286–315. https://doi.org/10.1002/jmr.675.

81. I. N. Maruyama, Activation of transmembrane cell-surface receptors via a common mechanism? The "rotation model." *BioEssays*, **37** (2015) 959–967. https://doi.org/10.1002/bies.201500041.

82. D. Drew & O. Boudker, Shared Molecular Mechanisms of Membrane Transporters. *Annual Review of Biochemistry*, **85** (2016) 543–572. https://doi.org/10.1146/annurev-biochem-060815-014520.

83. D. L. Nelson & M. M. Cox, *Lehninger Principles of biochemistry.*, 7th ed (New York, NY: W.H. Freeman, 2017).

84. T. Braun, M. K. Ghatkesar, N. Backmann, W. Grange, P. Boulanger, L. Letellier, H. P. Lang, A. Bietsch, C. Gerber, & M. Hegner, Quantitative time-resolved measurement of membrane protein-ligand interactions using microcantilever array sensors. *Nature Nanotechnology*, **4** (2009) 179–185. https://doi.org/10.1038/nnano.2008.398.

85. A. D. Howard, G. McAllister, S. D. Feighner, Q. Liu, R. P. Nargund, L. H. T. Van der Ploeg, & A. A. Patchett, Orphan G-protein-coupled receptors and natural ligand discovery. *Trends in Pharmacological Sciences*, **22** (2001) 132–140. https://doi.org/10.1016/S0165-6147(00)01636-9.

86. K. M. Giacomini, S. M. Huang, D. J. Tweedie, L. Z. Benet, K. L. R. Brouwer, X. Chu, A. Dahlin, R. Evers, V. Fischer, K. M. Hillgren, K. A. Hoffmaster, T. Ishikawa, D. Keppler, R. B. Kim, C. A. Lee, M. Niemi, J. W. Polli, Y. Sugiyama, P. W. Swaan, J. A. Ware, S. H. Wright, S. Wah Yee, M. J. Zamek-Gliszczynski, & L. Zhang, Membrane transporters in drug development. *Nature Reviews Drug Discovery*, **9** (2010) 215–236. https://doi.org/10.1038/nrd3028.

87. L. Kou, Y. D. Bhutia, Q. Yao, Z. He, J. Sun, & V. Ganapathy, Transporter-guided delivery of nanoparticles to improve drug permeation across cellular barriers and drug exposure to selective cell types. *Frontiers in Pharmacology*, **9** (2018) 1–16. https://doi.org/10.3389/fphar.2018.00027.

88. M. Kaksonen & A. Roux, Mechanisms of clathrin-mediated endocytosis. *Nature*

Reviews Molecular Cell Biology, 19 (2018) 313–326. https://doi.org/10.1038/nrm.2017.132.

89. J. Gruenberg & F. G. van der Goot, Mechanisms of pathogen entry through the endosomal compartments. *Nature reviews molecullar cell biology*, 7 (2006) 495–504. https://doi.org/10.1038/nrm1959.

90. R. S. Flannagan, V. Jaumouill, & S. Grinstein, The Cell Biology of Phagocytosis. *Annual Review of Pathology: Mechanisms of Disease*, 7 (2012) 61–98. https://doi.org/10.1146/annurev-pathol-011811-132445.

91. I. Canton & G. Battaglia, Endocytosis at the nanoscale. *Chemical Society Reviews*, 41 (2012) 2718–2739.

92. Z. Lu, Y. Qiao, X. T. Zheng, M. B. Chan-Park, & C. M. Li, Effect of particle shape on phagocytosis of CdTe quantum dot-cystine composites. *MedChemComm*, 1 (2010) 84–86. https://doi.org/10.1039/c0md00008f.

93. D. Paul, S. Achouri, Y. Z. Yoon, J. Herre, C. E. Bryant, & P. Cicuta, Phagocytosis dynamics depends on target shape. *Biophysical Journal*, 105 (2013) 1143–1150. https://doi.org/10.1016/j.bpj.2013.07.036.

94. V. Haucke & M. M. Kozlov, Membrane remodeling in clathrin-mediated endocytosis. *Journal of Cell Science*, 131 (2018) 1–10. https://doi.org/10.1242/jcs.216812.

95. H. T. McMahon & E. Boucrot, Molecular mechanism and physiological functions of clathrin-mediated endocytosis. *Nature Reviews Molecular Cell Biology*, 12 (2011) 517–533. https://doi.org/10.1038/nrm3151.

96. M. Mettlen, P. Chen, S. Srinivasan, G. Danuser, & S. L. Schmid, Regulation of Clathrin-Mediated Endocytosis. *Annual Review of Biochemistry*, 87 (2018) 871–96.

97. H. Gao, W. Shi, L. B. Freund, A. Chakraborty, N. R. Jana, A. Anas, T. Okuda, N. Kawashima, K. Nakayama, T. Itoh, M. Ishikawa, & V. Biju, Clathrin-Mediated Endocytosis of Living Cells. *Journal of Physical Chemistry Letters*, 3 (2015) 2419–2429.

98. C. Schieber, A. Bestetti, J. P. Lim, A. D. Ryan, T. L. Nguyen, R. Eldridge, A. R. White, P. A. Gleeson, P. S. Donnelly, S. J. Williams, & P. Mulvaney, Conjugation of transferrin to

azide-modified cdse/zns core-shell quantum dots using cyclooctyne click chemistry. *Angewandte Chemie - International Edition*, **51** (2012) 10523–10527. https://doi.org/10.1002/anie.201202876.

99. L. Pelkmans & A. Helenius, Endocytosis via caveolae. *Traffic*, **3** (2002) 311–320. https://doi.org/10.1034/j.1600-0854.2002.30501.x.

100. L. A. Carver & J. E. Schnitzer, Caveolae: Mining little caves for new cancer targets. *Nature Reviews Cancer*, **3** (2003) 571–581. https://doi.org/10.1038/nrc1146.

101. G. Sahay, J. O. Kim, A. V. Kabanov, & T. K. Bronich, The exploitation of differential endocytic pathways in normal and tumor cells in the selective targeting of nanoparticulate chemotherapeutic agents. *Biomaterials*, **31** (2010) 923–933. https://doi.org/10.1016/j.biomaterials.2009.09.101.

102. E. M. Damm, L. Pelkmans, J. Kartenbeck, A. Mezzacasa, T. Kurzchalia, & A. Helenius, Clathrin- and caveolin-1-independent endocytosis: Entry of simian virus 40 into cells devoid of caveolae. *Journal of Cell Biology*, **168** (2005) 477–488. https://doi.org/10.1083/jcb.200407113.

103. J. P. Lim & P. A. Gleeson, Macropinocytosis : an endocytic pathway for internalising large gulps. *Immunology and cell biology*, **89** (2011) 836–843. https://doi.org/10.1038/icb.2011.20.

104. T. G. Iversen, N. Frerker, & K. Sandvig, Uptake of ricinB-quantum dot nanoparticles by a macropinocytosis-like mechanism. *Journal of Nanobiotechnology*, **10** (2012) 1–11.

105. E. J. New & D. Parker, The mechanism of cell uptake for luminescent lanthanide optical probes : the role of macropinocytosis and the effect of enhanced membrane permeability on compartmentalisation. *Organic and biomolecular chemistry*, **7** (2009) 851–855. https://doi.org/10.1039/b822145f.

106. X. Liu & D. Ghosh, Intracellular nanoparticle delivery by oncogenic KRAS-mediated macropinocytosis. *International Journal of Nanomedicine*, **14** (2019) 6589–6600.

107. J. Zhao & M. H. Stenzel, Entry of nanoparticles into cells: The importance of nanoparticle properties. *Polymer Chemistry*, **9** (2018) 259–272.

https://doi.org/10.1039/c7py01603d.

108. P. R. Leroueil, S. A. Berry, K. Duthie, G. Han, V. M. Rotello, D. Q. McNerny, J. R. Baker, B. G. Orr, & M. M. B. Holl, Wide varieties of cationic nanoparticles induce defects in supported lipid bilayers. *Nano Letters*, **8** (2008) 420–424. https://doi.org/10.1021/nl0722929.

109. I. U. Foreman-Ortiz, D. Liang, E. D. Laudadio, J. D. Calderin, M. Wu, P. Keshri, X. Zhang, M. P. Schwartz, R. J. Hamers, V. M. Rotello, C. J. Murphy, Q. Cui, & J. A. Pedersen, Anionic nanoparticle-induced perturbation to phospholipid membranes affects ion channel function. *Proceedings of the National Academy of Sciences of the United States of America*, **117** (2020) 27854–27861. https://doi.org/10.1073/pnas.2004736117.

110. S. Zhang, J. Li, G. Lykotrafitis, G. Bao, & S. Suresh, Size-dependent endocytosis of nanoparticles. *Advanced Materials*, **21** (2009) 419–424. https://doi.org/10.1002/adma.200801393.

111. H. Yuan & S. Zhang, Effects of particle size and ligand density on the kinetics of receptor-mediated endocytosis of nanoparticles. *Applied Physics Letters*, **96** (2010) 1–4. https://doi.org/10.1063/1.3293303.

112. S. Zhang, H. Gao, & G. Bao, Physical Principles of Nanoparticle Cellular Endocytosis. *ACS Nano*, **9** (2015) 8655–8671. https://doi.org/10.1021/acsnano.5b03184.

113. B. D. Chithrani & W. C. W. Chan, Elucidating the mechanism of cellular uptake and removal of protein-coated gold nanoparticles of different sizes and shapes. *Nano Letters*, **7** (2007) 1542–1550. https://doi.org/10.1021/nl070363y.

114. Y. Qiu, Y. Liu, L. Wang, L. Xu, R. Bai, Y. Ji, X. Wu, Y. Zhao, Y. Li, & C. Chen, Surface chemistry and aspect ratio mediated cellular uptake of Au nanorods. *Biomaterials*, **31** (2010) 7606–7619. https://doi.org/10.1016/j.biomaterials.2010.06.051.

115. K. Kostarelos, L. Lacerda, G. Pastorin, W. Wu, S. Wieckowski, J. Luangsivilay, S. Godefroy, D. Pantarotto, J. P. Briand, S. Muller, M. Prato, & A. Bianco, Cellular uptake of functionalized carbon nanotubes is independent of functional group and cell type. *Nature Nanotechnology*, **2** (2007) 108–113. https://doi.org/10.1038/nnano.2006.209.

116. A. E. Porter, M. Gass, K. Muller, J. N. Skepper, P. A. Midgley, & M. Welland, Direct imaging of single-walled carbon nanotubes in cells. *Nature Nanotechnology*, **2** (2007) 713–717. https://doi.org/10.1038/nnano.2007.347.

117. D. Pantarotto, R. Singh, D. McCarthy, M. Erhardt, J.-P. Briand, M. Prato, K. Kostarelos, & A. Bianco, Functionalized Carbon Nanotubes for Plasmid DNA Gene Delivery. *Angewandte Chemie*, **116** (2004) 5354–5358. https://doi.org/10.1002/ange.200460437.

118. S. E. A. Gratton, P. A. Ropp, P. D. Pohlhaus, J. C. Luft, V. J. Madden, M. E. Napier, & J. M. DeSimone, The effect of particle design on cellular internalization pathways. *Proceedings of the National Academy of Sciences of the United States of America*, **105** (2008) 11613–11618. https://doi.org/10.1073/pnas.0801763105.

119. X. Bai, S. Wang, X. Yan, H. Zhou, J. Zhan, S. Liu, V. K. Sharma, G. Jiang, H. Zhu, & B. Yan, Regulation of Cell Uptake and Cytotoxicity by Nanoparticle Core under the Controlled Shape, Size, and Surface Chemistries. *ACS Nano*, **14** (2020) 289–302. https://doi.org/10.1021/acsnano.9b04407.

120. Y. C. Yeh, K. Saha, B. Yan, O. R. Miranda, X. Yu, & V. M. Rotello, The role of ligand coordination on the cytotoxicity of cationic quantum dots in HeLa cells. *Nanoscale*, **5** (2013) 12140–12143. https://doi.org/10.1039/c3nr04037b.

121. R. Vácha, F. J. Martinez-Veracoechea, & D. Frenkel, Receptor-mediated endocytosis of nanoparticles of various shapes. *Nano Letters*, **11** (2011) 5391–5395. https://doi.org/10.1021/nl2030213.

122. Z. Shen, H. Ye, X. Yi, & Y. Li, Membrane Wrapping Efficiency of Elastic Nanoparticles during Endocytosis: Size and Shape Matter. *ACS Nano*, **13** (2019) 215–228. https://doi.org/10.1021/acsnano.8b05340.

123. H. Tang, H. Zhang, H. Ye, & Y. Zheng, Receptor-Mediated Endocytosis of Nanoparticles: Roles of Shapes, Orientations, and Rotations of Nanoparticles. *Journal of Physical Chemistry B*, **122** (2018) 171–180. https://doi.org/10.1021/acs.jpcb.7b09619.

124. C. Huang, Y. Zhang, H. Yuan, H. Gao, & S. Zhang, Role of nanoparticle geometry in endocytosis: Laying down to stand up. *Nano Letters*, **13** (2013) 4546–4550.

https://doi.org/10.1021/nl402628n.

125. N. D. Donahue, H. Acar, & S. Wilhelm, Concepts of nanoparticle cellular uptake, intracellular trafficking, and kinetics in nanomedicine. *Advanced Drug Delivery Reviews*, **143** (2019) 68–96. https://doi.org/10.1016/j.addr.2019.04.008.

126. P. Foroozandeh & A. Aziz, Insight into Cellular Uptake and Intracellular Trafficking of Nanoparticles. *Nanoscale Research Letters*, **13** (2018) 1–12. https://doi.org/10.1186/s11671-018-2728-6.

127. S. A. Smith, L. I. Selby, A. P. R. Johnston, & G. K. Such, The Endosomal Escape of Nanoparticles: Toward More Efficient Cellular Delivery. *Bioconjugate Chemistry*, **30** (2019) 263–272. https://doi.org/10.1021/acs.bioconjchem.8b00732.

128. M. P. Stewart, R. Langer, & K. F. Jensen, Intracellular delivery by membrane disruption: Mechanisms, strategies, and concepts. *Chemical Reviews*, **118** (2018) 7409–7531. https://doi.org/10.1021/acs.chemrev.7b00678.

129. M. P. Stewart, A. Sharei, X. Ding, G. Sahay, R. Langer, & K. F. Jensen, In vitro and ex vivo strategies for intracellular delivery. *Nature Publishing Group*, **538** (2016) 183–192. https://doi.org/10.1038/nature19764.

130. P. Tiefenboeck, J. A. Kim, & J. C. Leroux, Intracellular delivery of colloids: Past and future contributions from microinjection. *Advanced Drug Delivery Reviews*, **132** (2018) 3–15. https://doi.org/10.1016/j.addr.2018.06.013.

131. S. O. Souza, R. B. Lira, C. R. A. Cunha, B. S. Santos, A. Fontes, & G. Pereira, Methods for Intracellular Delivery of Quantum Dots. *Topics in Current Chemistry*, **379** (2021) 1–32. https://doi.org/10.1007/s41061-020-00313-7.

132. A. K. Shalek, J. T. Robinson, E. S. Karp, J. S. Lee, D. R. Ahn, M. H. Yoon, A. Sutton, M. Jorgolli, R. S. Gertner, T. S. Gujral, G. MacBeath, E. G. Yang, & H. Park, Vertical silicon nanowires as a universal platform for delivering biomolecules into living cells. *Proceedings of the National Academy of Sciences*, **107** (2010) 1870–1875. https://doi.org/10.1073/pnas.0909350107.

133. Y. Qu, Y. Zhang, Q. Yu, & H. Chen, Surface-Mediated Intracellular Delivery by Physical

Membrane Disruption. *ACS Applied Materials and Interfaces*, 12 (2020) 31054–31078. https://doi.org/10.1021/acsami.0c06978.

134. S. Park, Y. S. Kim, W. B. Kim, & S. Jon, Carbon nanosyringe array as a platform for intracellular delivery. *Nano Letters*, 9 (2009) 1325–1329. https://doi.org/10.1021/nl802962t.

135. A. Tay & N. Melosh, Nanostructured Materials for Intracellular Cargo Delivery. *Accounts of Chemical Research*, 52 (2019) 2462-2471. https://doi.org/10.1021/acs.accounts.9b00272.

136. S. Gopal, C. Chiappini, J. Penders, V. Leonardo, H. Seong, S. Rothery, Y. Korchev, A. Shevchuk, & M. M. Stevens, Porous Silicon Nanoneedles Modulate Endocytosis to Deliver Biological Payloads. *Advanced Materials*, 31 (2019) 1806788. https://doi.org/10.1002/adma.201806788.

137. S. Y. Ho & G. S. Mittal, Electroporation of cell membranes: A review. *Critical Reviews in Biotechnology*, 16 (1996) 349–362. https://doi.org/10.3109/07388559609147426.

138. T. Y. Tsong, Electroporation of cell membranes. *Biophysical Journal*, 60 (1991) 297–306. https://doi.org/10.1016/S0006-3495(91)82054-9.

139. J. Shi, Y. Ma, J. Zhu, Y. Chen, Y. Sun, Y. Yao, Z. Yang, & J. Xie, A review on electroporation-based intracellular delivery. *Molecules*, 23 (2018). https://doi.org/10.3390/molecules23113044.

140. J. Gehl, Electroporation: Theory and methods, perspectives for drug delivery, gene therapy and research. *Acta Physiologica Scandinavica*, 177 (2003) 437–447. https://doi.org/10.1046/j.1365-201X.2003.01093.x.

141. J. B. Delehanty, H. Mattoussi, & I. L. Medintz, Delivering quantum dots into cells: Strategies, progress and remaining issues. *Analytical and Bioanalytical Chemistry*, 393 (2009) 1091–1105. https://doi.org/10.1007/s00216-008-2410-4.

142. A. M. Derfus, W. C. W. Chan, & S. N. Bhatia, Intracellular delivery of quantum dots for live cell labeling and organelle tracking. *Advanced Materials*, 16 (2004) 961–966. https://doi.org/10.1002/adma.200306111.

143. T. Kotnik, L. Rems, M. Tarek, & D. Miklavcic, Membrane Electroporation and Electropermeabilization: Mechanisms and Models. *Annual Review of Biophysics*, **48** (2019) 63–91. https://doi.org/10.1146/annurev-biophys-052118-115451.

144. S. Wang & L. J. Lee, Micro-/nanofluidics based cell electroporation. *Biomicrofluidics*, **7** (2013) 011301. https://doi.org/10.1063/1.4774071.

145. P. E. Boukany, A. Morss, W. C. Liao, B. Henslee, H. Jung, X. Zhang, B. Yu, X. Wang, Y. Wu, L. Li, K. Gao, X. Hu, X. Zhao, O. Hemminger, W. Lu, G. P. Lafyatis, & L. J. Lee, Nanochannel electroporation delivers precise amounts of biomolecules into living cells. *Nature Nanotechnology*, **6** (2011) 747–754. https://doi.org/10.1038/nnano.2011.164.

146. J. C. Bischof, J. Padanilam, W. H. Holmes, R. M. Ezzell, R. C. Lee, R. G. Tompkins, M. L. Yarmush, & M. Toner, Dynamics of cell membrane permeability changes at supraphysiological temperatures. *Biophysical Journal*, **68** (1995) 2608–2614. https://doi.org/10.1016/S0006-3495(95)80445-5.

147. L. Gu, A. R. Koymen, & S. K. Mohanty, Crystalline magnetic carbon nanoparticle assisted photothermal delivery into cells using CW near-infrared laser beam. *Scientific Reports*, **4** (2014) 1–10. https://doi.org/10.1038/srep05106.

148. Z. Lyu, F. Zhou, Q. Liu, H. Xue, Q. Yu, & H. Chen, A Universal Platform for Macromolecular Deliveryinto Cells Using Gold Nanoparticle Layers via the Photoporation Effect. *Advanced Functional Materials*, **26** (2016) 5787–5795. https://doi.org/10.1002/adfm.201602036.

149. H. Schneckenburger, Laser-assisted optoporation of cells and tissues – a mini-review. *Biomedical Optics Express*, **10** (2019) 2883. https://doi.org/10.1364/boe.10.002883.

150. D. J. Stevenson, F. J. Gunn-Moore, P. Campbell, & K. Dholakia, Single cell optical transfection. *Journal of the Royal Society Interface*, **7** (2010) 863–871. https://doi.org/10.1098/rsif.2009.0463.

151. J. Umanzor-Alvarez, E. C. Wade, A. Gifford, K. Nontapot, A. Cruz-Reese, T. Gotoh, J. C. Sible, & G. A. Khodaparast, Near-infrared laser delivery of nanoparticles to developing embryos: A study of efficacy and viability. *Biotechnology Journal*, **6** (2011) 519–524.

https://doi.org/10.1002/biot.201000205.

152. S. Snipstad, S. Hanstad, A. Bjørkøy, & Ý. Mørch, Sonoporation Using Nanoparticle-Loaded Microbubbles Increases Cellular Uptake of Nanoparticles Compared to Co-Incubation of Nanoparticles and Microbubbles. *Pharmaceutics*, **13** (2021) 1–15.

153. S. M. Chowdhury, L. Abou-elkacem, T. Lee, J. Dahl, & A. M. Lutz, Ultrasound and microbubble mediated therapeutic delivery : Underlying mechanisms and future outlook. *Journal of Controlled Release*, **326** (2020) 75–90. https://doi.org/10.1016/j.jconrel.2020.06.008.

154. L. B. Mullin, L. C. Phillips, & P. A. Dayton, Nanoparticle Delivery Enhancement With Acoustically Activated Microbubbles. *IEEE Transactions on Ultrasonics, Ferroelectrics, and Frequency Control*, **60** (2013) 65–77.

155. Y. Liu, J. Yan, & M. R. Prausnitz, Can Ultrasound Enable Efficient Intracellular Uptake of Molecules? A Retrospective Literature Review and Analysis. *Ultrasound in Medicine and Biology*, **38** (2012) 876–888. https://doi.org/10.1016/j.ultrasmedbio.2012.01.006.

156. S. O'Dea, V. Annibaldi, L. Gallagher, J. Mulholland, E. L. Molloy, C. J. Breen, J. L. Gilbert, D. S. Martin, M. Maguire, & F. R. Curry, Vector-free intracellular delivery by reversible permeabilization. *PLoS ONE*, **12** (2017) 1–23. https://doi.org/10.1371/journal.pone.0174779.

157. S. Esteban-Martín, H. Jelger Risselada, J. Salgado, & S. J. Marrink, Stability of asymmetric lipid bilayers assessed by molecular dynamics simulations. *Journal of the American Chemical Society*, **131** (2009) 15194–15202. https://doi.org/10.1021/ja904450t.

158. H. Moghadas, M. S. Saidi, N. Kashaninejad, & N. T. Nguyen, Challenge in particle delivery to cells in a microfluidic device. *Drug Delivery and Translational Research*, **8** (2018) 830–842. https://doi.org/10.1007/s13346-017-0467-3.

159. E. K. Sackmann, A. L. Fulton, & D. J. Beebe, The present and future role of microfluidics in biomedical research. *Nature*, **507** (2014) 181–189. https://doi.org/10.1038/nature13118.

160. C. M. B. Ho, S. H. Ng, K. H. H. Li, & Y. J. Yoon, 3D printed microfluidics for biological applications. *Lab on a Chip*, 15 (2015) 3627–3637. https://doi.org/10.1039/c5lc00685f.

161. H. Becker & L. E. Locascio, Polymer microfluidic devices. *Talanta*, 56 (2002) 267–287. https://doi.org/10.1016/S0039-9140(01)00594-X.

162. K. Raj M & S. Chakraborty, PDMS microfluidics: A mini review. *Journal of Applied Polymer Science*, 137 (2020) 1–14. https://doi.org/10.1002/app.48958.

163. J. Lee, A. Sharei, W. Y. Sim, A. Adamo, R. Langer, K. F. Jensen, & M. G. Bawendi, Nonendocytic delivery of functional engineered nanoparticles into the cytoplasm of live cells using a novel, high-throughput microfluidic device. *Nano Letters*, 12 (2012) 6322–6327. https://doi.org/10.1021/nl303421h.

164. A. Sharei, J. Zoldan, A. Adamo, W. Y. Sim, N. Cho, E. Jackson, S. Mao, S. Schneider, M. J. Han, A. Lytton-Jean, P. A. Basto, S. Jhunjhunwala, J. Lee, D. A. Heller, J. W. Kang, G. C. Hartoularos, K. S. Kim, D. G. Anderson, R. Langer, & K. F. Jensen, A vector-free microfluidic platform for intracellular delivery. *Proceedings of the National Academy of Sciences of the United States of America*, 110 (2013) 2082–2087. https://doi.org/10.1073/pnas.1218705110.

165. A. Sharei, R. Poceviciute, E. L. Jackson, N. Cho, S. Mao, G. C. Hartoularos, D. Y. Jang, S. Jhunjhunwala, A. Eyerman, T. Schoettle, R. Langer, & K. F. Jensen, Plasma membrane recovery kinetics of a microfluidic intracellular delivery platform. *Integrative Biology (United Kingdom)*, 6 (2014) 470–475. https://doi.org/10.1039/c3ib40215k.

166. B. Joo, J. Hur, G.-B. Kim, S. G. Yun, & A. J. Chung, Highly Efficient Transfection of Human Primary T Lymphocytes Using Droplet-Enabled Mechanoporation. *ACS Nano*, (2021) 12888–12898. https://doi.org/10.1021/acsnano.0c10473.

167. J. Hur & A. J. Chung, Microfluidic and Nanofluidic Intracellular Delivery. *Advanced Science*, 2004595 (2021) 2004595. https://doi.org/10.1002/advs.202004595.

168. J. Y.-T. K. Ming-Ju Chen, Kreuter, Nanoparticles and microparticles for drug and vaccine delivery. *Journal of anatomy*, 189 (Pt 3 (1996) 503–505. https://doi.org/10.1002/bit.

169. Y. Deng, M. Kizer, M. Rada, J. Sage, X. Wang, D. J. Cheon, & A. J. Chung, Intracellular

Delivery of Nanomaterials via an Inertial Microfluidic Cell Hydroporator. *Nano Letters*, **18** (2018) 2705–2710. https://doi.org/10.1021/acs.nanolett.8b00704.

170. M. E. Kizer, Y. Deng, G. Kang, P. E. Mikael, X. Wang, & A. J. Chung, Hydroporator: A hydrodynamic cell membrane perforator for high-throughput vector-free nanomaterial intracellular delivery and DNA origami biostability evaluation. *Lab on a Chip*, **19** (2019) 1747–1754. https://doi.org/10.1039/c9lc00041k.

171. G. Kang, D. W. Carlson, T. H. Kang, S. Lee, S. J. Haward, I. Choi, A. Q. Shen, & A. J. Chung, Intracellular Nanomaterial Delivery via Spiral Hydroporation. *ACS Nano*, (2020). https://doi.org/10.1021/acsnano.9b07930.

172. J. Hur, I. Park, K. M. Lim, J. Doh, S. G. Cho, & A. J. Chung, Microfluidic cell stretching for highly effective gene delivery into hard-to-transfect primary cells. *ACS Nano*, **14** (2020) 15094–15106. https://doi.org/10.1021/acsnano.0c05169.

173. A. J. Chung, A Minireview on Inertial Microfluidics Fundamentals: Inertial Particle Focusing and Secondary Flow. *Biochip Journal*, **13** (2019) 53–63. https://doi.org/10.1007/s13206-019-3110-1.

174. D. Di Carlo, Inertial microfluidics. *Lab on a Chip*, **9** (2009) 3038–3046. https://doi.org/10.1039/b912547g.

175. H. A. Stone, A. D. Stroock, & A. Ajdari, Engineering flows in small devices: Microfluidics toward a lab-on-a-chip. *Annual Review of Fluid Mechanics*, **36** (2004) 381–411. https://doi.org/10.1146/annurev.fluid.36.050802.122124.

176. H. M. Xia, J. W. Wu, J. J. Zheng, J. Zhang, & Z. P. Wang, Nonlinear microfluidics: Device physics, functions, and applications. *Lab on a Chip*, **21** (2021) 1241–1268. https://doi.org/10.1039/d0lc01120g.

177. J. P. Abraham, E. M. Sparrow, & W. J. Minkowycz, Internal-flow Nusselt numbers for the low-Reynolds-number end of the laminar-to-turbulent transition regime. *International Journal of Heat and Mass Transfer*, **54** (2011) 584–588. https://doi.org/10.1016/j.ijheatmasstransfer.2010.09.012.

178. D. Di Carlo, D. Irimia, R. G. Tompkins, & M. Toner, Continuous inertial focusing,

ordering, and separation of particles in microchannels. *Proceedings of the National Academy of Sciences of the United States of America*, **104** (2007) 18892–18897. https://doi.org/10.1073/pnas.0704958104.

179. D. R. Gossett, H. T. K. Tse, S. A. Lee, Y. Ying, A. G. Lindgren, O. O. Yang, J. Rao, A. T. Clark, & D. Di Carlo, Hydrodynamic stretching of single cells for large population mechanical phenotyping. *Proceedings of the National Academy of Sciences of the United States of America*, **109** (2012) 7630–7635. https://doi.org/10.1073/pnas.1200107109.

180. P. P. Brown & D. F. Lawler, Sphere Drag and Settling Velocity Revisited. *Journal of Environmental Engineering*, **129** (2003) 222–231. https://doi.org/10.1061/(asce)0733-9372(2003)129:3(222).

181. F. J. Armistead, J. Gala De Pablo, H. Gadêlha, S. A. Peyman, & S. D. Evans, Cells Under Stress: An Inertial-Shear Microfluidic Determination of Cell Behavior. *Biophysical Journal*, **116** (2019) 1127–1135. https://doi.org/10.1016/j.bpj.2019.01.034.

182. Y. Zheng, J. Nguyen, Y. Wei, & Y. Sun, Recent advances in microfluidic techniques for single-cell biophysical characterization. *Lab on a Chip*, **13** (2013) 2464–2483. https://doi.org/10.1039/c3lc50355k.

183. F. Armistead, J. GalaDePablo, S. Peyman, S. Evans, & H. Gadêlha, Physical Biomarkers of Disease Progression: On-Chip Monitoring of Changes in Mechanobiology of Colorectal Cancer Cells. *Scientific Reports*, **10** (2020). https://doi.org/10.1038/s41598-020-59952-x.

184. H. T. K. Tse, D. R. Gossett, Y. S. Moon, M. Masaeli, M. Sohsman, Y. Ying, K. Mislick, R. P. Adams, J. Rao, & D. Di Carlo, Quantitative diagnosis of malignant pleural effusions by single-cell mechanophenotyping. *Science Translational Medicine*, **5** (2013). https://doi.org/10.1126/scitranslmed.3006559.

185. S. Suresh, Biomechanics and biophysics of cancer cells. *Acta Materialia*, **55** (2007) 3989–4014. https://doi.org/10.1016/j.actamat.2007.04.022.

186. K. Molnar & M. Labouesse, The plastic cell: Mechanical deformation of cells and tissues. *Open Biology*, **11** (2021). https://doi.org/10.1098/rsob.210006.

187. K. Doubrovinski, M. Swan, O. Polyakov, & E. F. Wieschaus, Measurement of cortical elasticity in Drosophila melanogaster embryos using ferrofluids. *Proceedings of the National Academy of Sciences of the United States of America*, **114** (2017) 1051–1056. https://doi.org/10.1073/pnas.1616659114.

188. T. Mizutani, H. Haga, & K. Kawabata, Cellular stiffness response to external deformation: Tensional homeostasis in a single fibroblast. *Cell Motility and the Cytoskeleton*, **59** (2004) 242–248. https://doi.org/10.1002/cm.20037.

189. I. Gozen & P. Dommersnes, Pore dynamics in lipid membranes. *European Physical Journal: Special Topics*, **223** (2014) 1813–1829. https://doi.org/10.1140/epjst/e2014-02228-5.

190. Y. Zhen, M. Radulovic, M. Vietri, & H. Stenmark, Sealing holes in cellular membranes. *The EMBO Journal*, **40** (2021) 1–13. https://doi.org/10.15252/embj.2020106922.

191. A. M. Moe, A. E. Golding, & W. M. Bement, Cell healing: Calcium, repair and regeneration. *Seminars in Cell and Developmental Biology*, **45** (2015) 18–23. https://doi.org/10.1016/j.semcdb.2015.09.026.

192. A. J. Jimenez & F. Perez, Plasma membrane repair: the adaptable cell life-insurance. *Current Opinion in Cell Biology*, **47** (2017) 99–107. https://doi.org/10.1016/j.ceb.2017.03.011.

193. A. Horn & J. K. Jaiswal, Cellular mechanisms and signals that coordinate plasma membrane repair. *Cellular and Molecular Life Sciences*, **75** (2018) 3751–3770. https://doi.org/10.1007/s00018-018-2888-7.

194. A. Sharei, R. Poceviciute, E. L. Jackson, N. Cho, S. Mao, G. C. Hartoularos, D. Y. Jang, S. Jhunjhunwala, A. Eyerman, T. Schoettle, R. Langer, & K. F. Jensen, Plasma membrane recovery kinetics of a microfluidic intracellular delivery platform. *Integrative Biology (United Kingdom)*, **6** (2014) 470–475. https://doi.org/10.1039/c3ib40215k.

195. A. G. Pakhomov, S. Xiao, O. N. Pakhomova, I. Semenov, M. A. Kuipers, & B. L. Ibey, Disassembly of actin structures by nanosecond pulsed electric field is a downstream effect of cell swelling. *Bioelectrochemistry*, **100** (2014) 88–95. https://doi.org/10.1016/j.bioelechem.2014.01.004.

196. M. Antkowiak, M. L. Torres-Mapa, K. Dholakia, & F. J. Gunn-Moore, Quantitative phase study of the dynamic cellular response in femtosecond laser photoporation. *Biomedical Optics Express*, **1** (2010) 414. https://doi.org/10.1364/boe.1.000414.

197. Z. G. Li, A. Q. Liu, E. Klaseboer, J. B. Zhang, & C. D. Ohl, Single cell membrane poration by bubble-induced microjets in a microfluidic chip. *Lab on a Chip*, **13** (2013) 1144–1150. https://doi.org/10.1039/c3lc41252k.

198. K. K. Y. Ho, Y. L. Wang, J. Wu, & A. P. Liu, Advanced microfluidic device designed for cyclic compression of single adherent cells. *Frontiers in Bioengineering and Biotechnology*, **6** (2018) 1–13. https://doi.org/10.3389/fbioe.2018.00148.

199. M. Jang, S. S. Kim, & J. Lee, Cancer cell metabolism: Implications for therapeutic targets. *Experimental and Molecular Medicine*, **45** (2013) 1–8. https://doi.org/10.1038/emm.2013.85.

200. Green Douglas R. & Reed John C., Mitochondria and Apoptosis. *Science*, **281** (1988) 1309–1312.

201. C. Wang & R. J. Youle, The role of mitochondria in apoptosis. *Annual Review of Genetics*, **43** (2009) 95–118. https://doi.org/10.1146/annurev-genet-102108-134850.

202. F. Q. Schafer & G. R. Buettner, Redox environment of the cell as viewed through the redox state of the glutathione disulfide/glutathione couple. *Free Radical Biology and Medicine*, **30** (2001) 1191–1212. https://doi.org/10.1016/S0891-5849(01)00480-4.

203. A. Ayer, C. W. Gourlay, & I. W. Dawes, Cellular redox homeostasis, reactive oxygen species and replicative ageing in Saccharomyces cerevisiae. *FEMS Yeast Research*, **14** (2014) 60–72. https://doi.org/10.1111/1567-1364.12114.

204. B. Morgan, D. Ezeriņa, T. N. E. Amoako, J. Riemer, M. Seedorf, & T. P. Dick, Multiple glutathione disulfide removal pathways mediate cytosolic redox homeostasis. *Nature Chemical Biology*, **9** (2013) 119–125. https://doi.org/10.1038/nchembio.1142.

205. M. P. Gamcsik, M. S. Kasibhatla, S. D. Teeter, & O. M. Colvin, Glutathione levels in human tumors. *Biomarkers*, **17** (2012) 671–691. https://doi.org/10.3109/1354750X.2012.715672.

206. J. H. Ostrander, C. M. McMahon, S. Lem, S. R. Millon, J. Q. Brown, V. L. Seewaldt, & N. Ramanujam, Optical redox ratio differentiates breast cancer cell lines based on estrogen receptor status. *Cancer Research*, 70 (2010) 4759–4766. https://doi.org/10.1158/0008-5472.CAN-09-2572.

207. R. L. Patterson, D. B. Van Rossum, A. I. Kaplin, R. K. Barrow, & S. H. Snyder, Inositol 1,4,5-trisphosphate receptor/GAPDH complex augments Ca 2+ release via locally derived NADH. *Proceedings of the National Academy of Sciences of the United States of America*, 102 (2005) 1357–1359. https://doi.org/10.1073/pnas.0409657102.

208. P. C. Bradshaw, Cytoplasmic and mitochondrial NADPH-coupled Redox systems in the regulation of aging. *Nutrients*, 11 (2019). https://doi.org/10.3390/nu11030504.

209. X. Dai, H. Cheng, Z. Bai, & J. Li, Breast cancer cell line classification and Its relevance with breast tumor subtyping. *Journal of Cancer*, 8 (2017) 3131–3141. https://doi.org/10.7150/jca.18457.

210. M. Lacroix, G. Leclercq, & M.- Vi, Relevance of breast cancer cell lines as models for breast tumours : an update. *Breast Cancer Research and Treatment*, 83 (2004) 249–289.

211. R. M. Neve, K. Chin, J. Fridlyand, J. Yeh, F. L. Baehner, T. Fevr, L. Clark, N. Bayani, J. P. Coppe, F. Tong, T. Speed, P. T. Spellman, S. DeVries, A. Lapuk, N. J. Wang, W. L. Kuo, J. L. Stilwell, D. Pinkel, D. G. Albertson, F. M. Waldman, F. McCormick, R. B. Dickson, M. D. Johnson, M. Lippman, S. Ethier, A. Gazdar, & J. W. Gray, A collection of breast cancer cell lines for the study of functionally distinct cancer subtypes. *Cancer Cell*, 10 (2006) 515–527. https://doi.org/10.1016/j.ccr.2006.10.008.

212. A. Michaelides & C. Constantinou, Breast Cancer and Lymphedema: A Narrative Review. *International Journal of Medical Students*, 7 (2019) 66–72. https://doi.org/10.5195/ijms.2019.362.

213. Q. Yu & A. A. Heikal, Two-photon autofluorescence dynamics imaging reveals sensitivity of intracellular NADH concentration and conformation to cell physiology at the single-cell level. *Journal of Photochemistry and Photobiology B: Biology*, 95 (2009) 46–57. https://doi.org/10.1016/j.jphotobiol.2008.12.010.

214. O. I. Kolenc & K. P. Quinn, Evaluating cell metabolism through autofluorescence imaging of NAD(P)H and FAD. *Antioxidants and Redox Signaling*, **30** (2019) 875–889. https://doi.org/10.1089/ars.2017.7451.

215. Y. Wen, H. N. Xu, L. Privette Vinnedge, M. Feng, & L. Z. Li, Optical Redox Imaging Detects the Effects of DEK Oncogene Knockdown on the Redox State of MDA-MB-231 Breast Cancer Cells. *Molecular Imaging and Biology*, **21** (2019) 410–416. https://doi.org/10.1007/s11307-019-01321-w.

216. S. Jung & X. Chen, Quantum Dot–Dye Conjugates for Biosensing, Imaging, and Therapy. *Advanced Healthcare Materials*, **7** (2018) 1–14. https://doi.org/10.1002/adhm.201800252.

217. S. J. Clarke, C. A. Hollmann, Z. Zhang, D. Suffern, S. E. Bradforth, N. M. Dimitrijevic, W. G. Minarik, & J. L. Nadeau, Photophysics of dopamine-modified quantum dots and effects on biological systems. *Nature Materials*, **5** (2006) 409–417. https://doi.org/10.1038/nmat1631.

218. X. Ji, G. Palui, T. Avellini, H. Bin Na, C. Yi, K. L. Knappenberger, & H. Mattoussi, On the pH-dependent quenching of quantum dot photoluminescence by redox active dopamine. *Journal of the American Chemical Society*, **134** (2012) 6006–6017. https://doi.org/10.1021/ja300724x.

219. W. Ma, L. X. Qin, F. T. Liu, Z. Gu, J. Wang, Z. G. Pan, T. D. James, & Y. T. Long, Ubiquinone-quantum dot bioconjugates for in vitro and intracellular complex i sensing. *Scientific Reports*, **3** (2013) 1–9. https://doi.org/10.1038/srep01537.

220. X. Chen, A. Nazzal, D. Goorskey, M. Xiao, Z. A. Peng, & X. Peng, Polarization spectroscopy of single CdSe quantum rods. *Physical Review B - Condensed Matter and Materials Physics*, **64** (2001) 2453041–2453044. https://doi.org/10.1103/PhysRevB.64.245304.

221. X. Peng, L. Manna, W. Yang, J. Wickham, E. Scher, A. Kadavanich, & A. P. Alivisatos, Shape Control of CdSe Nanocrystals. *Letters to nature*, **404** (2000) 59–61. https://www.nature.com/articles/35003535

222. G. Jia, S. Xu, & A. Wang, Emerging strategies for the synthesis of monodisperse

colloidal semiconductor quantum rods. *Journal of Materials Chemistry C*, **3** (2015) 8284–8293. https://doi.org/10.1039/c5tc01234a.

223. K. Wu & T. Lian, Quantum confined colloidal nanorod heterostructures for solar-to-fuel conversion. *Chemical Society Reviews*, **45** (2016) 3781–3810. https://doi.org/10.1039/c5cs00472a.

224. H. Htoon, J. A. Hollingworth, A. V. Malko, R. Dickerson, & V. I. Klimov, Light amplification in semiconductor nanocrystals: Quantum rods versus quantum dots. *Applied Physics Letters*, **82** (2003) 4776–4778. https://doi.org/10.1063/1.1586460.

225. R. A. M. Hikmet, P. T. K. Chin, D. V. Talapin, & H. Weller, Polarized-light-emitting quantum-rod diodes. *Advanced Materials*, **17** (2005) 1436–1439. https://doi.org/10.1002/adma.200401763.

226. K. T. Yong, I. Roy, H. E. Pudavar, E. J. Bergey, K. M. Tramposch, M. T. Swihart, & P. N. Prasad, Multiplex imaging of pancreatic cancer cells by using functionalized quantum rods. *Advanced Materials*, **20** (2008) 1412–1417. https://doi.org/10.1002/adma.200702462.

227. L. Manna, E. C. Scher, & A. P. Alivisatos, Synthesis of Soluble and Processable Rod- , Arrow- , Teardrop- , and Tetrapod-Shaped CdSe Nanocrystals. *Journal of American Chemical Society*, **122** (2000) 12700–12706.

228. F. Shieh, A. E. Saunders, & B. A. Korgel, General Shape Control of Colloidal CdS , CdSe , CdTe Quantum Rods and Quantum Rod Heterostructures. *The Journal of Physical Chemistry B*, **109** (2005) 8538–8542.

229. A. Persano, G. Leo, L. Manna, & A. Cola, Charge carrier transport in thin films of colloidal CdSe quantum rods. *Journal of Applied Physics*, **104** (2008) 1–6. https://doi.org/10.1063/1.2988136.

230. L. Carbone, C. Nobile, M. De Giorgi, F. Della Sala, G. Morello, P. Pompa, M. Hytch, E. Snoeck, A. Fiore, I. R. Franchini, M. Nadasan, A. F. Silvestre, L. Chiodo, S. Kudera, R. Cingolani, R. Krahne, & L. Manna, Synthesis and Micrometer-Scale Assembly of Colloidal CdSe / CdS Nanorods Prepared by a Seeded Growth Approach. *Nano Lett*, **7** (2007) 2942–2950.

231. A. Sitt, A. Salant, G. Menagen, & U. Banin, Highly Emissive Nano Rod-in-Rod Heterostructures with Strong Linear Polarization. *Nano Letters*, **11** (2011) 2054–2060.

232. L. Manna, E. C. Scher, L. Li, & A. P. Alivisatos, Epitaxial Growth and Photochemical Annealing of Graded CdS / ZnS Shells on Colloidal CdSe Nanorods. *Journal of American Chemical Society*, **124** (2002) 7136–7145.

233. A. Cretí, M. Zavelani-rossi, G. Lanzani, M. Anni, L. Manna, & M. Lomascolo, Role of the shell thickness in stimulated emission and photoinduced absorption in CdSe core / shell nanorods. *Physical Review B*, **73** (2006) 1–4. https://doi.org/10.1103/PhysRevB.73.165410.

234. B. Ji, N. Waiskopf, S. Remennik, I. Popov, & U. Banin, Strain-controlled shell morphology on quantum rods. *Nature Communications*, **10** (2019) 1–9. https://doi.org/10.1038/s41467-018-07837-z.

235. T. Mokari & U. Banin, Synthesis and Properties of CdSe / ZnS Core / Shell Nanorods. *Chemistry of Materials*, **15** (2003) 3955–3960.

236. D. Chen, A. Wang, M. A. Buntine, & G. Jia, Recent Advances in Zinc-Containing Colloidal Semiconductor Nanocrystals for Optoelectronic and Energy Conversion Applications. *ChemElectroChem*, **6** (2019) 4709–4724. https://doi.org/10.1002/celc.201900838.

237. Y. Chen, W. Xing, Y. Liu, X. Zhang, Y. Xie, C. Shen, J. G. Liu, C. Geng, & S. Xu, Efficient and Stable CdSe/CdS/ZnS Quantum Rods-in-Matrix Assembly for White LED Application. *Nanomaterials*, **10** (2020) 1–13.

238. R. C. Page, D. Espinobarro-Velazquez, M. A. Leontiadou, C. Smith, E. A. Lewis, S. J. Haigh, C. Li, H. Radtke, A. Pengpad, F. Bondino, E. Magnano, I. Pis, W. R. Flavell, P. O'Brien, & D. J. Binks, Near-Unity Quantum Yields from Chloride Treated CdTe Colloidal Quantum Dots. *Small*, **11** (2015) 1548–1554. https://doi.org/10.1002/smll.201402264.

239. D. Espinobarro-Velazquez, M. A. Leontiadou, R. C. Page, M. Califano, P. O'Brien, & D. J. Binks, Effect of chloride passivation on recombination dynamics in cdte colloidal quantum dots. *ChemPhysChem*, **16** (2015) 1239–1244. https://doi.org/10.1002/cphc.201402753.

240. R. Kumar, H. Ding, R. Hu, K. T. Yong, I. Roy, E. J. Bergey, & P. N. Prasad, In vitro and in vivo optical imaging using water-dispersible, noncytotoxic, luminescent, silica-coated quantum rods. *Chemistry of Materials*, **22** (2010) 2261–2267. https://doi.org/10.1021/cm902610f.

241. D. Gao, P. Zhang, Z. Sheng, D. Hu, P. Gong, C. Chen, Q. Wan, G. Gao, & L. Cai, Highly bright and compact alloyed quantum rods with near infrared emitting: A potential multifunctional nanoplatform for multimodal imaging in vivo. *Advanced Functional Materials*, **24** (2014) 3897–3905. https://doi.org/10.1002/adfm.201304225.

242. W. Wang, Y. Kong, J. Jiang, X. Tian, S. Li, U. S. Akshath, C. Tiede, N. Hondow, A. Yu, Y. Guo, & D. Zhou, Photon induced quantum yield regeneration of cap-exchanged CdSe/CdS quantum rods for ratiometric biosensing and cellular imaging. *Nanoscale*, **12** (2020) 8647–8655. https://doi.org/10.1039/c9nr08060k.

243. A. J. Harvie, C. T. Smith, R. Ahumada-Lazo, L. J. C. Jeuken, M. Califano, R. S. Bon, S. J. O. Hardman, D. J. Binks, & K. Critchley, Ultrafast Trap State-Mediated Electron Transfer for Quantum Dot Redox Sensing. *Journal of Physical Chemistry C*, **122** (2018) 10173–10180. https://doi.org/10.1021/acs.jpcc.8b02551.

244. S. Satheesha, V. J. Cookson, L. J. Coleman, N. Ingram, B. Madhok, A. M. Hanby, C. A. B. Suleman, V. S. Sabine, E. J. Macaskill, J. M. S. Bartlett, J. M. Dixon, J. N. McElwaine, & T. A. Hughes, Response to mTOR inhibition: Activity of eIF4E predicts sensitivity in cell lines and acquired changes in eIF4E regulation in breast cancer. *Molecular Cancer*, **10** (2011) 19. https://doi.org/10.1186/1476-4598-10-19.

245. E. Oh, R. Liu, A. Nel, K. B. Gemill, M. Bilal, Y. Cohen, & I. L. Medintz, Meta-analysis of cellular toxicity for cadmium-containing quantum dots. *Nature Nanotechnology*, **11** (2016) 479–486. https://doi.org/10.1038/nnano.2015.338.

246. S. C. Wilschefski & M. R. Baxter, Inductively Coupled Plasma Mass Spectrometry: Introduction to Analytical Aspects. *Clinical Biochemist Reviews*, **40** (2019) 115–133. https://doi.org/10.33176/AACB-19-00024.

247. R. Freeman & I. Willner, Optical molecular sensing with semiconductor quantum dots (QDs). *Chemical Society Reviews*, **41** (2012) 4067–4085.

https://doi.org/10.1039/c2cs15357b.

248. N. Elgrishi, K. J. Rountree, B. D. McCarthy, E. S. Rountree, T. T. Eisenhart, & J. L. Dempsey, A Practical Beginner's Guide to Cyclic Voltammetry. *Journal of Chemical Education*, **95** (2018) 197–206. https://doi.org/10.1021/acs.jchemed.7b00361.

249. A. Liu, M. Islam, N. Stone, V. Varadarajan, J. Jeong, S. Bowie, P. Qiu, E. K. Waller, A. Alexeev, & T. Sulchek, Microfluidic generation of transient cell volume exchange for convectively driven intracellular delivery of large macromolecules. *Materials Today*, **21** (2018) 703–712. https://doi.org/10.1016/j.mattod.2018.03.002.

250. A. Liu, T. Yu, K. Young, N. Stone, S. Hanasoge, T. J. Kirby, V. Varadarajan, N. Colonna, J. Liu, A. Raj, J. Lammerding, A. Alexeev, & T. Sulchek, Cell Mechanical and Physiological Behavior in the Regime of Rapid Mechanical Compressions that Lead to Cell Volume Change. *Small*, **16** (2020). https://doi.org/10.1002/smll.201903857.

251. H. Mikami, J. Harmon, H. Kobayashi, S. Hamad, Y. Wang, O. Iwata, K. Suzuki, T. Ito, Y. Aisaka, N. Kutsuna, K. Nagasawa, H. Watarai, Y. Ozeki, & K. Goda, Ultrafast confocal fluorescence microscopy beyond the fluorescence lifetime limit. *Optica*, **5** (2018) 117. https://doi.org/10.1364/optica.5.000117.

252. H. Kanno, H. Mikami, & K. Goda, High-speed single-pixel imaging by frequency-time-division multiplexing. *Optics Letters*, **45** (2020) 2339–2342.

253. X. Zou, E. Ying, & S. Dong, Seed-mediated synthesis of branched gold nanoparticles with the assistance of citrate and their surface-enhanced Raman scattering properties. *Nanotechnology*, **17** (2006) 4758–4764. https://doi.org/10.1088/0957-4484/17/18/038.

254. K. C. Grabar, K. J. Allison, B. E. Baker, R. M. Bright, K. R. Brown, R. G. Freeman, A. P. Fox, C. D. Keating, M. D. Musick, & M. J. Natan, Two-dimensional arrays of colloidal gold particles: A flexible approach to macroscopic metal surfaces. *Langmuir*, **12** (1996) 2353–2361. https://doi.org/10.1021/la950561h.

255. Y. Jin, X. Kang, Y. Song, B. Zhang, G. Cheng, & S. Dong, Controlled nucleation and growth of surface-confined gold nanoparticles on a (3-aminopropyl)trimethoxysilane-modified glass slide: A strategy for SPR substrates. *Analytical Chemistry*, **73** (2001)

2843–2849. https://doi.org/10.1021/ac001207d.

256. J. Turkevich, P. C. Stevenson, & J. Hillier, A study of the nucleation and growth processes in the synthesis of colloidal gold. *Discussions of the Faraday Society*, **11** (1951) 55–75. https://doi.org/10.1039/DF9511100055.

257. F. Schulz, T. Homolka, N. G. Bastús, V. Puntes, H. Weller, & T. Vossmeyer, Little adjustments significantly improve the Turkevich synthesis of gold nanoparticles. *Langmuir*, **30** (2014) 10779–10784. https://doi.org/10.1021/la503209b.

258. J. Kimling, M. Maier, B. Okenve, V. Kotaidis, H. Ballot, & A. Plech, Turkevich method for gold nanoparticle synthesis revisited. *Journal of Physical Chemistry B*, **110** (2006) 15700–15707. https://doi.org/10.1021/jp061667w.

259. P. Dagtepe, V. Chikan, J. Jasinski, & V. J. Leppert, Quantized growth of CdTe quantum dots; observation of magic-sized CdTe quantum dots. *Journal of Physical Chemistry C*, **111** (2007) 14977–14983. https://doi.org/10.1021/jp072516b.

260. M. Grabolle, M. Spieles, V. Lesnyak, N. Gaponik, A. Eychmüller, & U. Resch-Genger, Determination of the fluorescence quantum yield of quantum dots: Suitable procedures and achievable uncertainties. *Analytical Chemistry*, **81** (2009) 6285–6294. https://doi.org/10.1021/ac900308v.

261. X. Huang, L. Jing, S. V. Kershaw, X. Wei, H. Ning, X. Sun, A. L. Rogach, & M. Gao, Narrowing the Photoluminescence of Aqueous CdTe Quantum Dots via Ostwald Ripening Suppression Realized by Programmed Dropwise Precursor Addition. *Journal of Physical Chemistry C*, **122** (2018) 11109–11118. https://doi.org/10.1021/acs.jpcc.8b01053.

262. M. Kominkova, V. Milosavljevic, P. Vitek, H. Polanska, K. Cihalova, S. Dostalova, V. Hynstova, R. Guran, P. Kopel, L. Richtera, M. Masarik, M. Brtnicky, J. Kynicky, O. Zitka, & V. Adam, Comparative study on toxicity of extracellularly biosynthesized and laboratory synthesized CdTe quantum dots. *Journal of Biotechnology*, **241** (2017) 193–200. https://doi.org/10.1016/j.jbiotec.2016.10.024.

263. O. Otto, P. Rosendahl, A. Mietke, S. Golfier, C. Herold, D. Klaue, S. Girardo, S. Pagliara, A. Ekpenyong, A. Jacobi, M. Wobus, N. Töpfner, U. F. Keyser, J. Mansfeld, E. Fischer-

Friedrich, & J. Guck, Real-time deformability cytometry: On-the-fly cell mechanical phenotyping. *Nature Methods*, **12** (2015) 199–202. https://doi.org/10.1038/nmeth.3281.

264. P. A. Boucher, B. Joós, M. J. Zuckermann, & L. Fournier, Pore formation in a lipid bilayer under a tension ramp: Modeling the distribution of rupture tensions. *Biophysical Journal*, **92** (2007) 4344–4355. https://doi.org/10.1529/biophysj.106.092023.

265. H. D. Summers, M. R. Brown, M. D. Holton, J. A. Tonkin, N. Hondow, A. P. Brown, R. Brydson, & P. Rees, Quantification of nanoparticle dose and vesicular inheritance in proliferating cells. *ACS Nano*, **7** (2013) 6129–6137. https://doi.org/10.1021/nn4019619.

266. S. Modi, M. G. Swetha, D. Goswami, G. D. Gupta, S. Mayor, & Y. Krishnan, A DNA nanomachine that maps spatial and temporal pH changes inside living cells. *Nature Nanotechnology*, **4** (2009) 325–330. https://doi.org/10.1038/nnano.2009.83.

267. R. J. Lee, S. Wang, & P. S. Low, Measurement of endosome pH following folate receptor-mediated endocytosis. *Biochimica et Biophysica Acta - Molecular Cell Research*, **1312** (1996) 237–242. https://doi.org/10.1016/0167-4889(96)00041-9.

268. C. Wang, T. Zhao, Y. Li, G. Huang, M. A. White, & J. Gao, Investigation of endosome and lysosome biology by ultra pH-sensitive nanoprobes. *Advanced Drug Delivery Reviews*, **113** (2017) 87–96. https://doi.org/10.1016/j.addr.2016.08.014.

269. C. Abe, Y. Uto, A. Kawasaki, C. Noguchi, R. Tanaka, T. Yoshitomi, Y. Nagasaki, Y. Endo, & H. Hori, Evaluation of the in vivo antioxidative activity of redox nanoparticles by using a developing chicken egg as an alternative animal model. *Journal of Controlled Release*, **182** (2014) 67–72. https://doi.org/10.1016/j.jconrel.2014.03.015.

270. R. M. Sainz, J. C. Mayo, D. X. Tan, S. Lopez-Burillo, M. Natarajan, & R. J. Reiter, Antioxidant activity of melatonin in Chinese hamster ovarian cells: Changes in cellular proliferation and differentiation. *Biochemical and Biophysical Research Communications*, **302** (2003) 625–634. https://doi.org/10.1016/S0006-291X(03)00230-4.

271. C. A. R. Auchinvole, P. Richardson, C. McGuinnes, V. Mallikarjun, K. Donaldson, H.

McNab, C. J. Campbell, D. O. Auchinvole, E. Document, P. R. Statement, & A. C. Society, Edinburgh Research Explorer Monitoring intracellular redox potential changes using SERS nanosensors SERS Nanosensors **. *ACS Nano*, **6** (2012) 888–896. https://doi.org/10.1021/nn204397q.

272. A. Liu, M. Islam, N. Stone, V. Varadarajan, J. Jeong, S. Bowie, P. Qiu, E. K. Waller, A. Alexeev, & T. Sulchek, Micro fl uidic generation of transient cell volume exchange for convectively driven intracellular delivery of large macromolecules. *Materials Today*, **21** (2018) 703–712. https://doi.org/10.1016/j.mattod.2018.03.002.

273. N. G. Bastús, J. Comenge, & V. Puntes, Kinetically controlled seeded growth synthesis of citrate-stabilized gold nanoparticles of up to 200 nm: Size focusing versus ostwald ripening. *Langmuir*, **27** (2011) 11098–11105. https://doi.org/10.1021/la201938u.

274. X. Ji, X. Song, J. Li, Y. Bai, W. Yang, & X. Peng, Size control of gold nanocrystals in citrate reduction: The third role of citrate. *Journal of the American Chemical Society*, **129** (2007) 13939–13948. https://doi.org/10.1021/ja074447k.

275. N. R. Jana, L. Gearheart, & C. J. Murphy, Seeding growth for size control of 5-40 nm diameter gold nanoparticles. *Langmuir*, **17** (2001) 6782–6786. https://doi.org/10.1021/la0104323.

276. N. G. Khlebtsov, Determination of size and concentration of gold nanoparticles from extinction spectra. *Analytical Chemistry*, **80** (2008) 6620–6625. https://doi.org/10.1021/ac800834n.

277. M. Y. Berezin & S. Achilefu, Fluorescence Lifetime Measurements and Biological Imaging. *Chemical Reviews*, **110** (2010) 2641–2684. https://doi.org/10.1021/cr900343z.Fluorescence.

278. M. Bier, S. M. Hammer, D. J. Canaday, & R. C. Lee, Kinetics of sealing for transient electropores in isolated mammalian skeletal muscle cells. *Bioelectromagnetics*, **20** (1999) 194–201. https://doi.org/10.1002/(SICI)1521-186X(1999)20:3<194::AID-BEM6>3.0.CO;2-0.

279. D. R. Gossett & D. Di Carlo, Particle focusing mechanisms in curving confined flows. *Analytical Chemistry*, **81** (2009) 8459–8465. https://doi.org/10.1021/ac901306y.

280. J. Gala de Pablo, F. J. Armistead, S. A. Peyman, D. Bonthron, M. Lones, S. Smith, & S. D. Evans, Biochemical fingerprint of colorectal cancer cell lines using label-free live single-cell Raman spectroscopy. *Journal of Raman Spectroscopy*, **49** (2018), 1323-1332. https://doi.org/10.1002/jrs.5389.

281. P. I. T. Thomson, V. L. Camus, Y. Hu, & C. J. Campbell, Series of quinone-containing nanosensors for biologically relevant redox potential determination by surface-enhanced Raman spectroscopy. *Analytical Chemistry*, **87** (2015) 4719–4725. https://doi.org/10.1021/ac504795s.

282. M. D. Bourn, D. V. B. Batchelor, N. Ingram, J. R. McLaughlan, P. L. Coletta, S. D. Evans, & S. A. Peyman, High-throughput microfluidics for evaluating microbubble enhanced delivery of cancer therapeutics in spheroid cultures. *Journal of Controlled Release*, **326** (2020) 13–24. https://doi.org/10.1016/j.jconrel.2020.06.011.

283. A. K. Srivastava, W. Zhang, J. Schneider, J. E. Halpert, & A. L. Rogach, Luminescent Down-Conversion Semiconductor Quantum Dots and Aligned Quantum Rods for Liquid Crystal Displays. *Advanced Science*, **6** (2019) 1–20. https://doi.org/10.1002/advs.201901345.